ACTIVITY REPORT 2021

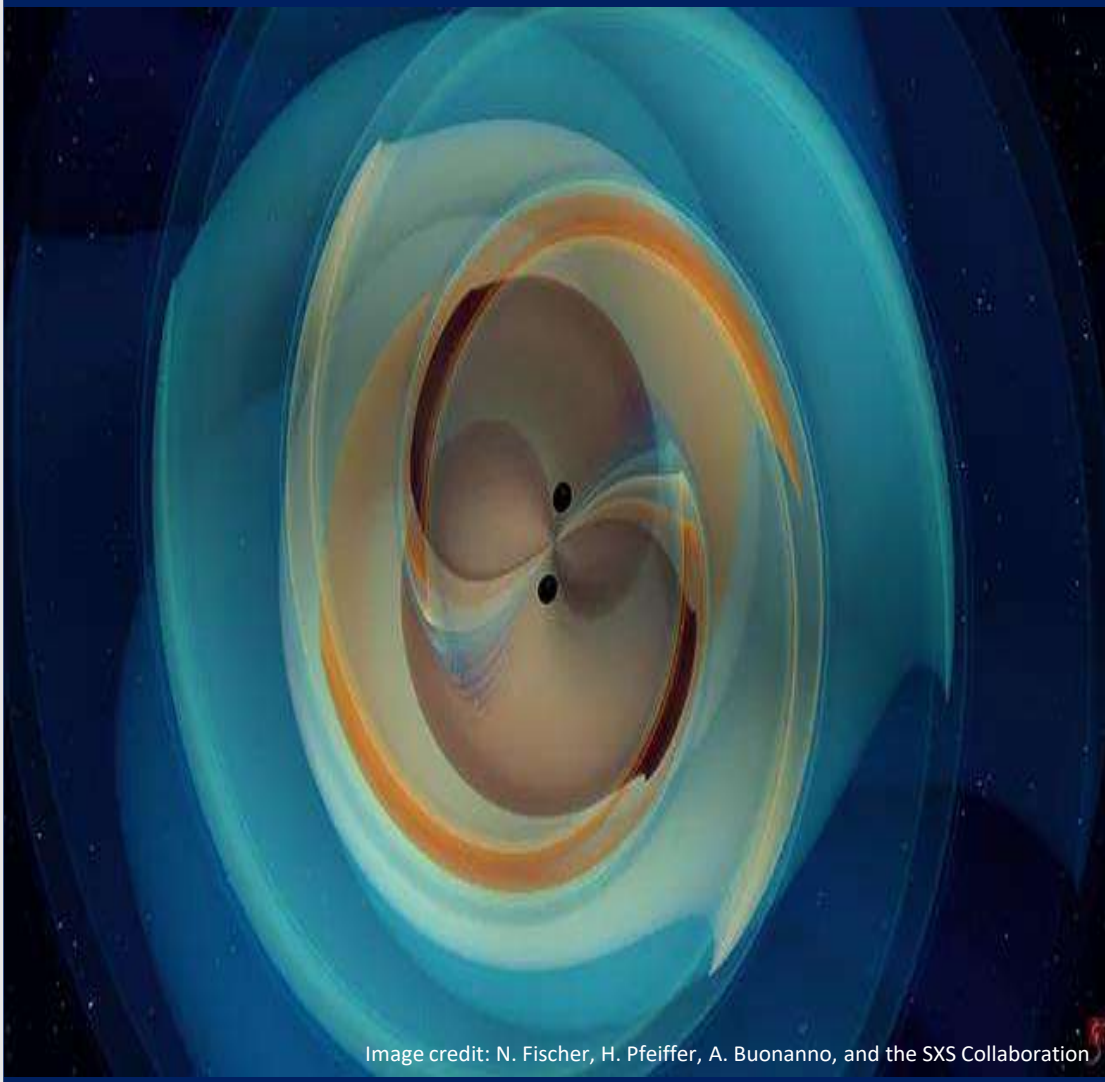

Image credit: N. Fischer, H. Pfeiffer, A. Buonanno, and the SXS Collaboration

CORSO DI DOTTORATO DI RICERCA IN FISICA
UNIVERSITÀ DEGLI STUDI DI MESSINA

Dipartimento di Scienze Matematiche e Informatiche, Scienze Fisiche e Scienze della Terra (MIFT)

ISSN: 2038-5889

COORDINATORE: VINCENZA CRUPI

Coordinatore del Dottorato di Ricerca in Fisica

Prof.ssa Vincenza Crupi

Comitato Organizzatore

Prof.ssa Vincenza Crupi
Dott. Giuseppe Paladini

Collegio Docente

Docenti e Ricercatori UNIME

Prof.ssa Branca Caterina
Dott. Calabretta Michele
Dott. Caridi Francesco
Dott. Corsaro Carmelo
Dott. Costa Dino
Prof.ssa Crupi Vincenza
Dott. Di Stefano Omar
Prof.ssa Fazio Enza
Prof. Magazù Salvatore
Prof. Majolino Domenico
Prof. Mandaglio Giuseppe
Dott. Munaò Gianmarco
Prof. Neri Fortunato
Prof.ssa Orecchio Barbara
Prof. Patanè Salvatore
Prof.ssa Presti Debora
Prof. Prestipino Giarritta Santi
Prof.ssa Saija Rosalba
Prof. Savasta Salvatore
Prof. Sergi Alessandro
Prof.ssa Silipigni Letteria
Dott. Stassi Roberto
Prof. Torrisi Lorenzo
Prof. Trifirò Antonio
Prof.ssa Trimarchi Marina
Prof.ssa Venuti Valentina
Prof. Wanderlingh Ulderico

Personale non accademico dipendente di altri Enti e Personale docente di Università Straniere

Dott.ssa Curatolo Maria Cristina
Dott.ssa Cutroneo Mariapompea
Dott. Gucciardi Pietro Giuseppe
Dr.ssa Iatì Maria Antonia
Dott. Maragò Onofrio
Dott.ssa Puglisi Rosaria Anna
Dott. Saija Franz
Dott. Trusso Sebastiano

I membri del collegio evidenziati in **grassetto** fanno parte del Consiglio ristretto di Dottorato.

DIPARTIMENTO DI SCIENZE MATEMATICHE E INFORMATICHE, SCIENZE FISICHE E SCIENZE DELLA TERRA

Dottorato di Ricerca in Fisica

Dottorato di Ricerca in Fisica
Università Degli Studi di Messina

ACTIVITY REPORT
2021

ISSN 2038-5889

Dipartimento di Scienze Matematiche e Informatiche, Scienze Fisiche e Scienze della Terra

Università degli Studi di Messina
Viale F. Stagno d'Alcontres 31, 98166, Messina

Vincenza Crupi Coordinatore

https://www.unime.it/it/dottorato/fisica

Indice

Reports Studenti di Dottorato Ciclo XXXV

L. Anoldo, G. Malta, B. Mazza, G. G. Piccione, A. Russo, M. Calabretta, S. Russo, A. Sitta, A. Messina, A. Lionetto, S. Patanè:
Multchip SiC-based compact module for automotive applications: a high speed thermal study 3

L. Biondo, G. Mandaglio:
π^0 *exclusive electroproduction - Trigger Efficiency Study for CLAS12 Forward Tagger* 7

R. Musotto, G. Pioggia, A. D'Ascola, S. Vasi, M. De Pittx, U. Wanderlingh:
Visualization of Astrocytes activity by fluorescence microscopy 11

A. Saidi, R. Saija:
PhD in Physics 2020-2021 Activities report 2nd year PhD (XXXV Cycle) 19

Reports Studenti di Dottorato Ciclo XXXVI

S. Grazzi, G. Mandaglio, M. Battaglieri:
Feasibility study of a coherent neutrino scattering experiment on nucleus at the JLAB and Streaming-Readout test facility for future detectors. 25

A. Grimaldi:
Spintronics-Compatible Probabilistic Computing Applied to Boolean Satisfiability Problems 29

G. Malta, F. Gabriele Campisi, G. Romano, S. Patanè:
Stress-Induced Frequency Shifts in Gallium Nitride (GaN) Devices Probed by Micro-Raman Spectroscopy 33

F. Mauceri, A. Mercurio:
Ultrastrong Coupling of a Qubit with a Nonlinear Optical Resonator 38

G. G. Piccione, G. Mauromicale, M. Calabretta, S. Patanè:
Investigation of the thermal behavior of a 7kW interleaved module for automobile fast charging 41

F. Risitano:
Calibration and Status of the CLIR Experiment at LNS 46

A. Semprebello, M. T. Caccamo, G. Castorina, S. Magazù:
WRF-Chem model applied to Etna volcanic ash transport and fallout 50

M. Vacalebre, R. Frison, E. Anastasi, E. Fazio, M. C. Curatolo:
An accurate approach to measure dioptric power of intraocular lenses 54

Reports Studenti di Dottorato Ciclo XXXVII

A. Fulci:
Jefferson Lab Intense Muon bEam (J-LIμE) simulations 59

S. Marrara, A. Mandanici, R. Saija, O. M. Maragò, M.G. Donato:

Acoustic tweezers and their optical characterization 64

C. Spampinato, S. Valastro, E. Smecca, G. Mannino, A. La Magna, F. Neri, E. Fazio, A. Alberti:
Spongy TiO_2 layers deposited by gig-lox sputtering processes for Perovskite Solar Cells 68

S. E. Spoto, F. Caridi, V. Venuti:
Archaeometric investigations of blue-pigmented plasters from the Church of the Annunciation (Tortorici, Italy) . 72

A. S. Triolo:
Characterization and commissioning of the upgraded Inner Tracking System (ITS2) of the ALICE experiment at LHC 75

V. Vecchio:
Optical Crystallographic and Petrographic Characterization of Medieval Stuccoes Coming from Reggio Calabria and Rossano (Italy) 80

Z. Dahrouch, C. Triolo, S. Santangelo, S. Patanè:
Synthesis, Characterization and Photocatalytic Activity of Electrospun Zinc and/or Titanium Oxide Nanofibers for Methylene Blue Degradation 84

Seminari del Dottorato di Ricerca in Fisica

Elenco dei Seminari Obbligatori 91

Premi e Riconoscimenti 97

Organizzazione del Dottorato di Ricerca in Fisica

Organizzazione 99

Collegio dei Docenti del Dottorato di Ricerca in Fisica

Collegio Docente 110

Tesi e Argomenti di Ricerca Studenti del Dottorato di Ricerca in Fisica

Tesi degli Studenti del Ph.D. in Fisica (Ciclo XXXIV) 112

Argomento di Ricerca degli Studenti del Ph.D. in Fisica (Cicli XXXV & XXXVI) 113

Pubblicazioni degli Studenti del Dottorato di Ricerca in Fisica

Pubblicazioni degli Studenti del Dottorato in Fisica (XXXV Ciclo) 116

Pubblicazioni degli Studenti del Dottorato in Fisica (XXXVI Ciclo) 118

Alta Formazione, Ricerca Scientifica e Relazioni Internazionali

Alta Formazione, Ricerca Scientifica e Relazioni Internazionali 122

Messina, 1 Ottobre 2021

Carissimi Colleghi e carissimi Studenti,

Ci accingiamo ad iniziare il nuovo Anno Accademico 2021-2022 ancora in emergenza pandemica, ma questa volta con la maggiore convinzione rispetto all'anno appena trascorso che tutto presto sarà superato, e ciò grazie alle promesse "mantenute" della ricerca scientifica che ha dimostrato ancora una volta di essere l'unica vera e concreta arma vincente.

Nonostante le difficoltà che sicuramente dovranno affrontare i dottorandi appena immatricolati del XXXVII ciclo insieme ai colleghi dei cicli già attivi, XXXVI e XXXV ciclo, sono certa che come già successo in passato l'offerta formativa del Corso di Dottorato di Ricerca in Fisica saprà dare il giusto input per una proficua attività di studio e di ricerca grazie alla sua completezza e al suo carattere fortemente interdisciplinare. A questo proposito, continuano infatti in piena sinergia le consolidate collaborazioni con aziende private di alta qualificazione scientifica che incentivano il settore R&D, quali ST-Microelectronics e SIFI. A partire da questo anno accademico, oltre alle convenzioni con le succitate aziende, è stata rinnovato l'accordo con il Distretto Tecnologico Sicilia Micro e Nano Sistemi, società consortile costituita da imprese, università ed enti pubblici e privati di ricerca.

Alle 5 borse di studio ministeriali di Ateneo assegnate al Corso di dottorato di Ricerca in Fisica relative al XXXVII ciclo, si aggiungono quest'anno due ulteriori posizioni con borse aggiuntive a valere sul PON "Ricerca e Innovazione" 2014-2020 Azioni IV.4 "Dottorati e contratti di ricerca su tematiche dell'innovazione" e Azione IV.5 "Dottorati su tematiche Green". Sottolineo con piacere che per il secondo anno consecutivo sono pervenute più di 30 domande, delle quali 21 da parte di candidati stranieri in possesso di laurea magistrale conseguita presso università straniere, confermando un trend sicuramente positivo che avvalora la qualità dell'offerta formativa del corso di dottorato.

Concludo questa mia breve introduzione, ringraziando tutti i Colleghi del Collegio di Dottorato, personale accademico e non, per l'entusiasmo che ogni anno mettono in ogni attività di approfondimento e di ricerca proposta ai dottorandi, stimolando una sempre vivace e rinnovata attività scientifica, ricca di contenuti attuali, all'avanguardia nel panorama della ricerca attuale.

Non mi resta che augurare a tutti noi, Buon Anno Accademico!

Reports

Studenti di Dottorato di Ricerca

Ciclo XXXV

Multchip SiC-based compact module for automotive applications: a high speed thermal study

L. Anoldo[1,2], G. Malta[1,2], B. Mazza[1,2], G. G. Piccione[1], A. Russo[2], M. Calabretta[2], S. Russo[2], A. Sitta[2], A. Messina[2,3], A. Lionetto [2], S. Patanè[1]

[1] *Dipartimento di Scienze Matematiche e Informatiche, Scienze Fisiche e Scienze della Terra, University of Messina, Viale F. S. d'Alcontres n 31, 98166 Messina Italy.*

[2] *STMicroelectronics, Stradale Primosole, 50, 95125 Catania, Italy*

[3] *CNR Institute for Microelectronics and Microsystems - 95121 Catania, Italy - Strada VIII, 5*

*Corresponding Author email: laura.anoldo@unime.it

Abstract

Nowadays the increasing demand of high-efficiency power devices for automotive framework, forced the scientific community to develop new technologies capable to operate under intense power loads. Among the broad scenario SiC-based substrates represent a promising solution. This study focuses on a high-speed thermal characterization of a power module designed by STMicroelectronics (ACEPACK Drive) with the aim to provide a map of the temperature values reached at the surface upon current-pulse stresses. Thermal images collected on one leg reveled a distribution of temperatures which is almost symmetric, with a maximum at around 60°C in order to avoid any reliability issue.

Keywords: Power electronic device, Silicon Carbide, Thermal mapping, Automotive..

Introduction

The growing interest in replacing internal combustion engine vehicles with highly efficient electric one, speeds up wide bandgap semiconductors (WBG) to penetrate the power electronic market. Remarkable attention has been paid to electronic devices designed to drive highly efficient and lightweight motors capable of reducing battery costs by improving vehicle performance. Among the WBGs, SiC exhibits fast switching speeds, low on-resistance and superior temperature handling, allowing the design of novel devices and systems [1]. The use of this new material unlocks new issues concerning the reliability and design both at device and system level [2]. One of the most demanding applications concerns the driving of electric motors as this requires excellent reliability reduced spaces and thermal compatibility with dissipation systems typically installed on cars. This application requires the use of power transistors capable of manage large current pulses with times of the order of a fraction of millisecond [3] [4]. These operating regimes require quite different analysis and techniques to evaluate the reliability compared to that usually used to qualify the power devices in switching applications. In fact, these systems operate at much higher frequencies, hence, due to the thermal capacity of the semiconductor and to the diffusive character of the thermal energy, the distribution of the heat on the device assumes an average value. Therefore, in normal switching application the thermal behavior can be considered almost continuous. In the case of systems driving the automotive motors, the involved frequencies range from a few tens of Hz to a few thousands Hz. The dynamic thermal behavior and temperature gradient inside SiC devices has to be accounted and analyzed for this frequency range. In other words, the thermal capacity of the devices is not large enough to mediate the temperature fluctuations induced by the current pulses. What above results in cyclic thermomechanical stresses following the current pulses and involving the semiconductor layers and the metal. The related aging phenomena is accelerated both by the number of cycles and by the speed with which the thermal swing is achieved. The objective of this study is to evaluate the real maximum temperature reached by commercial SiC MOSFET modules during operative commutation. A dedicated finite element model is developed to calculate the temperature profile of die top surface. Analysis is correlated with experimental evidence. In this frame, recently different solutions have been proposed to reduce space and without giving up the ability to manage large powers. One possible topology consists in integrating in a single package a 3-phase full bridge. This work deal on the thermal characterization of this kind of topology focusing on the already available on the market power module by ST Microelectronics named ACEPACK Drive. Fig. 1a shows the optical image of one leg of the ACEPACK Drive and its schematic diagram are shown in Fig. 1b.

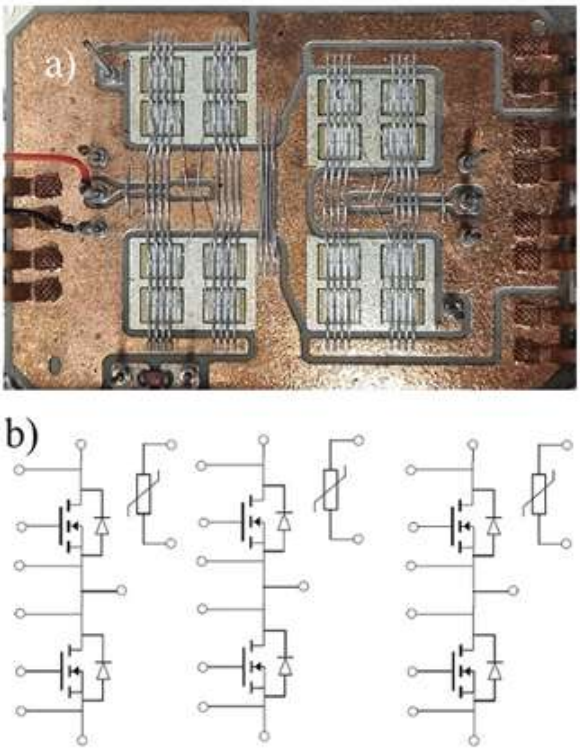

Figure 1: a) Optical image of one leg of the ACEPACK assembly, b) Schematic diagram

Device and Stress Procedure Description

The ACEPACK Drive power module features switch based on silicon carbide Power MOSFET and contains three legs each consisting of 8 silicon carbide devices, in two groups of 4. The device in this configuration exhibits an RDSON of 3.5mΩ, this is guaranteed for a block voltage of 1200V, and can handle currents of over 800A. This component therefore represents an excellent candidate for automotive applications and more generally for making electric motor drivers. The structure consists of a direct cooled Cu base plate with pin fins system and integrates 3 NTC temperature sensors. Particular attention has been paid to heat dissipation using a Si3N4 Active Metal Brazed which improves thermal dissipation. The very low switching energy losses helps to improve system efficiency. It is very interesting to evaluate the maximum thermal jump of the SiC MOSFETs that make the legs during a current pulse, as this information is crucial for the reliability assessment. For this purpose, we resort to high-speed thermal microscopy, this technique overcomes the limitations of the standard thermography and allows to follow the thermal behavior of the devices surface during the current pulses, [5] [6]. A photo of the experimental setup used is showed in 2, as described in details in the following section. Briefly, the measurement consists in acquiring the time dependent temperature values point by point rastering the surface. The thermal radiation is collected by a ZnSe optical lenses system and focused on a far infrared sensor able to work down to 14 μm. During the measurement the base plate was kept at room temperature, i.e. after each current pulse we wait a time interval large enough to dissipate the heat until the temperature come back to the starting value. The device in our experiment was connected in a short circuit configuration and undergoes to a one millisecond and 800A current pulse.

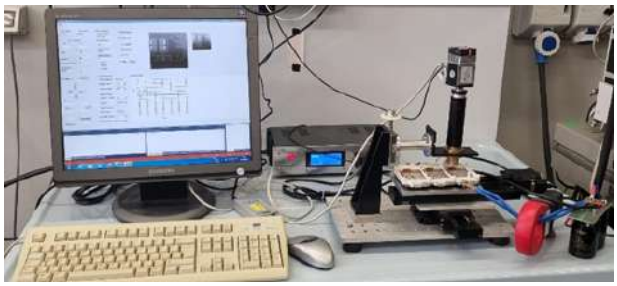

Figure 2: Experimental setup for the high-speed thermal measurement

Non invasive temperature measurement

Detecting small temperature differences on surfaces whose extension is sometimes less than one mm^2 is a challenge. In addition, in case of overloads, the transients last for some hundreds or tens of microseconds. Hence a conventional high-resolution thermal camera, whose frame rate is usually in the millisecond scale, cannot detect these thermal events. Therefore, we developed a setup to capture very high speed thermal transients [6]. It is based on the scanning technique thus acquiring the signal coming from each micrometric area (i.e. a pixel) at very high speed. The instrument is equipped with a XY mechanical scanner, a broadband reflective microscope objective and a high-speed optical detector optimized for the far infrared (see Fig. 3). The objective focuses the thermal radiation emitted from the surface onto the optical detector that evaluates, point by point, the temperature of the DUT. To collect the infrared radiations emitted by the DUT, a partial removal of the covering package over the die is often needed, except for those small devices characterized by a thin layer of package coverage. In those cases the opening process is not required, indeed, if the packaging layer is small enough, the temperature distribution on the external well represents the thermal behavior of the active parts underneath the insulating layer, thus allowing the reconstruction of the temperature on the covered chips. For each single pixel scanned on the surface the instrument performs an acquisition that is synchronized with a current pulse supplied to the DUT, capturing a temporal array with a time resolution of 5 μs (i.e. acquiring at 200 kS/s). The synchronization between the current pulse and the acquisition is accomplished by triggering the sampling process with the same signal that activates the DUT. It is also possible to insert a tunable

delay between the "enable" signal and the start of the acquisitions. Obviously, in order to spatially reconstruct the complete thermal evolution taking into account all the captured temporal arrays, the DUT undergoes a stressing event for each current pulse, i.e. for each pixel of the thermal map. For this reason, the time interval between two pulses has to be long enough to assure that the starting temperature is the same for each current pulse. This interval is experimentally defined through preliminary tests executed on the DUT, indeed it strongly depends on peculiar structure of the DUT and on the expected dissipated power during the current pulse. If the starting temperature and the thermal stress are the same for each acquired pixel, the thermal maps will correctly describe the temperature behavior due to the current pulses. A 36x lateral magnification objective has been used to collect the electromagnetic field emitted by the DUT and to focus on the 1 mm^2 active area of the detector. The optical assembly allows a resolution of about 27 μm x 27 μm squared area. The scanned grid can be suitably adjusted and adapted to the area of interest on the device surface. Analyzing the sequence of thermal maps, it is possible to localize the hot-spots and to acquire valuable information to improve the design of the protection control system, with a special attention to the correct position of the temperature sensors. Moreover, it is possible to reconstruct a thermal map that is not associated to a single instant of the acquired thermal event but rather on the whole acquired time-evolution. This remarkable thermal map will be obtained by plotting the maximum values of temperature for each temporal array acquired on the surface. Hence, this map describes the maximum temperature for each point on the surface and it localizes the hot-spot during the entire working cycle.

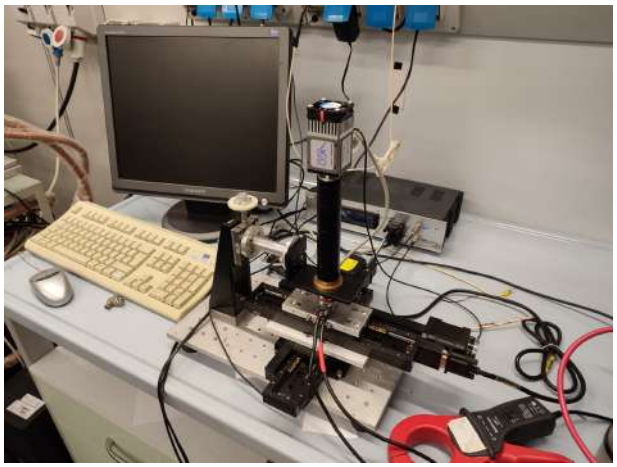

Figure 3: Measurement instrument

Results and Discussion

To evaluate the maximum temperature reached by the device's surface we collect the thermal image at 1ms after the current pulse starts (see Fig. 4). The thermal distribution is almost symmetric and involve the four devices of half leg in the same way. The shadow of the wire is well visible indicating their temperature is below the surface one. A more complete analysis, involving the entire leg is on the way. The maximum temperature reached by the surface is relatively low and does not exceed 60°C. Observing the ACEPACK Drive layout it highlights that it is not symmetric, hence a difference in the temperature reached by each of the groups, however unlikely it is possible. To clarify this point further investigations are in progress. Electro-thermal finite element analysis will be carried out to analyze the temperature distribution on dies' top surface replicating the same boundary conditions and forcing pulse (800A for 1ms).

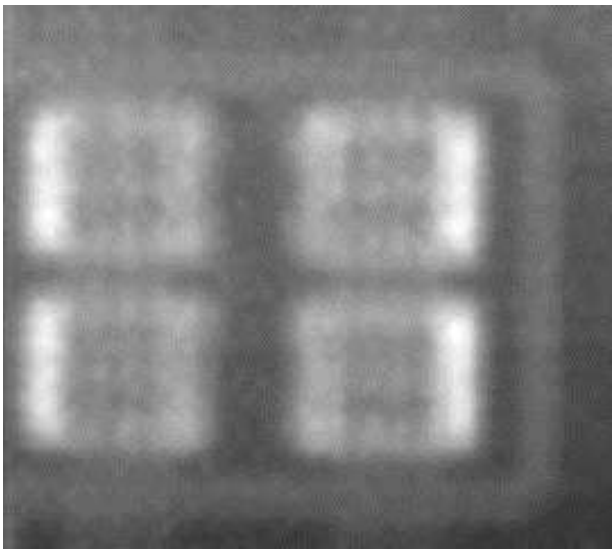

Figure 4: Thermal map acquired at 1ms after the current pulse starts

Conclusions

In conclusion the high-speed thermal mapping on silicon carbide Power MOSFET -based ACEPACK drive reveals the metal surface thermal swing reached during a one millisecond and 800A current pulse does not exceed 60°C. During the current cycling the temperature of the wires is relatively low, hence the thermomechanical stress is mainly borne by the metal. The study of this thermomechanical stress plays a key role in the assessment of the device lifetime and give an insight of its failure mechanisms, in order to improve its reliability.

References

[1] Roccaforte, Fabrizio, et al. : *"Emerging trends in wide band gap semiconductors (SiC and GaN) technology for power devices." Microelectronic Engineering 187 : 66-77.*. (2018).

[2] Wang, J., Jiang, X.: *Review and analysis of SiC MOSFETs' ruggedness and reliability. IET Power Electronics* **13(3)**, 445-455 (2020).

[3] Arumugam, P., Xu, Z.: *High-speed solid rotor permanent magnet machines: Concept and design. IEEE Transactions on Transportation Electrification,* **2(3)**, 391-400 (2016).

[4] Feng, W., Ding, H.: *Design of High Power Density 100 kW Surface Permanent Magnet Machine with No Heavy Rare Earth Material Using Current Source Inverter for Traction Application. In 2021 IEEE Transportation Electrification Conference Expo (ITEC) IEEE.* (pp. 1-6)(2021, June).

[5] Anoldo, L., Triolo, C., Panarello, S., Garescì, F., Russo, S., Messina, A. A., Patanè, S.: *Study of the Thermomechanical Strain Induced by Current Pulses in SiC-Based Power MOSFET. IEEE Electron Device Letters, 42(7), 1089-1092.* (2021).

[6] Panarello, S., Patanè, S.: *An infrared thermal measuring system for automotive applications and reliability improvement. In Sensors and Microsystems (pp. 461-465). Springer, Dordrecht.* (2011).

π^0 exclusive electroproduction - Trigger Efficiency Study for CLAS12 Forward Tagger

L. Biondo[1,2,3,*], G. Mandaglio[1,2]
[1] *Dipartimento MIFT, University of Messina, Messina, Italy*
[2] *INFN sezione di Catania, Catania, Italy*
[3] *Thomas Jefferson National Accelerator Facility, 628 Hofstadter Road, Suite 6, Newport News, VA 23606*

*Corresponding Author email: lbiondo@unime.it

Abstract

The CEBAF Large Acceptance Spectrometer for operation at 12 GeV beam energy (CLAS12) in Hall B at Jefferson Laboratory is used to study electro-induced nuclear and hadronic reactions. This spectrometer provides efficient detection of charged and neutral particles over a large fraction of the full solid angle. All the CLAS12 capabilities are being used in a broad program to study the structure and interactions of nucleons, nuclei, and mesons, using polarized and unpolarized electron beams and targets for beam energies up to 11 GeV. The MesonEx experiment use CLAS12 to investigate how the QCD partons manifest themselves under the strong interaction at the energy scale of the nucleon mass (GeV). In this paper we focus on the study of the Forward Tagger, a detector consisting of a calorimeter, scintillation hodoscope and tracking device, added to the standard equipment to detect the scattered electrons at low polar angles. With the focus of investigate exclusive π^0 electroproduction, Trigger efficiency for the Forward Tagger, analysis were carried on, in order to confirm the correct data acquisition. The latter were carried on in collaboration with INFN, and will be briefly presented. Analysis on different data samples showed a good efficiency of the Triggering System. Further investigations are needed to understand the presence of some trigger inefficiency in the off-diagonal area. Graphs showing the detector efficiency are also presented.

Keywords: Hadronic Resonances, Low-Q2 electron scattering, CLAS12, JLAB.

Introduction

CLAS12 has been part of the energy-doubling project of Jefferson Lab's Continuous Electron Beam Accelerator Facility, funded by the United States Department of Energy. Fig.[2] An international collaboration of over 40 institutions contributed to the design and construction of detector hardware, developed the software packages for the simulation of complex event patterns, and commissioned the detector systems. CLAS12 is based on a dual-magnet system with a superconducting torus magnet that provides a largely azimuthal field distribution that covers the forward polar angle range up to 35 deg, and a solenoid magnet and detector covering the polar angles from 35 deg to 125 deg with full azimuthal coverage. Trajectory reconstruction in the forward direction using drift chambers and in the central direction using a vertex tracker results in momentum resolutions of $< 1\%$ and $< 3\%$, respectively. Cherenkov counters, time-of-flight scintillators, and electromagnetic calorimeters provide good particle identification. These capabilities are being used in a broad program to study the structure and interactions of nucleons, nuclei, and mesons, using polarized and unpolarized electron beams and targets for beam energies up to 11 GeV. In MesonEx a comprehensive study of the meson spectrum with precise determination of resonance masses and properties with a high statistics and high resolution experiment is proposed. The meson spectrum in the mass range $1.5 - 2.5$ GeV will be studied looking for rare $q\bar{q}$ states and unconventional mesons with exotic quantum numbers. The technique, electroscattering at very low Q^2 ($10^{-2} - 10^{-1}$ GeV^2) provides a high photon flux and a high degree of linear polarization and represents a competitive and complementary way to study the meson spectrum and production mechanisms with respect to real photoproduction experiments. A Forward Tagger (FT) consisting of a calorimeter, scintillation hodoscope and tracking device will be added to the standard equipment to detect the scattered electrons in the angular range $\theta_{e'} = 2.5^\circ - 4.5^\circ$ and energy range $E_{e'} = 0.5 - 4.5$ GeV. Events will be selected by the FT only when meeting strict conditions. To check if the machinery works properly we selected the $\vec{e} + p \rightarrow e + p + \pi^0$ channel of reaction, and the respective triggering condition: 2 energy cluster produced by the scintillator, both with $500 < E < 8000$ MeV and with a difference in detection time not higher than 20 ns. Further analysis revealed the needs for supplementary investigation, aimed at a better understanding of the Trigger System.

Forward Tagger

The characteristics of the detector and the trigger conditions foreseen for the experiment - 11 GeV electron beam

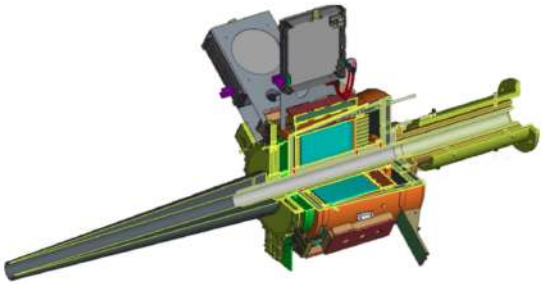

Figure 1: CAD drawing of the Forward Tagger. The FT calorimeter shown in cyan is located at about 185 cm from the beam-target interaction point and is enclosed in a copper and Rohacell case to provide thermal insulation. The scintillation counter (green) and the tracker (yellow) are located in front of the calorimeter. A tungsten cone (gray) shields the FT from Møller electrons and other electromagnetic background (low-energy photons) created by the beam. The left side of this figure represents the upstream end of the detector.

scattering on a 5cm long LH_2 target with multiple particles in the final state - will allow measurements of many final states simultaneously. While the hadrons will be detected in the CLAS12 spectrometer [1], the electron scattered at very small angles (2.5° to 4.5° in polar angle) and low four momentum transfer, Q^2, will be detected in the Forward Tagger (FT). The FT specifications were thus defined to have optimal electron detection in this angular range, compatible with the high rate of electromagnetic background. To reconstruct the quasi-real photon variables, it is necessary to measure the scattered electron three momentum. The relevant quantities are:

- The energy $E_{e'}$ since the photon energy is given by $E_\gamma = \nu = E_{beam} - E_{e'}$ and its linear polarization by $P_\gamma = \epsilon \sim (1 + \frac{\nu^2}{2E_{beam}E_{e'}})$;
- The azimuthal angle $\Phi_{e'}$ to determine the polarization plane,
- The polar angle $\theta_{e'}$ since: $Q^2 = 4_{Ebeam}E_{e'}sin^2(\theta_{e'}/2)$.

The FT is composed of an electromagnetic calorimeter (FT-Cal) to identify the electron in the energy range $0.5 - 4.5$ GeV by measuring its electromagnetic shower energy and to provide a fast trigger signal, a Micromegas tracker (FT-Trk) to measure the scattering angles ($\theta_{e'}$ and $\Phi_{e'}$), and a scintillation counter (FT-Hodo) to provide e/γ separation. The FT-Cal and FT-Hodo also provide fast signals to trigger the data acquisition [2] in coincidence with signals from CLAS12. All of these components were designed to fit within a 5.5 deg cone around the beam axis to have minimal impact on the operation and acceptance of the CLAS12 equipment in the forward direction. Figure [1] shows a CAD rendering of the FT.

The Micromegas Tracker (FT-Trk)

For a precise determination of the scattered electron angle, a tracker complements the FT-Cal and FTHodo detectors. The FT-Trk uses the same technology adopted by the CLAS12 central and forward Micromegas detectors. In this section we describe the specific design of the FT-Trk. Two double-layers of Micromegas detectors are located in front of the hodoscope, in the space between the FT and the HTCC [3]. The two detectors are indeed a good compromise to achieve an efficient background rejection and track reconstruction with a low material budget. Each layer is composed of a double-faced Micromegas disk built on a common printed circuit board (PCB). Each side of the PCB displays strips, the downstream strips being perpendicularly oriented to the upstream strips. This particular geometry enables the determination of the (x;y) coordinates (perpendicular to the beam z -axis) of a track. To limit the number of electronics channels, the pitch chosen was 500 μm, which leads to a resolution better than 150 μm. A drift space of 5 mm, together with an amplification gap of 128 μm, provides good efficiency. The two double layers, centered on the beam axis, cover polar angles from 2.5 deg to 4.5 deg with an active area defined between a 70 mm inner radius and a 143 mm outer radius. The total number of channels is 3072. Figure 13 shows the CAD implementation of the detector. The FT-Trk read out uses the same data acquisition scheme adopted for the CLAS12 Barrel Micromegas Tracker (BMT) [4], which consists of a Front-End Unit (FEU) and a Back-End Unit (BEU). The front-end electronics are responsible for signal preamplification, shaping, buffering during the trigger generation process, data digitization, and compression. Due to the limited space available, the front-end electronics are designed to be placed off-detector. The back-end electronics are responsible for data concentration, providing the interface to the CLAS12 event building system and are the same units used for the BMT [4].

The Hodoscope (FT-Hodo)

The primary aim of the FT-Hodo is to discriminate between photons and electrons that produce an electromagnetic shower in the calorimeter. Specifically, electrons are identified by hits in the hodoscope array that are correlated in both position and time with a cluster observed in the calorimeter. The FT-Hodo is comprised by an array of 232 plastic scintillator (Eljen-204) tiles segmented in two layers to suppress contributions from the splash-back of the electromagnetic shower created by events depositing energy in the FT-Cal. The scintillators provide fast timing and sufficient resistance to radiation damage for use in the high-rate and high-dose environment of the FT. The geometry and readout of the hodoscope are constrained by the surrounding apparatus. Specifically, the device is positioned upstream of the FT-

Cal, fitting into a circular disk of diameter 330 mm and 42 mm depth. The readout is achieved using 3×3 mm^2 Hamamatsu S13360-3075PE SiPMs (50% photon detection efficiency for 450nm photons) coupled to 5-m-long clear optical fibers (Kuraray clear-PSM with attenuation length >10m), which are fusion spliced to ∼30-cm-long wavelength shifting (WLS) Kuraray Y11 fibers, embedded in the scintillator tiles. The splicing induces a photon losìs of less than 2%, where the use of optical fibers allows the captured light to be transported with a light loss of less than ∼ 40% over the 5-m path to the SiPM. This readout design of the FT-Hodo addresses the need to minimize material in the detector acceptance, to operate in regions of high magnetic fields produced by the CLAS12 solenoid and torus magnets, and to tolerate the high-background radiation environment. The FT-Hodo is comprised of two segmented plastic scintillator (Eljen-204) tile arrays, which are embedded with wavelength shifting (WLS) fibres. Read out is achieved using 3×3 mm^2 silicon photomultipliers (SiPM) via clear optical fibres. The plastic scintillators provide fast timing and sufficient resistance to ptva radiation damage for use in the high rate environments of the CLAS12 Forward Tagger.

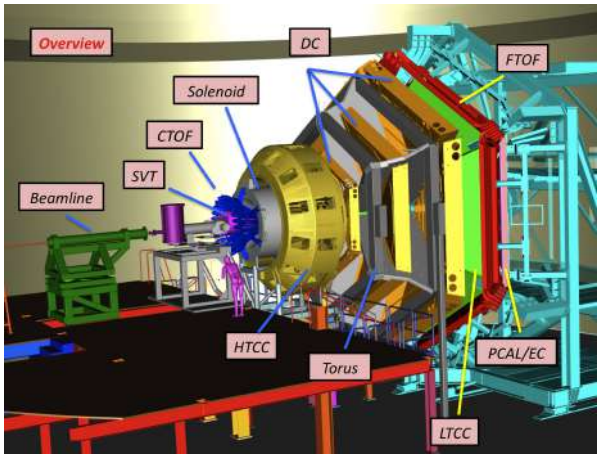

Figure 2: Scheme of CLAS12 spectrometer. All the components of the system are here highlighted: Beamline, Silicon Vertex Tracker (SVT), Central Time-of-Flight (CTOF), Solenoid, High Threshold Cherenkov Counter (HTCC), Drift Chamber (DC), Torus, Forward Time-of-Flight (FTOF), Low Threshold Cherenkov Counter (LTCC), Preshower Calorimeter &x Electromagnetic Calorimeter (PCAL/EC).

The Calorimeter (FT-Cal)

The FT-Cal has to fulfill demanding requirements in terms of: radiation hardness, light yield, shower containment (small radiation length and Moliere radius), scintillation decay time, and good energy and time resolution. The electron energy resolution is a crucial factor to determine precisely the photon energy and to ensure the exclusivity of the measured reaction via the missing mass technique. However, since we are interested in low-energy electrons and high-energy photons, the energy resolution on the latter is significantly better than the resolution of the electron. The FT-Cal should have a fast scintillation decay time ($\tau \sim 10$ ns) to sustain high rates with small pile-up effects and to provide the scattered electron interaction time with good accuracy (< 1 ns) in order to reject background and to identify the relevant signals via coincidence with CLAS12. Due to the expected high rate from electromagnetic background (∼120 MHz at the nominal luminosity of 10^35 cm^{-2}s−1), the calorimeter should be highly segmented in the transverse direction. The size of each detection element should be comparable with the characteristic transverse size of the electromagnetic shower (Moliere radius) to contain the shower produced by incident electrons to a few readout cells, thus minimizing rates and pile-up. Finally, the photodetectors for the light read out should work in a sizable magnetic field and fit within the available space. Thus, standard photomultipliers (PMTs) cannot be used, while photodetectors based on semiconductors, e.g. avalanche photodiodes (APDs), have been shown to meet the required criteria. To match the necessary requirements, lead tungstate ($PbWO_4$) was chosen as the scintillating material and Large-Area APDs (LAAPDs) as the readout sensors. The FT-Cal is made from 332 15 × 15 × 200 mm^3 parallelepiped $PbWO_4$ Type-II crystals arranged around the beamline with full azimuthal angular coverage ($0^\circ < \Phi < 360^\circ$) and small forward angle acceptance ($2^\circ < \theta < 5^\circ$). The crystals are placed with their long side parallel to the beamline to form a ring.

Data Analysis

Different analysis, using special runs data (runs from #004784 to #004789), were carried out to investigate trigger efficiency. In the special runs, of $\vec{e}+p \rightarrow e+p+\pi^0$ type, two different kind of trigger were used, which can be summarized as follow:

- Trigger Bit 27 (TB27): wide conditions (at least one energy cluster with $E > 100$ MeV. This trigger were used for flagging the events and to start the data acquisition also. It has to be noticed that TB27 has no time conditions, needing just one energy cluster to be fired.
- Trigger Bit 26 (TB26): same strict conditions used in normal runs (at least two energy cluster with $500 < E < 8000$ MeV and with a difference in detection time not higher than 20 ns). This trigger is used for flagging the events with the right conditions.

The analysis was carried out using *Clas12root*, an analysis tool based on Root (C++) and developed by CLAS12 collaboration. TB27 flagged data can be used as a comparison to investigate possible events losses, once filtered using both energy and time TB26 conditions.
Histogram c) from Fig. [3] was produced using

$$\frac{\#Events_{TB26}(E_{EC1}; E_{EC2})}{\#Events_{TB27}(E_{EC1}; E_{EC2})},$$

where the numerator and denominator are the number

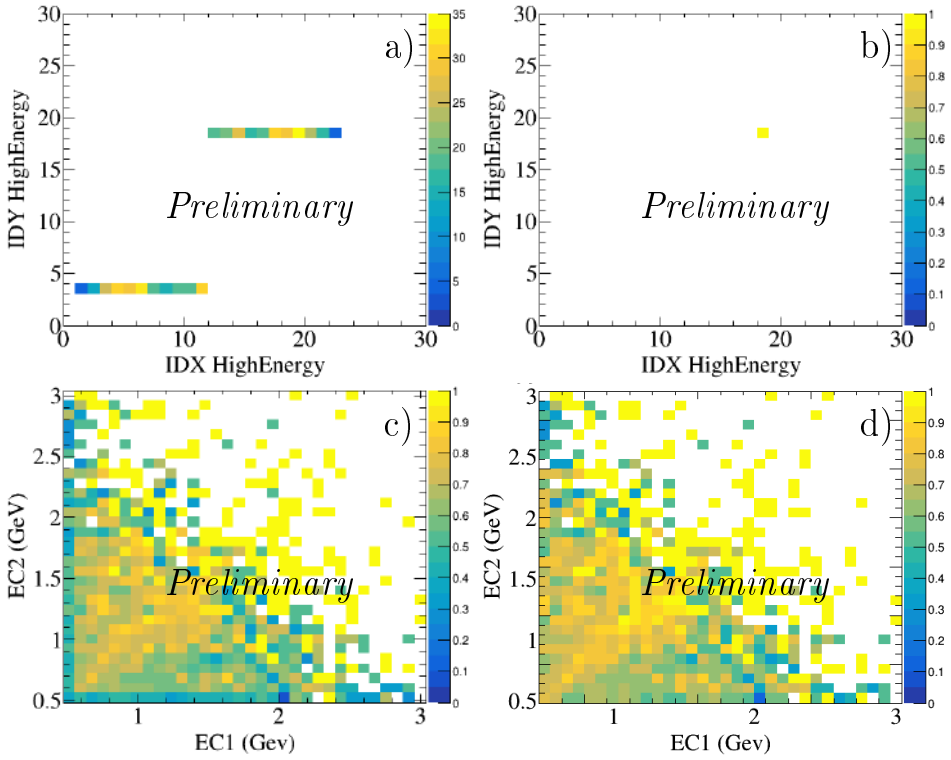

Figure 3: Trigger efficiency studies: difference between before (panels a,c) and after(panels b,d) excluding the broken run events. The b panel, reproducing the detector APD surface, shows how, excluding the broken run, the bad events can be reduced to only one, versus the almost 500 of the panel a. As can be seen watching the c and d panel, Trigger Efficiency calculated by triggering events against valid events is shown as energy varies. The efficiency increases after removing the broken run, especially in the outer zone of the graph.

of events, as the energy of the 2 energy clusters varies, which triggered the TB26 and TB27, respectively.
During data analysis 543 events with ideal time and energy conditions, but without TB26 flag, were noticed. In the a) histogram from Fig. [3] the aforementioned events are exposed, reporting the (x,y) coordinates of the hits of the energy clusters on the detector and showing a discrepancy with the expected result, awaiting an homogeneous distribution. All the events (except for one), as can be seen from b) histogram in Fig. [3], can be excluded cutting out one of the special run used for the analysis (#004787). Possible data corruption or incorrect data acquisition due to hardware problems is hypothesized. The trigger efficiency after the broken run exclusion is shown in d) histogram from Fig [3], showing good acquisition efficiency, especially in the diagonal area (the most interesting area for the ongoing studies).

Conclusion

In this paper trigger efficiency studies for forward tagger, used in MesonEx experiment for hadronic spectroscopy studies, were presented, giving an insight on CLAS12 and FT detectors structure. The analysis, carried out thanks to the Root-based software Class12root and made on special runs with two different type of trigger, show good results. The forward tagger trigger for π^0-production events works with a good efficiency. Further investigations are needed to understand the presence of trigger inefficiency in the off-diagonal area.

References

[1] V. D. Burkert, et al., The CLAS12 Spectrometer at Jefferson Laboratory, to be published in Nucl. Instrum. Meth. A, (2021).

[2] S. Boyarinov, et al., The CLAS12 data acquisition system, to be published in Nucl. Instrum. Meth. A, (2021).

[3] Y. G. Sharabian, et al., The CLAS12 high threshold Cerenkov counter, to be published in Nucl. Instrum. Meth. A, (2021).

[4] A. Acker, et al., The CLAS12 Micromegas vertex tracker, to be published in Nucl. Instrum. Meth. A, (2021).

Visualization of Astrocytes activity by fluorescence microscopy

R. Musotto[1–3,*], G. Pioggia[3], A. D'Ascola[2], S. Vasi[1], M. De Pittà[4], U. Wanderlingh[1]
[1] *University of Messina, Department of Physics, Messina, Italy*
[2] *University of Messina, Department of Microbiological, Genetic and Molecular Sciences , Messina, Italy*
[3] *National Research Council of Italy (CNR), Institute for Biomedical Research and Innovation (IRIB), Messina, Italy*
[4] *Krembil Research Institute, Toronto, Canada, University of the Basque Country, Basque center for applied mathematics, Bilbao, Spain.*

[*]Corresponding Author email: romusotto@unime.it

Abstract

Recent studies have confirmed the active role of astrocytes as an integral part in synapses. The Ca^{2+} signal is the main way that astrocyte cells have to transmit information intra and extracellular and with neurons. Fluorescence microscopy, through the use of specific fluorochromes, appears to be one of the most powerful methods for analyzing the modulation of calcium within various cells. In order to perform measurement on astrocytes colture in controlled environments (incubator) we have developed an house-made fluorescence microscopy suited to this scope.

Keywords: Astrocytes, Calcium Imaging, Fluorescence, Calcium signaling.

Introduction

Astrocytes are the most numerous cells in the Central Nervous System (CNS). Until a few years ago it was thought that astrocytes were mere support cells with similar characteristics in various brain areas. Recent discoveries have revolutionized the role of astrocytes that from passive cells have been seen to be polyvalent cells involved in almost all the processes of the CNS, they function as local integration units and bridges between synaptic and non-synaptic communication [1]. Although astrocytes are not electrically excitable cells, in particular they cannot generate action potentials, they possess a form of chemical excitability based on changes in their intracellular calcium concentration. The presence, on astrocytes, of receptors for neurotransmitters has been seen by researcher as evidence of the neuron-glia signalling[2]. It was subsequently shown that these receptors can be activated by the diffusion of neurotransmitters during synaptic activity and cause an increase in Ca^{2+} in astrocytes. This event can in turn cause the release by the astrocytes of chemical transmitters called "glyotransmitters", such as glutamate, ATP, D-serine, and lead to intercellular communication between astrocytes and neurons [3]. The glyotransmitters released by astrocytes are able to activate neuronal receptors and thus modify neuronal electrical excitability and synaptic transmission [4] [5]. These observations led to the concept of "tripartite synapses", according to which astrocytes are considered to be the third element of the signal integration unit [6] [3]. The calcium signal is recognized as the main way that astrocyte cells have to transmit information from the outside of the cell to the inside, through the cell membrane and inside the cell into the cytoplasm.
Thanks to the availability of indicators to monitor intercellular and intracellular Ca^{2+} , calcium signaling is the most studied of a possible glial codes. There are various techniques to monitor all the variations of Ca^{2+} , however, the imaging methodologies through the use of fluorescent indicators are the best application for the analysis of these signals.
On the other way the physico-chemical laws can be expressed in terms of differential equations describing the reaction kinetics. then Ca^{2+} concentration and diffusion within and trough membranes can be studied. In fact, the dynamics of Ca^{2+} have been the subject of many theoretical studies that have provided important physical-mathematical models [7] [8] [9].

Astrocytes signaling

Astrocytes, a type of glial cell of the central nervous system, have emerged as detectors and regulators of neuronal information processing[10]. Astrocytes, unlike neurons, do not show electrical excitability however, they express voltage-gated channels [11]. Astrocyte excitability derives from Ca^{2+} signals that can modulate neuronal communication. Calcium astrocytic signals are associated with brain functioning, including memory and learning, and are impaired in the diseased brain as non-excitable CNS cells [3] . The variations of Ca^{2+} represent a sophisticated signaling mechanism at the base of numerous cellular processes. It has been established that changes in Ca^{2+} in astrocytes cause the release of gly-

otransmitters, which thus act on adjacent neurons, glial cells and blood vessels. The release of gliotransmitters is caused by the activation of G protein-coupled receptors (GPCRs), followed by an increase in the concentration of 1,4,5-inositol triphosphate (IP_3), which causes the release of Ca^{2+} from the endoplasmic reticulum [12] [13]. One aspect of astrocytic signals is their ability to propagate as regenerative Ca^{2+} waves intracellular, i.e. within the same cell, and intercellular, i.e. through different cells. In this way, the processing of synaptic activity by Ca^{2+} in one region of the astrocytes can extend not only to other regions of the same cells but also to neighboring cells, potentially adding non-local interactions to the repertoire of neuron-glia interactions [14] [15]. Furthermore, calcium signals can be located in synapses [16], propagate along processes, lead to cellular events or even propagate to other cells [17]. However, it is still unknown whether this space-time variability of calcium signals is associated with the different physiological functions and whether this signal could be reflected in the integration of the different neural circuits.

Calcium Imaging

There are a multitude of calcium signals that are used by different types of cells, from micro-domains of Ca^{2+} to the waves of the same ion that propagate in astrocytes [18]. This diversity explains how there is no single technique to monitor all Ca^{2+} variations, however, imaging methodologies through the use of fluorescent indicators are the best application for analyzing these signals. In order to obtain a good analysis, it is necessary to carefully choose the indicator based on the Ca^{2+} signal to be measured, the importance of having quantitative or qualitative data. The fluorophor efficiency dependes on many factors such as: its concentration, cytosolic localization and excitation wavelength and duration (photbleaching), extrusion or compartmentalization of the indicator; furthermore, other changes such as that of pH or viscosity can alter the properties of the dye used.
In this work Flu-8 fluorochrome (abcam-Italy) was used due to its optimal performances in astrocyte cells. In the sample preparation, cells were preloaded with Fluo-8 which can cross the cell membrane. Once inside the cell, the Fluo-8 blocking lipophilic groups are cleaved by esterases, resulting in a negatively charged fluorescent dye that remains inside the cells and its fluorescence is greatly enhanced when it binds to calcium. In Fig.1 the excitation and emission band for Fluor8 are illustrated . Fluo-8 was chosen to measure the intracellular concentration of Ca^{2+}, since it has a series of advantages over the classic fluorescent dyes: it is much brighter than the fluorophores of the same category, the loading of the cell can be carried out at room temperature, i.e. in less difficult conditions than other fluorophores that require 37x C for optimal loading; it can cross the cell membrane.

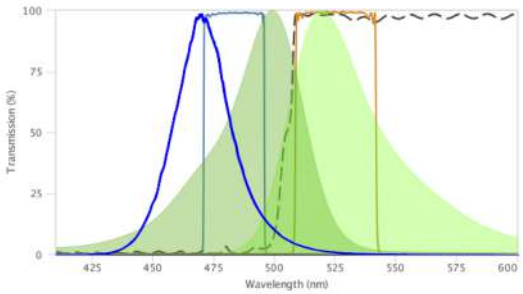

Figure 1: Excitation and emission band of fluo8: broad green bands, Excitation filter: green line, Emission filter: orange line, Dichroic mirror: dashed line.

Optical Systems

The fluorescence microscope [19] appears to be a powerful tool for visualizing and monitoring the production and distribution of proteins and other molecules within living cells. Through the use of fluorescent molecules it is possible to mark and monitor instantaneous changes of the different proteins within the cell as well as the variation of chemical-physical factors. For the study of living cells, the component of interest in the sample is specifically marked with a fluorescent molecule. The sample is then illuminated with a beam of light at the specific excitation wavelength, which is absorbed by the fluorophore, causing it to emit light at longer wavelengths. The exciting light is separated from the emitted light, which is much weaker, thanks to the use of optical filter and dichroic mirror, chosen on the basis of the excitation and emission characteristics of the fluorophore used, as it is show in Fig.1.
The typical components of a fluorescence microscope are: a light source (xenon arc lamp, or mercury vapor, or high power LED), an excitation filter, a dichroic mirror, an emission filter Fig.2. In this microscopes the excitation light transmitted trough the objective and the emission light is collected trough the same objective, as well.

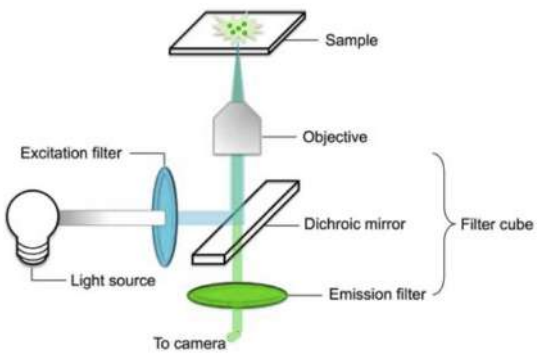

Figure 2: Scheme of a fluorescence microscope

While the basic theoretical concept is very simple, a fluorescence microscope for biological analysis on cells can be quite large and expensive. Since we want to study our system in physiological condition, i.e. T=35° , controlled CO_2 saturation and humidity, we need perform measurements inside a biological incubator. This is a limiting factor for microscope size and electronics. To this end, we have adapted an ordinarily inverted microscope to be suited for our purposes.

Materials and Methods

To study the dynamics of Ca^{2+} in astrocytes, a small, inexpensive and high-performance inverted fluorescence microscope is required. The instrument we have adapted is an Inverted Microscope for tissue and cell culture, phase contrast, Olympus CK2 with 10X and 20X objectives.

Light source

Fluorescence microscopy requires an intense light source, as only a narrow band of wavelengths is absorbed by the fluorophore, whose concentration and absorption coefficient can be low. Lasers offer great spectral purity and extreme intensity but their high cost makes them unsuitable for our purposes. After recent advances in manufacturing, LEDs, inexpensive light sources, can provide adequate intensity and spatial uniformity. However, the challenge that remains in using them for fluorescence microscopy is to adequately attenuate long wavelength emissions. Single color LEDs which have a relatively narrow bandwidth are ideal as single channel light sources for fast imaging. Since many LEDs have wide emission angles, it is important to collimate the LED's emission before the short pass excitation filter. Some LEDs also have significant long-wave and infrared emissions which, if ignored, can result in reduced contrast ("clouding") and sensitivity.

Filters

Filters are critical to instrument performance and are not an element that has had recent advances that significantly reduce instrument costs. The modified instrument mounts high performance fluorescence band pass filters. The high transmission of the fluorescence filters ensures the brilliance of the images possible, while the deep blocking ensures that no unwanted light arrives, the images will be brighter and have a much higher signal-to-noise ratio.

Raspberry Camera

The telescope mounts, on the eyepieces, a Raspberry Pi camera capable of taking high-resolution photographs and Full HD 1080p video, which can be fully programmatically controlled. The system is based on a single board computer Raspberry Pi 4 (RPi), which also provides sufficient computing power for basic data analysis, word processing and accessing the Web using a range of source software solutions pre-installed on the supplied SD card image The Python-based PiCamera library allowed us to gain easy, high-level access to framerate, sensitivity, contrast and white balance. In addition, a simple time-lapse function allows you to specify an image capture rate and duration with subsequent stitching of individual images into a movie. This is valuable for visualizing the movement, growth or proliferation of cells over long periods of time. Photo data (static and time-lapse) and video are stored in jpeg format and the sequence of images is read from the Fiji analysis package.

The resulting device is compact, portable and easy to use, the ability to place the microscope inside a cell culture incubator allows for experiments that are otherwise only available with expensive field-of-application environmental chambers. Simply adding a web access utility allows remote monitoring of cell growth.

Astrocyte cultures

Immortalized human astrocytes were provided from Innoprot (Spain). Cells were cultured in polyxLxlysine coated 25 cm2 plastic flasks containing 5 ml of a specific Astrocytes medium (Innoprot, Spain) with the addition of 2% fetal bovine serum(FBS), astrocyte grow supplements (CGS) and penicillin/streptomycin solution (100 U/mL, 100 xg/mL) (Innoprot, Spain). Cells were incubated in a humidified atmosphere containing 5% CO^{2+} at 37xC. Cell cultures between the third and the seventh passage were used for the experiments.

Cell treatment

Astrocytes were seeded in polyxLxlysine coated 24-well culture plates at a density of 8.0 x105 cells/well. After 24 h, the medium was replaced by 1.5 ml of the fresh medium with 0.5% FBS (except for the FBS the medium maintained the same composition of these used for each cell culture) and Fluo-8 AM, green fluorescent calcium binding dye (Abcam, USA), was added at doses of $2\mu g/ml$. After 45 min, cells were washed and medium was replaced with HHBS (Hank's Buffer with Hepes) 5 min before the addition of glutamic acid at $50\mu g/ml$ (Sigma-Aldrich, USA). Plates were placed on the stage of an inverted fluorescence microscope (Olympus CK2) for viewing and imaging.

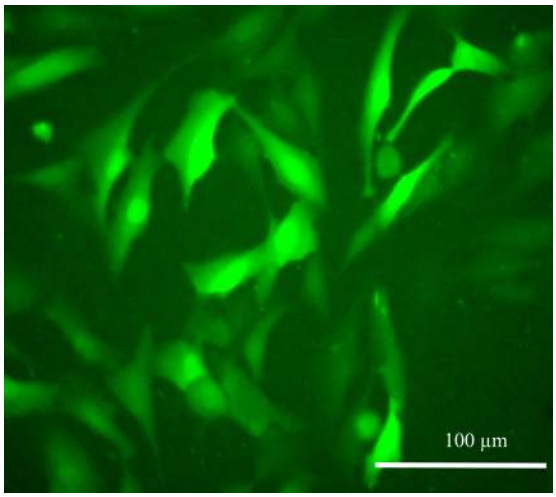

Figure 3: Example of fluorescent image of astrocytes in vitro cultures

Conclusions

The specially adapted inverse fluorescence microscope proved to be a powerful analytical tool capable of visualizing astrocyte cells, following the calcium signal in space and time within the cells and the distribution and through the networks of astrocytes. Through its use it was possible to follow the dynamics of Ca^{2+} in astrocytic networks is made up of discrete individual events that emerge in different places and times. These events differ widely in magnitude and duration; quite often, nearby events can spread and merge into larger events that have distinct spatiotemporal dynamics. Several methods and algorithms have been adopted to follow the spatio-temporal patterns of Ca^{2+} astrocytic events. The next challenge is to determine the number, dimensions and relative positions detected individually and evaluated through the use of specific software for image analysis in order to develop new analytical tools and computational models.

References

[1] Araque, Alfonso and Parpura, Vladimir and Sanzgiri, Rita P and Haydon, Philip G: *Tripartite synapses: glia, the unacknowledged partner.* Trends in neurosciences, **22**(5), 208–215 (1999).

[2] Maurizio De Pittx and Hugues Berry: *Computational Glioscience.* Springer Series in Computational Neuroscience, *https* : *//doi.org*/10.1007/978−3 − 030 − 00817 − 8_1

[3] Araque, A., Sanzgiri, R. P., Parpura, V., and Haydon, P. G.: *Astrocyte-induced modulation of synaptic transmission.* Canadian journal of physiology and pharmacology, **77**(9), 699-706 (1999).

[4] Fellin, T., Pascual, O., Gobbo, S., Pozzan, T., Haydon, P. G., and Carmignoto, G.: *Neuronal synchrony mediated by astrocytic glutamate through activation of extrasynaptic NMDA receptors.* Neuron, **43**(5), 729-743.(2004).

[5] Schipke, C. G., and Kettenmann, H.: *Astrocyte responses to neuronal activity.* Glia, **47**(5), (3), 226-232 (2004).

[6] Volterra, A., Magistretti, P. J., and Haydon, P. G. : *The tripartite synapse: glia in synaptic transmission.* (No. BOOK). Oxford University Press

[7] De Young, G. W., and Keizer, J.: *A single pool inositol 1, 4, 5 trisphosphate receptor based model for agonist stimulated oscillations in Ca^{2+} concentration.* Proceedings of the National Academy of Sciences, **89**(20), 9895-9899 (1992).

[8] Li, Y.X., Rinzel, J: *Equations for InsP3 receptor-mediated Ca^{2+} oscillations derived from a detailed kinetic model: a HodgkinxHuxley like formalism* Journal of Theoretical Biology **166**461x473(1992).

[9] Keizer, J., and Levine, L: *Ryanodine receptor adaptation and Ca^{2+} induced Ca^{2+} release-dependent Ca^{2+} oscillations* Biophysical journal **71**(6), 3477-3487(1996).

[10] Orkand RK, Nicholls JG, Kuffler SW: *Effect of nerve impulses on the membrane potential of glial cells in the central nervous system of amphibia* Journal of Neurophysiology **29**(4):788x806.

[11] Sontheimer H.: *Voltage-dependent ion channels in glial cells* Glia, **11**(2),156x172.

[12] Bezzi, P., Gundersen, V., Galbete, J. L., Seifert, G., Steinhxuser, C., Pilati, E., and Volterra, A.: *Astrocytes contain a vesicular compartment that is competent for regulated exocytosis of glutamate*Nature neuroscience, **7**(6), 613-620 (2004).

[13] Marchaland, J., Calx, C., Voglmaier, S. M., Li, H., Regazzi, R., Edwards, R. H., and Bezzi, P.: *Fast subplasma membrane Ca^{2+} transients control exo-endocytosis of synaptic-like microvesicles in astrocytes.* Journal of Neuroscience, **28**(37), 9122-9132.

[14] Bazargani, N., and Attwell, D.: *Astrocyte calcium signaling: the third wave.* Nature neuroscience, **19**(2), 182-189 (2016).

[15] De Pittx, M., Volman, V., Berry, H., Parpura, V., Volterra, A., and Ben-Jacob, E. *Computational quest for understanding the role of astrocyte signaling in synaptic transmission and plasticity.* Frontiers in computational neuroscience, **6**(2), 98 (2012).

[16] Panatier A, Vallxe J, Haber M, Murai KK, Lacaille JC, Robitaille R.C. *Astrocytes are endogenous regulators of basal transmission at central synapses* Cell, **146**(5), 785x798 (2011).

[17] Beierlein M, Regehr WG. Brief Bursts of Parallel Fiber. *Trigger Calcium Signals in Bergmann Glia* Journal of Neuroscience, **26**(26):6958x6967 (2006).

[18] Berridge, M. J. *Calcium microdomains: organization and function* Cell calcium, **40**(5-6), 405-412 (2006).

[19] Lichtman , J. W., and Conchello, J. A *Fluorescence microscopy* Nature methods, **2**(12), 910-919 (2005).

K*(892)$^{\pm}$ Resonance Production in pp collisions at $\sqrt{s} = 13$ TeV as a function of charged particle multiplicity

A. Rosano[1,2*], G. Mandaglio[1,2]
[1] *MIFT Department, University of Messina, Messina, Italy*
[2] *INFN Sezione di Catania, Catania, Italy*

*Corresponding Author email: arosano@unime.it

Abstract

Short-lived hadronic resonances, like K*(892)$^{\pm}$, are perfect probes to characterize the evolution of the fireball created in ultra-relativistic heavy-ion collisions. Since they have lifetimes comparable to the fireball one, the measured yields may be sensitive to the re-scattering and regeneration competing mechanisms. Recent measurements of resonances production in small systems showed typical features of heavy-ion collisions, like collective behaviour and suppression of short-lived resonances (as ρ^0 and K*^{0}). Multiplicity dependent analysis of K*(892)$^{\pm}$ production in pp collisions at $\sqrt{s} = 13$ TeV can provide further evidences to confirm and even improve the observed trend, and the preliminary results are shown in this work.

Keywords: hadronic resonances, heavy-ion collisions, resonance production, ALICE, QGP, hadronic phase.

Introduction

ALICE (A Large Ion Collider Experiment [1]) is one of the largest experiments hosted at CERN. The detector is mainly designed to study ultra-relativistic heavy-ion collisions in order to investigate the physics of strongly interacting matter at extreme energy densities, where the Quark Gluon Plasma (QGP) formation is expected [2]. Short-lived resonances, like K*(892)$^{\pm}$ (in the following simply K*$^{\pm}$, $\tau \sim 4$ fm/c), are perfect probes to investigate the properties of the hadronic medium, as they have lifetime comparable to the fireball one (~ 10 fm/c). If the hadronic phase lasts enough, resonances may decay inside the medium and their decay products can interact with the other particles. This would result in a suppression of the resonances measured yields. The process just described is known as re-scattering. In another way a competing mechanism, known as regeneration, can also occurred. Resonances can be regenerated in pseudo-elastic collision of the medium particles and, as a consequence, the measured yield will be enhanced [3]. Elementary collisions are normally used as baseline for nucleus-nucleus (A–A) collisions, since QGP formation is not expected. However, recent measurements of resonances production in high multiplicity pp and p–Pb collisions have also shown the onset of phenomena typical of heavy-ion collisions, as the hardening of p_{T} spectra with increasing multiplicity, that should be related to collective expansion of the fireball [4, 5] and the suppression of short-lived resonances measured yield, due to daughters re-scattering in the hadronic medium [6]. These evidences seem to suggest the presence of a non zero hadronic phase lifetime and a possible formation of QGP droplets even in smaller collision systems.

K*(892)$^{\pm}$ analysis

Data-set and Event Selection

The preliminary results of K*$^{\pm}$ analysis, produced at mid-rapidity ($|y| \leq 0.5$) in pp collisions at $\sqrt{s} = 13$ TeV as a function of charged-particle multiplicity are briefly described. K*$^{\pm}$ is reconstructed via its hadronic decay channel K*$^{\pm} \rightarrow \pi^{\pm}$+ K$^0_{\mathrm{S}}$ (B.R. 33.3% [7]) and K$^0_{\mathrm{S}}$ is reconstructed via K$^0_{\mathrm{S}} \rightarrow \pi^+ + \pi^-$ (B.R. 69.2% [7]). Primary pions are identified by energy loss measurements while K$^0_{\mathrm{S}}$ is identified by applying topological cuts on the daughters tracks (secondary pions). Here there is the main difference between K*$^{\pm}$ and K*^{0} analyses. K*^{0} is reconstructed via K*$^0 \rightarrow \pi^{\pm}$+ K$^{\mp}$ with $\pi^{\pm}$ and K$^{\mp}$ **directly identified** by the detectors. The inclusive analysis of K*$^{\pm}$ production in pp collisions [7] showed lower systematic uncertainties on K*$^{\pm}$ measurement than K*^{0} results, because of the different strategies used for K$^0_{\mathrm{S}}$ and K$^{\pm}$ identification in ALICE. Therefore the goal of this analysis is to complement and improve K*^{0} results thanks to smaller systematic uncertainties.
The ALICE sub-detectors involved in this analysis are:

- ITS (Inner Tracking System), TPC (Time Projection Chamber), and TOF (Time Of Flight) for ver-

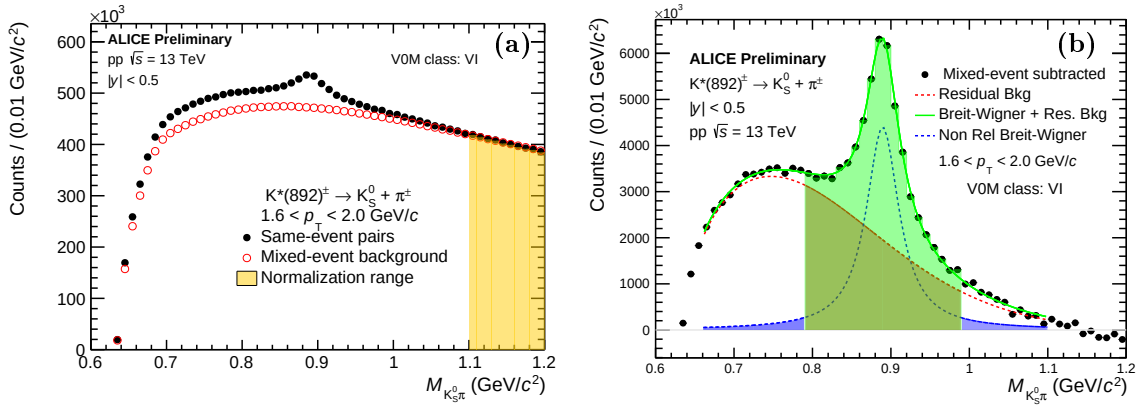

Figure 1: $K^0_S\pi^\pm$ *invariant mass distribution: the background shape, evaluated via event mixing technique, (red open circle) and the normalization region (yellow-filled area), are also shown* **(a)**. *Invariant mass distribution obtained after background subtraction: the solid green curve is the result of the final fit. The dashed red line describes the residual background, while the blue one is the non relativistic Breit-Wigner function. Colored regions show the areas interested in the bin counting method* **(b)**.

texing, tracking, and particle identification.

- V0 scintillators (V0A and V0C) for triggering and charged-particle multiplicity estimation at forward rapidities.

More details about the ALICE apparatus can be found in Ref. [1]. The average charged-particle multiplicity densities corresponding to the different multiplicity classes are listed in Tab. 1. The first class is related to the most central collisions (higher multiplicity), while the last one refers to the most peripheral collisions (lower multiplicity).

Multiplicity (%)	V0M Class	$\langle dN_{ch}/d\eta \rangle_{\lvert\eta\rvert < 0.5}$
0-100	INEL > 0	6.94 ± 0.10
0-1	I	26.02 ± 0.35
1-5	II	20.02 ± 0.27
5-10	III	16.17 ± 0.22
10-15	IV	13.77 ± 0.19
15-20	V	12.04 ± 0.17
20-30	VI	10.02 ± 0.14
30-40	VII	7.95 ± 0.11
40-50	VIII	6.32 ± 0.09
50 -70	IX	4.50 ± 0.07
70-100	X	2.55 ± 0.04

Table 1: *Average charged-particle multiplicity densities at midrapidity for each multiplicity class.*

Signal Extraction

K*$^\pm$ is reconstructed via the invariant mass distribution of the decay daughters ($K^0_S\pi^\pm$). The distribution obtained is a peak over a large combinatorial background whose shape has been estimated via the event-mixing technique. After the uncorrelated background subtraction, the remaining distribution is fitted with a non relativistic Breit-Wigner to describe the resonance peak, and a suitable function for the residual background F_{BG} :

$$\frac{D}{2\pi}\frac{\Gamma_0}{(M_{K\pi}-M_0)^2+\frac{\Gamma_0^2}{4}} + F_{BG}(M_{K\pi}) \qquad (1)$$

$$F_{BG}(M_{K\pi}) = \\ = [M_{K\pi}-(m_\pi+m_K)]^n\, e^{(A+BM_{K\pi}+CM^2_{K\pi})} \qquad (2)$$

where D is the integral of the peak function from 0 to ∞, M_0 and Γ_0 are the mass and the width of K*$^\pm$, $m_\pi = 139.57$ GeV/c^2 [8] and $m_K = 497.61$ GeV/c^2 [8] are the pion and K^0_S masses, while n, A, B and C are fit parameters. To have a good fit the width was fixed to PDG value [8]. The raw yields of K*$^\pm$ have been extracted using the bin counting method. An example of the spectra obtained before (a) and after (b) the combinatorial background subtraction is shown in Fig. 1.

Corrected Yields

Starting from row counts some corrective factors have to be considered in the final equation for K*$^\pm$ yields reconstruction (eq. 3). They are:

- **BR**: the decay Branching ratio for K*$^\pm \to \pi^\pm$K^0_S (BR = 33.3%);
- ϵ_{rec}: geometrical acceptance and detector efficiency;
- f_{SL}: signal-loss correction factors.
- f_{norm}: efficiency of trigger selection for inelastic pp collisions [9].
- f_{vertex} : the signal loss introduced by the requirement to reconstruct a primary vertex [9].

In addition a one-half factor has been considered because both K*$^+$ and K*$^-$ are taken into account. Then the yield for each multiplicity was eventually estimated using the following formula:

$$\frac{d^2N}{dp_T dy} = \frac{1}{2}\frac{RawCounts}{N_{evt}\times\Delta p_T\times\Delta y}\frac{f_{SL}\times f_{norm}\times f_{vertex}}{BR\times\epsilon_{rec}} \qquad (3)$$

where N_{evt} is the number of accepted events, Δp_T is the transverse momentum step and Δy is the rapidity interval.

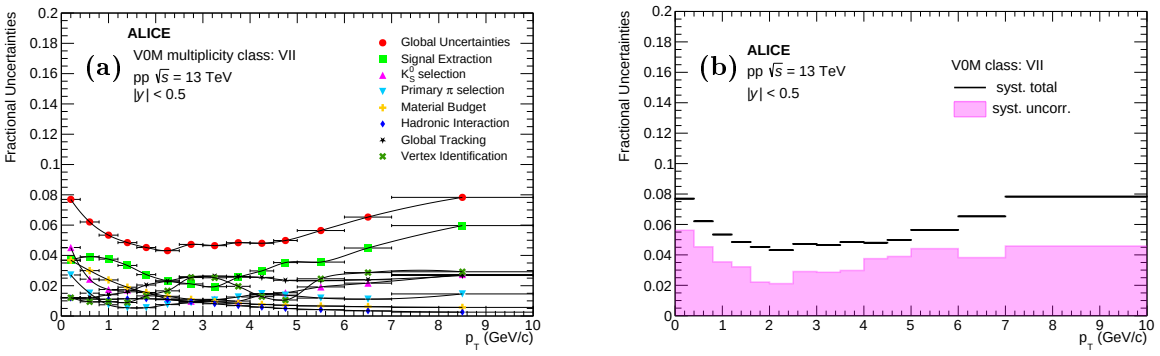

Figure 2: *p_T distributions of the systematic uncertainty from the different sources in the VII V0M class* ***(a)****. Total p_T distribution of the systematic uncertainty (black line) and of uncertainty uncorrelated with multiplicity (shaded pink area)* ***(b)****.*

Systematic Uncertainties

In this section is briefly described the procedure followed for estimating the systematic uncertainties related to $K^{*\pm}$ yields evaluation. The same yield have been computed many times with different analysis parameters. In particular the sources of systematic uncertainties considered are: primary pions selection, secondary tracks and K^0_S selection, vertex identification, signal extraction procedure, material budget, hadronic interaction and global tracking. The total systematic uncertainties are estimated with the grouping method passing through the Barlow check. For each multiplicity class the global systematic uncertainty is obtained by adding in quadrature the uncertainties from the different sources. For the estimation of the fraction of systematic uncertainties uncorrelated with multiplicity (i.e. that depends on multiplicity) the R method was used. The complete process followed to estimate the systematic uncertainties is fully described in Ref. [10]. Fig. 2 shows the p_T distributions of the systematic uncertainties of the sources previously described (a) as well as the fraction of systematic uncertainty uncorrelated with multiplicity (b), in the VII V0M class. Similar spectra have been obtained also for the other multiplicity classes.

Results and Conclusions

Preliminary results of $K^{*\pm}$ resonance production at mid-rapidity in pp collisions at $\sqrt{s} = 13$ TeV in different multiplicity classes were reported here. $K^{*\pm}$ measurements are compared to K^{*0} results for the same collision system and energy [4]. Fig. **??** shows a comparison between the $K^{*\pm}$ and K^{*0} p_T spectra. A very good agreement is observed between the charged and neutral $K^*(892)$ spectra. $K^{*\pm}$ differential p_T spectra get harder from peripheral to central collisions for $p_T < 5$ GeV/c. This behaviour is qualitatively similar to the trend observed in heavy-ion collisions, where this effect is due to the collective expansion of the fireball. However, in small collision systems, colour re-connection mechanism can mimic flow-like effects [11]. On the contrary, the same spectral shape can be noticed for all multiplicity classes at higher p_T values. Fig. 4 shows the $K^{*\pm}$ and K^{*0} comparison for the p_T-integrated yields and the mean p_T spectra. The slightly differences in the $\langle dN_{ch}/d\,\eta\rangle_{|\eta|<0.5}$ values are due to the different data periods analysed. The results obtained are fully in agreement within the systematic and statistical uncertainties. In addition, as expected, $K^{*\pm}$ results exhibit lower systematic uncertainties than K^{*0} one. Therefore $K^{*\pm}$ data not only confirm but also improve the previous results, fulfilling the goal of this analysis.
In Fig. **??** the p_T integrated yields ratio of $K^{*\pm}$ and K^{*0} to K^0_S are shown. The suppression trend, already outlined in K^{*0} analysis [4] has been confirmed by $K^{*\pm}$ results with smaller systematic uncertainties, passing from peripheral to central pp collisions. In addition the decreasing trend is more evident in $K^{*\pm}$ ratios if the most peripheral point (lowest multiplicity) and the most central point (highest multiplicity) are compared. Indeed they are not consistent within the systematic uncertainties, as it instead happens for the K^{*0} ratios. This evolution is consistent with the hypothesis of the re-scattering of the decay daughters typical of heavy-ion collisions and it seems to suggest that also in elementary collisions collective-like phenomena are at play with the presence of a short-lived hadronic phase which may affect the measured resonance yields.

References

[1] ALICE Collaboration: Aamodt, K. et al.: *The ALICE experiment at the CERN LHC.* Journal of Instrumentation 3.08, S08002, (2008).

[2] Bazavov, A. et al.: *Chiral and deconfinement aspects of the qcd transition.* Physical Review D 85, 054503, (2012).

[3] Sahu, D. et al.: *Role of event multiplicity on hadronic phase lifetime and QCD phase boundary*

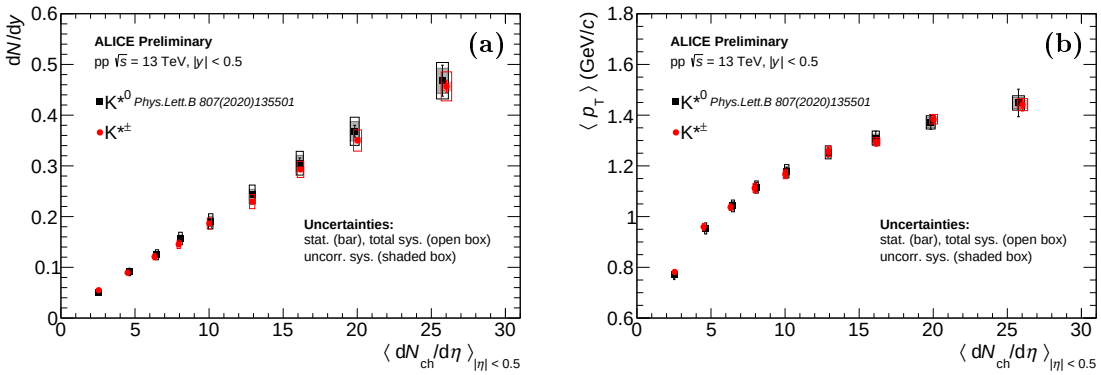

Figure 4: *Integrated yields dN/dy* **(a)** *and mean transverse momenta $\langle p_T \rangle$* **(b)** *for $K^{*\pm}$ and K^{*0} as a function of $\langle dN_{ch}/d\eta \rangle_{|\eta|<0.5}$. Bars represent statistical uncertainties, open boxes represent total systematic uncertainties, and shaded boxes are the systematic uncertainties uncorrelated with multiplicity.*

in ultrarelativistic collisions at energies available at the BNL Relativistic Heavy Ion Collider and CERN Large Hadron Collider. Physical Review C 101, 014902 (2020).

[4] ALICE Collaboration: Acharya, S. et al.: *Multiplicity dependence of $K^*(892)^0$ and $\Phi(1020)$ production in pp collisions at $\sqrt{s} = 13$ TeV.* Physics Letters B 807, 135501 (2020).

[5] ALICE Collaboration: Acharya, S. et al: *Investigations of anisotropic flow using multi-particle azimuthal correlations in pp, p-Pb, Xe-Xe, and Pb-Pb collisions at the LHC* Phys. Rev. Lett. 123 142301 (2019).

[6] Khuntia, A. for the ALICE Collaboration: *Latest results on the production of hadronic resonances in ALICE at the LHC.* arXiv:2001.09023 [hep-ex].

[7] ALICE Collaboration: Acharya, S. et al: *"Measurement of $K^*(892)^{\pm}$ production in inelastic pp collisions at the LHC.* arXiv:2105.05760 [nucl-ex] (2021).

[8] Particle Data Group Collaboration: Zyla, P.A. et al: *The Review of Particle Physiscs.* Prog. Theor. Exp. Phys. 083C01 (2020).

[9] *https://indico.cern.ch/event/1001718/contributions/4218507/attachments/2183582/3689068/210203_Resonance_BHLIM.pdf.*

[10] Rosano A. et al: *Charged-particle multiplicity dependence of $K^*(892)^{\pm}$ resonance production in pp collisions at $\sqrt{s} = 13$ TeV with ALICE.* https://alice-notes.web.cern.ch/system/files/notes/analysis/1237/2022-03-25-Analysis_note_KStar_pp_13TeV_mult_v3.pdf.

[11] Ortiz Velasquez, A. et al.: *Color reconnection and fow-like patterns in pp collisions* Phys. Rev. Lett. 111, 042001 (2013).

PhD in Physics 2020-2021 Activities report 2nd year PhD (XXXV Cycle)

A. Saidi[1], R. Saija[1]
[1] *Dipartimento di Scienze matematiche e informatiche, scienze fisiche e scienze della terra (MIFT), University of Messina, Messina, Italy*

*Corresponding Author email: asidi@unime.it, rsaija@unime.it

Abstract

In this work, we utilize the full light scattering theory in the T-matrix formalism to analyse the optical behaviour and to compute optical trapping properties of a class of complex nano and micro particles whose nature is similar to that found in the extra-terrestrial environment. Using the real mineral composition of trapped dust particles as a main basis, we report the main results considering different strategies: firstly, to speed up the simulations, we use spherical grains with an effective refractive index using Bruggeman mixing rule [1], after, taking into account the non-homogeneity in the matter distribution, we consider a spherical grain with an series of different homogeneous inclusions representing the real composition of the material [2]. Finally, choosing an even more complex and more computationally demanding model, we took into account both the anisotropy in shape and the non-homogeneity in composition using a cluster model [2].

Keywords: electromagnetic scattering, Transition Matrix, dust grains, Optical Properties.

Introduction

Cosmic dust is the key ingredient in the formation of stars, planets, comets, and asteroids all across the universe [3]. Moreover, the surface of cosmic dust grains serves as a platform for the formation of molecular hydrogen and simple organic compounds [4]. For all these reasons the study of the composition, shape and optical properties of dust grains is a relevant question in space science. To do this end, some space missions have been planned over the years with the aim of recovering and sending dust samples to Earth for chemical and physical analysis in the laboratory. More challenging is the possibility to analyse dust grains in situ so as to avoid contamination with the terrestrial environment. One of the possible solutions to this demand, intriguing from a scientific point of view, is the design and realization of a scientific instrument that can be sent into space, to the heart of which there is an optical tweezers [5, 6] system capable of contactless trapping and manipulation of extra-terrestrial particle matter . In this context it is also necessary to have a reliable theoretical approach through which, thanks to the study of the interaction with the radiation field, we can not only verify whether the extra-terrestrial conditions would allow the trapping and manipulation of particles but also infer the main information about the nature of the trapped grains [7].

Materials and Methods:

Transition Matrix

We need to resort to full electromagnetic theory and the T-Matrix formalism has proved to be computationally advantageous [2, 8, 9]. Any particle can be modelled through a sphere, clusters or aggregates of spheres, spheres with spherical (eccentric) inclusions, and multi-layered spheres [2]. This formalism consists in the expansion of the electromagnetic fields into a basis of vector spherical harmonics applying the boundary conditions across the particle surface [2, 10]. The incident and the internal fields inside the particle have to be regular at the origin while the scattered field is such as to satisfy the radiation condition at infinity [2, 11, 12]. The transition matrix, T, connects the amplitudes of the scattered fields to the amplitudes of the incident ones upon a multipole expansion of the fields.

Investigated Samples

The investigated samples have terrestrial and extra-terrestrial origins. We started to analyse some reference samples similar to the samples used to calibrate the dust analyser Giada on board of Rosetta space mission [13]. In doing this we aimed to reproduce the well-known results found in literature for these samples, validating the application of optical manipulation techniques to cosmic dust. In particular, for this purpose we used two terrestrial mineral samples: HE-1, and an extra-terrestrial sample A-1. The sample HE-1 is an Hawaiite sample

from Etna volcano in Italy, containing several minerals, such as augite, magnetite and fayalite. After these reference sample we investigated cosmic dust from a lunar meteorite (DEW 12007) found in Antarctica [14].

In order to calculate the radiation force on the particles using the T matrix formalism, for simplicity, despite their irregular shape, we modelled the particles as microsphere the diameter is 1 *um*. The impinging incident radiation is a Gaussian Laser Beam in which the wavelength is *830 nm* and the power equal to *50 milliwatt,* focused by a High NA objective.

In order to model the particles we start from the real mineral composition and we adopt two different strategies to calculate the radiation force.

We used in the first case a single sphere with an effective refractive index obtained according to the Bruggeman Mixing Rules And this tables summarized the used vales .This mixing rule is in principle different from the Maxwell Garnet effective refractive index, because it is able to consider a situation in which small fractions of materials are dispersed in an homogeneous matrix)

To take better into account of the dis-homogeneities that are non-uniformly distributed in the material, the Second model we used is a non-homogeneous distribution in which we consider an external sphere formed by the main composition and inside we consider internal spheres formed by the other elements. In this case the size of the spheres, the refractive index and the number of the internal sphere depend on the composite itself.

Results

Trapping Efficiency: Bruggeman Mixing Rule Model

In order to calculate the radiation force on the particles using the T matrix formalism , for simplicity, despite their irregular shape, we modelled the particles as microsphere the diameter is 1 *um*. The impinging incident radiation is a Gaussian Laser Beam in which the wavelength is *830 nm* and the power equal to *50 milliwatt*, focused by a High NA objective.

In order to model the particles we start from the real mineral composition and we adopt two different strategies :

1. We used in the first case a single sphere with an effective refractive index obtained according to the Bruggeman Mixing Rules. To take better into account of the dis-homogeneities that are non-uniformly distributed in the material.
2. The second model we used is a non-homogeneous distribution in which we consider an external sphere formed by the main composition and inside we consider internal spheres formed by the other elements. The size of the spheres, the refractive index and the number of the internal sphere depend on the composite itself.

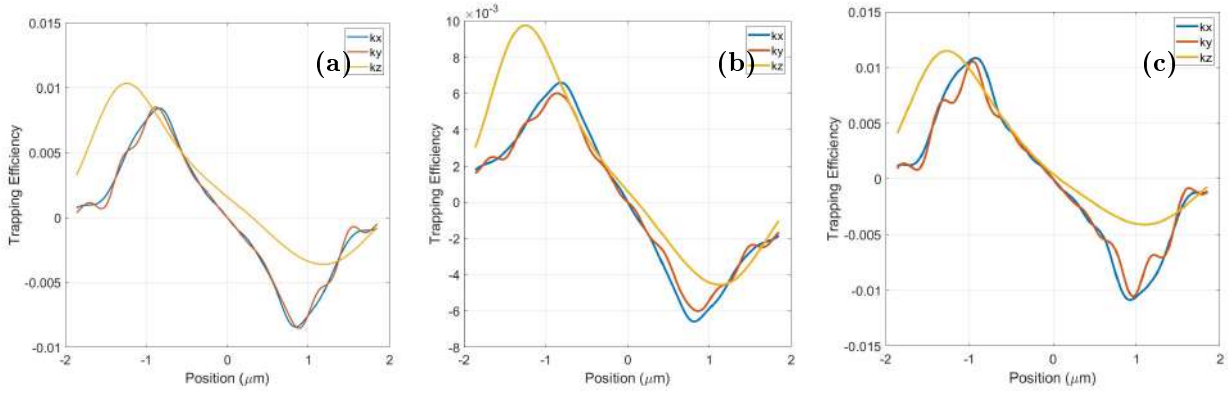

Figure 1: *Trapping effieciency of the three Samples:* **(a)** *Allende A-1 - MAB,* **(b)** *Dew 12007 and* **(c)** *HE-1 (Hawaiite)*

.

These are the initial results regarding the stiffness when we simulate the dust grain as a single sphere using a the Bruggeman mixing rule.
In figure 1 , we show the transversal and longitudinal trapping efficiencies as a function of position of the particle in the focal region. Here, from the yellow line we can determine the stiffness *Kz* along the longitudinal direction z with *x=y=0* , the red and blue lines gives us the stiffness *kx* ,*ky* along the transversal direction with z=0. From the analysis of these curves, we observe that the trapping efficiency along x and y axis for the Allende is effective only at *z0=0.186 um*, For the Dew, the grain is trapped along z at *z=0.47*, for the Hawaiite at *z0=-0.46 um*.

Trapping Stiffness: Bruggeman Mixing Rule Model

Also we studied for these three samples the trapping stiffness as function of the radius fig 2, by analysing these curves we observe that the stiffness of terrestrial and extra-terrestrial samples, decreased with the Radius, and for a single trapped grain of each sample, it is possible to notice that the stiffness decrease almost linearly with the Radius. The difference between the stiffness along the x and y directions is due to the polarization of the incident field. Usually the values of the stiffness along z are lower than the values of the stiffness along x and y due to the radiation pressure that pushes and destabilize the particle along this direction. The stiffness strength along x and y are large for smaller dimension of the particle and decrease with the increase of the size.

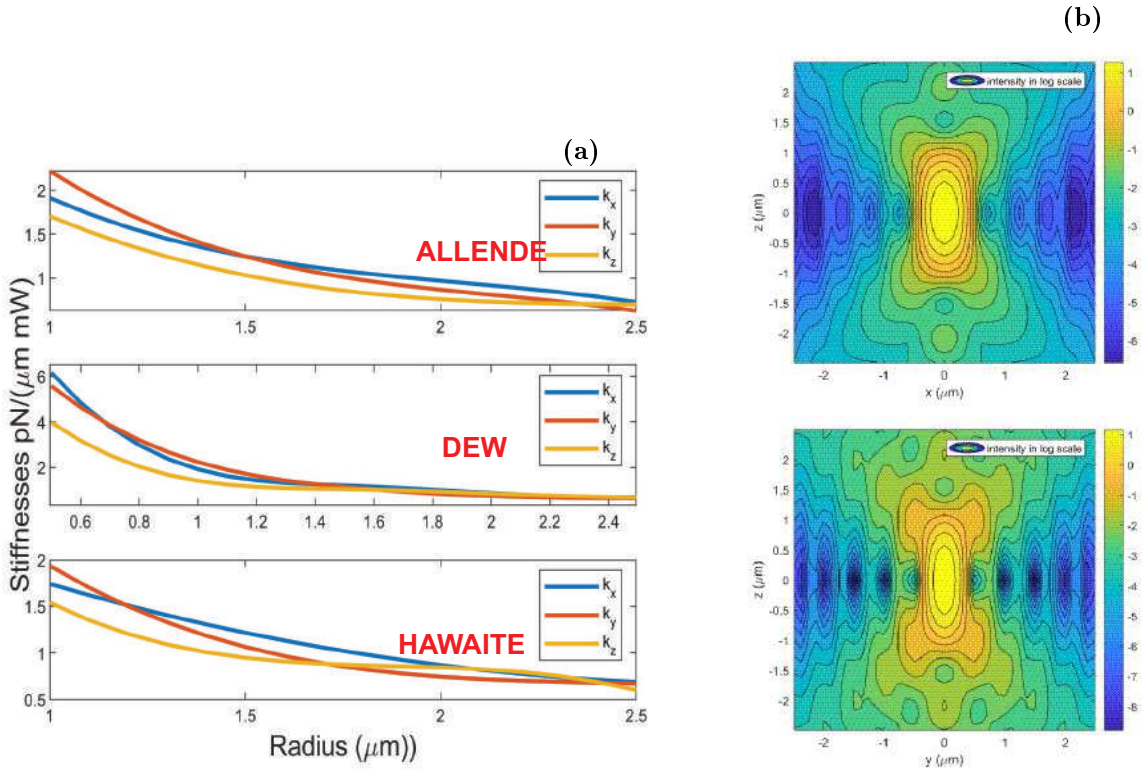

Figure 2: *Trapping Stiffness: Bruggeman Mixing Rule Model.* **(a)** *Trapping Stiffness;* **(b)** *Intensity maps of the Incident focused field.*

Trapping efficiencies: the case of non-homogeneous distribution

In order to take into account the anisotropy and the heterogeneity of the real dust grains in which we still consider a 1 *um* homogenous sphere formed by the Olivine 80%, but we add 4 spherical inclusions. The inclusions are made of the secondary constituents of the Allende meteorite , in particular we considered 2 inclusions made of Clinoenstatite and Enstitite having 12% of the total volume of the modelled grain, and 2 inclusions of Diopside and Pigeonite with a 8% of the total volume. As showed in the first figures 3a 3b it is possible to notice how trap efficiency is affected by the internal structure presenting several equilibrium points and presenting that along the *z-axis*, there are some different point in which the grain can be trapped. While the trapping efficiencies along x and y are effective only at *z0=-1.681 micron.*

In the case of Hawaiite 3c, 3d we still consider a 1 *um* homogenous sphere formed by the Plagioclase and the Olivine 91%, with a refractive index obtained according to Bruggeman Mixing rule. The inclusions are made of the secondary constituents of the Hawaiite, in particular we considered 2 inclusions made of Olivine in which the radius is *341 nm*, 8% of the total volume of the modelled grain, and 2 inclusions of Magnetite , the radius is equal to *171 nm*, having 1% of the total volume. We also calculated the Optical forces and the transversal and the longitudinal trap efficiency *kx, ky, kz.* presenting different equilibrium points in which the grain can be trapped. However in this case the trapping efficiencies along x and y are effective only at *z0=1.307* micron.

In the case of Dew ,we still considered an homogeneous sphere, with a refractive index obtained according to the Bruggeman mixing rule but, 4 spherical inclusions. These inclusions are made of the secondary constituents of the lunar meteorite, we considered 2 inclusions made of Olivine having a 10% each of the total volume, and 2 inclusions of Ilmenite with a 2% each of the total volume. Similarly to the previous model, we calculate the optical forces and the longitudinal trap efficiency , as showed in these figures 3e 3f, presenting that along the *z-axis*, there are some different point in which the grain can be trapped. But the trapping efficiencies along x and y are effective at *z0=0.452* micron. By analysing the Results of the model of the non-homogeneous distribution of the samples, we can notice that in any case the trap efficiency is affected by the internal structure, which is not present for the case in which we used the Bruggeman mixing Rules. This is a confirmation of the fact that the manipulation of nanoparticles through an optical tweezer is strongly dependent on the size and on the optical properties of the nanoparticle.

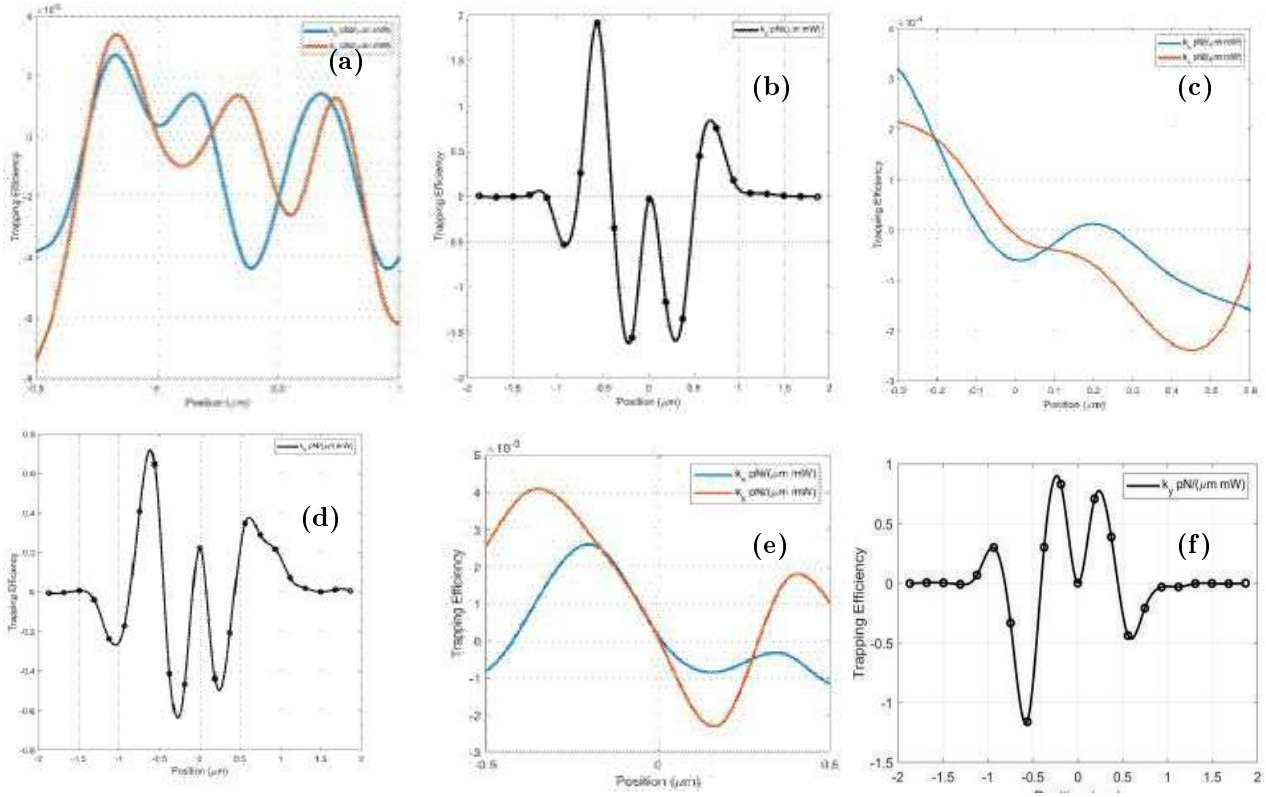

Figure 3: *Trapping efficiencies: the case of non homogeneous distribution.*

Conclusion

We calculated single-beam optical trapping properties for cosmic dust modelled particles both with parameters close to typical optical tweezers experiments in the near infrared. We used T-Matrix formalism to trap single micron-sized dust particles of astrophysical interest to characterize their Optical Properties. We used two different methods to model the dust particles, first using Bruggeman mixing Rules then a Non homogenous distribution. We confirm that manipulation of nanoparticles through an optical tweezer is strongly dependent on the size and on the optical properties of the nanoparticle. The application of optical Tweezers techniques to solar system study, e.g., cometary particles analyses including the volatile component, dust particles in the Martian atmosphere and Lunar surfaces.

Projects

1. ASI-INAF "Space Tweezers" (4 February 2019 – in course)
2. Prin 2020 (22 January 2020– in course)

Conferences

- ELS Conference 2021 "On the Simulation of the Absorbance of Ag-Au Alloyed Nanoparticles"
- Conference Photoptics 2022 "Optical trapping of individual dust particles in the T-matrix formalism"

Seminars

- 30 April 2021 Seminario: "Computational Glioscience: Computational Methods and Modeling of Astrocyte Physiology and Neuron-Glia.
- 21 April 2021 From a catalogue of metastable nanoalloys to the study of the structure-property relationship for nanomedicine, plasmonics or catalysis. Vincenzo Amendola
- 6 May 2021 Machine learning against epidemics Giovanni Volpe (Department of Physics, University of Gothenburg, Sweden) In collaborazione col Dottorato di Ricerca in Fisica.
- 10 May 2021 "Lancio della Start Cup UNIME 2021"
- 11 May 2021 VERSO I NUOVI BANDI DELLE AZIONI MARIE SKLODOWSKA-CURIE (MSCA) IN HORIZON EUROPE
- 12-13 May 2021 Dott.ssa Puglisi. Avvierò il collegamento per la videolezione
- 18 May 2021, seminario specialistico del Dott. R. Stassi.
- 20 May 2021 Webinar UniMe-SIFI - Anatomy and Physiology of the eye

References

[1] Bohren, C. F. and Huffman, D. R.: *Absorption and scattering of light by small particles.*. John Wiley & Sons (2008).

[2] Borghese, F., Denti, P., and Saija, R.: *Scattering from model nonspherical particles: theory and applications to environmental physics.*. Springer Science & Business Media. (2007).

[3] Greenberg, J. M.: *Cosmic dust and our origins*. Surface Science, 500(1-3):793–822. (2002).

[4] Millar, T. J.: *Dust and chemistry in astronomy*. Routledge (2019).

[5] Ashkin, A., J.M., D., J.E., B., and S., C.: *Observation of a single-beam gradient force optical trap for dielectric particles.*. ptics Letters, 11(5):288–290. (1986).

[6] P. H. Jones, O. M. Marago, and G. Volpe: *Optical tweezers: Principles and applications.*. Cambridge University Press, Cambridge, UK, (2015).

[7] Polimeno, P., Magazz'u, A., Iat'i, M., Saija, R., Folco, L., Ciriza, D. B., Donato, M., Foti, A., Gucciardi, P., Saidi, A., et al.: *Optical tweezers in a dusty universe.*. The European Physical Journal Plus, 136(3):1–23. (2021).

[8] P.C. Waterman: *Symmetry, unitarity, and geometry in electromagnetic scattering.*. Phys. Rev. D 3(4), 825. (1971)

[9] F. Borghese, P. Denti, G. Toscano, O.I. Sindoni: *An addition theorem for vector Helmholtz harmonics.*. J. Math. Phys. 21(12), 2754–2755 (1980).

[10] M.I. Mishchenko, L.D. Travis, A.A. Lacis: *Scattering, Absorption, and Emission of Light by Small Particles.*. Cambridge University Press, Cambridge (2002)

[11] E. Fucile, P. Denti, F. Borghese, R. Saija, O.I. Sindoni: *Optical properties of a sphere in the vicinity of a plane surface.*. Journal of the Optical Society of America A 14, 1505–1514 (1997).

[12] A. Ishimaru: *Wave propagation and scattering in random media and rough surfaces.*. Proc. IEEE 79(10), 1359–1366 (1991).

[13] L. Colangeli, J. Lopez-Moreno, P. Palumbo, J. Rodriguez, M. Cosi, V. Della Corte, F. Esposito, M. Fulle, M. Herranz, J. Jeronimo et al.: *The grain impact analyser and dust accumulator (giada) experiment for the rosetta mission: design, performances and first results.*. pace Sci. Rev. 128, 803–821 (2007).

[14] A. Collareta, M. D'Orazio, M. Gemelli, A. Pack, and L. Folco: *High crustal diversity preserved in the lunar meteorite mount dewitt 12007 (victoria land, antarctica).*. Meteorit. & Planet. Sci. 51, 351–371 (2016).

Reports

Studenti di Dottorato di Ricerca

Ciclo XXXVI

Feasibility study of a coherent neutrino scattering experiment on nucleus at the JLAB and Streaming-Readout test facility for future detectors.

S. Grazzi[1,3*], G. Mandaglio[1,2], M. Battaglieri[3,4]
[1] *MIFT Department, University of Messina, Messina, Italy*
[2] *INFN Sezione di Catania, Catania, Italy*
[3] *INFN Sezione di Genova, Genova, Italy*
[4] *Thomas Jefferson National Accelerator Facility (Jefferson Lab, JLAB), Newport News, VA 23606, USA*

[*]Corresponding Author email: stegrazzi@unime.it

Abstract

Neutrino-Nucleus Coherent Scattering (CEνNS) occurs at incident neutrino energies <1 GeV. A small amount of energy is transferred to the target nucleus in the collision. Different detection techniques are needed to detect neutrinos produced from different sources since the range varies in a large range. Currently CEνNS has been measured with high reliability by the Coherent collaboration using a CsI scintillation detector and neutrinos produced by the ORNL spallation source. In my PhD project I'm performing a feasibility study to measure CEνNS in the experiment nuBDX running at Jefferson Lab (JLAB) that will make use of the high intensity electron beam over a Beam Dump and a LAr detector. As a parallel activity, I set up a bench test for future nuBDX detectors development. The test facility uses EEE telescopes (made by three MRPC)s in conjunction with the specimen detector read out by e low-cost, streaming-compatible 12ch, 250MHz, 14 bits digitizer (INFN-WaveBoard or WB) developed by the JLAB12 Collaboration. Charged muons tracks, identified by the EEE telescopes are linked to signals form the tested detector using a similar DAQ framework used for the ASTRO and ASTROPLANO detectors. The facility will be duplicated to instrument in a similar way the EEE telescope located at Messina University providing a general-purpose detector test bench.

Keywords: cosmic muons, MRPC, Fluka, CEνNS, TPC, scintillator, Streaming Readout.

Neutrino-Nucleus Coherent Scattering

Coherent elastic neutrino-nucleus scattering (CEνNS) is a process in which neutrinos scatter on a nucleus which acts as a single particle. Within the Standard Model (SM), CEνNS is fundamentally described by the neutral current interaction of neutrinos and quarks, and due to the nature of SM couplings it is proportional to the neutron number squared [1]. Though the total cross section is large by neutrino standards, CEνNS has long proven difficult to detect. In 2017, the COHERENT collaboration announced the detection of CEνNS using a stopped-pion source with a CsI[Na] scintillating crystal detector. CEνNS experiments proposed so far use nuclear reactors, spallation sources or proton beams to produce neutrinos. With these three methods, the pion yield, and, in turn, the neutrino yield, is maximized. On the other hand, neutrons, the main background for CEvNS experiments, are copiously produced[2] limiting the sensitivity of the experiment. CEνNS signal is accessed by detecting the recoil target nucleus. Neutron elastic scattering provides the same signal making difficult, if not impossible, to be distinguished by neutrino interaction. It is therefore of paramount importance deploy a highly efficient neutron detector to tag and remove neutrons.

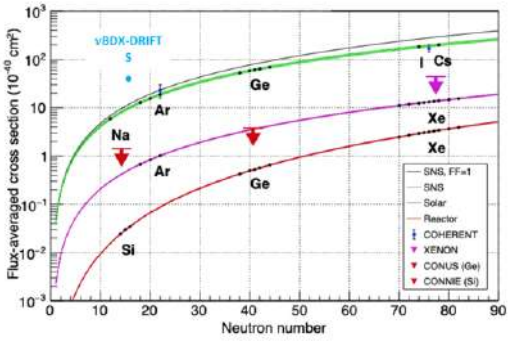

Figure 1: CEνNS Cross-section in function of nucleus neutron number

νBDX-Drift

CEvNS can be detected on a low pressure electro-negative gaseous detector (negative ion chambers or NITPCs) drifting the ionization charges in a large electric field. These detectors, usually, use light nuclei providing an interesting extension to a yet unexplored regime. Despite the CEvNS cross-section is suppressed for light nuclei, the recoil energy is larger providing a net advantage wrt heavy (and larger N) nuclei.

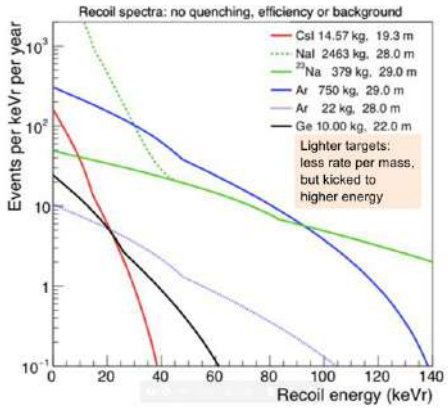

Figure 2: Recoil spectra calculate by Coherent Collaboration.

The negative ion chamber νBDX-Drift [3] was proposed to study CEνNS and light dark matter scattering making use of FNAL secondary beams. The detector has 1 m^3 of active volume filled with CS2 or CF4 gas. An electric field conveys ions to the chamber's sides where the charge is readout by planar MWPCs. The spatial resolution is 2 mm along the x component and 0.1 mm along the y. The time resolution is 200 us.
νBDX-Drift operates with a threshold corresponding to 100 keVr of recoil energy. The signal energy window is limited to large values by the target nucleus form factor that decreases as the recoil energy increases. The CS2 is operated with a maximum energy of 2640 keVr. These parameters limit the CEνNS neutrino energy between 40 and 200 MeV. The resulting number of CEvNS events is rather low. To obtain a larger sensitivity, the gas pressure could be raised. A higher pressure, however, implies shorter track recoils requiring higher thresholds or the use of a higher drift fields (with all issues related to a larger diffusion) and / or requiring detectors with a better spatial resolution. The main backgrounds for this experiment are related cosmic and beam-related neutrons. A neutron veto to mitigate the effects currently under study. The presence of radioactive nuclei in the detector materials represents another source of background.

CENNS-10

Coherent Collaboration reported a 3σ CEνNS signal using a LArTPC [4]. The detector used was a compact single-phase liquid Argon TPC equipped with a top and bottom PMT, capable of measuring (only) the scintillation light produced by the nucleus recoil ionization. Neutrino were produced by the Oak Ridge National Lab Spallation Source. Using the LAr pulse shape discrimination (PSD) capability, it was possible to separate scattering on electrons (1.6 ms) and nuclei (6 ns). PSD was also used to reduce some of the background. As already mentioned, the main background sources are related to cosmic rays, beam-related neutrons and β emitted by ^{39}Ar contamination. Cosmic rays and ^{39}Ar backgrounds were reduced by requiring a tight time coincidence with the spill of the (pulsed) beam. Beam related neutrons were reduced by a water shielding. The remaining background was then subtracted comparing beam-on and beam-off runs. The recoil threshold was set to 20 keVr while the maximum energy was 120 keVr. In about 1 year run, CENNS-10 detected about 130 CEνNS events. The collaboration is currently working to a new, larger detector. A new run is expected in the near future.

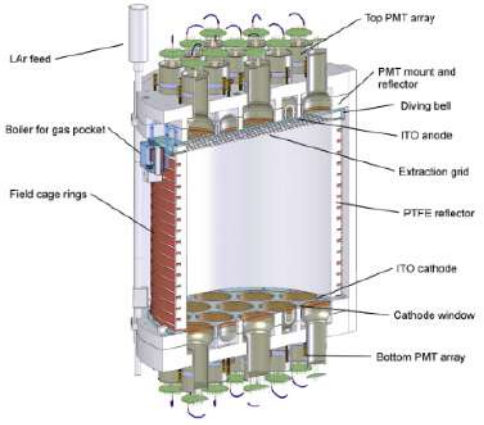

Figure 3: DarkSide-50 Detector

DarkSide

DarkSide experiment uses a liquid and gaseous argon double phase LArTPC to study cosmic dark matter. A possible DM-nucleus interaction, similarly to CEνNS, is detected via target nuclei recoil [5]. On the top of the chamber a layer of gas-phase Ar creates a charge acceleration zone used to amplify the ionization signal. PMTs installed above and below the interaction volume detect the scintillation light produced by charges crossing the gas. Two distinct signals, one prompt associated to the primary ionization in the liquid Ar and the other, delayed, associated with the gas Ar in the provide a clean signature of a scattering. The interaction vertex z coordinate is obtained by the top-bottom time difference, while the x and y coordinates are reconstructed, at cm level, via the light distribution on top PMTs. PSD is used to discriminate between electron signals and nuclear recoil. The minimum recoil threshold is 13-16.9 keVr. The main backgrounds of the experiment are due to cosmic rays and ^{39}Ar. Argon-39 contamination is reduced since the detector uses ultra-pure Ar underwent to a purification cycle. The effect of cosmic rays is mitigated using a 10

m diameter water veto and an LVF veto for the neutron component.

CEνNS at JLAB

The idea of proposing a CEνNS experiment at JLAB arrive from the first estimates of the neutrino flux produced in the Beam-Dump by the JLAB electron beam.

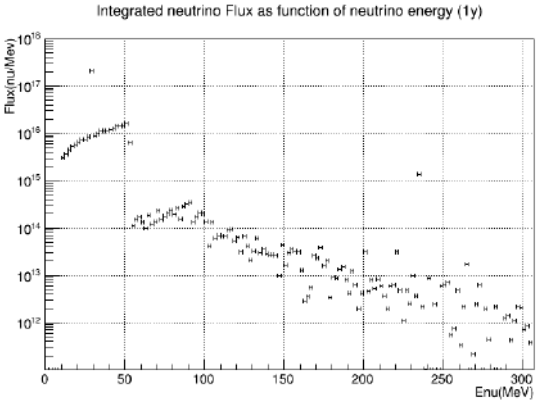

Figure 4: Simulated neutrino flux at JLAB for a cube meter detector at 12 m distance from beam dump, perpendicular respect beam axis

When compared to the proposed νBDX-drift experiment, the JLab neutrino flux would be about 1-2 orders of magnitude higher making it attractive for a CEνNS experiment. Furthermore, the number of neutrons produced by the electron beam is expected to be lower than those produced by proton beams. To quantify signal and background yields, a detailed study based on FLUKA and GEANT simulations is currently in progress. Based on positive preliminary results, we are considering a CEνNS experiment at JLab using the same detection technology proposed by νBDX-drift. As a cross check with simulations, we calculated analytically the CEνNS cross section and the expected yield for the estimated neutrino flux. The algorithm makes use of the target nucleus form factor[6] using the CEνNS cross section [7]:

$$\frac{d\sigma_{\rm coh}}{dT_A} \approx \frac{G_F^2 m_A}{\pi}\left(1-\frac{T_A}{T_A^{\rm max}}\right)|F_n|^2\,(g_V^n)^2\,N^2, \qquad (52)$$

Provided the neutrino flux as a function of the energy, it is possible to estimate the yield for a given target as a function of the minimum detectable recoil energy. For a gaseous detector it is possible to derive the dependence of the number of detectable events from the gas pressure. One of the main issue to use a gaseous detector in the low-recoil energy regime is connected to the fact that a gaseous detectors must operate at low pressure in order to detect the recoil tracks produced by the interaction. This, however, means that the target material mass is lower reducing the expected yield. This effect can be partially mitigated by using higher energy neutrinos, at the price, however, of producing a larger background of non-coherent scattering events. From our investigation, it results that JLab energy spectrum is dominated by neutrinos produced by decays at rest (DAR), with energies of a few tens of MeV. If projected on a νBDX-drift like experiment this would not match the preferred detector sensitivity, resulting in only few CEνNS per year. This led us to evaluate the possibility of proposing an experiment with a denser target material such as LAr. We recalculated the yield considering a LArTPC detector. The preliminary estimates provided few hundreds CEνNS scatterings per m^3 per year providing a significant physics reach for the JLab experiment. We are currently deploying a prototype of a LArTPC detector for a precise in-situ background assessment. A similar detector could, in principle, make use of other noble gases, such as Krypton and Xenon, to study the CEνNS dependence on the the neutron number N. We are also investigating the use of CsI scintillating crystals readout by a front end electronics similar to the one used in the EEE experiment, to detect CEνNS at JLab. It worth mentioning that Coherent Collaboration reported the first CEνNS observation by using a CsI(Na) detector.

EEE cosmic muon test detector facility

Extreme Energy Events (EEE) detectors are designed to measure secondary cosmic ray tracks, mainly muons, to study high energy primary cosmic rays. The EEE 'telescope' is made by 3 Multigap Resistive Plate Chamber (MRPC), each with an active area of 160x82 cm^2. Each detector is part of a large web of about sixty telescopes spread over the Italian territory. GPS time synchronization of the telescopes allows the detection of extensive air showers produced by high energy primary cosmic ray interactions in the Earth atmosphere. Due to the good tracking capabilities (100 ps time resolution and O(cm) spatial resolution) the EEE telescope can be used also as test station for large area detectors. The link between the EEE track and signals from the specimen detector is obtained by implementing a streaming DAQ. The EEE GPS signal is split to provide a common time reference to the EEE DAQ and digitizers connected to the detector under test. These is a new cosmic muon test facility made with the MRPC telescopes and based on the low-cost, streaming-compatible 12ch, 250MHz, 14 bits digitizer (INFN-WaveBoard or WB) developed by the JLAB12 Collaboration. Depending on the detector used, different measurements can be performed: efficiency and light attenuation can be e easily measured for scintillating detectors. In a first test run we characterized some PbWO4 crystals of the POKER detector. The system can be easily replicated, instrumenting any EEE existing Telescopes, and providing a convenient cosmic ray test facility across Italy.

AstroPlano

A new version of the AstrO detector [8], is in final phase of test. AstroPlano is a portable cosmic muon detector developed at the National Institute of Nuclear Physics, Genoa section (INFN-GE), designed for both educational and scientific purposes. The detector is made of eight plastic scintillator bars arranged in two parallel planes. Two long bars (54 x 5 x 2.5 cm^3), read at both ends, and two short ones (20 x 5 x 2.5 cm^3), placed perpendicularly below the long ones to form a grid, define two identical sets of hodoscopes.

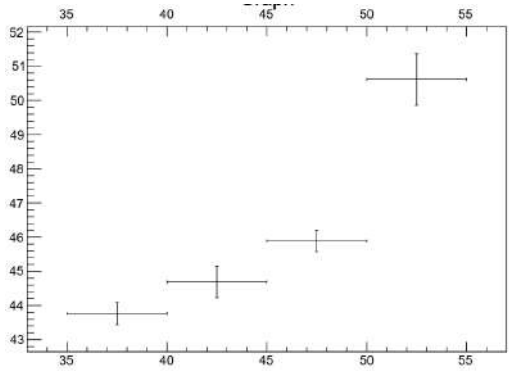

Figure 5: Preliminary result of combined analysis of EEE cosmic muon test detector facility. The plot show the amplitude of Scintillator Crystal signal in function of position in EEE telescope geometry system.

AstroPlano detector presents some improvements with respect to Astro: newer and better performing SiPMs, thinner bars with better optical coupling, the WB digitizer capable of continuously acquiring data (Streaming Readout) and which allows us to sample the signal waveform, a new, and more performing GPS. The technology used is the same of EEE testing facility and this makes the AstroPlano detector easily integrated into the test system with the EEE chambers. A possible upgrade of the AstroPlano would be to wrap scintillator bars with Gadolinium-lined Mylar foils to enhance the sensitivity to neutrons. We are planning to to use AstroPlano, in conjunction with the EEE facility to study cosmic ray and neutron background for future CEνNS detectors (in particular CsI crystals).

Future

To access the possibility of running a CEνNS experiment at JLab the in-situ background measurement is required. For that purpose we plan to deploy a small scale prototype of LArTPC detector (30 Kg). GEANT simulations of the detector and estimates of beam-related neutron background represents the first step toward the experiment. The EEE test detector facility will be used to characterize the LArTPC and CsI crystal-based prototypes with cosmic muons. Further tests are planned in Messina by duplicating the EEE test detector facility making use of the newly installed EEE telescope.

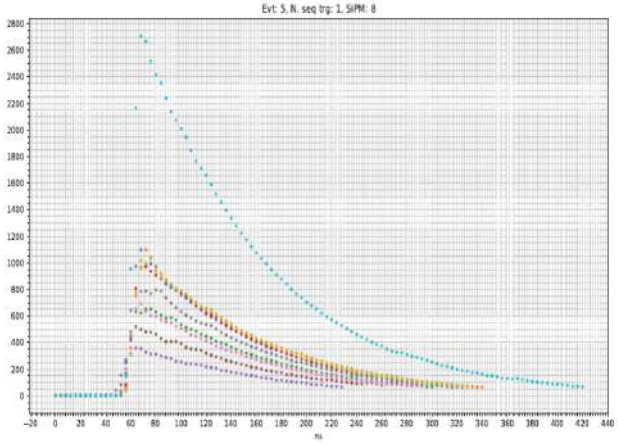

Figure 6: Some Sipm signals captured by digitalizer used by Astroplano Detector.

References

[1] Daniel Z. Freedman, Coherent effects of a weak neutral current, Phys. Rev. D 9, 1389

[2] D. Akimov et al. (COHERENT Collaboration), Measurement of the Coherent Elastic Neutrino-Nucleus Scattering Cross Section on CsI by COHERENT, arXiv:2110.07730 .

[3] D. Aristizabal Sierra, Bhaskar Dutta, Doojin Kim, Daniel Snowden-Ifft, and Louis E. Strigari, Coherent elastic neutrino-nucleus scattering with the νBDX-DRIFT directional detector at next generation neutrino facilities,Phys. Rev. D 104, 033004 – Published 26 August 2021

[4] D. Akimov et al. (COHERENT Collaboration), First Measurement of Coherent Elastic Neutrino-Nucleus Scattering on Argon,Phys. Rev. Lett. 126, 012002

[5] N. Canci (on behalf of DarkSide-50 Collaboration), Long term operation with the DarkSide-50 detector, arXiv:1912.05461

[6] Richard H. Helm, Inelastic and Elastic Scattering of 187-Mev Electrons from Selected Even-Even Nuclei, Phys. Rev. 104, 1466 – Published 1 December 1956

[7] Vadim A. Bednyakov and Dmitry V. Naumov (Dubna, JINR), Coherency and incoherency in neutrino-nucleus elastic and inelastic scattering, Published in: Phys.Rev.D 98 (2018) 5, 053004

[8] S. Grazzi, M. Battaglieri, F. Fontanelli, et al. (2020). AstrO: A portable cosmic ray telescope. Nuclear Instruments and Methods in Physics Research Section A: Accelerators, Spectrometers, Detectors and Associated Equipment. 976. 164275. 10.1016/j.nima.2020.164275.

Spintronics-Compatible Probabilistic Computing Applied to Boolean Satisfiability Problems

A. Grimaldi[1,*]
[1]*Dipartimento di Scienze Matematiche e Informatiche, Scienze Fisiche e Scienze della Terra, Università degli Studi di Messina, Messina, Italy*

*Corresponding Author email: angrimaldi@unime.it

Abstract

The search of hardware-compatible strategies for solving NP-hard combinatorial optimization problems is an important challenge of today's computing research because of their wide range of applications in real world optimization problems. In this research, I studied an unconventional scalable approach to face a subset of Boolean satisfiability problems called maximum satisfiability, which combines probabilistic computing with p-bits, parallel tempering, and the concept of invertible logic gates. To simulate a future spintronics implementation of this approach, I use a model based on a coupled set of Landau-Lifshitz-Gilbert equations, showing a potential path for energy efficient and very fast (p-bits exhibiting ns time scale switching) architecture for the solution of COPs.

Keywords: probabilistic computing, MTJ, spintronics, unconventional computing, Boolean satisfiability, parallel tempering.

Introduction

One of the most important class of mathematical problems with practical applications on today's world is that of combinatorial optimization problems (COPs). Outside of research-related applications in fields like computer science and math, this problems are used on a daily basis in logistics, job-scheduling, water distribution network design and more. Most of this problems, however, are nondeterministic polynomial-time complete (NP-complete) or NP-hard in terms of complexity. This means that the quality of a solution of one of this problems can be determined in polynomial time, but that reaching the optimal solution typically requires exponential time.
For this reason, conventional algorithms designed for the standard Von Neumann computer architecture often struggle to scale to bigger instances[1]. As a consequence, many unconventional approaches are being researched in the last years. Some of these take inspiration from physical models, such as memcomputing[2], simulated bifurcation[3] and probabilistic computing (PC)[4]. The latter is a computing paradigm based on the Ising model. The solving strategy consists in encoding a problem in order to obtain an Ising Hamiltonian whose energy landscape perfectly traces the solution space of the problems, with its absolute minimum corresponding to the optimal solution of the instance.
Originally developed as a toy model to describe ferromagnetism, the Ising model consists of a d-dimensional lattice in which each site is characterized by a discrete variable m_i, with $m_i \in \{-1, +1\}$, named "spin". Each ith site is biased by an external field h_i and interacts with the jth site via an exchange interaction coefficient J_{ij}. Ising Hamiltonians are usually represented in the form

$$H(\boldsymbol{m}) = -\sum_{i,j} J_{ij} m_i m_j - \sum_i h_i m_i \ . \tag{1}$$

In probabilistic computing, the discrete variable m_i represents the base unit of computation, similar to the standard digital bit. This unit, called probabilistic bit, or p-bit, is a tunable bistable stochastic element whose behavior can be expressed by the relation

$$m_i(t) = \mathrm{sgn}\left(\mathrm{rand}(-1, +1) + \tanh(I_i(t))\right) \ , \tag{2}$$

where I_i is the input signal that the p-bit receives from its neighbors, $\mathrm{rand}(-1, +1)$ is a random real number between -1 and $+1$ and m_i is magnetization of the unit, which is the state of the p-bit[5]. In this ideal configuration each p-bit can only assume a value of -1 or $+1$, which correspond to the Boolean 0 and 1.
The input signal of each p-bit is calculated with the following equation:

$$I_i(t) = I_0 \left(h_i(t) + \sum_j J_{ij} m_j(t) \right) \ , \tag{3}$$

where I_0 is a scaling coefficient that establishes the overall strength of the interactions and acts as an inverse temperature, h_i is the bias of p-bit i and J_{ij} is the interaction between p-bit j and p-bit i. This equation closely resembles Eq. 1, and it is the reason why the evolution drives the system toward the minimum of the energy landscape of the problem.

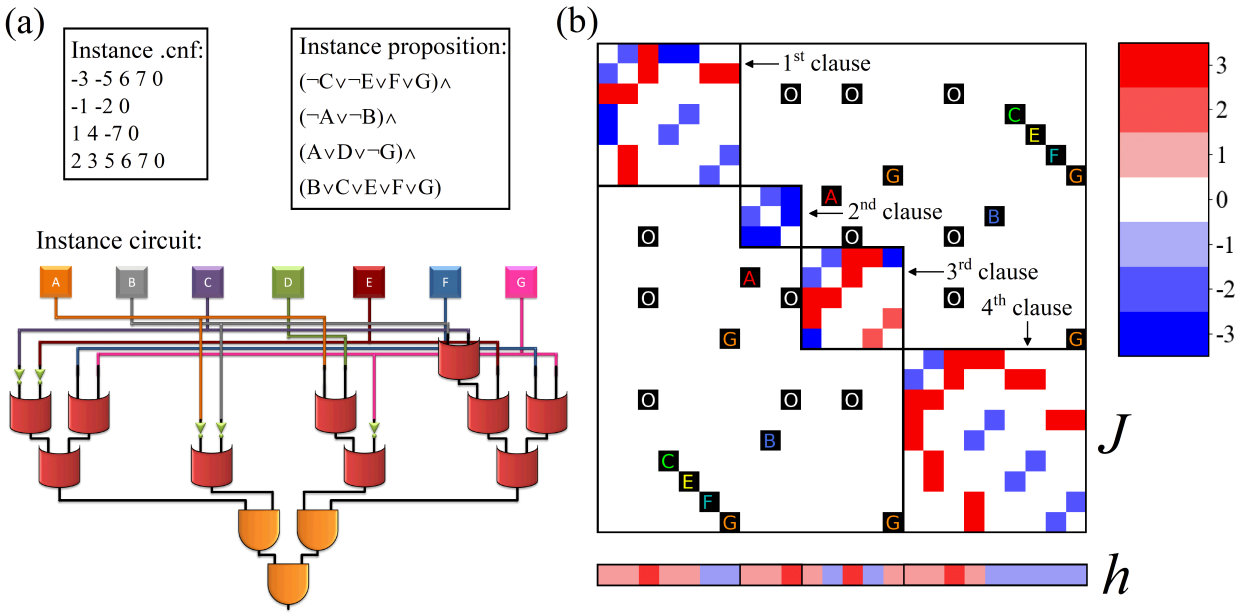

Figure 1: (a) A toy instance in its ".cnf" file format (top left), its logical proposition form where the letters from A to G are the variables from 1 to 7 (top right) and its circuit scheme (bottom). (b). The exchange matrix J and bias field h of the toy instance of Max-SAT shown in (a). The full interaction matrix takes the form of a block matrix where each block represents a clause of the instance. The connections between p-bits are described with off-diagonal positive non-zero elements in the interaction matrix (the black squares in the picture). The clauses are connected to each other by their output p-bits (their connections are marked with an O). The connection between p-bits that represent the same variable (letters A to G) is handled in the same way. The color bar is used to show the values of the matrix element.

In order to solve a problem with PC, one first has to encode the problem in its own J interaction matrix and h bias vector. The update algorithm is required to be asynchronous, meaning that p-bits will be updated randomly and sequentially.
One of the most effective methods to encode a problem consists in writing a probabilistic spin logic (PSL) circuit of Boolean logic gates. These circuits can be operated both in the standard, "direct" mode and in reverse: by clamping some p-bits to a specific state by changing their bias, the other p-bits take on the values compatible with the fixed ones thanks to the modified energy landscape. This allows for straightforward representation of complicated problems by building a circuit which solves the reverse problem and clamping its output. For instance, factorization can be encoded with a multiplier circuit with its output p-bits fixed to the value to factorize[6].

Aims

The goal of this research is to create a CMOS-compatible scalable solver able encode maximum satisfiability (Max-SAT) instances and find the optimal solution. In addition to this, computer simulations of a Landau-Lifshitz-Gilbert (LLG) model of superparamagnetic magnetic tunnel junctions (MTJs)[7, 8] aim to take advantage of the probabilistic nature of the switching between two states of the MTJs to reach the estimated solution of a problem in remarkably short times (< 100ns). The algorithm is benchmarked with hard Max-SAT instances from the 2016 Max-SAT competition (e.g., "HG-4SAT-V150-C1350-1.cnf" which can be described with 2851 p-bits), including weighted Max-SAT and Max-Cut problems.

Methods

Max-SAT PC encoding

Max-SAT is a generalization of the Boolean satisfiability problem and, as such, consists of a Boolean formula in conjunctive normal form which can be converted in a Boolean circuit realized with AND and OR logic gates. The goal of Max-SAT is to satisfy as many clauses as possible. This can be seen as an energy minimization process, where the absolute minimum value is defined as the 'optimal' solution cost (number of unsatisfied clauses).
Fig. 1(a) shows the logic circuit for a toy instance of Max-SAT, which is shown in its ".cnf" file format in the top left. This format is the international standard way of formatting a Max-SAT instance. "cnf" stands for "conjunctive normal form", the logical scheme of a Max-SAT instance.

On the top right the same instance is shown in literal proposition form which can be turned into the circuit scheme on the bottom of Fig. 1(a). This logic circuit is mapped in the exchange and field matrices as indicated in Fig. 1(b). Each clause matrix constitutes a block of the complete exchange matrix J. All the blocks are in an AND relation and are thus connected with each other by an off-diagonal positive element (marked with an O in the figure). These p-bits are the outputs of the circuit and are clamped to 1. Along with the exchange matrix, each clause is also characterized by a bias field vector h.

Parallel tempering

To perform the calculations, an annealing algorithm that drives the PC to minimize the number of unsatisfied clauses is required. I decided to use parallel tempering (PT) over a more standard simulated annealing schedule because of the high parallelization potential of PT.
PT is a method devised for Monte Carlo simulations which uses a set of interacting replicas of the system at different temperatures. The computation of the state for each replica occurs in parallel at several different pseudo-temperatures. If a high temperature replica lands on better state than its colder neighbor, they exchange state.
Fig. 2 shows an example illustrating the implementation of parallel tempering used here considering two replicas. Each starts with a state, in the example of Fig. 2 we named them as State 1 (continuous line) and State 2 (dashed line), evolving in the hotter and colder temperature replica respectively. If the replica energies, evaluated as the number of unsatisfied clauses in the case of Max-SAT problems, intersect at a given iteration, switching occurs (switching time in Fig. 2) and State 1 is now evolving in the colder replica while State 2 in the hotter one.

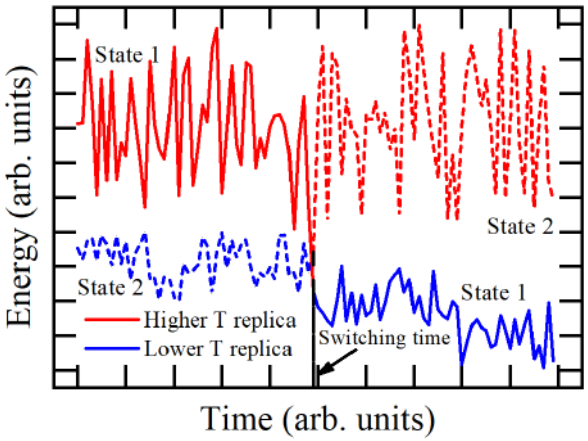

Figure 2: (a) A schematic representation of parallel tempering with two replicas at low and high temperature, blue and red lines, respectively. Replicas hold a state of the system (the continuous and dashed lines) and evolve it with the evolution algorithm. The State 1 switches with the State 2 at the iteration (switching time) when its energy become smaller than the State 2 energy.

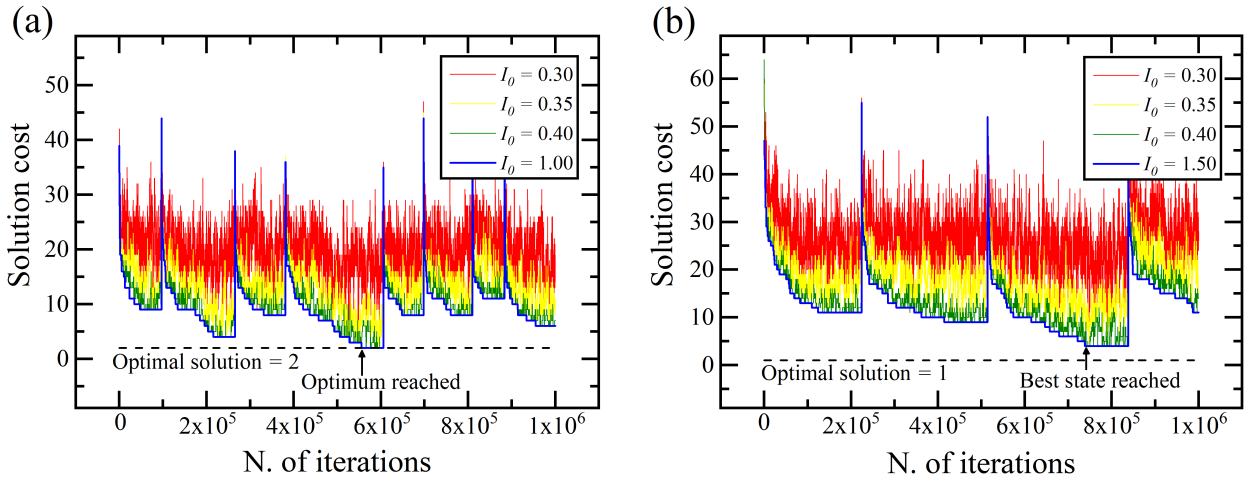

Figure 3: Solution of the Max-SAT instances "HG-4SAT-V100-C900-2.cnf" (a) and "HG-4SAT-V150-C1350-1.cnf" (b) with the probabilistic solver. Four replicas are used, one with a substantially colder temperature in order to have a frozen-like state. When this replica remains stuck in the same state for a given number of iterations, all states are reset and the solver starts from scratch. In (a) the instance has 100 variables and 900 clauses and it is encoded with 1901 p-bits. The optimal solution is 2 and the system obtains it at less than $6 \cdot 10^5$ iterations. In (b) the instance has 150 variables and 1350 clauses and it is encoded with 2851 p-bits. While the optimal solution is not reached within the 10^6 iterations limit, the results are still remarkable as the solver manages to get to a nearly optimal result.

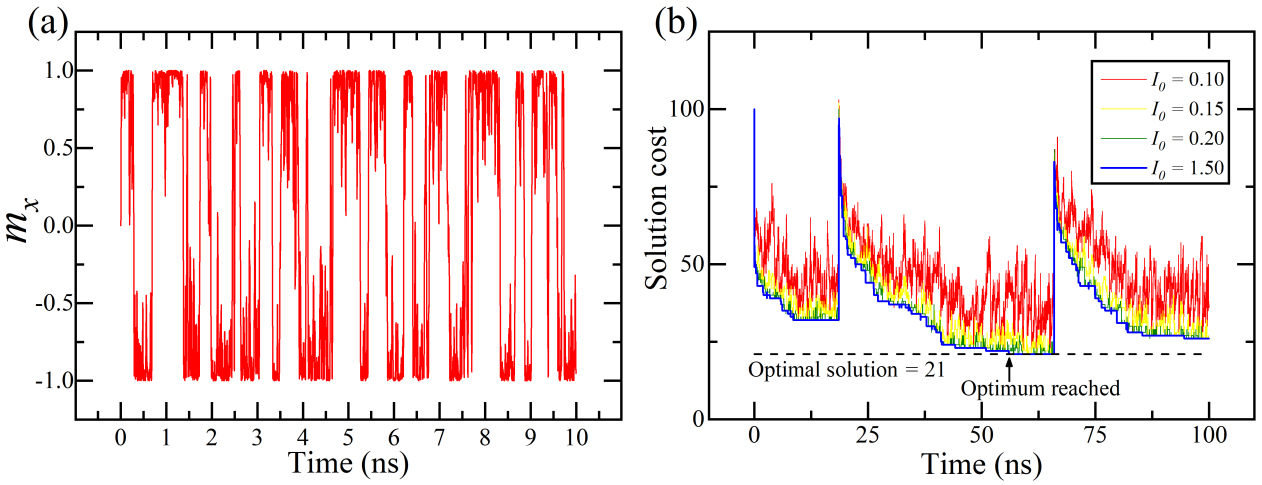

Figure 4: (a) Time domain traces of the three components of the magnetization dynamics of a superparamagnetic MTJ, the x-component is the one related to the p-bit dynamics. The simulation dynamics has been computed numerically with the LLG equation within the macrospin approximation. (b) Solution of the Max-3SAT instance "s3v70c700-1.cnf" (70 variables and 700 clauses, 771 p-bits) with the spintronic based PC solver. The timestep is 10^{-3}ns.

Results and Discussion

Here, the computational achievements for two hard Max-4SAT instances, "HG-4SAT-V100-C900-2.cnf" and "HG-4SAT-V150-C1350-1.cnf" are shown. 4SAT means that each clause contains 4 literals. The former instance is characterized by 900 clauses and 100 variables, a medium-hard instance in its category, which is solved in less than $6 \cdot 10^5$ iterations. The number of p-bits for such a system is 1901. The latter has 1350 clauses and 150 variables, one of the hardest instances in the competition, described by 2851 p-bits is brought to a nearly optimal solution (4 unsatisfied clauses instead of the optimal 1) in less than $8 \cdot 10^5$ iterations. The results are summarized in Fig. 3 which shows an example of the time domain evolution of the cost function for 1 million of iterations (each replica has a different color), computed as the number of unsatisfied clauses for both instances.
By making use of LLG equation, it's possible to emulate a p-bit behavior with a superparamagnetic MTJ tuned with an external magnetic field, as shown in Fig. 4(a). In Fig. 4(b) this simulation is applied to a real instance, similarly to Fig. 3. The optimal solution is reached in less than 100ns.

Conclusions

This work extends the use of invertible logic to design sparse-graph representations for real-world MAX-SAT instances. Moreover, it reinforces the potential of CMOS-compatible spintronic technology that can achieve orders of magnitude speed-up in specialized, energy-efficient hardware.

References

[1] M. R. Garey and D. S. Johnson: *Computers and Intractability: A Guide to the Theory of NP-Completeness.* W. H. Freeman & Co., 2004.

[2] F. L. Traversa and M. Di Ventra: *Polynomial-time solution of prime factorization and NP-complete problems with digital memcomputing machines.* Chaos, **27**, 023107 (2017).

[3] K. Tatsumura, M. Yamasaki, and H. Goto: *Scaling out Ising Machines Using a Multi-Chip Architecture for Simulated Bifurcation.* Nature Electronics, **4**, 208 (2021).

[4] R. Faria, K. Y. Camsari, and S. Datta: *Low-Barrier Nanomagnets as p-Bits for Spin Logic.* IEEE Magnetics Letters, **8**, 1-5 (2017).

[5] K. Y. Camsari et al.: *Stochastic p-bits for invertible logic.* Physical Review X, **7**, 031014 (2017).

[6] W. A. Borders et al.: *Integer factorization using stochastic magnetic tunnel junctions.* Nature, **573**, 390–393 (2019).

[7] K. Y. Camsari, S. Salahuddin, and S. Datta: *Implementing p-bits with Embedded MTJ.* IEEE Electron Device Letters, **38**, 1767–1770 (2017).

[8] J. Cai et al.: *Voltage-Controlled Spintronic Stochastic Neuron Based on a Magnetic Tunnel Junction.* Physical Review Applied, **11**, 034015 (2019).

Stress-Induced Frequency Shifts in Gallium Nitride (GaN) Devices Probed by Micro-Raman Spectroscopy

G. Malta[1–2*], F. Gabriele Campisi[2], G. Romano[2], S. Patanè[1]
[1] *Dipartimento di Scienze Matematiche e Informatiche, Scienze Fisiche e Scienze della Terra, Università degli studi di Messina, Messina, Italia*
[2] *STMicroelectronics S.r.l., Stradale Primosole, 50, 95125 Catania*

*Corresponding Author email: giumalta@unime.it

Abstract

The engineering of high-quality Gallium Nitride (GaN) semiconductors for power devices has gained, only in recent years, considerable attention by the scientific community. This is due not only to their unique structural properties and higher electrical performances with respect to standard silicon-based technologies, but also to their increasing demand/attention in the automotive, renewable energies and aerospace industries. Monitoring the internal stresses occurring in GaN crystals allows the development of high-quality substrates which positively affect the yield of the final device. In this sense, micro-Raman spectroscopy proved to be a valuable tool for the evolution of localized residual stresses inside GaN substrates, starting from the analysis of the frequency shifts exhibited by specific spectral features upon mechanical perturbation. In this study, the variation of the A_1(TO), E_1(TO) and E_2(high) peaks in a GaN epitaxy layer, grown on 6" n-Si(111) substrate, was evaluated following the application of a uniaxial tensile stress. The correlation between the applied stress and Raman shift for each contribution was properly quantified using an in-house three-point mechanical configuration, revealing a diminishing of the corresponding frequencies with respect to those calculated in a stress-free material (used as reference). The proposed methodology could, in principle, be implemented in large-scale semiconductor industrial processes with the aim to assess the quality of GaN substates, prior the "growth" of the final device.

Keywords: Gallium Nitride, Wide Bandgap Semiconductors (WBS), Micro-Raman Spectroscopy.

Introduction

Among the Wide Bandgap Semiconductor (WBS) Gallium nitride (GaN) is emerging as the latest breakthrough in the development of novel energy-efficient power electronic devices and optoelectronic components. It is characterized by a crystallographic arrangement typical of wurtzite, which consists of Gallium (Ga) and Nitrogen (N) atoms spatially arranged to form a superimposed hexagonal packed lattice (Fig.1). Such spatial atom distribution has no inversion symmetry in the [0001] direction, which means that two different types of orientation in GaN crystals can be distinguished, namely the Ga-face (Fig.1a) and the N-face (Fig.1b), each characterized by different chemical properties. In particular, the Ga-face easily incorporates acceptors and is more chemical inert than the N-face, which, instead, easily incorporates donors. In particular, Ga atoms are tetrahedrally covalent bonded with four surrounding N atoms of the lattice (see Fig.1), although the ionic contribution, due to the remarkable difference in electronegativity between the Ga and N atoms, plays also a key role in the formation of the structure. Taking into account all these forces, the lattice parameters of the GaN hexagonal structure turns out to be 5.18Å (c_0) and 3.19Å (a_0) [1–3].

In the development of power electronic and optoelectronic devices based on GaN technology, one of the main challenges is represented by the epitaxial growth of GaN semiconductors, due to the high cost and small size of the crystals itself. For this reason, a suitable substrate must be chosen [4]. Nowadays, commonly employed substrates are sapphire (Al_2O_3), silicon carbide (SiC) and silicon (Si) [5]. In the case of sapphire and SiC, high amount of crystallographic defects are introduced within the GaN crystal lattice during the epitaxy process. This aspect, together with the high costs and possibility to produce only small-sized wafers, led to a massive uses of Si-based substrates in the industrial production. Unfortunately, the presence of a not-negligible lattice mismatch between the GaN(0001) and Si(111) (-17%) layers (see Fig.2) leads to high dislocation density (up to 10^9 cm^{-2}) within the material, negatively affecting the quality of the active area. In addition, the aforementioned lattice mismatch causes the occurrence of a measurable residual-strain at the GaN/Si interface, which propagate along the device [6].

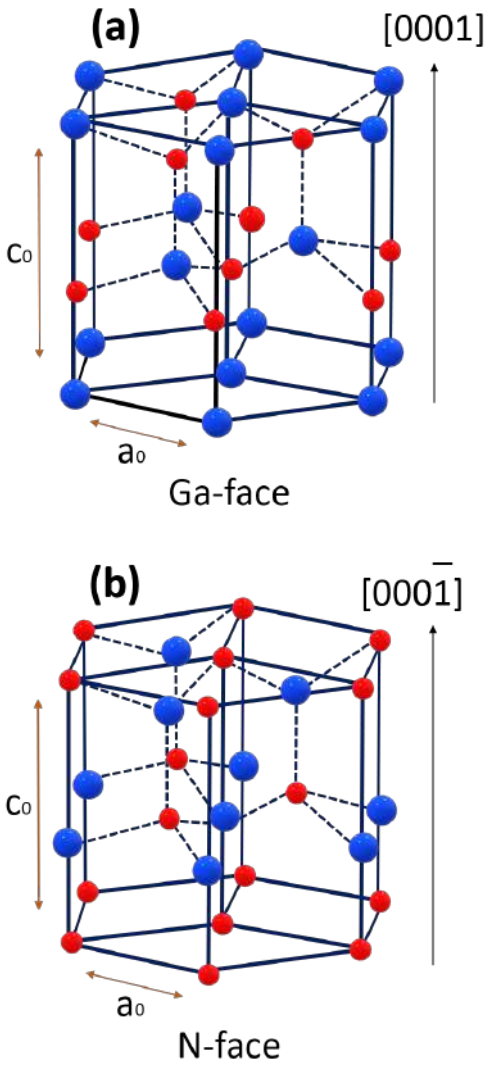

Figure 1: Representation of a typical GaN crystal structure (wurtzite), with the blue and red dots representing Ga and N atoms, respectively. Detail of the structure as seen from the Ga-face (a) and N-face (b). Continuos lines highlight the unit cell, while the dashed lines indicate the Ga—N bonds.

In this sense, different "strain management" techniques are employed to monitor the crack formation in the GaN epitaxial layers, and prevent premature failures of the final device. Micro-Raman spectroscopy can be used to evaluate the evolution of localized residual stresses inside GaN samples. As a matter of fact, when crystals are subjected to an external mechanical stress, their characteristic Raman peaks exhibit a frequency shift due to stress-induced phonon deformations. In this context, the focus of this preliminary investigation was to quantify the frequency shifts observed for three characteristic Raman modes of a GaN epitaxy layer, grown on 6" n-Si(111) substrate, subjected to a uniaxial tensile mechanical perturbation.

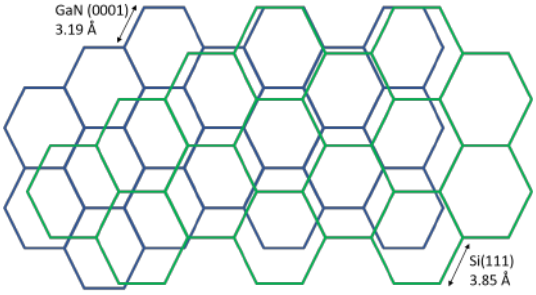

Figure 2: Representation of the reticular mismatch at the GaN-on-Si interface. GaN(0001) reticular dimension is 3.19Å while for Si(111) is 3.85Å.

Material and methods

Material

The GaN epitaxy layer investigated in this work belongs to a more complex structure as reported in Fig.3.

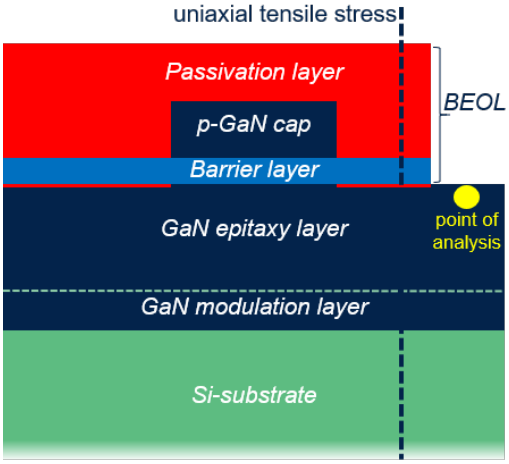

Figure 3: Schematic representation of the GaN-based device investigated in this work. The vertical black dashed line indicates the direction of the applied uniaxial tensile stress, while the yellow dot highlights the point where Raman measurements were collected.

In particular, it consists of an initial *GaN(0001) modulation layer* grown on a n-Si(111) substrate through metal–organic chemical vapor deposition (MOCVD). The n-Si(111) is characterized by a triangular symmetry which better support the hexagonal structure of GaN itself. Such modulation layer is generally grown at low temperature to mitigate the mechanical strain and reduce the crystallographic defects and dislocation density. It also plays a key role in reducing the reticular mismatch between the Si-substrate and the GaN epitaxy layer of interest, grown over it. In our case, experimental micro-Raman spectra were collected on a specific point (yellow dot in Fig.3) of the GaN epitaxy layer, following the ap-

plication of a uniaxial tensile stress along the device (vertical black dashed line in Fig.3). Finally, depending on the electrical characteristics of the final device, a barrier, metallization and passivation layers (here all grouped under the heading *BEOL* (*back-end of line*), see Fig.3) are built on the structure with different designs.
A home-made set-up, consisting of a three-point assembly, two supporting pins and a loading one, was used to generate the uniaxial tensile stress along the device. It is equipped with a manual micrometer with a screw pitch of 0.5 mm - and division on thimble 50 - to monitor and regulate the strain applied to the GaN layer (see Fig.4). In our case, the total deformation applied on the system was of $\sim$ 200 μm, achieved in 10 steps.

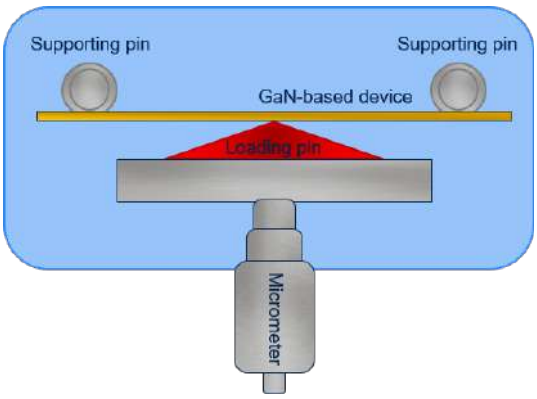

Figure 4: Schematic representation of the home-made set-up used in this work.

Method

Micro-Raman spectra were collected at room temperature (RT) through a confocal microscope NT-MDT NTEGRA Spectra in reflection mode, with an excitation wavelength of 532 nm (Nd:YAG laser), a maximum laser power of 1 mW and a IDUS type Andor camera cooled with a triple Peltier stage as detector. For the purpose of this study, the 500-600 cm^{-1} spectral range was investigated with a resolution $<$ 0.1 cm^{-1} (adjustable by neutral density filters) and integration time of 60 s. A 100X objective with a working-distance of 6 mm and a numerical aperture of 0.7 was used to focalize the laser beam on the surface of the sample with a spot size of $\sim$ 350 nm. In our case, all measurements were carried out in backscattering geometry, using the microscope lens of the instrument to optimize the collection of the scattered light.

Results and discussion

Fig.5 show a typical micro-Raman spectrum of a MOCVD-grown GaN film, with no tensile stress applied, in the frequency region between 500 and 600 cm^{-1}.

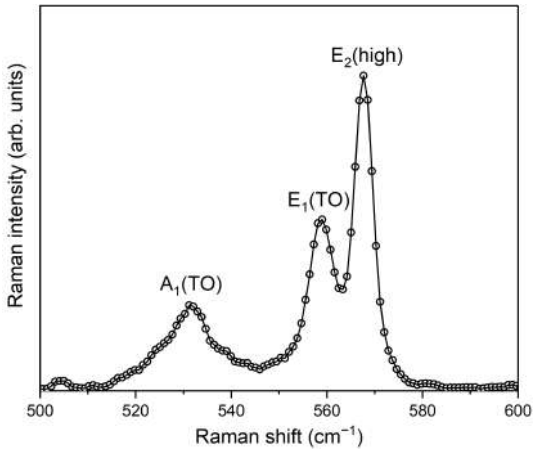

Figure 5: Stress-free micro-Raman spectrum collected on the investigated point of analysis of the MOCVD-grown GaN epitaxy layer with excitation of 532 nm in backscattering geometry at RT in the 500 - 600 cm^{-1} wavenumber range.

The hexagonal structure of wurtzite belongs to the crystallographic C_{6v}^4 space group, which predicts 8 different optical modes: two A_1, two E_1, two E_2 and two B_1. However, only 4 of the aforementioned modes are Raman active, i.e. one A_1(TO), one E_1(TO) and two E_2(*low* and *high*, respectively), and hence observable through Raman spectroscopy [7]. The detected micro-Raman profile (see Fig.5) revealed all these first-order Raman modes other than the E_2(low) symmetry mode which falls outside the investigated wavenumber range (141 cm^{-1}). In particular, the A_1(TO), E_1(TO) and E_2(high) modes can be clearly distinguished (see Fig.5), respectively falling at 531.7 cm^{-1}, 558.7 cm^{-1} and 567.7 cm^{-1}. It is worth of note that if, on one side, the observed peak's width and intensity provide valuable information about the quality of the substrate, on the other side, their frequency-centre can be used to monitor internal stresses occurring in the epitaxial film of GaN crystals. Accordingly, with the aim to evaluate the evolution of localized residual stresses inside the MOCVD-grown GaN substrate, a detailed analysis of the frequency shifts exhibited by the aforementioned spectral features upon mechanical perturbation was accomplished [8]. For this purpose, the MOCVD-grown GaN epitaxy layer was subjected to ten different tensile loads up to 5.8 GPa (above which the sample break down), and for each configuration a micro-Raman spectrum was collected. The A_1(TO), E_1(TO) and E_2(high) peaks were first fitted with Lorentzian lineshapes profiles (see Fig6a) and then their position was extrapolated as a function of the applied stress. The correlation between the tensile stress and Raman shift for each mode (A_1(TO), E_1(TO) and E_2(high)) is reported in Fig6b. In all cases, frequency-centres (ω) were found to monotonically decrease as the uniaxial tensile stress increases. More in detail, the E_2(high) mode appears to be more susceptible to the mechanical perturbation with respect to both A_1(TO) and E_1(TO), in agreement with literature [9].

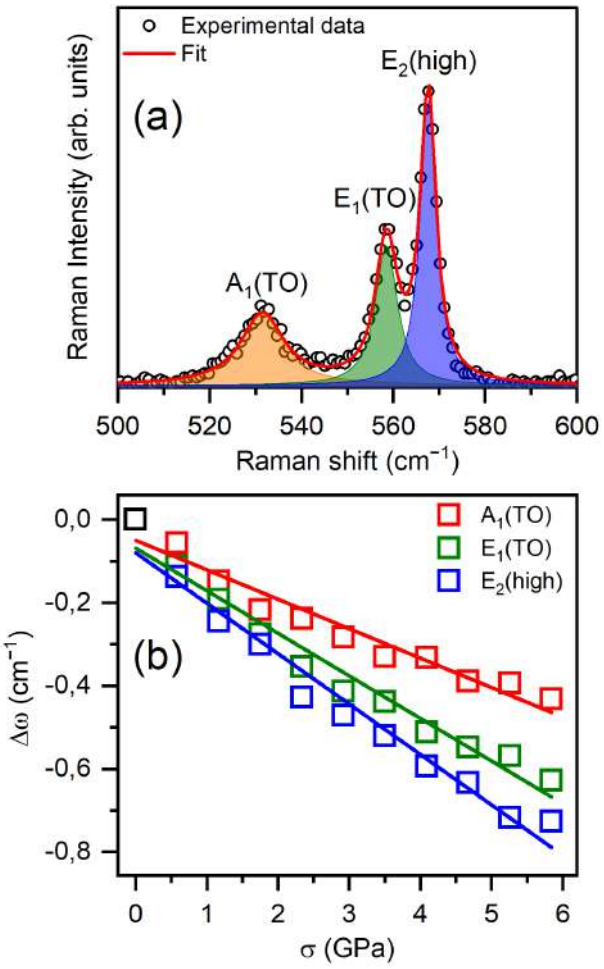

Figure 6: (a) Experimental micro-Raman spectrum of MOCVD-grown GaN epitaxy layer (black dots), together with the obtained fitting curve (red line) using Lorentzian functions. (b) Raman frequency shifts, $\Delta\omega = \omega - \omega_0$ (where ω_0 accounts for the corresponding stress-free peak position), for all the investigated modes upon increase in the tensile stress. Stress values, in GPa, were calculated starting from the applied manual deformation values and considering the Young module of the GaN material (that is 295 GPa). Coloured lines account for the linear fits of the observed frequency shift trends (see text for details).

This can be reasonably due to the fact that the E_2(high) mode involves atomic oscillations almost perpendicular to the c-axis of wurtzite, and hence more sensitive to the stress along the chosen axis (see Fig.3). Going on, the observed trends reported in Fig. 6b allowed us to calculate the residual stress inside the GaN substrate. As a matter of fact, the frequency shift ($\Delta\omega$) behaviour usually trace a linear relationship with the applied stress (σ) which can be modeled, in the case of polycrystalline structure, through the following statistical relation:

$$\langle\Delta\omega\rangle = \Psi_{PS}\langle\sigma\rangle, \quad (1)$$

where Ψ_{PS} is the piezo-spectroscopic coefficient equal to the trace of the piezo-spectroscopic tensor. Based on the assumption that, in first approximation, the residual stress Ψ_{RS} can be considered as equi-triaxial [10], it can be calculated as:

$$\Psi_{RS} = 3\Psi_{PS}. \quad (2)$$

Based on the aforementioned considerations, starting form the linear regressions of the Raman frequency shifts upon increase in the tensile stress shown in Figure 6b, the Ψ_{PS} values associated to the A_1(TO), E_1(TO) and E_2(high) modes were found to be equal to -0.08 cm^{-1} GPa^{-1}, -0.012 cm^{-1} GPa^{-1} and -0.013 cm^{-1} GPa^{-1}, respectively. According to eqn.2, the obtained values of Ψ_{PS} provides residual stresses Ψ_{RS} equal to -0.24 cm^{-1} GPa^{-1}, -0.36 cm^{-1} GPa^{-1} and -0.39 cm^{-1} GPa^{-1}.

Conclusions

In this work, micro-Raman spectroscopy was successfully employed in order to measure the residual stresses in a GaN film. In particular, a diminishing of the frequency-centre value of different specific modes of the material (i.e. A_1(TO), E_1(TO) and E_2(high)), upon increasing of the uniaxial tensile load, was observed. A linear regression procedure allowed us to properly calculate the residual stresses Ψ_{RS}, starting from the evaluation of the piezo-spectroscopic coefficient Ψ_{PS}. Obtained values of Ψ_{RS} were -0.24 cm^{-1} GPa^{-1}, -0.36 cm^{-1} GPa^{-1} and -0.39 cm^{-1} GPa^{-1}, respectively from the A_1(TO), E_1(TO) and E_2(high) frequency-centre behaviour. With the aim to further improve the overall quality of the data, a computer-controlled micrometer will be implemented in the experimental set-up, together with a steel wedge (instead of a plastic wedge). Finally, the influence of applied stress over the device active area will be also the subject of future investigations.

References

[1] Leszczynski, M., Teisseyre, Ha., Suski, T., Grzegory, I., Bockowski, M., Jun, J., Porowski, S., Pakula, K., Baranowski, JM., Foxon, CT., et al. *Lattice parameters of gallium nitride.* Applied Physics Letters, **69**(1), 73–75 (1996).

[2] Taniyasu, Y., Kasu, M., Kobayashi, N. *Lattice parameters of wurtzite $Al_{1-x}Si_xN$ ternary alloys.* Applied Physics Letters, **79**, 4351–4353 (2001).

[3] Paszkowicz, W., Adamczyk, J., Krukowski, S., et al. *Lattice parameters, density and thermal expansion of InN microcrystals grown by the reaction of nitrogen plasma with liquid indium.* Philosophical Magazine, **79**, 1145–1154 (1999).

[4] Kizilyalli, IC., Bui-Quang, P., Disney, D., Bhatia, H., Aktas, O. *Reliability studies of vertical GaN devices based on bulk GaN substrates.* Microelectronics Reliability, **55**(9–10), 1654–1661 (2015).

[5] Liu, L., Edgar, J.H. *Substrates for gallium nitride epitaxy.* Materials Science and Engineering: R: Reports, **37**(3), 61–127 (2002).

[6] Roccaforte, F., Leszczynski, M. *Introduction to gallium nitride properties and applications.* Nitride Semiconductor Technology: Power Electronics and Optoelectronic Devices, 1–39 (2020).

[7] Feng, ZC., Wang, W., Chua, SJ., Zhang, PX., Williams, KPJ., Pitt, GD. *Raman scattering properties of GaN thin films grown on sapphire under visible and ultraviolet excitation.* Journal of Raman Spectroscopy, **32**(10), 840–846 (2001).

[8] Zhang, JM., Ruf, T., Cardona, M., Ambacher, O., Stutzmann, M., Wagner, J-M., Bechstedt, F. *Raman spectra of isotopic GaN.* Physical Review B, **56**(22), 14399 (1997).

[9] Sugie, R., Uchida, T. *Determination of stress components in 4H-SiC power devices via Raman spectroscopy.* Journal of Applied Physics, **122**(19), 195703 (2017).

[10] Lee, CJ., Pezzotti, G., Okui, Y., Nishino, S. *Raman microprobe mapping of residual microstresses in 3C-SiC film epitaxial lateral grown on patterned Si (1 1 1).* Applied surface science, **228**(1–4), 10–16 (2004).

Ultrastrong Coupling of a Qubit with a Nonlinear Optical Resonator

F. Mauceri[1,*], A. Mercurio[1]
[1] *Dipartimento di Scienze Matematiche e Informatiche, Scienze Fisiche e Scienze della Terra, Università di Messina, Messina, Italy.*

*Corresponding Author email: fabio.mauceri@unime.it

Abstract

The aim of this work was to build a gauge independent model to describe the interaction of a two-level atom with a single-mode nonlinear electromagnetic resonator, considering coupling strengths ranging from zero to the so-called deep strong coupling regime. Additionally, we tested the reliability of the standard Kerr model for the resonator.

Keywords: USC, Cavity-QED.

The USC regime

The strength of the light-matter interaction is fixed by nature through the fine structure constant α. In 1946, Purcell [1] discovered that the interaction strength of an oscillator with light can be increased or decreased by changing the electromagnetic conditions of the environment in which it is located. From this discovery, a whole field of research was born called cavity quantum electrodynamics (Cavity-QED), where the natural coupling constant is replaced by a coupling constant g that quantifies the strength of interaction between light and matter. An important regime is the Strong Coupling (SC) obtained when the coupling strength is bigger than the losses of the system. Dividing g by the cavity frequency ω_c, the dimensionless parameter $\eta = g/\omega_c$ is obtained, and it is commonly stated that the Ultrastrong Coupling (USC), another regime of light-matter interaction, is achieved when $0.1 < \eta < 1$. The parameter η allows us to determine if the perturbation theory can be used and which approximation can be made in the light-matter interaction. In particular, the SC regime can be described through the Jaynes-Cummings model, while the USC by the quantum Rabi model (QRM). An interesting property of the USC is that the ground state does not conserve the number of excitations and it contains virtual excitations. This means that the ground state is a superposition of states with different number of excitations.
Fig. 1 shows a microwave spectroscopy of a system with a superconducting flux qubit coupled to a coplanar-waveguide resonator [2]. The system displays a normalized coupling strength $\eta = g/\omega_c = 0.12$. The plot shows the cavity transmission as a function of probe frequency ω_{probe} and flux offset, which tunes the qubit frequency. The avoided level crossing indicates a coupling between states with different numbers of excitations (one state has a single photon in the third resonator mode; the other state has one qubit excitation and one photon in the first resonator mode). Such a coupling requires the so called counter-rotating terms and is not reproduced by the Jaynes-Cummings approximation. The USC regime can improve the performance of already existing devices built in the SC regime [3], and even open new areas of research since some effects cannot be seen outside of this regime. This allows for suitable applications, such as the realization of new kind of quantum gates on specific short life time system [4], to some theoretical one as the emergence of new phenomena, such as quantum phase transition.

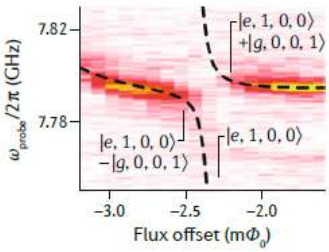

Figure 1: Avoided level crossing typical of USC.

Gauge independent QRM

The USC regime enhanced some theoretical problem that could have been ignored safely for lower coupling strengths. One of them was the gauge-dependent energy spectra for the QRM. As shown in [5], the eigenvalues of the Hamiltonian obtained in the Couloumb gauge ($\hat{\mathcal{H}}_C$) differ from the one obtained in the dipole gauge ($\hat{\mathcal{H}}_D$). Moreover, if one considers the full Hamiltonian, i.e. the Hamiltonian without applying the two level truncation, it validates the dipole-gauge Hamiltonian results. Respec-

tively, the Hamiltonians for the QRM in the dipole and Coulomb gauges read

$$\hat{\mathcal{H}}_D = \omega_c\,\hat{a}^\dagger\hat{a} + \frac{\omega_q}{2}\hat{\sigma}_z + i\omega_c\eta\left(\hat{a}^\dagger - \hat{a}\right)\hat{\sigma}_x + \omega_c\eta^2\mathbb{1}\,, \quad (1)$$

$$\hat{\mathcal{H}}_C = \omega_c\,\hat{a}^\dagger\hat{a} + \frac{\omega_q}{2}\hat{\sigma}_z + \omega_c\,\eta\,(\hat{a}^\dagger + \hat{a})\,\hat{\sigma}_y + \omega_c\eta^2(\hat{a}^\dagger - \hat{a})^2\,. \quad (2)$$

This problem was solved in Ref. [6], where the authors showed that the two-level truncation introduced a non local potential, leading to gauge dependent spectra. They also found a solid procedure, based on the minimal coupling replacement, to obtain the correct expression for the Hamiltonian in the Couloum gauge ($\hat{\mathcal{H}}'_C$):

$$\hat{\mathcal{H}}'_C = \omega_c\,\hat{a}^\dagger\hat{a} + \frac{\omega_q}{2}\left(\hat{\sigma}_z cos[2\eta(\hat{a}^\dagger+\hat{a})] + \hat{\sigma}_y sin[2\eta(\hat{a}^\dagger+\hat{a})]\right). \quad (3)$$

As show in Fig. 2, the eigenvalues of $\hat{\mathcal{H}}'_C$ and $\hat{\mathcal{H}}_D$ overlap, proving that $\hat{\mathcal{H}}'_C$ is the correct form for the QRM in the Couloumb gauge.

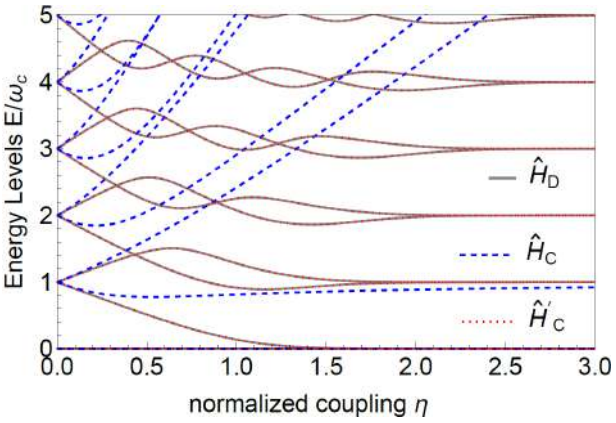

Figure 2: Quantum Rabi model eigenvalues as a function of the normalized coupling η for the Hamiltonian in the Dipole Gauge ($\hat{H}_D$), in the standard Coulomb gauge ($\hat{H}_C$), and in correct Coulomb gauge ($\hat{H}'_C$)

Additionally, they presented a quantum gauge transformation ($\hat{\mathcal{T}}$) that allows to correctly move from one gauge to another:

$$\hat{\mathcal{T}} = \exp\left[-i\eta\hat{\sigma}_x\left(\hat{a} + \hat{a}^\dagger\right)\right], \quad (4)$$

$$\hat{\mathcal{H}}_{Coulomb} = \hat{\mathcal{T}}^\dagger\hat{\mathcal{H}}_{dipole}\hat{\mathcal{T}}\,, \quad (5)$$

$$\hat{\mathcal{H}}_{dipole} = \hat{\mathcal{T}}\hat{\mathcal{H}}_{dipole}\hat{\mathcal{T}}^\dagger\,. \quad (6)$$

In the following sections we are going to present the results for a qubit interacting with a nonlinear quantum electromagnetic oscillator, published very recently in Ref. [7].

Nonlinear quantum electromagnetic resonator

Before studying the interaction between a qubit and a nonlinear quantum electromagnetic resonator, we have to understand how to correctly write the Hamiltonian of the nonlinear resonator. Possible choices are the following:

$$\hat{\mathcal{H}}_{c,+} = \omega_c\,\hat{a}^\dagger\hat{a} + \frac{j}{6}\left(\hat{a} + \hat{a}^\dagger\right)^4, \quad (7)$$

$$\hat{\mathcal{H}}_{c,-} = \omega_c\,\hat{a}^\dagger\hat{a} + \frac{j}{6}\left(\hat{a} - \hat{a}^\dagger\right)^4. \quad (8)$$

Since they are connected by a unitary transformation ($\hat{a} \to i\hat{a}$ and $\hat{a}^\dagger \to -i\hat{a}^\dagger$), they provide the same eigenvalues. However, when we add the qubit to the system, the eigenvalues can be different, if the qubit-resonator coupling is not modified accordingly. In order to obtain the correct Hamiltonian we developed a polariton model. Considering that the only way to obtain a nonlinear interaction for such a system is through the interaction with a matter system, the starting point of our model are two interacting bosonic oscillators, one describing the cavity field and the other a matter collective excitation. Following [8], the system Hamiltonian is:

$$\mathcal{H}_d = \omega_0\,\hat{a}^\dagger\hat{a} + \omega_b\,\hat{b}^\dagger\hat{b} + \omega_0\left[i\lambda(\hat{a}^\dagger - \hat{a})(\hat{b} + \hat{b}^\dagger) + \lambda^2(\hat{b} + \hat{b}^\dagger)^2\right]. \quad (9)$$

Now we proceed to the diagonalization of Eq.(9) with a Bogoliubov transformation, obtaining

$$\hat{\mathcal{H}}_{diag} = \sum_{n=1,2}\omega_n\hat{P}_n^\dagger\hat{P}_n\,, \quad (10)$$

with $\hat{P}_n$ and $\hat{P}_n^\dagger$ (polariton operators) linear combination of $\hat{a}$, $\hat{a}^\dagger$, $\hat{b}$ and $\hat{b}^\dagger$.
Now we add a nonlinear interaction term V_{nl} and we express it in the polariton basis:

$$V_{nl} = \frac{j}{6}(\hat{b}+\hat{b}^\dagger)^4 = \frac{j}{6}\left[iC_1\left(\hat{P}_1 - \hat{P}_1^\dagger\right) + C_2\left(\hat{P}_2 - \hat{P}_2^\dagger\right)\right]^4. \quad (11)$$

The Hamiltonian becomes:

$$\hat{\mathcal{H}}_{polariton} = \omega_1\hat{P}_1^\dagger\hat{P}_1 + \omega_2\hat{P}_2^\dagger\hat{P}_2 + \frac{j}{6}\left[iC_1\left(\hat{P}_1 - \hat{P}_1^\dagger\right) + C_2\left(\hat{P}_2 - \hat{P}_2^\dagger\right)\right]^4. \quad (12)$$

If we consider well separated energy levels, $\lambda \ll |\omega_0 - \omega_b|$ and a frequency $\omega \sim \omega_0$ we can ignore the contribution from $\hat{P}_2$, thus obtaining:

$$\hat{\mathcal{H}}_{polariton} \approx \omega_1\hat{P}_1^\dagger\hat{P}_1 + \frac{\sim j}{6}\left(\hat{P}_1 - \hat{P}_1^\dagger\right)^4. \quad (13)$$

We can identify the bosonic operator $\hat{P}$ with the photon operator $\hat{a}$, ω_1 with ω_c and $\sim j$ with j, leading to

$$\hat{\mathcal{H}}_{c,-} = \omega_c\,\hat{a}^\dagger\hat{a} + \frac{j}{6}\left(\hat{a} - \hat{a}^\dagger\right)^4. \quad (14)$$

We thus obtained the correct expression for the nonlinear interaction Hamiltonian.

Qubit interacting with a nonlinear quantum electromagnetic resonator

Having found the correct Hamiltonian for a nonlinear quantum electromagnetic resonator, we add the interacting qubit. To this end we write a generic Hamiltonian for this system:

$$\hat{\mathcal{H}} = \omega_c \hat{a}^\dagger \hat{a} + \hat{\mathcal{H}}_{nl} + \frac{\omega_q}{2}\hat{\sigma}_z + \hat{\mathcal{H}}_{int}\,.$$

We already proved that the correct form for $\hat{H}_{nl}$ is $\frac{j}{6}\left(\hat{a}-\hat{a}^\dagger\right)^4$, but we still have to find the correct form for the qubit-resonator interaction ($\hat{\mathcal{H}}_{int}$).
One possibility is to use the standard qubit-cavity interaction that in the dipole gauge is (see Eq.(1)):

$$\hat{\mathcal{H}}_{int} = i\omega_c\eta\left(\hat{a}^\dagger - \hat{a}\right)\hat{\sigma}_x + \omega_c\eta^2\mathbb{1}\,, \tag{15}$$

but this would violate the gauge principle. Indeed, we can see that the non linear term $\left(\hat{a}-\hat{a}^\dagger\right)^4$ does not commute with $\hat{\mathcal{T}}$ (Eq.(4)). We have to apply the same procedure showed in [6] to all the terms of the Hamiltonian, leading to:

$$\hat{\mathcal{H}}_D^- = \omega_c\,\hat{a}'^\dagger\hat{a}' + \frac{\omega_q}{2}\hat{\sigma}_z + \frac{j}{6}\left(\hat{a}'-\hat{a}'^\dagger\right)^4\,, \tag{16}$$

where we have defined

$$\begin{aligned}\hat{a}' &= \hat{a} + i\eta\hat{\sigma}_x\,,\\ \hat{a}'^\dagger &= \hat{a}^\dagger - i\eta\hat{\sigma}_x\,.\end{aligned} \tag{17}$$

In Fig. 3 we can see a comparison between the eigenenergies of this system $\hat{\mathcal{H}}_D^-$ with:

$$\begin{aligned}\hat{\mathcal{H}}_D^+ &= \omega_c\,\hat{a}'^\dagger\hat{a}' + \frac{\omega_a}{2}\hat{\sigma}_z + \frac{j}{6}\left(\hat{a}+\hat{a}^\dagger\right)^4\,,\\ \hat{\mathcal{H}}_D^K &= \omega_c\,\hat{a}'^\dagger\hat{a}' + \frac{\omega_a}{2}\hat{\sigma}_z + j\,\hat{a}'^\dagger\hat{a}'^\dagger\hat{a}'\hat{a}'\,,\end{aligned} \tag{18}$$

where the Hamiltonian $\hat{\mathcal{H}}_D^+$ has the nonlinear interaction term with the plus sign, that we have discarded in the previous section, and $\hat{\mathcal{H}}_D^K$ is the Kerr Hamiltonian, usually used to describe third-order nonlinear processes in a single-mode resonator, and obtained by applying the rotating wave approximation to the full nonlinear term $\left(\hat{a}-\hat{a}^\dagger\right)^4$. It is interesting to see the impact of using these Hamiltonians instead of the correct one $\hat{\mathcal{H}}_D^-$. We observe that the differences increase with the energy level, showing a very small window where we can consider the two Hamiltonians Eq.(18) an acceptable approximation of $\hat{\mathcal{H}}_D^-$. Additionally, the eigenvalues of $\hat{\mathcal{H}}_D^K$ display the largest differences with respect to those of $\hat{\mathcal{H}}_D^-$, since they also show an offset on the energy of the excited levels for $\eta = 0$.

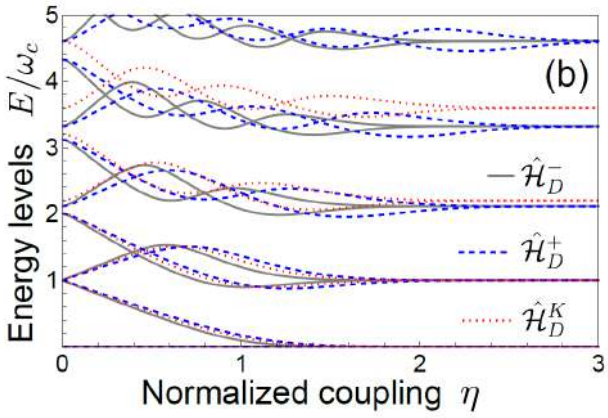

Figure 3: Comparison between the lowest energy energy levels of $\hat{\mathcal{H}}_D^\pm$, and $\hat{\mathcal{H}}_D^K$ as function of the normalized coupling η for $j = 0.1\,\omega_c$. The eigenvalues of $\hat{\mathcal{H}}_D^\pm$ and $\hat{\mathcal{H}}_D^K$ are compared assuming the respective ground state energy equal to zero at each value of η.

Acknowledgment

We thank S. Savasta and O. Di Stefano for useful discussions and suggestions.

References

[1] E. M. Purcell, Spontaneous emission probabilities at radio frequencies, Phys. Rev. 69, 681 (1946)

[2] T. Niemczyk et al., Circuit quantum electrodynamics in the ultrastrong coupling regime, Nat. Phys. 6, 772(2010)

[3] A. F. Kockum et al., Frequency conversion in ultrastrong cavity QED, Sci. Rep. 7, 5313 (2017)

[4] G. Romero et al., Ultrafast Quantum Gates in Circuit QED, Phys. Rev. Lett. 108, 120501

[5] D. De Bernardis et al., Breakdown of gauge invariance in ultrastrong-coupling cavity QED, Physical Review A 98.5 (2018): 053819

[6] O. Di Stefano et al., Resolution of gauge ambiguities in ultrastrong-coupling cavity quantum electrodynamics, Nat. Phys. 15, 803–808 (2019)

[7] F. Mauceri et al., Ultrastrong coupling of a qubit with a nonlinear optical resonator, Physical Review A 105.2 (2022): 023719

[8] L. Garziano et al., Gauge invariance of the Dicke and Hopfield models, Phys. Rev. A 102, 023718 (2020)

Investigation of the thermal behavior of a 7kW interleaved module for automobile fast charging

G. G. Piccione[1], G. Mauromicale [2], M. Calabretta[2], S. Patanè[1],
[1]*Dept.Scienze Matematiche e Informatiche, Scienze Fisiche e Scienze della Terra, University of Messina, Messina, Italy*
[2]*ST-Microelectronics Catania, Italy*

*Corresponding Author email: giupiccione@unime.it

Abstract

As a result of environmental concerns, in recent years electric vehicles (EVs) have received significant attention in order to remedy to the tougher CO2 emission and develop new more performant technology for sustainable mobility. In this framework, power semiconductor devices based SiC introduce a higher level of power flow, which need proper thermal techniques to be developed. Battery reliability and charging are two critical issues in plug–in EVs, both for the car and for the integrated grid infrastructure. In this paper we propose a thermal simulation of a novel scalable On–Board Charger (OBC) able to perform a power flow up to 7 kW, using the finite–element based COMSOL Multiphysics. A more detailed validation of the proposal thermal model is represented by a parametric study obtained by varying the convective heat transfer coefficient with the goal to give customers precious information about the proper cooling system to install.

Keywords: automotive, DC–DC converter, fast charger, LLC, power MOSFET, on board charger, power factor corrector, silicon, silicon carbide, thermal simulation..

Introduction

The fast-spreading of plug–in full and hybrid vehicles has unquestionably pushed up the new power semiconductor technologies based on wide band–gap materials such as silicon carbide (SiC) and gallium nitride (GaN). They allow improved efficiency and higher power density from both a device and architecture standpoint [1, 2] and are today employed in complex architectures together with silicon (Si) –based devices in resonant converters [3]. The charging can be installed both on–board and off–board. Furthermore, the so–called "on–board integrated chargers," which take into account existing motors or converters inside the EV, are being developed, although their technology still appears immature comparing to other solutions [4].
On-board chargers (OBCs) can be unidirectional or bidirectional, with the possibility to allow power exchange from vehicle to grid [5]. There are many modulation schemes and control modes for OBCs, such as DC fast charging stations, which are off–board solutions [6]. In this framework, the converter to charge the batteries is off–board and placed in the stations. Various AC and DC charging modes exist. Another charging mechanism in development is wireless power transmission based on induction law [7]. It would shorten the time necessary to charge the battery and improve the system's safety and reliability; nevertheless, in comparison to wired modes, this opportunity is still in its infant stage. In relation to this power transfer mechanism, vehicle–to–vehicle recharging has been proposed, in which two cars can swap power, one from the other, during a journey [8]. Fast charging can be obtained also with AC–based OBC topologies. The considered architectures can be either single–phase or three–phase (Fig. 2). Among the possible converter types, there are: conventional, interleaved, or phase shifted semi–bridgeless boosts, but also bridgeless interleaved topologies, also in resonant version [9]. A comprehensive overview of the possible topologies for off–, on–board, and integrated chargers, employing Si, SiC, or GaN devices, can be found in [10] and [11]. Usually, a filter is placed in the system, before the power factor corrector (PFC) stage, to mitigate the electromagnetic interference. Considering a system with AC input, then there is AC–DC converter. The converter considered in this paper, briefly described hereafter, has an input voltage ranging between 85 and 265 V, while the voltage frequency falls in the range 45–65 Hz. Thermal control of power devices in these high–performance converters is inextricably linked to system longevity [2]. The device's junction temperature must remain below a threshold defined by the Coffin Manson model to guarantee that reliability targets are met and preventing early failures [12–14]. The aim of this paper consists of design a finite–element based thermal model able to simulate the OBC and to evaluate temperature values of the active devices in a typical operation state. The work is structured as follows: in Section II, we explain the thermal management for the investigated module, including information on the power losses computation for the PFC and LLC stages in the fast OBC. Section III goes through the important factors

that go into building a scalable system capable of handling 7 kW per module. Section IV describes the parameters and model used to simulate the thermal behavior of the system at steady-state conditions in order to calculate the maximum temperature achieved during normal operation. Conclusions and future works are presented in Section V.

Modular solution description

In this Section, we describe the OBC structure. The 7 kW AC–DC power converter module take advantage of innovative SiC devices, allowing for the parallelization of multiple MOSFETs in an interleaved stacked system capable of reaching up to 21 kW and being configured for mono and three phase inputs, as shown in Fig.2.

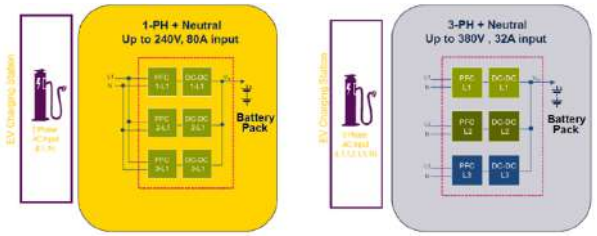

Figure 1: Single and three phase configuration schemes

The suggested method aims to provide an AC–DC power converter that can be integrated into an electric car's OBC as well as a DC wall–box. In compared to normal AC wall–boxes, the final alternative would be regarded as a novel method for drastically lowering charging time. As shown in Fig. 3, the reference design has two sections: an interleaved totem pole PFC using SiC MOSFETs and a dual galvanic isolated full bridge LLC DC–DC ZVS resonant converter based on MDmesh DM6 super–junction power MOSFETs.

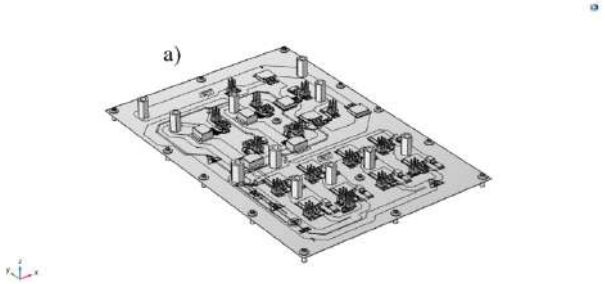

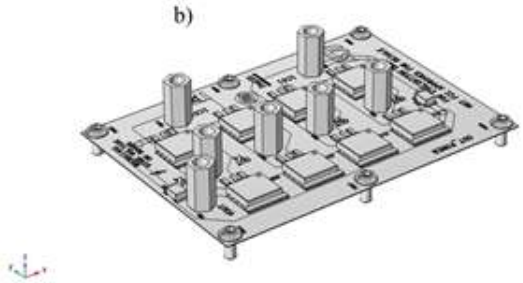

Figure 2: Global geometry of a) PFC and LLC stages and b) output stage

The PFC section uses a variety of signals, including sinusoidal mains voltage zero crossing signals, mains signals, current sensors for the first and second totem pole inductors, comparators for maximum current limits, SiC driver signals, SCR driver signals, bus voltage, and PFC temperature sensing signals. The bus voltage galvanically isolated sensing signal, resonant current of the resonant cells, output current and output voltage, LLC temperature, and MOSFET driving signals for the two full bridge LLCs are all used in the DC–DC converter dual full bridge LLC section. The PFC section is an interleaved totem pole that uses 2 x 510 μH inductors and 2240 μF bulk capacitors. The switching frequency is 70 kHz. The high frequency legs use SiC MOSFETs (STB47N60DM6AG) and the low frequency leg is SCR–based (TN3050H-12GY-TR). This PFC is meant to operate in continuous conduction mode (CCM), with two separate current loops (type II or PID controllers), mains voltage feedforward, and PWM startup at zero crossing to prevent current spikes. The switching frequency of the interleaved totem pole PFC is 70 kHz, whereas the dual DC–DC LLC resonant converter ranges between 80 kHz and 310 kHz. The DC–DC LLC has an output current balance control, while the interleaved totem pole has an inductor current balanced control. These design ensure that the parallel connection stages have a balanced current. The AC–DC totem pole PFC section converts an input voltage of 85 VAC to 265 VAC into 400 V. The maximum input current is 32 A at 50 Hz or 60 Hz. The PFC works in CCM. With a dynamic resistance of 14 mΩ, the TN3050H-12GY-TR SCR thyristors implement inrush current. Two independent current loop regulators are used by PID or 2p2 controllers to regulate current. The SPC58NN84E7 MCU controller is used to implement these controls. The second converter is the dual resonant DC–DC LLC based on super junction MOSFETs. The output DC–DC voltage is in the range of 250 VDC to 450 VDC. Two independent constant current loops (CC) and one constant voltage loop (CV) plus current balancing are implemented on a second SPC58NN84E7 MCU controller. The 7 kW AC–DC power module consists of the following blocks, that are showed in Fig.4:

- EMI Filter/front end rectifier;
- SiC interleaved totem pole PFC stage to ensure the optimal interfacing with the mains [15];

- DC \DC converter based on interleaved Full Bridge (FB)-LLC with SiC synchronous rectifier–box [16].

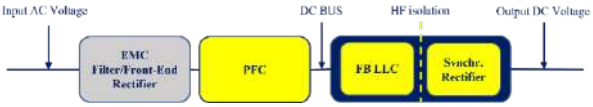

Figure 3: block diagram of the DC–DC converter

The goal is to use interleaved solutions for the SiC PFC stage (totem pole) and the high voltage side of the DC–DC converter (FB LLC) to gain the configuration flexibility needed to provide the required power size (up to 21 kW by stacking three modules) and the AC mains interfacing via a 7 kW module, used alone or in parallel, to match mono phase (1 Phase+ N) and three phase (3 Phases + N) assembly modes. The top and exploded views of the OBC are shown in Figs. 5 and 6, respectively.

Figure 4: Top view of the OBC structure

Figure 5: Exploded view of the OBC structure

Thermal simulation setup and results

The aim of the thermal simulations is to estimate the maximum temperature reached by the devices, to obtain a proper lifetime reliability model to learn about the behavior and reliability of the system with typical operating settings. The simulations are run on COMSOL Multiphysics, a cross–platform finite element method (FEM) analytical program that supports traditional physics–based user interfaces as well as coupled systems of partial differential equations (PDEs). With the FEM approach, PDEs may be converted into algebraic equations. We focused on the thermal behavior of PFC and DC–DC converters, which are the two critical point of the system. Fig. 7 depicts the investigated vehicle on–board charger, with the simulated elements highlighted.

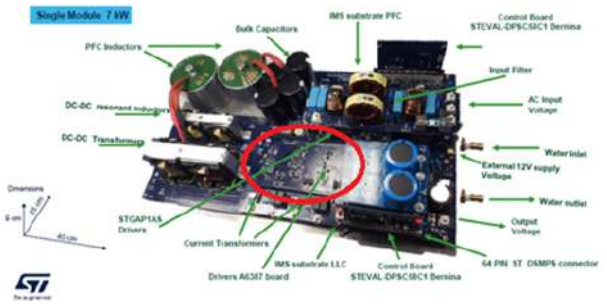

Figure 6: Picture of the on–board charger. The red ellipses highlight the parts we focused for the thermal simulation (LLC and PFC stages).

The complex multilayered mechanical structure is described as follow:

- An aluminum baseplate, which is connected to the external cooling system (420x200x6 mm);
- A thermal grease thin layer with the same area having a thickness of 180 μm, useful to improve thermal conductivity;
- Right up two IMSs, one for the PFC stage (203x139x1.5 mm) and the other for the LLC stage (91x65x1.5 mm), at a distance of 105 mm from each other;
- Both stages have on top a copper layer of 105 μm, which hosts all the active components (diodes, thyristors, and transistors), all dies have the real size, those are undisclosed information;
- The entire structure is incapsulated in the epoxy resin;
- The copper and epoxy resin of each device as the size of the package of the component.

An important task is providing a model in which the trade–off between approximations and computational times is acceptable. In this work, three boundary conditions were used. The first concerns the active component dies that work as heat sources. This condition was accurately employed by using the complementary COMSOL functionalities “work plane” and “partition objects”; this procedure assures the solving of some mesh problems and the decrease of the computation time.

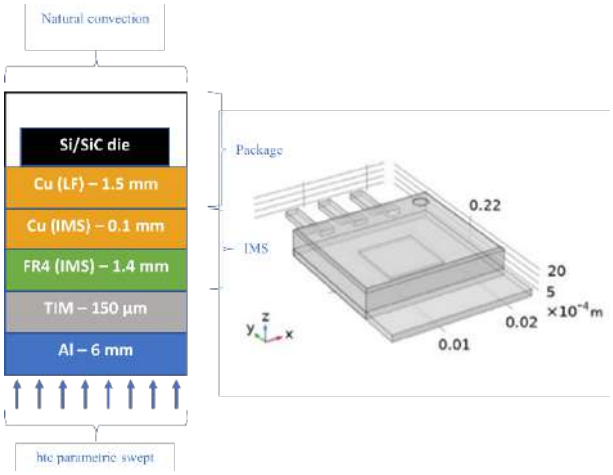

Figure 7: a) Details of the layers used to simulate the structure; b) the model used to simulate the system (on the left) and a power device structure (on the right).

The second condition regards the simulation of the cooling system. The bottom layer of the aluminum baseplate produces a convective heat flux. The heat transfer coefficient (htc) has been parameterized and a sweep has been performed to allow us drawing some curves to evaluate the working temperature of devices starting from the performances of the heatsink. The last boundary condition is the heat flow from the device package, that describes the natural convective flux to which each devices undergoes during the normal operations. The htc due to this convective flux has been settled at 4 W/m2 K. The complex geometry and the large difference in thicknesses of the layers represent a challenge in realizing a mesh suitable to perform a model able to find a convergence in a reasonable time. To overcome this issues we used a trick consisting in associate to the die of every active component a "work plane", than, using the "partition objects" every device can be mapped by smaller domains obtaining a suitable mesh. At the end of the procedure, all the device surface is "mapped" meshed (and therefore further divided) in elements which area is smaller than one millimeter squared. The mesh of the device is finally obtained by extruding the upper mapped meshed surface from top to bottom. This procedure must be repeated for each component. The IMS layers, the corresponding copper films, the thermal grease and the baseplate were then covered with a "non–structured quadrilateral" mesh and extruded following the above procedure. About the parametric simulation results, we find that at lower htc values the thermal jump is more evident, this is a predictable result but also qualify the model. Using an htc=10 W/m2 K the resulting thermal gradient is about 56,85K. Fig. 10 shows the temperature versus the htc. The Higher htc values lead to a plateau in the thermal jump. This can be easily understood taking into account that higher htc values means that the heatsink works like a thermostat, therefore the temperature is almost constant i.e. the heatsink is able to remove almost all the heat produced by the devices. Figure 9 shows the thermal distribution obtained with an htc of 10000 W/m2, that is a value largely compatible with the automotive standard.

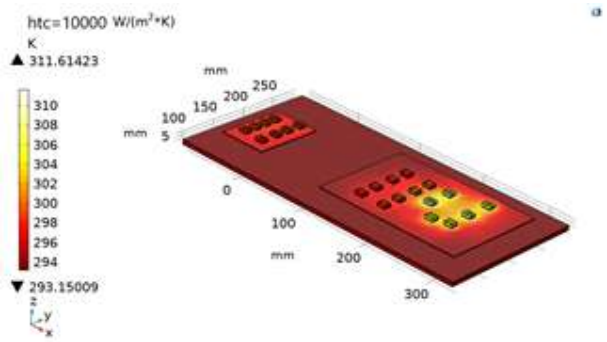

Figure 8: Curve of the $T_{max} - T_{ext}$ as a function of the heat transfer coefficient.

The small temperature difference in comparison to the large htc difference suggests that the PFC and LLC stages under study offer improved thermal performance. We evaluate the thermal gradient for values of htc of 1, 2, 3, 4, 5, 6, 7, 8, 9, 10, 100, 1000, 10000, 100000 W/m^2K. To better clarify the curve of the $T_{max} - T_{ext}$ as a function of the heat transfer coefficient (as shown in Fig.11), we judged it relevant to investigate in greater accuracy the range from $htc = 1W/m^2K$ to $htc = 10W/m^2K$, and therefore we opted to continue in unit steps in this range, in which a logarithmic scale for x-axes is used.

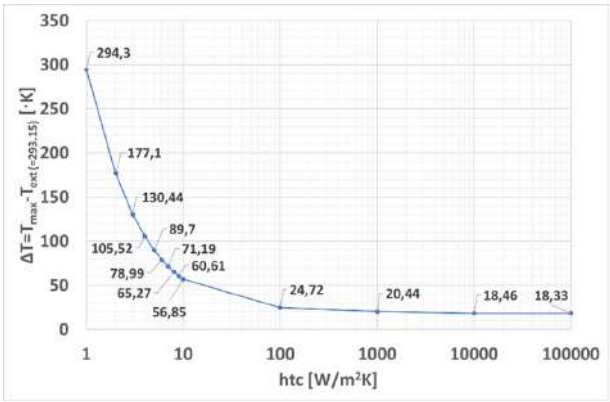

Figure 9: The obtained thermal jump for htc=10000 W/m^2K parametric swept, in which the maximum is located on the SiC Power MOSFETs.

The computation time for the parametrization is of 1 hour, 11 minutes and 10 seconds, in order to solve 1382337 degrees of freedom (df), in which 305 s are spent for each simulation for the setted values.

Conclusion

Using a FEM simulation, we investigated the thermal behavior of an OBC's PFC and LLC stages. In order to evaluate the maximum temperature reached by the semiconductor dies, a complex multilayered mechanical topology was built and three boundary condition was used. In our simulation, all dies work as heat source, a natural convection is applied to the external active component boundary (htc=4 W/m^2K). We calculated the maximum temperature versus the htc obtaining a curve suitable to design the system heatsink. The results highlight a thermal jump of about 20 ° C when the htc is higher 100 W/m^2K, these values are largely compatible with the use in automotive environment and allow to qualify the system reliability.

References

[1] Li, S., Lu, S., Mi, C. C.: *Revolution of Electric Vehicle Charging Technologies Accelerated by Wide Bandgap Devices*. Proceedings of the IEEE, doi: 10.1109/JPROC.2021.3071977.

[2] Roccaforte, F., Fiorenza, P., Greco, G., Nigro, R.L., Giannazzo, F., Iucolano, F., Saggio, M.: *Emerging trends in wide band gap semiconductors (SiC and GaN) technology for power devices.* in Microelectronic Engineering, 2018.

[3] Glitz, E. S., Ordonez, M.: *MOSFET Power Loss Estimation in LLC Resonant Converters: Time Interval Analysis.* in IEEE Transactions on Power Electronics.

[4] Metwly, M, Y,. Abdel-Majeed, M. S., Abdel-Khalik, A. S., Hamdy, R. A., Hamad M. S., Ahmed, S.: *A Review of Integrated On-Board EV Battery Chargers: Advanced Topologies, Recent Developments and Optimal Selection of FSCW Slot/Pole Combination.* ," in IEEE Access.

[5] Yuan, J., Dorn-Gomba, L., Callegaro, A. D., Reimers J., Emadi, A.: *A Review of Bidirectional On-Board Chargers for Electric Vehicles.* in IEEE Access.

[6] Rafi, M. A. H., Bauman, J.: *A Comprehensive Review of DC Fast Charging Stations with Energy Storage: Architectures, Power Converters, and Analysis.* in IEEE Transactions on Transportation Electrification.

[7] Ahmad, A., Alam, M. S., Chabaan, R.: *A Comprehensive Review of DC Fast Charging Stations with Energy Storage: Architectures, Power Converters, and Analysis.* in IEEE Transactions on Transportation Electrification.

[8] Nezamuddin, O. N., Nicholas, C. L., Santos, E. C.: *The Problem of Electric Vehicle Charging: State-of-the-Art and an Innovative Solution.* in IEEE Transactions on Intelligent Transportation Systems.

[9] Mauromicale, G., Raciti, A., Rizzo, A. S., Susinni, G., Parise, G. Parise, L.: *E-mobility: Safety, Service Continuity and Penetration of Charging Systems* 2019 AEIT International Conference of Electrical and Electronic Technologies for Automotive (AEIT AUTOMOTIVE).

[10] Rivera, S., Kouro, S., Vazquez, S., Goetz, S. M., Lizana, R., Romero-Cadaval, E.: *Electric Vehicle Charging Infrastructure – From Grid to Battery* in IEEE Industrial Electronics Magazine.

[11] Khaligh, A., D'Antonio, M.: *Global Trends in High-Power On-Board Chargers for Electric Vehicles* in IEEE Transactions on Vehicular Technology.

[12] Durand, C., Klingler, M., Coutellier, D., Naceur, H.: *Power Cycling Reliability of Power Module: A Survey* in IEEE Transactions on Device and Materials Reliability.

[13] Russo, S. et al: *Reliability Assessment of Power MOSFETs Working in Avalanche Mode Based on a Thermal Strain Direct Measurement Approach* in IEEE Transactions on Industry Applications.

[14] Gupta, K. et al: *Reliability Assessment of Power MOSFETs Working in Avalanche Mode Based on a Thermal Strain Direct Measurement Approach* in IEEE Transactions on Industry Applications.

[15] Huang, Q., Huang, A. Q.: *Review of GaN totem-pole bridgeless PFC* in CPSS Transactions on Power Electronics and Applications.

[16] Nardo, D., Scuto, A.,Buonomo, S.: *Evaluation of primary-side MOSFETs losses in resonant LLC converters* in PCIM Europe digital days 2021.

Calibration and Status of the CLIR Experiment at LNS

F. Risitano[1,2,*]
[1] *Dipartimento di Scienze Matematiche e Informatiche, Scienze Fisiche e della Terra, Università di Messina, Messina, Italy*
[2] *INFN Sezione di Catania, Italy*

*Corresponding Author email: farisitano@unime.it

Abstract

The *CLIR* experiment, performed in 2015 at *INFN - Laboratori Nazionali del Sud*, aimed primarily at the investigation of exotic structures in light radioactive nuclei, via break-up reactions. A radioactive beam was produced at the FRIBs@LNS facility, containing several radioactive isotopes of interest, such as ^{6}He, $^{7,8,9}Li$, $^{10,11,12}Be$, $^{13,14,15}B$, $^{16,17}C$. Identification of all the isotopes of the radioactive cocktail beam has been performed by means of a ΔE–ToF tagging system. A $(CH_2)_n$ target was used to trigger break-up reactions, whose products were collected by the FARCOS and CHIMERA detectors. In this paper an overview of the status of the experiment and of the detectors calibrations will be given.

Keywords: Radioctive beams, In-Flight fragmentation, FARCOS, CHIMERA.

Introduction

A powerful tool to study the behaviour of nuclear forces in the interactions of nucleons is based on the investigation of the cluster structure of light nuclei. It is in fact well known that self-conjugated nuclei can present α particle cluster structures, due to reorganization of nucleons in much stable sub-units [1]. Clustering effects have been observed even in non self-conjugated nuclei, in which extra nucleons behave similarly to electrons in atomic molecular bonds, leading to the formation of nuclear molecular structures, introducing high deformations in the nucleus.

The *CLIR* (Clustering in Light Ion Reactions) experiment, performed in 2015 at *INFN - Laboratori Nazionali del Sud*, aimed in particular at the study of cluster structures in radioactive light ions. In this paper the CLIR experiment will be described, giving a full overview of the experimental setup, which in particular involved the production of a radioactive ion beam by the FRIBs (*In-**F**light **R**adioactive **I**on **B**eams*) facility, based on the In-Flight fragmentation technique [2]. In this case a ^{18}O beam (55 MeV/u) was accelerated by the Superconducting Cyclotron (SC) and fragmented on a 1500 µm ^{9}Be target. The fragmentation produced a cocktail beam of several isotopic species, from ^{6}He to ^{17}C, with many interesting cases like ^{10}Be and ^{16}C, for which cluster chain-like structures have been already observed in previous experiments [3]. The resulting cocktail beam was then injected in the fragment separator FRIBs, selecting the ions with a rigidity $B\rho \approx 2.8$ Tm. Ions of the cocktail beam have been identified in charge and mass by means of a tagging system, by using the $\Delta E - TOF$ method. The tagging system was made of a microchannel plate detector, measuring the start of the Time-of-Flight, and a Double Sided Silicon Strip Detector (DSSSD), 156 µm-thick, measuring the stop of the TOF and the energy loss ΔE [4]. The experimental data was gathered by four FARCOS telescope [5], coupled with the CHIMERA 4π multidetector [6]. CHIMERA consists of 1192 two-stage Si-CsI(Tl) telescopes, covering about 94% of the whole solid angle. For CHIMERA, two different reaction targets were used, a $(CH_2)_n$ polyethylene 50 µm-thick target, and a ^{12}C 75 µm-thick one. Moreover, between ring 9 and CHIMERA sphere, four FARCOS telescopes have been placed at small angles, covering a polar angle between 1° and 9°. Each telescope is made of three stages: the first two are DSSSD, 300 and 1500 µm-thick respectively, made of a grid of 32 × 32 front-back strips, covering a total area of 6.4 × 6.4 mm^2; the third stage consists of four CsI(Tl) scintillators 6 cm-thick, readout by a photodiode. The excellent characteristics of high granularity, due to the presence of many front-back strips, and high angular and energetic resolution make the FARCOS detectors ideal for this kind of studies, in which high precision in Q-value and angular momentum calculations are required at small angles.

In the following sections the status of the calibration of the tagging system and of the different FARCOS stages will be described, as well as the identifications of the cocktail beam isotopes by means of a study on the $\Delta E - TOF$ tagging matrix.

Experimental details

Tagging system calibration

Calibration of the tagging system has been obtained by simulating the production of the radioactive cocktail beam, its energy loss on the DSSSD detector and its time of flight through the beam line. Simulations have been performed by means of the LISE++ software [7], allowing to simulate the configuration of the FRIBs fragment separator and the yield of fragmentation products through the spectrometer. Each of the 32 front vertical strips of the tagging system have been individually calibrated, by associating the energy loss ΔE and TOF of each isotope gathered from the simulated data. This allowed us to merge $\Delta E - TOF$ plot of each different strip, thus obtaining matrices as that shown in Fig. 1.

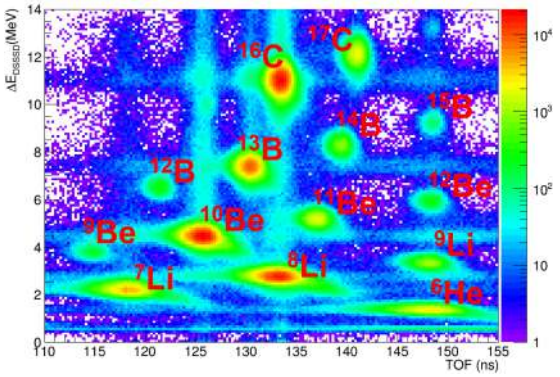

Figure 1: $\Delta E - TOF$ plot obtained from each of the 32 DSSSD strips, calibrated via simulation. All the isotopic species of the cocktail beam have been identified

The $\Delta E - TOF$ plot has also allowed us to perform a study on the horizontal distribution of each radioactive isotope of the cocktail beam. For this analysis, Fig. 2 shows the production yield of each ion in legend, for each of the 32 vertical strips on the horizontal axis: from this preliminary result it can be noted that the most produced fragments are ^{16}C, ^{10}Be and ^{8}Li.

FARCOS calibrations

The three stages of each FARCOS telescope have to be calibrated individually to carry out precise spectroscopy studies. Moreover, depending on the stage, different techniques have to be independently applied. The FARCOS calibration procedure began by calibrating especially the second 1500 µm stage, particularly important because more precise information about the emission angle of the fragments and a more accurate value of energy loss can be obtained. In this case, $\Delta E - E$ plots have been produced for each pixel of the 1500 µm DSSSD stage and the corresponding CsI(Tl) scintillator stages.

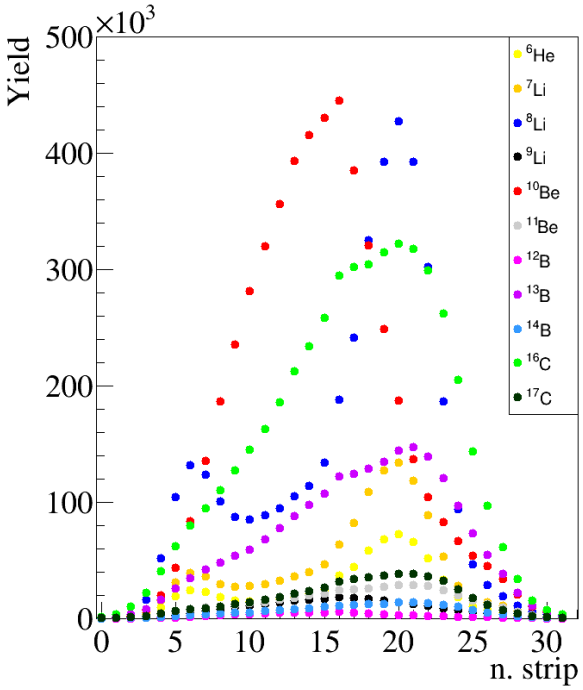

Figure 2: Total yield of each radioactive species of the cocktail beam, obtained for each vertical front strip of the DSSSD detector

Different techniques have also been used to improve the quality of the $\Delta E - E$ matrices, reducing background noise by selecting a TOF window coherent with the study done on the $\Delta E - TOF$ tagging system, and by discarding all interstrip events involving two adjacent strips. Different $\Delta E - E$ plots have been produced, as the one shown in Fig. 3, in which all ridges have been recognized by performing graphical cuts on the $\Delta E - TOF$ plot. Moreover, relevant distributions at the end of each ridge have been recognized as unreacted radioactive beam passing through CHIMERA's target.

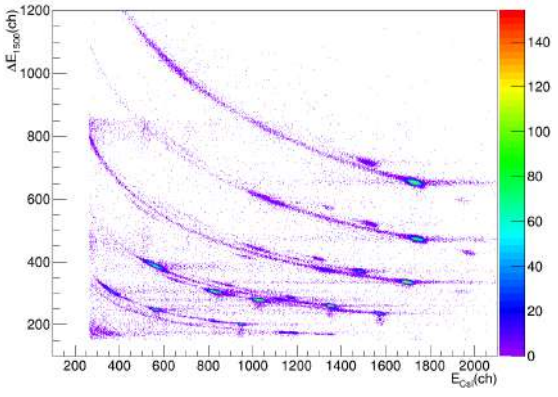

Figure 3: $\Delta E - E$ plot obtained from the data of a single pixel for the 1500 µm stage and the corresponding CsI scintillator

These distribution have been used in particular to perform precise calibrations on both the 1500 µm and CsI stages, by studying the energy loss of each unreacted beam through the different FARCOS stages, and associating each energy loss with corresponding position on the plot. Fig. 4 shows an example of a linear calibration for the energy loss ΔE in MeV for a single strip of the second stage, for which each strip has to be calibrated individually.

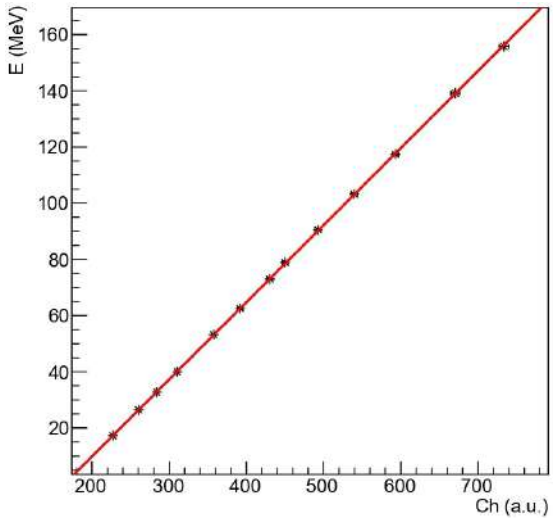

Figure 4: Linear calibration relative to a single strip of a 1500 µm stage of a FARCOS detector

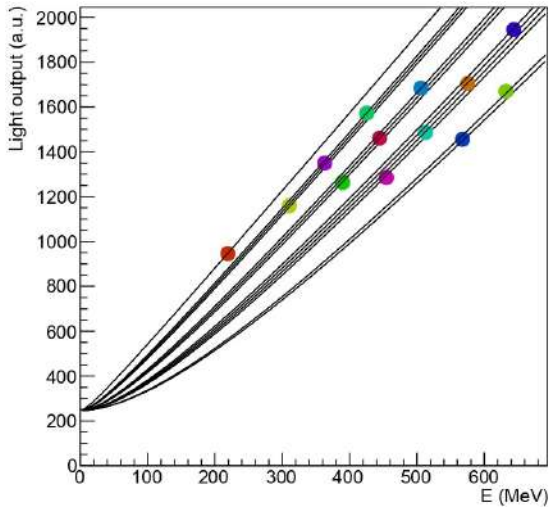

Figure 5: Preliminary calibration obtained for a CsI crystal of the third stage of a FARCOS detector, using the Horn formula as fit function

For the CsI(Tl) scintillator stage, preliminary calibrations have also been obtained. In this case, the Horn formula [8] was used, due to the non-linear behaviour of the light output of a CsI scintillator as the energy, charge and mass of the impinging ion vary, shown in Eq. 1:

$$L = a_0 + a_1 E - a_1 a_2 A Z^2 ln \left| \frac{E + a_2 A Z^2}{a_2 A Z^2} \right| \qquad (1)$$

However, due to the complexity of the fit and the lack of calibration data at low energies, mainly due to the lack of experimental data and calibration runs, further studies are required to perform a better calibration. Moreover, even without calibration runs, it has been possible to calibrate the majority of the strips of the 1500 µm stage, especially at small angles in which most of the data of physical interest are detected.

Calibration of the first 300 µm stage of the FARCOS detector will be possible by using the *punching through* technique. This could be done by associating the spots on a $\Delta E_1 - \Delta E_2$ plot, relative to the energy loss of the ions on the first and second stage, in which the curvature of the ion's ridge changes slope. This spot corresponds to the maximum energy for which the ion is unable to penetrate the second 1500 µm thick DSSSD stage, hence called *punching through*. Since the traces of the ridges of the many ions of the cocktail beam are overlapped, as it can be seen in Fig. 6, a selection on the $\Delta E - TOF$ tagging plot will be done selecting by means of graphical cuts the region relative to each isotope, thus making possible a more accurate localization of the punching through point.

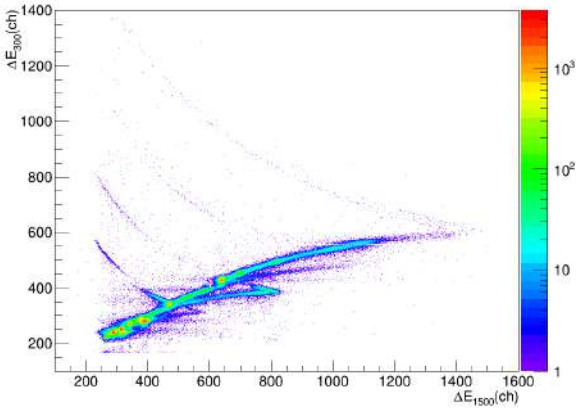

Figure 6: $\Delta E_1 - \Delta E_2$ plot, relative to the energy loss of the ions on the first and second stage. Punching through points can be seen at the inversion of each ridge, relative for each ion

The calibration of several strips of the 1500 µm thick stage has also allowed to obtain $\Delta E - E$ calibrated plots in which all the data of each calibrated strip for each CsI scintillator has been plotted (Fig. 7).

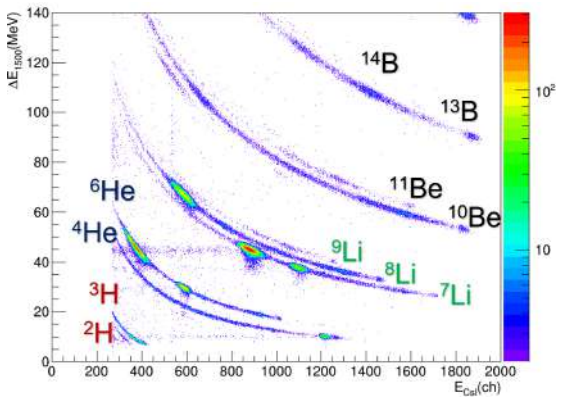

Figure 7: $\Delta E - E$ plot of the calibrated strips and its subsequent CsI scintillator

In this case, a good isotopic separation can be appreciated, in particular for light ions like lithium, helium or even hydrogen, for which several isotopes can be distinguished.

Preliminary work on ion selection

The good performances of the FRIBs tagging system previously described, coupled with the CHIMERA multidetector and FARCOS arrays, has also allowed to perform a preliminary work on the ion selection to observe break-up products expected for isotopic species of interest. This was done by performing graphical cuts on the $\Delta E - TOF$ tagging plot, by selecting a single isotope, and by plotting calibrated data of the 1500 µm stage and the correspondent CsI scintillator. Fig. 8 shows an example for the case of the selection of ^{10}Be, for which also the ^{6}He and ^{4}He ridges appear, evidencing the presence of such reaction products in emission from ^{10}Be clustering states.

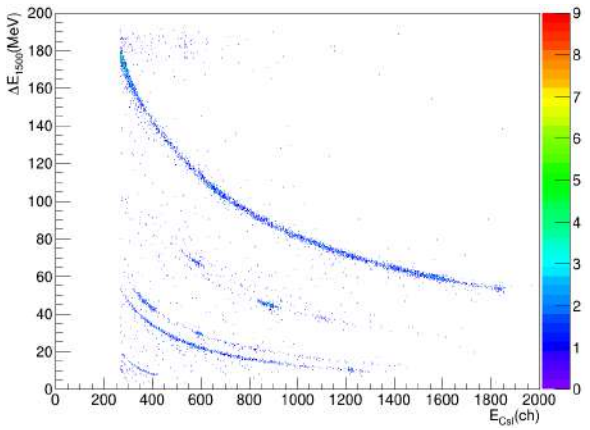

Figure 8: $\Delta E - E$ plot obtained by plotting the calibrated data for the second DSSSD stage, with a selection the ^{10}Be region on the tagging $\Delta E - TOF$ matrix

Conclusions

In this paper, the research work done during the first year of PhD study in Physics has been shown. The CLIR experiment has been described starting from the experimental details, involving production and use of a radioactive ion beam with the FRIBs facility at LNS. Calibrations of the tagging system have been performed by means of LISE++ simulations, allowing both the calibration in energy and TOF for each of the 32 front DSSSD strips. This study also allowed us to gather informations on the horizontal distribution of all the ions of the cocktail beam, containing in particular high yields of ^{16}C, ^{10}Be and ^{8}Li, interesting from the research point of view. Calibrations of the FARCOS detectors have also been studied, starting from the second 1500 µm thick DSSSD stage, performing linear calibrations for the majority of the available strips, by studying the unreacted cocktail beam energy loss passing through CHIMERA's reaction target and the various FARCOS stages. A preliminary study on the CsI stage calibration has also been shown, in which a non-linear fit was performed with the Horn light-output formula. This also allowed us to evidence a good ions identification of the isotopes of the cocktail beam, showing also evidence of interesting reaction products expected in emission from break-up reactions.

References

[1] Ikeda, K. et al.: *The Systematic Structure-Change into the Molecule-like Structures in the Self-Conjugate 4n Nuclei.* Prog. Theor. Phys. Suppl. E68, 464 (1968).

[2] Russotto, P. et al.: *Status and Perspectives of the INFN-LNS In-Flight Fragment Separator.* Jour. of Phys.: Conf. Series, 1014 (2018), 012016 and ref. therein.

[3] Dell'Aquila, D. et al.: *New experimental investigation of the structure of ^{10}Be and ^{16}C by means of intermediate-energy sequential breakup.* Phys. Rev. C, Vol. 93, p. 024611, 2016.

[4] Lombardo, I. et al.: *Use of Large Surface MicroChannel Plates for the Tagging of Intermediate Energy Exotic Beams.* Nucl. Phys. B, Vol. 215, 272 (2011).

[5] Pagano, E.V. et al.: *Status and perspective of FARCOS: A new correlator array for nuclear reaction studies.* EPJ Web of Conferences, vol. 117, p. 10008, 2016.

[6] Pagano, A. et al.: *Fragmentation studies with the CHIMERA detector at LNS in Catania: recent progress.* Nucl. Phys. A734, (2004) 504.

[7] LISE++ website: *http://lise.nscl.msu.edu/lise.html.*

[8] Horn, D. et al.: *The mass dependence of CsI(TI) scintillation response to heavy ions.* Nucl. Inst. Meth. A320, (1992) 273.

WRF-Chem model applied to Etna volcanic ash transport and fallout

A. Semprebello[1,*], M. T. Caccamo[1], G. Castorina[1,2], S. Magazù[1]

[1] *Department of Mathematical and Informatics Sciences, Physical Sciences and Earth Sciences of Messina University, Viale Ferdinando Stagno D'Alcontres 31, 98166 Messina, Italy*

[2] *Istituto Nazionale di Geofisica e Vulcanologia - Sezione di Palermo, Via Ugo La Malfa 153, 90146 Palermo, Italy*

[*] Corresponding Author email: semprebelloa@unime.it

Abstract

This contribution summarizes the main results related to the research activity carried out during the year 2021, focused on the themes of atmospheric physics. The main purpose of the research was to use the WRF-Chem model for the estimation of the transport into the atmosphere and of the fallout on the ground of volcanic ash following paroxysmal events recorded in the Sicilian volcanic areas, with particular reference to Etna volcano, in order to test its performance and implement specific optimizations. Furthermore, a study was carried out on the effects of the variation of the eruptive source parameters on volcanic plume transport, which highlighted the need for a joint approach between an online chemical transport model, such as WRF-Chem, and a measurement system placed near the eruptive source. Finally, two of the cases studied are reported as an example.

Keywords: WRF-Chem, numerical weather prediction, volcanic eruption, ash fallout.

Introduction

The research activity presented is based on use and optimization of the physical-mathematical model *Weather Research and Forecasting - Chemistry* (**WRF-Chem**).
WRF-Chem is a physical-mathematical environmental model developed on the basis of the *Weather Research and Forecasting* (WRF) *Limited Area Model* (LAM), an open-source meteorological model, that operates in the field of *Numerical Weather Prediction* (NWP), designed both for research applications in the field of atmospheric sciences and for operational meteorological forecasts[1, 2].
WRF-Chem module integrates the WRF options allowing to evaluate even chemical processes, such as the emission, transport, transformation, dispersion and sedimentation of any type of pollutant in the atmosphere, both of natural origin and anthropic. However, WRF-Chem model can be used only for the simulation of meteorological parameters[3].
WRF-Chem is defined as an "online" type model; this type of models allow the coupled evaluation of meteorological conditions and various chemical processes, associated with the presence of chemical species in the atmosphere, allowing, at the same time, to consider the effects on meteorological phenomena directly or indirectly caused by the compounds chemicals present. In particular, some of the main effects recorded on meteorological conditions are related to the microphysics of clouds, with particular reference to the processes of nucleation and formation of hydrometeors[4].
In addition, it should be emphasized that meteorological phenomena are the main factors for air quality. In this framework, models based on the "online" approach are preferable to those of the "offline" type, in which the description of the chemical and physical transport processes takes place separately, leaving out the reciprocal interactions.
The main disadvantage related to the use of online modeling systems, which limits their diffusion within the forecasting operational centers, is represented by the greater computation time and greater computational resources required compared to offline systems.[5].
In the specific case studies presented in the following sections, WRF-Chem model was used to estimate the transport and deposition on the ground of volcanic ash emitted following paroxysmal events of the Etna volcano.
With specific reference to the sector of application considered, WRF-Chem online model offers the possibility of evaluating the dispersion phenomena of volcanic ash more efficiently than most it Volcanic Ash Transport and Dispersion (VATD) models that operate offline mode[6].

WRF-Chem model

As mentioned in the introductory section, WRF-Chem weather-environmental model is developed on the basis of WRF model. Therefore, the calculation of the meteorological parameters is carried out with the same procedure and with the same calculation routines present in the relative meteorological model; the package archi-

tecture is always developed on the *WRF Software Framework* (WSF) central core which includes pre-implemented parameterization and assimilation schemes[7].
Also as regards the pre-processing section, WRF Preprocessing System (WPS) is used which consists of the sequential execution of three calculation routine: `geogrid.exe`, `ungrib.exe` and `metgrid.exe`, to define the spatial domain of the model and interpolate it with the meteorological data.
The dynamic cores available are **ARW**, *Advanced Research WRF*, which operates on different spatial resolution scales in non-hydrostatic mode, and **NMM**, *Non-hydrostatic Mesoscale Model*, which allows to operate both in hydrostatic and non-hydrostatic mode. To conduct the research presented, the choice fell on the first one, more expensive from the point of view of computing resources but more performing for research activities.
The chemical pre-processing phase include a further package called PREP-CHEM-SRC is used; it is a software written in a hybrid programming language between FORTRAN90 and C. The software also offers the possibility of reading and using databases, such as Global Emissions, for emissions of anthropogenic pollutants.[8].
The ESP to be provided are typically: volcanic plume height, eruption time, geographic coordinates of the volcano, mass eruption rate, ash granulometry. In particular, WRF-Chem package provides that the particles classified as ash (diameter $d \leq 2mm$) are arranged on a 10-bin histogram, which correspond to a certain range of diameters; the first bin is used for particles whose $1\ mm \leq d \leq 2\ mm$, while the last one for ashes with $d < 3.9\mu m$; central bins are reserved for all to the intermediate values. Conventionally, granulometry is expressed with the percentage of mass fraction of the particles that fall into the various bins; WRF-Chem model associates to each bin a variable called `vash_n`, with $1 \leq n \leq 10$.
PREP-CHEM-SRC, starting from input data provided by the user, called *Eruption Source Parameters (ESP)*, generates binary files that include parameters of the eruption and coordinates of the volcano in the numerical domain[9].
However, it is necessary to convert the generated files into NetCDF format so that they can be processed by WRF-Chem; for decoding and subsequent writing in NetCDF format is used `convert_emiss.exe` routine, included in the Chem package[10].
After the pre-processing phase, it is advisable to run the real.exe routine with the chemical options disabled, in order to verify the correct functioning of the chain for the meteorological aspect. After this step it is possible to execute real.exe and wrf.exe routines with the chemical options enabled, completing the simulation.
At the end of the simulation it is possible to proceed with data analysis and graphic post-processing.

Equations of the model

WRF-Chem model, also under the aspect of the equations used for the calculation of meteorological parameters, operates by numerically integrating Navier-Stokes equations, discretized on a grid, in their Eulerian approximation, neglecting viscosity but taking into account compressibility and non-hydrostatic conditions, similarly to what happens for WRF-ARW. In this framework reference, fundamental equations of the model are:

$$\partial_t U + (\boldsymbol{\nabla} \cdot V u) + \mu_d \alpha \partial_x p + \left(\frac{\alpha}{\alpha_d}\right)\partial_\eta p \partial_x \phi = F_U \quad (1)$$

$$\partial_t V + (\boldsymbol{\nabla} \cdot V v) + \mu_d \alpha \partial_y p + \left(\frac{\alpha}{\alpha_d}\right)\partial_\eta p \partial_y \phi = F_V \quad (2)$$

$$\partial_t W + (\boldsymbol{\nabla} \cdot V w) - g\left[\left(\frac{\alpha}{\alpha_d}\right)\partial_\eta p - \mu_d\right] = F_W \quad (3)$$

$$\partial_t \Theta + (\boldsymbol{\nabla} \cdot V\theta) = F_\Theta \quad (4)$$

$$\partial_t \mu_d + (\boldsymbol{\nabla} \cdot V) = 0 \quad (5)$$

$$\partial_t \phi + \mu_d^{-1}[(V \cdot \boldsymbol{\nabla}\phi) - gW] = 0 \quad (6)$$

$$\partial_t Q_m + (\boldsymbol{\nabla} \cdot \boldsymbol{V} q_m) = F_{Qm} \quad (7)$$

Where the different components indicated with F that appear in the equations (1), (2), (3) and (4) are the forcing terms due to the physics of the model, *mixing* turbulent, factors of spherical projections and effects of the rotation of the earth globe; α_d is inverse of dry air density ρ_d ($\alpha_d = 1/\rho_d$); $\phi = gz$ is the geopotential, $\partial_\eta \phi = -\alpha\mu$ the diagnostic relation for the density of the equation of state in the form $p = p_0(\frac{R_d\theta}{p_0\alpha})^\gamma$, where R_d refers to the constant of gas for *dry air*.
The term indicated in the equation (7) takes into account the *mixing* between the various water phases. In which:

$$Q_m = \mu_d q_m \quad (8)$$

In this q_m is *mixing ratio* of the different hydrometeors:

$$q_m = q_v, q_c, q_i, q_r, q_s \quad (9)$$

Flux-form variables considered in the derivation of the equations are as follows:

$$\boldsymbol{V} = \mu_d \boldsymbol{v} = (U, V, W); \qquad \Omega = \mu_d \dot{\eta}; \qquad \Theta = \mu_d \theta$$

In which $\boldsymbol{v} = (u, v, w)$ is the covariant velocity in the horizontal and vertical directions, $\dot{\eta}$ is the contravariant vertical velocity such that $\omega = \dot{\eta}$ and θ is the potential temperature.
It should also be noted that it is appropriate to consider unknown the vertical speed and to use, along the vertical axis, the *terrain-following* coordinates[11]:

$$\eta = \frac{p_{dh} - p_{dht}}{\mu_d}; \qquad \mu_d = p_{dhs} - p_{dht}$$

p_{dh} is the components of hydrostatic pressure, (p_{hs} is surface pressure associated with the value $\eta = 1$) and (p_{ht} is pressure on the fictitious layer that limits the atmosphere above, associated with $\eta = 0$). The subscript d indicates that the respective term refers to dry air.
The estimate of the transport into the atmosphere and the fallout of the volcanic ash particles on the ground is calculated with a semi-empirical method, starting from the sedimentation velocity v_s, calculated in a simple way, as a module of the drift velocity $\boldsymbol{v}_d$, defined as[6]:

$$\boldsymbol{v}_d = \frac{D}{kT}\boldsymbol{F}_{ext} \quad (10)$$

Where D is the diffusion coefficient, obtained from the Stokes relation corrected by the Cunnigham slip factor:

$$D = \frac{kT(1 + \alpha N_{Kn})}{6\pi\eta_\alpha r} \tag{11}$$

with k Boltzmann constant, η_α air viscosity and T temperature. The quantity in parentheses is called Cunningham slip factor and depends on the Knudsen number N_{Kn} and from numerical value α, defined as:

$$N_{Kn} = \frac{kT}{\sqrt{2}\pi r^2 PL} \quad ; \quad \alpha = A + Be^{-C/NKn} \tag{12}$$

In the second relation A, B and C are constant, whose values are determined empirically: $A = 1,257$, $B = 0,400$ e $C = 1,100$.
The term $\boldsymbol{F}_{ext}$ represents the gravitational force acting on the mass particle ρ:

$$\boldsymbol{F}_{ext} = \frac{4\pi}{3} {r_h}^3 (\rho - \rho_\alpha)\boldsymbol{g} \tag{13}$$

where ρ_α is the air density and r_h the aerodynamic radius for the various classes of *vash*. The latter is:

$$r_h = \frac{1}{2}\left(\frac{d_{sup} + d_{inf}}{2}\right) \tag{14}$$

in which d_{sup} and d_{inf} are respectively the maximum and minimum diameters allowed by the bin. Putting the previous relationships together, the sedimentation rate can be calculated v_s:

$$v_s \equiv |\boldsymbol{v}_d| = \frac{2(1 + \alpha N_{Kn})r^2(\rho - \rho_\alpha g)}{9\eta_\alpha} \tag{15}$$

However, it should be noted that the present method provides a good estimate only for the smallest diameter particles, in particular up to the particle size range indicated as *vash_5*. For particles with a larger diameter, the sedimentation velocity is overestimated; further studies are underway to improve this aspect.

Results and discussion

In light of the intense eruptive activity of Etna volcano recorded during the first quarter of the year 2021, a series of simulations were carried out using WRF-Chem model. The simulations were carried out using two nested spatial domains: *parent domain* with 9 km resolution of the horizontal spatial grid; nested domain with 3 km horizontal resolution, in order to obtain greater precision in the areas closest to the volcano.
For the granulometry of the ashes the values foreseen by the Mastin classification were used, considering Etna volcano belonging to the M1 category[10], however, research activities are underway aimed at initializing WRF-Chem using experimentally measured particle sizes.
The meteorological input data used were those of the GFS global model; moreover, the meteorological part of the chain, in relation to Sicilian complex orography, was configured with specific optimizations studied at Messina University.
Two of the most significant results obtained with the application of WRF-Chem environmental models on Etna volcano will be shown below.

Case Study of February 16th, 2021

On February 16th, 2021, a violent paroxysmal event occurred in the volcanic area of Etna, characterized by a volcanic plume higher than 10 km.
This eruptive event, associated with the presence of winds from the north-western quadrants, caused the spread of large quantities of ash south of the volcano, forcing the suspension of the activities of the Catania-Fontanarossa International Airport.
In this reference framework, a simulation was carried out with WRF-Chem model in order to estimate the transport and the fallout on the ground of the erupted ashes.

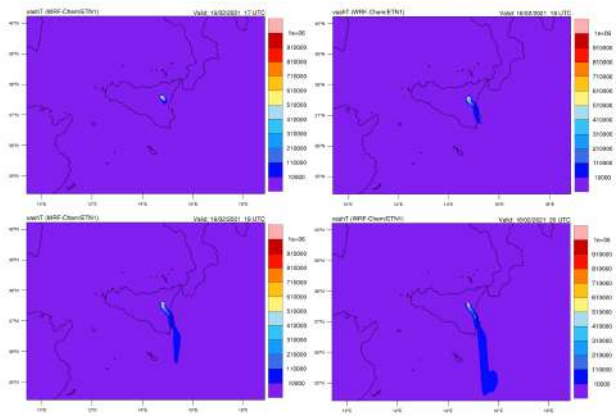

Figure 1: Estimation of the transport of volcanic ash carried out using WRF-Chem model, with 3 km horizontal spatial resolution.

In order to evaluate the performance of the aforementioned modeling chain, we proceeded with a qualitative visual comparison (using the method called "Eyeball") between the simulated data with 3 km nesting, of the transport of the *vash_5* component of the volcanic ash (ashes with size between 62.5 and 125 μm - 34% of total mass eruption rate) emitted into the atmosphere after the paroxysmal event considered, with the observations from the Hotvolc network, a reporting system based on satellite data dedicated to the real-time observation of volcanic products, developed and managed by the *Observatoire de Physique du Globe de Clermont-Ferrand* (OPGC). These comparisons show good agreement between expected and observed data (Fig. 2).

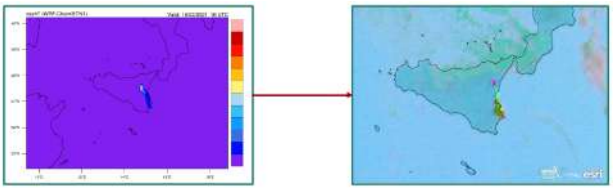

Figure 2: Comparison between transport of volcanic ash carried out using WRF-Chem model, with 3 km horizontal spatial resolution (left) and observations processed by the Hotvolc satellite system (right).

Case study: Etna paroxysm of November 23rd, 2013

In relation to the violent eruption of Etna volcano November rd 2013, characterized by a north-east transport of ash and gas, caused by a low pressure system in northern Italy, a study was conducted in collaboration with other national and international research institutes and led to the publication of a paper.
The activity was conducted using an innovative approach, characterized by the initialization of WRF-Chem model with real data measured by the VOLDORAD-2B (V2B) Doppler radar system, located near Etna; this configuration did not require PREP-CHEM-SRC preprocessor.
This made it possible to include the transient and fluctuating nature of volcanic emissions, thus optimizing the eruption source parameters (ESP); the technique used has brought substantial improvements in the modeling accuracy the atmospheric dispersion of ash and gas.
Comparisons were made between the graphic products relating to the classic configuration of WRF-Chem model and between those deriving from the simulation initialized with satellite data; subsequently both were compared with the calculations of the Aerosol Index estimated by the Suomi NPP OMPS satellite. Visual comparisons, as shown in Fig. 3, show that the new configuration provides much more precise estimates of the transport of volcanic ash into the atmosphere[12].

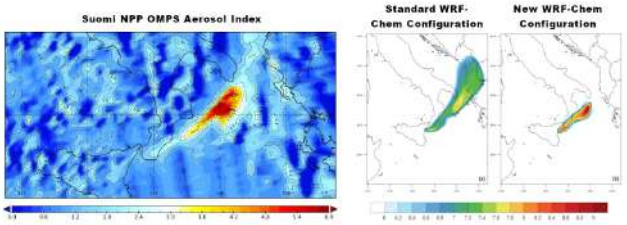

Figure 3: Comparison between Suomi NPP OMPS Aerosol Index (a), standard WRF-Chem configuration (b) and new WRF-Chem configuration (c).

Conclusions

Based on the various results obtained through the use of WRF-Chem model applied to the transport of volcanic ash in the atmosphere following eruptions, with specific reference to Etna volcano, it can be concluded that the modeling chain provides results in good agreement with the observed data, proposing itself as an excellent tool of ex ante forecasting for the development of advanced decision-making supports aimed at identifying specific risk scenarios (eg air traffic, airport security, urban mobility, health), as well as finding numerous applications in the purely scientific field.
Furthermore, the results obtained with the recently developed configuration, still under study today, indicate that an integrated approach between an environmental model and an experimental measurement system, located near the volcano, allows for further improvement of the accuracy of the results obtained.

References

[1] Powers, J. G. et al: *The Weather Research and Forecasting Model: Overview, System Efforts, and Future Directions*. Bulletin of the American Meteorological Society. **98**(8), 1717-1737 (2017).

[2] Castorina, G. et al: *Multiscale mathematical and physical model for the study of nucleation processes in meteorology*. AAPP. **96**(S3), A6-1-A6-12 (2018).

[3] Grell, G. et al: *Fully coupled online chemistry within the wrf model*. Atmospheric Environment. **39**(37), 6957-6975 (2005).

[4] McDonald, J. E.: *The physics of rainclouds*. cambridge university press, new york, 1962. 386 pp. illus. 11.50. Science, **143**(3603):236–236, (1964).

[5] Grell, G., Baklanov, A.: *Integrated modeling for forecasting weather and air quality: A call for fully coupled approaches*. Atmospheric Environment. **35**(38), 6845-6851 (2011).

[6] Rizza, U. et al: *Analysis of the ETNA 2015 Eruption Using WRF–Chem Model and Satellite Observations*. Atmosphere. **11**(11), 1168 (2020).

[7] Skamarock, W. C. et al: *A Description of theAdvanced ResearchWRF Model Version 4*. Mesoscale and Microscale Meteorology Laboratory NCAR, Colorado, USA, 2019.

[8] Freitas, S. R. et al.: *Prep-chem-src 1.0: a pre-processor of trace gas and aerosol emission fields for regional and global atmospheric chemistry models.*. Geoscientific Model Development. **4**(2):419–433, (2011).

[9] Mastin, L. G. et al: *A multidisciplinary effort to assign realistic source parameters to models of volcanic ash-cloud transport and dispersion during eruptions*. Journal of Volcanology and Geothermal Research. **186**(1), 10-21 (2009).

[10] Stuefer, M. et al: *Inclusion of ash and* SO_2 *emissions from volcanic eruptions in WRF-Chem: development and some applications*. Geoscientific Model Development. **6**(2), 457-468 (2013).

[11] Laprise, R.: *The Euler Equations of Motion with Hydrostatic Pressure as an Independent Variable*. Monthly Weather Review, American Meteorological Society. **120**(1), 197-207 (1992).

[12] Rizza, U. et al: *Effects of Variable Eruption Source Parameters on Volcanic Plume Transport: Example of the 23 November 2013 Paroxysm of Etna*. Remote sensing. **13** 4037, 2021.

An accurate approach to measure dioptric power of intraocular lenses

M. Vacalebre[1,*],R. Frison[2], E. Anastasi[3], E. Fazio[1], M. C. Curatolo[3]
[1] *Department of Mathematical and Computational Sciences, Physics Sciences and Earth Sciences (MIFT), University of Messina, Messina, Italy*
[2] *Optical Consultant SIFI SpA, Catania, Italy*
[3] *Business and Portfolio Development Department, SIFI SpA, Catania, Italy*

*Corresponding Author email: mvacalebre@unime.it

Abstract

This contribution proposes a method to test intraocular lenses (IOLs) by measuring their dioptric powers. This approach is in accordance with international standard ISO 11979-2:2014 and aims to prevent mislabelling of IOL powers. Inaccurate measurements could lead to poor patients' satisfaction and, in the worst cases, to failed cataract surgeries. As a matter of fact, the temperature and the medium where the IOL is inserted affect the dioptric power. Errors due to measurement conditions and to spherical aberrations are taken into account and proper power corrections are suggested. A test bench was used to measure dioptric powers of three hydrophilic IOLs and the obtained results were used to validate the theoretical calculations.

Keywords: Intraocular lenses, IOL, dioptric power, ISO 11979, effective focal length, test bench, power corrections.

Introduction

Cataract entails the progressive opacification of the natural eye lens and is one of the main causes of either vision impairment or blindness worldwide [1]. Intraocular lenses (IOLs) are medical devices conceived to replace crystalline lens in patients who undergone cataract surgery. Generally, IOLs are implanted with the aim to restore distance vision [2]. Thus, patients are still dependent on spectacles for daily activities that engage near vision. Starting in the 1980s, the development of new categories of lenses, known as multifocal IOLs, provided the possibility to restore a good quality of vision for both far and near distance [2]. However, regardless of its optic design, intraocular lenses on the market must meet the optical requirements described in the international standard ISO 11979-2:2014 [4]. In this standard, reference methods are provided to assess the dioptric power, the image quality and the spectral transmittance [4]. In this report, we propose an accurate approach to evaluate the dioptric power of an intraocular lens by using the appropriate power corrections. As a matter of fact, the results obtained for the same IOL may vary by using different instruments [5]. Thus, a scrupulous assessment of its dioptric power plays a key-role in providing the best outcome after implantation.

Figure 1: Intraocular lens.

Method

The dioptric power (D) is the ability of a lens to focus the light rays on an image plane [2]. It is defined as the reciprocal of the paraxial focal length f of the lens multiplied by the refractive index of the medium (n_{med}) that surrounds the IOL (Eq.1) [6].The value of the dioptric power is provided *in situ* condition, by considering aqueous humour at 35,0° ± 2,0° as surrounding medium [4].

$$D = \frac{n_{med}}{f} \tag{1}$$

In this report, three hydrophilic refractive IOLs with a nominal power of +10 D, + 20 D and +30 D respectively were tested. OptiSpheric®IOL PRO 2 (Trioptics GmbH, Germany) was used to assess their effective focal length (EFL). A light source with a wavelength equal to 546 nm was used and the aperture diameter was set at 3 mm. The measurements were carried out at room temperature (approximately 20°) in saline solution. As shown in Fig.2, in the presence of spherical aberration, light rays coming from paraxial region and from marginal zone focus on different points on the optical axis. These focal points are referred as 'edge focal point' and 'paraxial focal point' and the distance between them is known as 'longitudinal spherical aberration' (LSA) [5].The 'best focus point' is located between the two aforementioned points and its position is determined by where the instrument finds the image plane with the highest resolution[7]. Thus, the measurement of EFL, and consequentially the measured dioptric power, is not centered on the paraxial focus but on the plane with the best image quality[7]. In order to obtain the paraxial focal point from the measured EFL, a correction must be applied, as shown in Eq.2

$$f = EFL + Defocus \tag{2}$$

where the power correction is expressed in terms of *Defocus* (Eq. 3).

$$Defocus = -\frac{LSA}{2} \tag{3}$$

In this study, LSA was calculated by using Zemax OpticStudio software (Zemax, LLC, Kirkland, WA). An IOL model was inserted in Arizona model eye and an aperture stop equal to 3 mm was taken into account [8]. The simulations were carried out for three different IOLs in order to evaluate the behaviour of the IOLs with different ranges of dioptric power.

Following the correction due to the aberrations, it is important to consider the applied conditions for the measurements. A correction factor Q is necessary to convert the results from the applied conditions to *in situ* conditions (Eq. 4).

$$Q = \frac{D_{insitu,nom}}{D_{roomT,nom}} \tag{4}$$

The terms expressed in Eq. 4 are obtained from refractive indices of both IOL and medium and from geometrical parameters of the IOL under evaluation, such as the lens thickness (d) and the radii of the front and back surfaces ($radius_{front}$ and $radius_{back}$) [4]. Equations 5 was used to calculate both terms of Eq. 4. In this case, the saline solution at 20° has a refractive index equal to 1,336. As stated in the ISO standard 11979, the refractive index of the aqueous humor at 35° is 1,336 [4]. By considering a wavelength equal to 546 nm, the refractive index of the IOL ranges from 1,460 to 1,464 on the basis of the material batch. In this case, n_{IOL} is 1,4627 at 20° and 1,4618 at 35°.

$$D_{nom} = D_{front} + D_{back} - \left(\frac{d}{n_{IOL}}\right) D_{front} D_{back} \tag{5}$$

D_{front} and D_{back} are expressed in Eq. 6 and Eq. 7 respecitvely.

$$D_{front} = \frac{n_{IOL} - n_{med}}{radius_{front}} \tag{6}$$

$$D_{back} = \frac{n_{med} - n_{IOL}}{radius_{back}} \tag{7}$$

Eq. 8 was used to obtain the dioptric powers of the IOLs *in situ* conditions [4].

$$D_{insitu,measured} = D_{roomT,measured} * Q \tag{8}$$

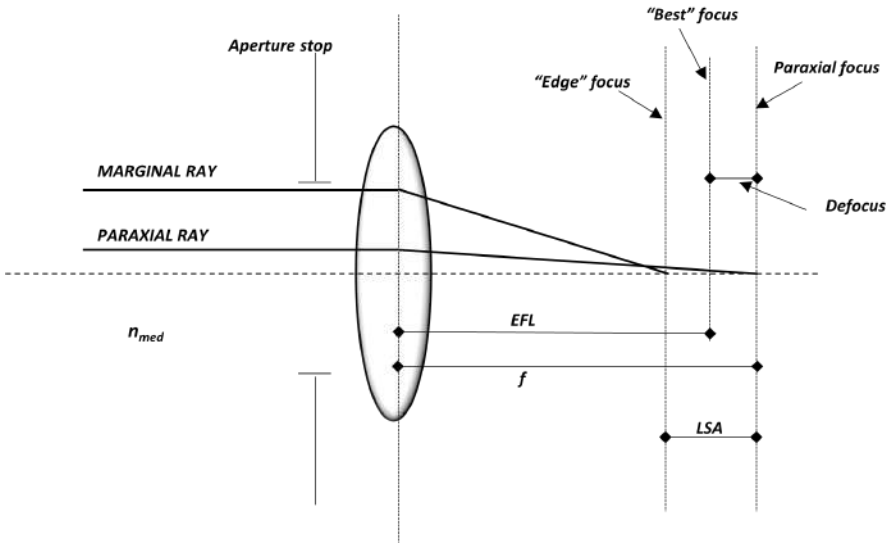

Figure 2: Schematic diagram of the intraocular lens under evaluation.

Results and Validation

Firstly, the correction factor due to the conditions of measurement was calculated. In Table 1, the theoretical calculations obtained from Eq. 4 are summerized for the three IOLs. Independently from their nominal dioptric power, the correction factor Q is about 0,9929.

Nominal Dioptric Power [D]	$D_{roomT,nom}$ [D]	$D_{insitu,nom}$ [D]	Q
IOL 10 D	10.01747	9.46157195	0.99288
IOL 20 D	20.02988	19.88757	0.99289
IOL 30 D	30.22788	30.01381	0.99292

Table 1: Calculations for the correction factor Q

Successively, the error due to spherical aberrations was evaluated on a model eye by using Zemax softare. The theoretical values of LSA and Defocus are reported in Table 2.

Nominal Dioptric Power [D]	LSA [mm]	Defocus [mm]
IOL 10 D	0.8	-0.4
IOL 20 D	0.68	-0.34
IOL 30 D	0.46	-0.23

Table 2: Values of longitudinal spherical aberration (LSA) for the three IOLs.

Lastly, the measurements of effective focal length were carried out by using a bench test. The measured EFLs and the obtained dioptric powers are reported in Table 4. Paraxial focal length was obtained by applying Eq. 2 to the measured EFL. Successively, the reciprocal of paraxial focal length was calculated to obtain the dioptric power at room temperature ($D_{roomT,measured}$). Finally, the correction factor reported in Table 1 was applied in Eq. 8 to obtain the dioptric power *in situ* ($D_{insitu,measured}$).
The values of dioptric power *in situ* reported in the last column in Table 4 are in accorandance with the tolerance limits set by the international standard ISO 11979:2 [4]. Thus, the theoretical values of LSA are validated. The standard reference is reported in Table 3.

Nominal Dioptric Power [D]	Minimum [D]	Maximum [D]
IOL 10 D	9.7	10.3
IOL 20 D	19.6	20.4
IOL 30 D	29.5	30.5

Table 3: Tolerance limits for measurements of dioptric powers set in the international standard ISO 11979-2 [4].

Nominal Dioptric Power [D]	Defocus [mm]	Measured EFL [mm]	Paraxial focal length [mm]	$D_{roomT,measured}$ [D]	$D_{insitu,measured}$ [D]
IOL 10 D	-0.4	97.495	97.095	10.299	10.226
IOL 20 D	-0.34	49.894	49.494	20.204	20.061
IOL 30 D	-0.23	32.864	32.634	30.643	30.425

Table 4: Measurements of effective focal length for the three IOLs and followig calculations to obtain the corrisponding dioptric powers *in situ* conditions.

Conclusion

In this report, an approach to accurately measure dioptric power and to assess the necessary power corrections was established, in accordance with the international standard ISO 11979. The errors due to measurement conditions and spherical aberrations were addressed. The corrections applied to the measured effective focal length to obtain the paraxial focal length was equal to -0.4 mm, -0.34 mm and -0.23 mm for IOLs with a nominal dioptric power equal to +10 D, 20 D D and + 30 D respectively. A correction factor equal to 0.9929 was obtained to convert the measurements from room temperature to *in situ* conditions, regardless of the nominal dioptric power. Further efforts are necessary to cover the complete range of nominal dioptric powers. Furthermore, increasingly complex optical designs of intraocular lenses will require the most accurate strategies to test their optical properties.

References

[1] Hashemi, H. et al.: *Global and regional prevalence of age-related cataract: a comprehensive systematic review and meta-analysis.*, Eye (Lond), 34(8), 1357-1370 (2020).

[2] Cherrier M. et al.: *Characterization of intraocular lenses: a comparison of different measurement methods.*, In: Design and Quality for Biomedical Technologies III, SPIE, 167-178 (2010).

[3] Rabsilber, T. M.et al.: *Multifocality Over the Years.*, Cataract refract. surg. today, 54-65, (2011).

[4] International Organization of Standardization: *ISO:11979-2. Ophthalmic implants - Intraocular lenses. Part 2: Optical properties and test methods.*, 2014.

[5] Zhang, J. et al.: *A New Calibration Method for the Dioptric Power of Intraocular Lenses.*, In: 13th International Congress on Image and Signal Processing, BioMedical Engineering and Informatics (CISP-BMEI), 2020.

[6] Smith, W. J.: *Modern optical engineering.*, Tata McGraw-Hill Education, 2008.

[7] Neubert, W. J.: *Spherical aberration, intraocular lens power, and image quality.*, In: Ophthalmic Technologies III SPIE, 1877, 190-201 (1993).

[8] Schwiegerling, J. et al.: *Field guide to visual and ophthalmic optics.*, Spie, 2004.

Reports

Studenti di Dottorato di Ricerca

Ciclo XXXVII

Jefferson Lab Intense Muon bEam (J-LIμE) simulations

A. Fulci[1]
[1] *MIFT, University of Messina, Messina, Italy*

*Corresponding Author email: antoninofulci@gmail.com

Abstract

In this work is presented the study regarding the set up of an intense muon beam at the Jefferson Laboratory (JLab) that can be used to carry out a high-precision $\mu - p$ scattering experiment. The interaction of the JLab electron beam with the beam-dump in Hall-A was studied using the montecarlo software FLUKA. Also, a tagging system was proposed in order to identify each muon before the scattering event.

Keywords: muon beam, JLab, tagging system, montecarlo simulations, FLUKA.

Introduction

The proton is the major component of the visible matter of our universe, so being able to determine its fundamental properties, such as its charge radius, is of vital importance. In recent years, several experiments have been performed for the accurate measurement of the proton radius with different experimental techniques. The main and most common are based on two different techniques: $e - p$ scattering and Lamb shift spectroscopy of regular hydrogen atoms. The latter can also be performed on muonic hydrogen atoms with a significant improvement in accuracy. Recent measurements that use this method have highlighted a discrepancy between the results obtained through electron scattering and those obtained with the spectroscopic technique leading to the so-called "proton radius puzzle". The explanation of why this difference between the measured values exists is still a matter of discussion.

The last attempt to address the puzzle was the PRad Experiment [1]. It was performed with a unique experimental setup that gave the scientists an excellent control on the systematic errors that are usually present in electron-proton scattering experiments. This has significantly increased the precision of the measurement, bringing it in the same area as the spectroscopic ones done on muonic hydrogen atoms, which are considered the most precise. However, to solve the puzzle once and for all, even more precise electron scattering measurements are needed. Alternatively, new methods can be used, such as eg. muon-proton scattering at low transferred momenta in order to lower the systematic errors that comes with the measurement.

This work tries to address this problem by studying the set up of an intense muon beam at the Jefferson Laboratory (JLab) that can be used to carry out a high-precision $\mu - p$ scattering experiment. Using Montecarlo simulations the muon production resulting from the interaction of the primary electron beam with the beam-dump at JLab Hall-A was studied. The simulations were performed using the FLUKA package [2].

Also, a tagging system was proposed in order to identify each muon before the scattering event. The tagging system will allow to know with good precision ($O(1/1000)$) the energy of each muon of the beam. Based on the results obtained, an event generator that incorporates the detailed description of the muon beam (energy, position, emittance) was created. It was useful to define and optimize the experimental setup for a future measurement of the proton radius at the JLab.

The simulations

The simulations performed made use of the Hall-A beam dump geometry and materials implemented in FLUKA-2011.2c.5 by JLab Radiation Control Deparment and used in PR12-16-001 by the Beam-Dump eXperiment (BDX) [3, 4]. The BDX configuration was modified (Fig. 1) removing the iron shielding and adding some sampling surfaces in the concrete vault wall downstream of the beam-dump in order to sample muon, gamma, and neutron flux (Fig. 2).

Two simulations were made, the first one simulated an 11 GeV electron beam and the second one simulated a 6 GeV electron beam. Only a specific set of physics processes were activated in FLUKA and a tuned set of biasing weights were used to speed up the running time while preserving the accuracy of the results.

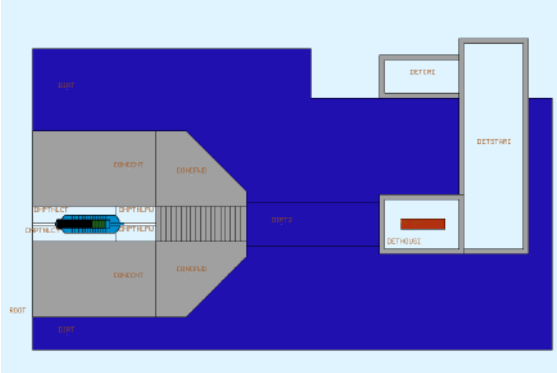

Figure 1: Beam dump configuration used for the simulation

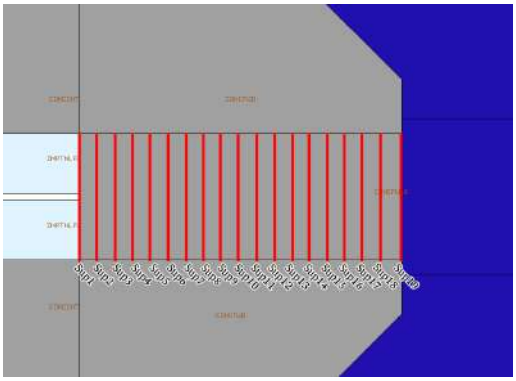

Figure 2: Surfaces used to sample muon, gamma and neutron flux

The sampling surfaces were evenly spaced, except for the last one, which was situated at the exit of the concrete surrounding the dump.

Results for an 11 GeV electron beam

Results presented here are based on a simulation of 10^8 electron on target (EOT) with a momentum $p_{e^-} = 11$ GeV. In Fig. 3 each point correspond to a different depth in the concrete wall downstream of the dump where the muon, gamma, neutron flux were sampled. Each flux were sampled with the following cut on the kinetic energy:

$$T_{\mu,n,\gamma} > 100 \text{ MeV} \quad (1)$$

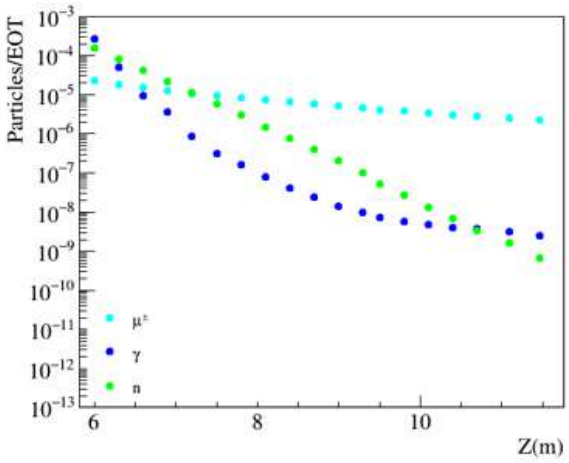

Figure 3: Particles fluxes per EOT at different depths in the concrete downstream of the dump for an 11GeV electron beam.

Relevant muon observables (space distribution, momentum distribution, ecc) were obtained for each sampling surface (see Fig. 2 for location). In addition, the spatial and momentum distributions were fitted with a standard ROOT gaussian[1] (plus a constant) function and a hyperbolic function (eq. 2 and eq. 3).

$$f(x) = p_0 \cdot e^{-\frac{1}{2}\left[\frac{(x-p_1)}{p_2}\right]^2} + p_3 \quad (2)$$

$$f(x) = p_0 \frac{1}{x} + p_1 \quad (3)$$

The resulting fit parameters for only the first and the last surface for the muons are reported in Tab. 1.

Results for a 6GeV electron beam

A second simulation of 10^8 was made using electrons of $p_{e^-} = 6$ GeV. Like in the previous section, in Fig. 4 each point correspond to a different depth in the concrete wall downstream of the dump where the muon, gamma, neutron flux were sampled. Each flux were sampled with the same showed in Eq. 1.

[1] https://root.cern.ch/root/htmldoc/guides/users-guide/FittingHistograms.html

Surface Index	Surface position	Energy cut (GeV)	No. of μ/EOT		σ_x (cm)	σ_y (cm)	σ_{p_x} (MeV)	σ_{p_y} (MeV)
			213,36x213,36 cm^2	20x20 cm^2				
N.Sup = 1	$z = 600$	$T_\mu > 0.1$	2.33×10^{-5}	2.36×10^{-6}	12.46 ± 0.04	12.55 ± 0.04	51.06 ± 0.2	53.96 ± 0.3
		$T_\mu > 1$	0.84×10^{-5}	1.96×10^{-6}	11.77 ± 0.02	11.91 ± 0.02	80.53 ± 0.1	80.64 ± 0.1
N.Sup = 19	$z = 1146.5$	$T_\mu > 0.1$	0.22×10^{-5}	0.27×10^{-6}	21.5 ± 0.04	21.69 ± 0.04	46.98 ± 0.3	46.72 ± 0.3
		$T_\mu > 1$	0.11×10^{-5}	0.19×10^{-6}	18.56 ± 0.03	18.71 ± 0.03	77.64 ± 0.1	77.56 ± 0.1

Table 1: Parameters of the muons' fitted histograms.

Surface Index	Surface position	Energy cut (GeV)	No. of μ/EOT		σ_x (cm)	σ_y (cm)	σ_{p_x} (cm)	σ_{p_y} (cm)
			213,36x213,36 cm^2	20x20 cm^2				
N.Sup = 1	$z = 600$	$T_\mu > 0.1$	7.09×10^{-6}	4.46×10^{-7}	22.29 ± 0.06	20.36 ± 0.06	$5.58 \times 10^{-2} \pm 0.01 \times 10^{-2}$	$5.93 \times 10^{-2} \pm 0.01 \times 10^{-2}$
		$T_\mu > 1$	1.77×10^{-6}	2.9×10^{-7}	18.09 ± 0.03	17.26 ± 0.03	$7.21 \times 10^{-2} \pm 0.01 \times 10^{-2}$	$7.19 \times 10^{-2} \pm 0.01 \times 10^{-2}$
N.Sup = 19	$z = 600$	$T_\mu > 0.1$	9.96×10^{-8}	7.78×10^{-9}	28.89 ± 0.1	29.22 ± 0.1	$4.33 \times 10^{-2} \pm 0.02 \times 10^{-2}$	$4.36 \times 10^{-2} \pm 0.02 \times 10^{-2}$
		$T_\mu > 1$	4.28×10^{-9}	4.74×10^{-10}	22.86 ± 0.4	21.69 ± 0.3	$6.24 \times 10^{-2} \pm 0.14 \times 10^{-2}$	$6.10 \times 10^{-2} \pm 0.14 \times 10^{-2}$

Table 2: Parameters of the muons' fitted histograms for a 6 GeV electron beam.

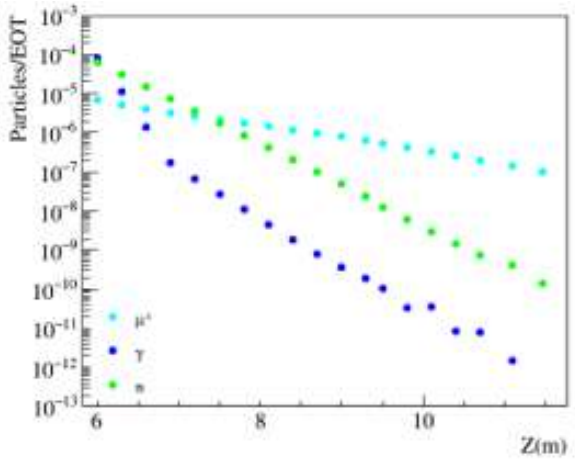

Figure 4: Particles fluxes per EOT at different depths in the concrete downstream of the dump for a 6 GeV electron beam.

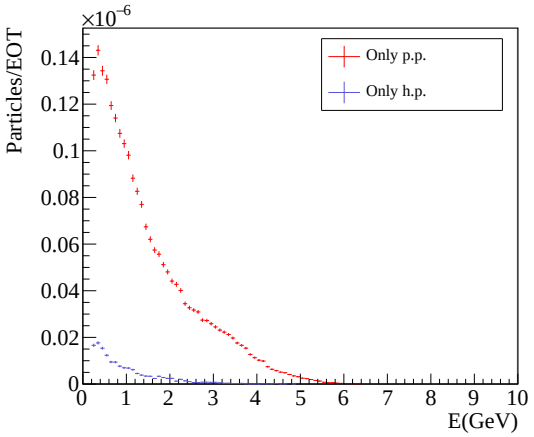

Figure 5: Muon energy distribution for only photoproduction processes (red cross) and only hadronic decays (blue cross).

Relevant muon observables (space distribution, momentum distribution, ...) were obtained for each sampling surface (see Fig. 2 for location). Even in this case spatial and momentum distribution were fitted with eq. 2 and eq. 3. The resulting fit parameters are reported in Tab. 2.

Beam characteristics

Two simulations were made in order to assess the efficiency of photoproduction process over the decay one. In the first simulation the FLUKA cards that control the decay of pions and kaons in muons were removed. Instead, in the second one, the cards that control the photoproduction process of $\mu^+\mu^-$ pairs were removed. Then, for both of the simulations, the flux was sampled on the last surface available, the one at the exit of the concrete downstream of the beam dump. The comparison of the two fluxes is shown in Fig. 5.

From this histogram it is possible to extract the number of muons per Electron On Target (EOT). When only the photoproduction processes are turned there are 2.26689×10^{-6} muons/EOT. On the other hand, when only the hadronic decay processes are turned on we have 1.49733×10^{-07} muons/EOT.

Muon beam tagging system

The proposed muon tagging system (Fig. 6) is based on the time-of-flight technique. It aims to measure the time it takes for a particle to travel from three detectors equally spaced from each other. The major problem to overcome in system like this is the very intense and concentrated muon beam. To overcome this issue, the three detectors designed, 40x40cm^2 each, consist of a myriad of sub-detectors, which for simplicity can be thought of as pixels on a screen. Each pixel will therefore be the

real detector that will score the time of passage of the particle through the surface. Having a detector made up of several pixels has two purposes. The first is to reduce the overall rate on the detector, as now the rate that a single detector undergoes will be equal to the inverse of the total number of pixels. The second one is to provide positional information of the particle (although with low precision), which can be used as an additional check to tag the muons.

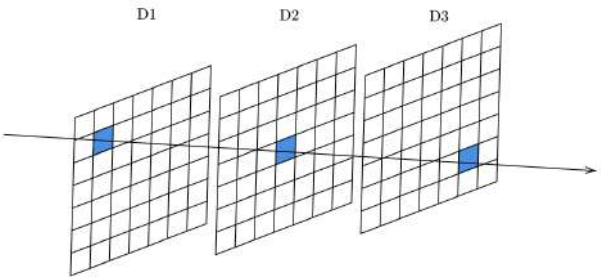

Figure 6: The proposed muon tagging system.

Simulation: the event generator

An event generator was coded in C++ in order to simulate the proposed muon tagging system. The event generator is able to produce muons with a spatial distributions almost identical to the real one. In addition, to each generated event is assigned a start time t_1 that follow a Poisson distribution (the probability function that describes event-counting rates). In this way, the event generator is able to reproduce a realistic beam with proper rates and characteristics.

Let's call with t_1^μ the arrival time of the muon at the first detector, with t_2^μ at the second one, and with t_3^μ at the third one. Then call with Δt_{21} the time the muon takes to travel from the first detector to the second one, Δt_{31} the time the muon takes to travel from the first detector to the third one and with Δt_{32} the time the muon takes to travel from the second detector to the third one.

The correct association of the particle was performed by making the following considerations:

- The time it takes the particle to travel the space between the first and second detectors must be less than the time it takes a photon to travel at the speed of light the same distance. The same applies to the travel time between the first and third detector.

$$\Delta t_{21_\mu} < \Delta t_{21_\gamma} \quad \text{or} \quad \Delta t_{31_\mu} < \Delta t_{31_\gamma}$$

- The time it takes the particle to travel the space between the first and second detectors must be greater than the time the slowest particle takes to travel from the first to the second detector. The same applies to the travel time between the first and third detector.

$$\Delta t_{21_\mu} > \Delta t_{21_{\mu^{\text{slowest}}}} \quad \text{or} \quad \Delta t_{31_\mu} > \Delta t_{31_{\mu^{\text{slowest}}}}$$

- The particle detected on the first detector may be on the second within a time frame of:

$$t_1^\mu - 1 < t_2^\mu < t_1^\mu + 15 + t_{\text{delay}}$$

where t_{delay} is a delay calculated as the difference between Δt_{21} for the fastest particle and the slowest.

This three conditions return a set of particles that can be associated with the signal received at the first detector. Assuming that the muons have straight trajectories from one detector to another (and this is especially true when there are no magnetic fields between the detectors) to properly associate them several checks are made in the following order:

1. the difference $\Delta t_{31} - \Delta t_{21}$ must be contained within a time interval of $\pm$ 0.5 ns to take into account the detector resolution and how this propagates through several time measurement and calculations. In mathematical term:

$$-0.5 \leq \Delta t_{31} - \Delta t_{21} \leq 0.5$$

2. the difference $\Delta t_{32} - \Delta t_{21}$ must be contained within a time interval of $\pm$ 0.5 ns:

$$-0.5 \leq \Delta t_{32} - \Delta t_{21} \leq 0.5$$

After this procedure the particle can be considered tagged and a momentum can be associated calculated from the time of flight of the particle from the first to the last detector:

$$v = \frac{l}{t_{\text{tof}}} \Rightarrow p = m_\mu \times v$$

where l is the distance between the first and the last detector.

Within this framework several simulations were made varying some parameters, such as the initial electron current and Δt_D.

Conclusions

Beam simulations

The simulations performed show that at the Jefferson Lab there is a muon beam coming from the interaction of the electron beam with Hall-A's beam-dump. Moreover, this beam is also quite focused because the muons are produced mainly by pair production processes. Thus demonstrates that with a bit of effort it is possible to create a more focused beam that can be used for experiment such as the measurement of the proton radius thorugh μ-p scattering.

Tagging system simulations

From the studied simulations it is clear that setting high electron currents reduce the amount of tagged particles. This is due to the fact that the muons are very close to

each other temporally and therefore the detector is unable to detect them all, so a large part of them is lost even before the association algorithm takes action. Instead when the electron current is lowered to 50 µA, the percentage of lost particles is significantly lowered, then it ends up around ≈ 1 % if a current of 25 mu A is used.

References

[1] A. Gasparian et al.: *A small proton charge radius from an electron–proton scattering experiment.* Nature volume 575, pages 147–150 (2019)

[2] FLUKA Team: *The official FLUKA site* http://www.fluka.org/fluka.php.

[3] Battaglieri, M. et al. *Dark matter search in a Beam-Dump eXperiment (BDX) at Jefferson Lab*

[4] Battaglieri, M. et al. *Dark matter search in a Beam-Dump eXperiment (BDX) at Jefferson Lab: an update on PR12-16-001*

ACTIVITY REPORT 2021
DOTTORATO DI RICERCA IN FISICA
UNIVERSITÀ DEGLI STUDI DI MESSINA

Acoustic tweezers and their optical characterization

S. Marrara[1–2,*], A. Mandanici[1–2], R. Saija[1–2], O. M. Maragò[2], M. G. Donato[2]
[1] *MIFT Department, Viale Ferdinando Stagno d'Alcontres 31 - 98166 Messina, Italy*
[2] *IPCF-CNR, Viale Ferdinando Stagno d'Alcontres, n. 37 – 98158 Messina, Italy*

*Corresponding Author email: sonia.marrara@studenti.unime.it

Abstract

The ability to move objects without touching them might seem an appealing dream only, but is now becoming a real opportunity for new applications in biology and chemistry. In fact, acoustic tweezers are gaining more and more attention as they allow accurate contactless particle manipulation. Through the acoustic field, objects, such as cells, bacteria, or even interstellar dust could be manipulated and studied in optimized experimental conditions. In this article, we report on a research project concerning particle trapping with an innovative method based on an ultrasonic phased array system. We want to characterize the strength of the acoustic traps with a suitable optical detection setup. Here we present our preliminary results.

Keywords: acoustic trapping, tweezers, ULTRAINO.

Introduction

Arthur Ashkin (1922-2020), Nobel Prize in Physics in 2018, proposed the technology known as optical trapping that uses light for the manipulation of microscopic particles without direct contact. However, recent advances have shown that even sound waves can be used to manipulate objects of different sizes and materials through air, water and tissues [1]. An acoustic wave involves a pressure oscillation that transports energy across a solid, liquid or gas substance. It is characterized by three quantities: wavelength, frequency, and amplitude. Since objects can absorb, diffuse and reflect an acoustic wave, an exchange of energy and momentum will take place between the particles constituting matter and the acoustic wave itself, generating an acoustic radiation force (ARF) on the target [2, 3]. Acoustic tweezers can trap larger particles (or collections of particles) than optical tweezers with even stronger forces at the same wave intensity [4]. Moreover, they do not require the particles to have special optical properties or be accessible via an optically transparent path. Acoustic tweezers may have many applications: for instance, they can be used to trap, hold and move cells and to collect them in a controlled environment, providing a non-contact alternative to micropipettes. In 1991, Wu demonstrated that latex particles and frog eggs could be manipulated by acoustic tweezers using two collimated focused ultrasonic transducers [2, 5]. Ultrasonic waves may be less disruptive to bio-materials than light; this allows the manipulation of cells, liquids, compounds or living beings. Further developments in the technology could allow the trapping and manipulation of particles in the body, and, as an example, to hold drug capsules at specific points.
In this work, we present the research activity concerning the realization of an acoustic tweezers setup based on an innovative, low-cost and open phased array setup, recently proposed [1, 6]. We will give details on the experimental setup and we will show some preliminary results obtained by acoustically trapping a styrofoam millimetric particle.

Methods

In this section, we focus our attention on the method used to perform acoustic trapping. First of all, we use ULTRAINO (ULTRAsound with arduINO) [7], an open GitHub project including the instructions to build the acoustic tweezers setup and all the drivers and software controlling it. More specifically, the acoustic tweezers setup is based on a square 8×8 array of 40 kHz transducers (Murata MA40S4S). The phase of each transducer is controlled via software so to realize a trapping point at selected positions above the array itself. The driving signals are generated by the Arduino microcontroller (see Fig. 1), according to the phase values imposed by the software. The signals are then amplified and sent to the transducers.
The sum of all the signals produced by the transducers gives a pressure field distribution, producing a trapping point a selected position. Furthermore, if necessary, ARF could be calculated, by means of the theory of acoustic trapping. In this framework, the gradient of the Gor'kov potential U describes the force $\vec{F}$ exerted on a spherical particle with size smaller than the sound wavelength (in our case, approximately 8.6 mm):

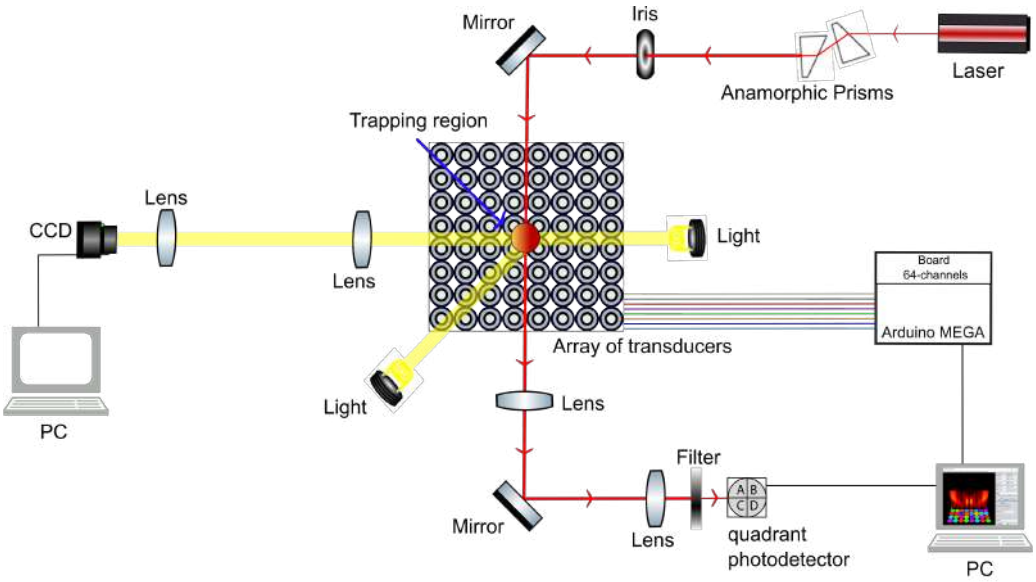

Figure 1: Scheme of the experimental set-up used in this work to perform acoustic trapping measurements. Refer to the text for the components.

$$\mathbf{F} = -\nabla U. \tag{1}$$

with

$$U = \frac{1}{4}V\left(\frac{1}{c_0^2\rho_0} - \frac{1}{c_p^2\rho_p}\right)(|P|^2) + \\ -\frac{3}{4}V\left(\frac{\rho_p - \rho_0}{\omega^2\rho_0(\rho_0 + 2\rho_p)}\right)\left(\left|\frac{\partial P}{\partial x}\right|^2 + \left|\frac{\partial P}{\partial y}\right|^2 + \left|\frac{\partial P}{\partial z}\right|^2\right), \tag{2}$$

where V is the volume of the particle, c is the speed of sound, ρ is the density and ω is the angular frequency of the emitted waves. The subscripts 0 and p are used to distinguish the host medium and the particle material, respectively.
The complex acoustic pressure P produced at point $\mathbf{r}$ by each transducer, in the so-called circular piston model [6], is:

$$P(\mathbf{r}) = P_0 A \frac{D_f(\theta)}{d} \exp[i(\phi + kd)], \tag{3}$$

where P_0 is a constant related to the power efficiency of the transducer, A is the peak-to-peak amplitude of the excitation signal, and D_f is a far-field directivity function that depends on the angle θ between the transducer normal and $\mathbf{r}$, d is the propagation distance in free space, k the wavenumber and ϕ is the initial phase of the piston.

Experimental set-up

In this work, we are interested not only to acoustically trap a particle, but also in measuring the trapping forces. To this aim, we collect the particle position fluctuations in the trap as is commonly done in optical tweezers, by using both videomicroscopy and laser interferometry [8]. Our set-up is shown in figure 1.
We obtain the images of the trapped particle by a CCD camera and a telescope based on a 3:1 lens system. Two lamps are available in the setup to illuminate the particle. In particular, the lamp in front of the camera is used to project the particle shadow on the CCD. The second lamp, not used in the measurements shown in this report, is a light source that we switch on to acquire images of the particle. The particle position is obtained running a video tracking software to analyze the video files acquired during the trapping experiments. The acquisition rate achieved is of about 100 frames per second (fps). The image of a trapped styrofoam bead (approximately 1.6 mm in radius) extrapolated from the CCD video is shown in Figure 2.

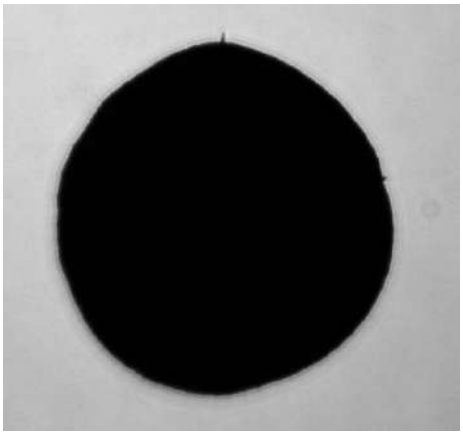

Figure 2: Single frame of a video of the trapped particle, acquired by means of the CCD.

Aiming at increasing the acquisition rate of our measurements (in principle, up to 65 kHz with our detector and connected electronics), we use a Quarter Photodiode (QPD), which is a position sensitive detector [8]. A laser beam is directed on the particle, and the fluctuations of the particle shadow are collected by the QPD (see Fig. 1). We used an acquisition rate of 5 kHz, with a measurement time of 100 s. It is worth noting that the QPD is at 90 degrees with respect to the CCD camera on the horizontal plane. The two detection tools are not operated at the same time. Moreover, depending on the kind of trap, the pressure field and the trap stiffness might be different along the x and the y axis (Fig. 3). For this reason, when measuring with the QPD, we rotated by 90 degrees the phase pattern sent to the transducers array.

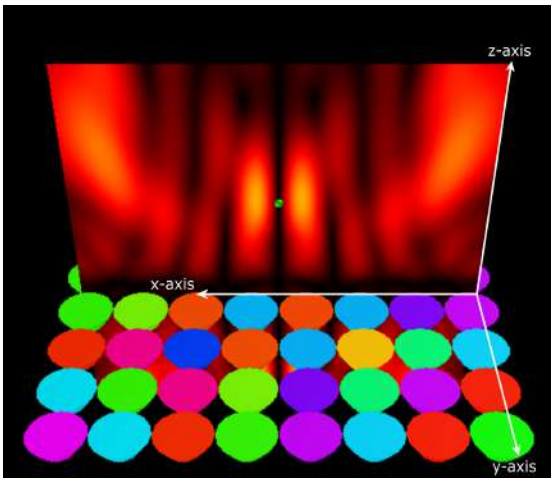

Figure 3: Example of the ultrasonic field modeled by the software.

Both the QPD signals and the video tracking data were analysed by means of their power spectra, because in this case, periodic oscillations in the particle movement give recognizable peaks at certain frequencies. In our case, we are interested in particle displacements in x, y and z directions (see figure 3).

Results

This section presents one of the first series of measurements that we obtained with this setup. Specifically, a styrofoam sphere with a radius of $\simeq 1.6$ mm and a mass of approximately 6.5×10^{-7}kg was acoustically trapped. Figure 4 shows the power spectra for the z direction obtained with CCD (upper curve) and QPD signals (lower curve), respectively. Three measurements were made for each method in order to average and thus have more precise results. The curves are shifted due to the different units of the signals involved (pixels for the CCD tracking data, Volts for the QPD signals). A peak is clearly observed at approximately 6 Hz in the spectrum. Based on a simple harmonic oscillator model [9], $f = \frac{1}{2\pi}\sqrt{\frac{k}{m}}$, a force costant k_z=$(9.2 \pm 2.2) \times 10^{-4}$N/m in the z direction is obtained. This value is comparable with the value of the spring constant expected for this setup [1, 6].

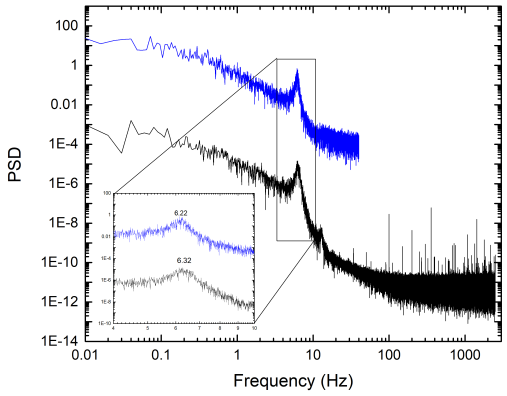

Figure 4: Power spectra obtained from CCD tracking data (upper curve) and QPD signals (lower curve). In the inset, a zoom of the peak region is shown.

Conclusions

Acoustic trapping offers interesting solutions to trap and manipulate millimetric particles avoiding any kind of contamination and modification of the material. This work describes a new particle trapping method that involves the use of ultrasounds, and a preliminary characterization of the trapping strength with optical detection techniques. The set-up we built turned out to be very promising already from the first measurements carried out, but the road to go is still quite long. Possible advances of this work will involve the realization of a standing-wave levitator as well as the trapping of particles of different compositions and their spectroscopic characterization coupling the acoustic tweezers with a Raman spectrometer.

Acknowledgements

The authors wish to thank Dr. David Bronte Ciriza and Dr. Alessandro Magazzù of the NanoSoftLab (IPCF-CNR, Messina), Mr. Roberto Caruso and Mr. G. Lupò of the electronic workshop (IPCF-CNR, Messina) and Mr. D. Arigò of the mechanical workshop (IPCF-CNR, Messina).

References

[1] A. Marzo, et al.: *Holographic acoustic elements for manipulation of levitated objects.* Nature Communications, **6**, 8661 (2015).

[2] L. Meng, et al.: *Acoustic tweezers.* J. Phys. D: Appl. Phys., **52**, 273001 (2019).

[3] J. Friend, and L. Y. Leo: *Microscale acoustofluidics: microfluidics driven via acoustics and ultrasonics.* Rev. Mod. Phys., **83**, 647 (2011).

[4] M. Baudoin, and J.-L. Thomas: *Acoustic Tweezers for Particle and Fluid Micromanipulation.* Annual Review of Fluid Mechanics, **52**, 205 (2019).

[5] J. Wu: *Acoustical tweezers.* J. Acoust. Soc. Am., **89**, 2140 (1991).

[6] A. Marzo, T. Corkett, and B. W. Drinkwater: *Ultraino: An Open Phased-Array System for Narrowband Airborne Ultrasound Transmission.* IEEE Transactions on Ultrasonics, Ferroelectrics, and Frequency Control, **65**, 102 (2018).

[7] https://github.com/asiermarzo/Ultraino (2021).

[8] P. H. Jones, O. M. Maragò, G. Volpe: *Optical Tweezers: Principles and Applications,* Cambridge University Press (2015).

[9] M. A. B. Andrade, et al.: *Experimental study of the oscillation of spheres in an acoustic levitator.* J. Acoust. Soc. Am., **136**, 1518 (2014).

Spongy TiO_2 layers deposited by gig-lox sputtering processes for Perovskite Solar Cells

C. Spampinato[1,2*], S. Valastro[2,3], E. Smecca[2], G. Mannino[2], A. La Magna[2], F. Neri[1], E. Fazio[1], A. Alberti[2]

[1] *Dipartimento Scienze Matematiche e Informatiche, Scienze Fisiche e Scienze della Terra, Università Degli Studi di Messina, Messina, Italia*

[2] *National Research Council-Institute for Microelectronics and Microsystems (CNR-IMM), Zona Industriale – Strada VIII no. 5, Catania 95121, Italy.*

[3] *Dipartimento di Fisica ed Astronimia, Università degli Studi di Catania, Catania, Italy.*

*Corresponding Author email: carlo.spampinato@imm.cnr.it

Abstract

The use of nanostructured materials represents a breakthrough in many fields of applications owing to their enhanced functionalities. One application of high interest is in the architecture of perovskite solar cells (PSC) characterized by high photoconversion efficiency values that makes PSC able to compete with silicon solar cells. In this framework, we deposited TiO_2 sponges by reactive sputtering based on a grazing-incidence geometry combined with the local oxidation of species using a method developed at CNR-IMM (gig-lox). The deposited material gains 50% porosity in volume through depths of hundreds of nanometers and consists of a forest of uniform rods separated by meso-pores (pipelines) arising from the grazing geometry; the rods, on their side, have an internal branched structure creating an interconnected network of nano-pores with sizes in the 3–5 nm range. The gig-lox TiO_2 is conceived to improve the efficiency of perovskite cells.

Keywords: Perovskite, Sputter, Deposition.

Introduction

Hybrid organic–inorganic perovskites are worldwide one of the most investigated materials nowadays, due to their unique properties impacting various fields such as photovoltaics [1], Light Emission Devices (LEDs) and photodetectors.

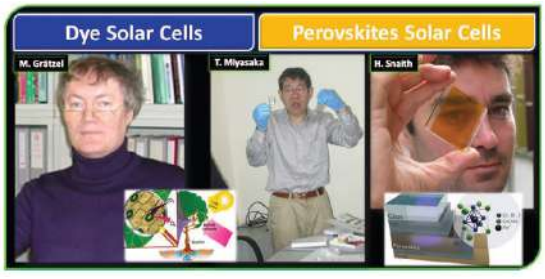

Figure 1: the famous inventors of highly performing Hybrid Sola Cells technologies. From left to right: M. Graatzel (EPFL, Lausanne, Switzerland), T. Miyasaka (Toin Univeristy of Yokohama, Japan), H. Snaith (Oxford University, UK).

In the photovoltaic field, thanks to the wide absorption range and excellent charge carrier lifetime and diffusion of the material, Perovskite Solar Cells (PSCs) were able to reach an exceptional goal of 25.5% of efficiency [2] just of ten years after the first publication of Miyasaka et al. in 2009 (figure 1).

All their exceptional properties, derived from the possibility of preparing high quality films in terms of crystallinity, thickness and low defect density, are strictly related. Those advantages are counterbalanced by issues still open. They are related to the device stability particularly under humid air ambient [3], and to the realization of high-quality large area films via wet deposition approaches, which cool down their attractiveness from the industrial point of view. A great effort was dedicated to improving the stability and crystallinity of perovskite polycrystalline films [4].

A possible way to act on some of these issues are the use, the implementation and the tailoring of highly performing nano-materials. Among them Titanium dioxide (TiO_2), since its discovery for water photolysis by Fujishima and Honda in 1972 [5], has progressively raised interest and has consequently been used in many fields such as photocatalytic degradation of pollutants, photocatalytic CO_2 reduction into energy fuels, water splitting, solar cells, supercapacitors, biomedical devices, and lithium-ion batteries [6]. In the photovoltaic field, recent advances linked to the application of porous TiO_2 in hybrid solar cell architectures have led to increased ef-

ficiency. In the standard scheme of a photo-anode [7], a mesoporous layer of nano-sized TiO_2 crystals is deposited on a Transparent Conductive Oxide (TCO), annealed for grain sintering plus anatase crystallization (typically at 500° C), and subsequently soaked with a photoactive dye. The use of chemical methods is the widespread and versatile way to generate nano-TiO_2 architectures with mesoporous or hierarchical structures with high infiltration capability. Instead, a different approach in the context of physical deposition solutions, concerning the advent of modified sputtering methodologies to grow highly porous TiO_2 scaffolds, would open the field to a higher throughput.
In this respect, we report on designed local oxidation coupled with grazing incidence sputtering methodologies used to grow multi-porosity TiO_2 layers. It proposes the first proof-of-concept of an industrially implementable approach which combines the reproducibility of the materials with the upscalability of the deposition process [6]. Another important aspect is the possibility of depositing metal oxides on different substrates.

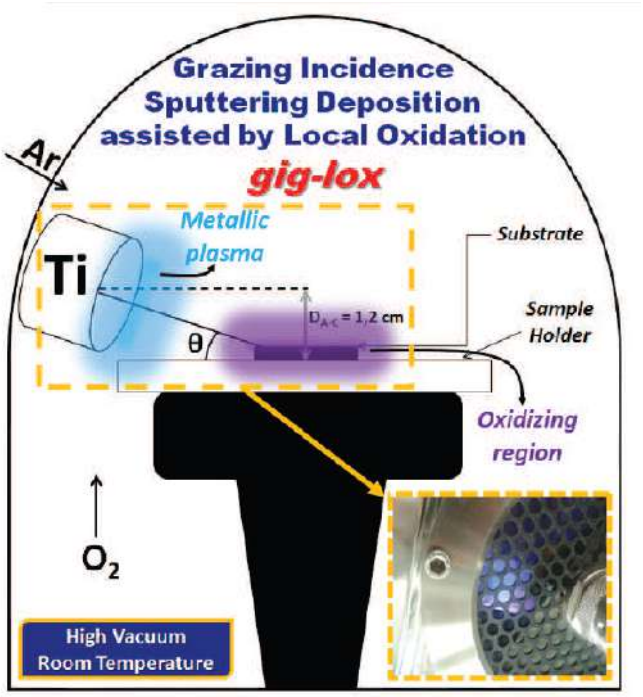

Figure 2: Customized Sputtering system, which allows working in a separately-charged- regime of the plasma (note that the Ar and O_2 sources are separated); this is combined with shadowing effects. θ is the inclination angle of the source. The inset is a picture of the double plasma (blue is metallic and violet is oxidizing) established inside the chamber [8] [9].

Materials and Methods

TiO_2 deposition

Spongy TiO_2 layers were grown by an approach based on grazing incidence sputtering deposition of Ti species from a metallic source coupled with the progressive local oxidation of the generated species at the growing front. This growth method, discussed in detail elsewhere,[8] was further improved optimizing the angular configuration to further increase the porosity and to tailor highly performing photoanode architectures. Our approach enables the following actions: (1) a high deposition rate (4 nm/min) due to the metallic plasma established at the source side (charging effects by surface oxidation are indeed avoided); (2) the progressive local oxidation of the landing species at the anode side; (3) the shadowing effect from the starting seeds due to the inclined (off-axis) Ti flux. These factors provide the material with additional meso-porosity (besides the nano-porosity arising from Thornton's approach) that is maintained during (eventually needed) post-deposition thermal treatments and up to 1000 nm. The experimental setup is reported in figure 2.

In figure 3 an example of TiO_2 gig-lox deposited on a perovskite solar cell.

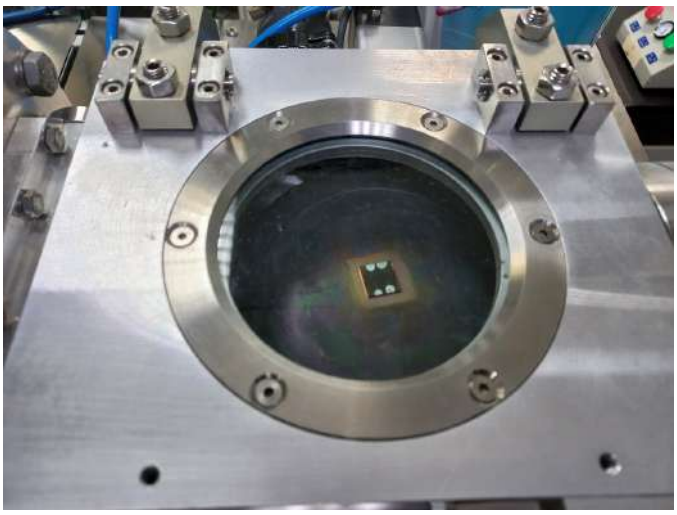

Figure 3: An example of TiO_2 gig-lox deposited on a perovskite solar cell. In the picture, a typical titanium iridescence is visible.

Results and discussion

TEM analyses

To deepen the knowledge on the porous structure a possible analysis is Transmission Electron Microscopy (TEM) on the sample.

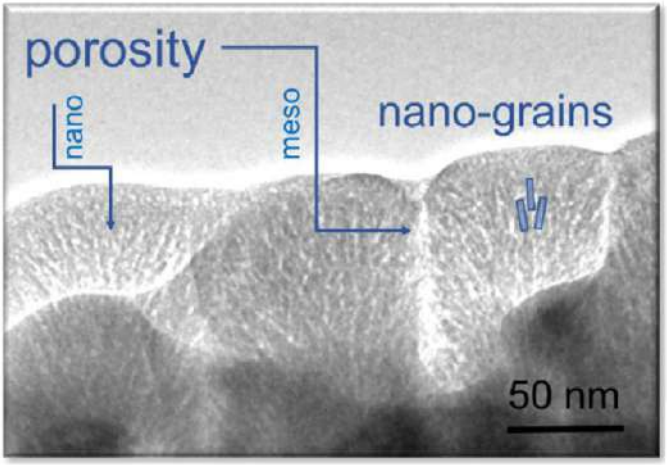

Figure 4: TEM cross section of the as deposited layer, showing the material assemblyby nano-grains in a matrix of pores [10].

An example of TEM analysis is reported in figure 4. Here it is possible to observe TEM cross section of a sample, the nano-pores and the meso-pores are clearly visible with their different dimensions [10].

Deposition in different substrates

A strength of the gig-lox method is the possibility to deposit the material potentially on any kind of different substrates. This particularity is due to the fact that the deposition takes place at low temperature and low pressure in the chamber. Figure 5 shows the TiO_2 deposited in substrates of different nature.

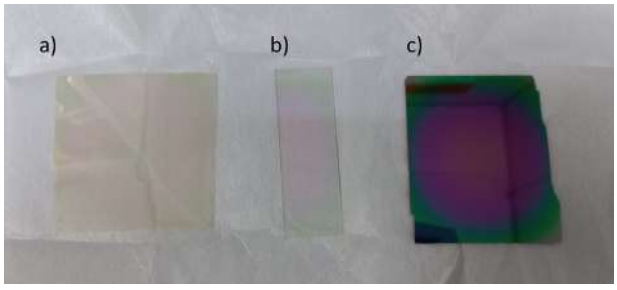

Figure 5: a) TiO_2 deposited on PEN, b) TiO_2 deposited on glass, c) TiO_2 deposited on SiO_2.

Figure 5(a) shows TiO_2 deposited on PEN (Polyethylene naphthalate) a flexible and semi-transparent substrates. Figure 5(b) shows TiO_2 deposited on glass (fully transparent) and figure 5(c) shows TiO_2 deposited on SiO_2. This deposition versatility allows having TiO_2 films deposited on substrates with different chemical/physical and mechanical characteristics that is useful for many applications [9].

Conclusions

In the framework of the engineering of nano-materials for energy conversion, we illustrated the enhancement offered by the spongy TiO_2 layers deposited by a reactive sputtering method. This method is based on Grazing-Incidence Geometry coupled with Local OXidation (gig-lox) we are experimenting in the landscape of the nanostructured materials growth. It represents a feasible way to force sputtering methods, naturally addressed to compact layers, to arrange spongy materials via a progressive bottom-up oxidation of building blocks. The technique is intrinsically up-scalable and therefore industrially compatible, and can be, in principle, extended to any reactive metallic source to produce porous oxides. The spongy gig-lox TiO_2 is unique in its twofold structure. It consists of a regular array of rods, separated by meso-pores (tens of nanometers) as the result of applying the grazing geometry. The rods, on their side, have an internal branched structure that give rise to an interconnected network of nano-pores (a few nanometers) related to the proper partial pressure of Ar used for sputtering. The overall bimodal porosity of the layer amounts to 50% of the volume [6] for thicknesses tunable up to (at least) 1000 nm. To conclude, the preliminary results show good practical perspectives around the full-building of photo-anodes in a sputtering chamber for perovskite solar cells. This deposition method could improve the efficiency of perovskite solar cells. Further studies will be conducted in this way to optimize the junction between TiO_2 layers and perovskite material by TiO_2 functionalization.

Acknowledgement

The authors wish to thank the FSE (Fondo Sociale Europeo) and "Programma Operativo Nazionale" (PON) for Sicily 2014-2020.

References

[1] S. Mathew, A. Yella, P. Gao, R. Humphry-Baker, B. F. E. Curchod, N. Ashari-Astani, I. Tavernelli, U. Rothlisberger, M. K. Nazeeruddin and M. Gratzel,: *Nat.Chem., 2014, 6, 242.*.

[2] A. Kojima, K. Teshima, Y. Shirai and T. Miyasaka, J. Am.: *Chem. Soc., 2009, 131, 6050–6051.*

[3] E. Smecca, Y. Numata, I. Deretzis, G. Pellegrino, S. Boninelli,T. Miyasaka, A. La Magna and A. Alberti: *Phys. Chem. Chem.Phys., 2016, 18, 13413–13422.*

[4] A. Alberti, I. Deretzis, G. Mannino, E. Smecca, F. Giannazzo, A. Listorti, S. Colella, S. Masi and A. La Magna: *Adv. Energy Mater., 2019, 9, 1803450.*

[5] A. Fujishima and K. Honda: *Nature, 1972, 238, 37.*

[6] Salvatore Sanzaro, Enza Fazio, Fortunato Neri, Emanuele Smecca,Corrado Bongiorno, Giovanni Mannino, Rosaria Anna Puglisi, Antonino La Magna and Alessandra Alberti: *J. Mater. Chem. A, 2017, 5,25529.*

[7] A. Alberti, G. Pellegrino, G. G. Condorelli, C. Bongiorno,S. Morita, A. La Magna and T. Miyasaka: *J. Phys. Chem. C,2014, 118, 6576.*

[8] S. Sanzaro, E. Smecca, G. Mannino, C. Bongiorno, G. Pellegrino, F. Neri, G. Malandrino, M. R. Catalano, G. G. Condorelli, R. Iacobellis, L. De Marco, C. Spinella, A. La Magna and A. Alberti: *Sci. Rep., 2016, 6, 39509.*

[9] S. Sanzaro, F. Neri, A. Aberti: *PhD thesis, UNIVERSITÀ DEGLI STUDI DI MESSINA.*

[10] A. Alberti, L. Renna, S. Sanzaro, E. Smecca, G. Mannino, C. Bongiorno, C. Galati, L. Gervasi, A. Santangelob, A. La Magna: *Sensors and Actuators B: Chemical.*

Archaeometric investigations of blue-pigmented plasters from the Church of the Annunciation (Tortorici, Italy)

S. E. Spoto[1*], F. Caridi[1], V. Venuti[1]
[1] *Dipartimento di Scienze Matematiche e Informatiche, Scienze Fisiche e Scienze della Terra, Università degli studi di Messina, Messina, Italia*

*Corresponding Author email: sebastiano.spoto@studenti.unime.it

Abstract

Blue-pigmented plasters of the Church of the Annunciation (Tortorici, Sicily) were characterized, for the first time, both at the elemental and molecular levels, by means of portable X-ray fluorescence (XRF) and Raman spectroscopy. The understanding of their nature can provide information about the realization of the wall paintings in the Church. In this sense, the results obtained in this brief report provide relevant information to identify and address building materials' characterization and the time frame of the ralization of the original wall paintings.

Keywords: Plasters, Raman spectroscopy, XRF spectrometry, Ultramarine blue, Pigments.

Introduction

The importance of multi-technique characterization of materials is linked to the possibility to evaluate, on one side, any change in their physical state starting from the production of the specimen from the raw geological/mineralogical materials, and, on the other side, their diffusion through trade, use, and deployment in the archaeological record [1, 2]. In the variety of techniques employed in different research areas of archaeometry, X-ray fluorescence (XRF) spectroscopy has an extensive use, being a well-established analytical method both in the laboratory and industry for the evaluation of the elemental composition. The employment of the XRF technique for the analysis of archaeological specimens lies in its remarkable combination of practical and economic advantages [1, 2]. Raman spectroscopy is another analytical technique widely used in archaeometry [1, 2], offering the advantage that, being a molecular spectroscopic technique, it can deal with inorganic and organic materials, including ancient objects and modern artists' specimens. For both methodologies, the development of mobile instrumentation is becoming available to the community to analyze art objects directly in situ [1, 2].

Site description and methods

Site description

The Church of the Annunciation is a masonry Roman Catholic Church located in the center of Tortorici, a municipality in the Metropolitan City of Messina (Sicily, Southern Italy). The investigated Church belongs to a period of architectural transition in Sicily, between the XVIII and XIX centuries, where Baroque and neoclassical motifs were combined in the main Sicilian cities. Many of the religious buildings built in this period were destroyed or not completed, due to earthquakes, limited financial resources, and changes in taste by developers or designers.

Figure 1: Measurement areas of plasters at the Church of the Annunciation.

In the light of this, the investigated Church can be considered as a structure of significant level in the context of this peculiar rural and local architecture, up to now not well known or studied. It is worth noting that only incomplete and inaccurate information regarding the Church's role in local society are available. What is certainly known is that the Church served religious functions until 1963, when it was closed to the public due to its highly deteri-

orated state. Since then, the Church fell into a state of disrepair. Only at the end of the 20th century, the local authorities undertook a significant restructuring. Actually, the Church shows several extended fractures, of dubious origin, on its internal walls and no longer plays a role in the religious community, having become the center of artistic and cultural events in Tortorici [1]. Among all pigmented areas, three points, representative of blue-pigmented plasters (P8 and P9) and preparatory ground (PG), of the interior of the Church, were investigated (see Fig.1).

Methods

The investigation was performed in situ by using portable XRF and Raman instrumentations. XRF measurements were carried out using a portable XRF Alpha 4000 analyzer (Innov-X systems, Inc., Woburn, MA, USA), which allows the detection of chemical elements with an atomic number (Z) between phosphorus and lead. It is equipped with a Ta anode X-ray tube as source and a Si PIN diode (active area of 170 mm^2) as detector. The instrument was controlled by a Hewlett-Packard iPAQ Pocket PC (HP, Inc., Palo Alto, CA, USA), which was also used for the data storage. Raman measurements were performed by using a portable "BTR 111 Mini-RamTM" (B&W TEK Inc., Newark, NJ, USA) spectrometer with an excitation wavelength of 785 nm (diode laser), a maximum laser power of 280 mW at the excitation port, and a charge coupled device (CCD) detector (thermoelectric cooled, TE). The laser output power was continuously adjusted by maximizing the signal-to-noise ratio while minimizing the integration time [1]. The abbreviations of minerals reported in the present study follow the list approved by the International Mineralogical Association (IMA) Commission on New Minerals, Nomenclature and Classification (CNMNC) [3].

Results and discussion

Fig.2 reports the XRF and Raman results concerning points P8 and P9, representative of a dark and light blue pigmented area of the Church, respectively. In particular, XRF spectra of points P8 and P9 (not shown) can be overlapped, indicating a similar elemental composition, with the presence of Ca, Fe, Ti, and S in quite large amounts. Going on, Raman measurements in both points show two clear peaks at ∼546 and ∼1087 cm^{-1}, which can be assigned to the presence of an ultramarine blue pigment [1] and to the calcium carbonate ($CaCO_3$) [4] from preparation ground, respectively. There is much confusion in the literature between ultramarine blue (a pigment obtained from ground lapis lazuli), lapis lazuli (an aggregate of minerals), and lazurite (the most valuable 'blue' mineral component of the lapis lazuli) [1, 5]. Lapis lazuli is a complex rock whose composition is defined by the presence of the mineral lazurite $(Na,Ca)_8(AlSiO_4)_6(SO_4,S,Cl)_2$, which is responsible for its overall blue hue [6]. Inclusions of several other minerals are also common, including pyrite (FeS_2), calcite ($CaCO_3$), diopside ($CaMgSi_2O_6$), forsterite ($MgSiO_4$), and wollastonite ($CaSiO_3$), in varying amounts [6]. Lazurite itself is a member of the sodalite group, which includes sodalite, nosean, and hauyne, and is typically considered a sulfur-rich hauyne [1]. The sodalite minerals contain frameworks of alternating silica and alumina tetrahedra creating large cubo-octahedral cages, known as β-cages; extra-framework cations (Ca^{2+}, K^+, or Na^+), anions (Cl^-, OH^-, or Sn^-), and neutral species (H_2O) are entrapped within these cages [6]. Lazurite's blue color is attributed to sulfur polyanion radicals trapped in the β-cage structure. Variations in color appear to be related to ratios between various sulfur species: the trisulfur radical (S^{3-}) is mainly responsible for the blue color, but contributions from disulfur (S^{2-}) and tetrasulfur (S^{4-}) radicals can shift the color towards yellow or red, respectively [1, 6].

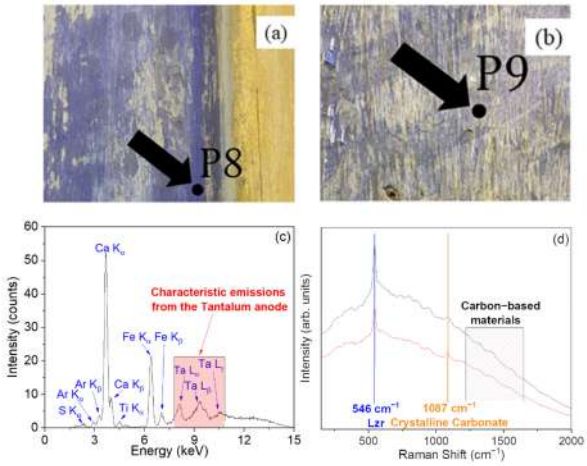

Figure 2: Photo of the point P8 (dark blue) (a). Photo of the point P9 (light blue) (b). XRF spectrum recorded on the point P8, reported as an example (c). Raman spectra recorded on the points P8 (grey line) and P9 (red line) (d). In the figure, Lzr: lazurite.

Based on comparison with literature [1, 6], it is possible to identify the ultramarine blue as synthetic. Interestingly, only in the year 1828, Jean-Baptiste Guimet, in France, and Friedrich August Kottig, in Germany, published the production process for a synthetic ultramarine [1, 7]. In particular, it consisted of four steps: (i) clay activation, (ii) blending and heating of the raw materials, (iii) oxidation, (iv) purification and refinement. The raw materials used are kaolinitic clay, feldspar, anhydrous sodium carbonate, sulfur, and a reducing agent such as oil, pitch, or coal. In this context, the ultramarine blue pigment found in the blue pigmented plasters in the investigated site played a key role in the understanding of the period of realization of the wall painting. In fact, as can be seen from Fig.2, no minerals commonly associated with the lapis lazuli were detected. Noteworthy, the presence of iron in the corresponding area, as detected by XRF, can be reasonably due to the raw minerals used

for the production of the synthetic ultramarine blue. Fe-bearing minerals, as, for instance, illite, can be used in the industrial process to produce the pigment [1, 8]. In the Raman spectra observed, there is no trace of pyrite, the common Fe-bearing mineral associated with the natural lapis lazuli. The Church was built in 1757, and the synthetic ultramarine blue was commercialized only after the second decade of the XIX century. The finding of the synthetic ultramarine blue allowed us to hypothesize that such first phase belongs to an age later than the first two decades of 1800, which, as a matter of fact, could be considered as the original wall painting of the investigated Church. As far as the preparation ground is concerned, identified as point PG, the Raman spectrum collected on it (see Fig.3) revealed an intense peak at ∼1080 cm^{-1}, along with other contributions at ∼162, ∼282, ∼712, and ∼1435 cm^{-1}, all associated to the presence of calcite, the most stable polymorph of calcium carbonate ($CaCO_3$) [1, 4].

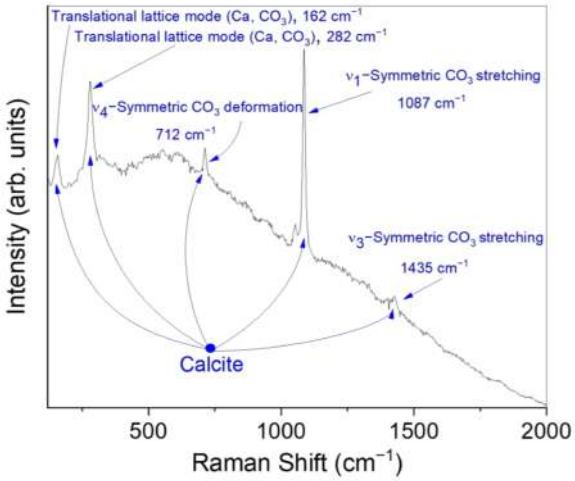

Figure 3: Raman spectrum recorded on the preparatory ground.

Conclusions

In this brief report, blue-pigmented plasters of the Church of the Annunciation (Tortorici, Sicily) were characterized by means of portable XRF and Raman instrumentations. The presence of the ultramarine blue as synthetic pigment gives us the information that the plasters belong to an age later than the first two decades of 1800.

References

[1] Spoto, S.E., Paladini, G., Caridi, F., Crupi, V., D'Amico, S., Majolino, D., Venuti, V. *Multi-Technique Diagnostic Analysis of Plasters and Mortars from the Church of the Annunciation (Tortorici, Sicily).* Materials, **15**(3), 958 (2022).

[2] Crupi, V., La Russa, M.F., Venuti, V., Ruffolo, S., Ricca, M., Paladini, G., Albini, R., Macchia, A., Denaro, L., Birarda, G., Bottari, C., D'Amico, F., Vaccari, L., Majolino, D. *A combined SR-based Raman and InfraRed investigation of pigmenting matter used in wall paintings: The San Gennaro and San Gaudioso Catacombs (Naples, Italy) case.* The European Physical Journal Plus, **133**, 1–8 (2018).

[3] Warr, L. *IMA–CNMNC approved mineral symbols.* Mineralogical Magazine, **85**, 291–320 (2021).

[4] Rutt, H.N., Nicola, J.H. *Raman spectra of carbonates of calcite structure.* Journal of Physics C: Solid State Physics, **7**, 4522–4528 (1974).

[5] Ganio, M., Pouyet, E., Webb, S., Schmidt Patterson, C., Walton, M. *From lapis lazuli to ultramarine blue: Investigating Cennino Cennini's recipe using sulfur K-edge XANES.* Pure and Applied Chemistry, **90**, 463–475 (2018).

[6] Chukanov, N., Sapozhnikov, A., Shendrik, R., Vigasina, M., Steudel, R. *Spectroscopic and Crystal-Chemical Features of Sodalite-Group Minerals from Gem Lazurite Deposits.* Minerals, **10**, 1042 (2013).

[7] Delamare, F. *Blue Pigments. 5000 Years of Art and Industry.* Archetype Publications Ltd.: London, UK, (2013).

[8] Hsiao, Y.H., Shen, Y.H., Ray, D.T. *Synthesis of Ultramarine from Reservoir Silts* Minerals, **7**, 69 (2017).

ACTIVITY REPORT 2021
DOTTORATO DI RICERCA IN FISICA
UNIVERSITÀ DEGLI STUDI DI MESSINA

Characterization and commissioning of the upgraded Inner Tracking System (ITS2) of the ALICE experiment at LHC

A. S. Triolo[1–3,*]
[1] *Dipartimento di Scienze Matematiche e Informatiche, Scienze Fisiche e Scienze della Terra, Università degli Studi di Messina, Messina, Italy*
[2] *INFN - Sezione di Catania, Catania, Italy*
[3] *CERN, Geneve, Switzerland*

*Corresponding Author email: andrea.triolo@studenti.unime.it

Abstract

The Inner Tracking System (ITS) is the innermost detector surrounding the beam pipe located in the central barrel of ALICE, one of the four experiments located at LHC, CERN.
The ALICE experiment is dedicated to the study of the strongly interacting matter.
The Upgrade of ALICE, and in particular of the ITS, which will last until the data-taking period of LHC Run 3, is done to improve the detector resolution and to reduce its material budget, thanks to the new monolithic chips ALPIDE and to the new configuration of the ITS.
In this work the analysis of the upgraded ITS commissioning-phase data will be presented. In particular, a study of the Fake Hit Rate and of the Charge Threshold of the sensors will be shown in details.

Keywords: ITS, ITS Upgrade, ITS2, ALICE, ALPIDE, fake hit rate.

Introduction

ALICE (A Large Ion Collider Experiment) is one of the four largest experiments at LHC (Large Hadron Collider) at CERN, and it is dedicated to the study of the strongly interacting matter.
The innermost detector of ALICE is the ITS (Inner Tracking System). Its purposes are: localize the primary vertex of interaction, reconstruct the secondary vertices from the decays of particles, and track and identify particles produced in collisions.
The ALICE experiment is going through an upgrade phase, started in 2019, whose main feature is the replacement of the beam pipe with a smaller one, with the aim to bring the detectors closer to the interaction point. Consequently, some detectors themselves will be modified to suit the new configuration. In this work in particular the main features of the upgrade of the ITS will be presented.

ITS Upgrade

There are several reason for the ITS Upgrade. Firstly, the precision of the ITS1 in the determination of the track distance of closest approach was insufficient to study the production of particles via their decay at values of transverse momentum below 1 GeV/c [1]. Moreover, the impact parameter resolution of the ITS1 was not low enough to detect particles with decay length under 100 µm. Another limitation was given by its limited read-out rate capabilities. Indeed, it could run at a maximum rate of 1 kHz, and this rate constraint prevented ALICE from using the full Pb-Pb collision data rate of 8 kHz that LHC can currently deliver. Finally, there was the impossibility to access the ITS1 detector for maintenance and repair interventions during the LHC shutdowns: this was a major limitation in sustaining high data quality.
For all these reasons the ITS is completing a significant upgrade. The key features of the ITS upgrade are [1]:

- The reduction of the distance between the interaction point and the ITS, crucial to improve the impact parameter resolution and to allow the detection of particles with a short lifetime.
- The reduction of the material budget of the detector, necessary to improve the tracking performance and momentum resolution.
- The new ITS2 will not measure the energy loss of the particles in the silicon layers, already measured thanks to the TPC ALICE detector [2].
- The read-out rate was also improved to be adequate to exploit the expected Pb-Pb and p-p interaction rates.

A key feature introduced to achieve all these requirements is the introduction of new chips called ALPIDE, whose specifications will be discussed below. Moreover, the ITS is renewed also in the way the sensing layers are organized around the beam pipe. The old six SPD, SDD

and SSD layers have been replaced with seven layers of ALPIDE chips. In this way, the first layer could be closer to the interaction point, enhancing the coverage in transverse momentum, in particular down to extremely low momenta.

ALPIDE chip

An ALPIDE chip is a CMOS (Complementary Metal-Oxide Semiconductor) MAPS (Monolithic Active Pixels Sensors). It was developed on purpose for the ALICE Upgrade, and it innovation is that both the sensitive volume and the front-end readout logic are located in the same piece of silicon. Each ALPIDE chip measure 15×30 mm^2 and includes a matrix of 512×1024 pixel cells, each one measuring 29.24 µm×26.88 µm. Analog biasing, control, readout and interfacing functionalities are implemented in a peripheral region of 1.2×30 mm^2. Each pixel cell contains a sensing diode, a front-end amplifier and shaping stage, a discriminator and a digital section.

The new configuration for the ITS: ITS2

The ITS2 is composed by seven layers of ALPIDE chips, that could be grouped into two separate barrels: the Inner Barrel (IB) and the Outer Barrel (OB).
The IB is composed by the first three layers of the ITS, named L0, L1 and L2. The OB is composed by the other four layers, named L3, L4 (Middle Layers - ML), L5, L6 (Outer Layers - OL).
All the seven layers are azimuthally segmented in units named Staves. Each stave is mechanically independent from the others and fixed to a support structure in carbon fiber, half-weel shaped, to form the so called Half-Layers. A single stave contains all the structural and functional components; as a result, it is the smallest operable component of the detector.
Schematic drawings of the IB and OB staves could be seen in Figure 1. Each IB stave is composed by 7 chips, each OB stave is composed by 112 (ML) or 196 (OL) chips. The spacial organization of the staves could be seen in Figure 2.

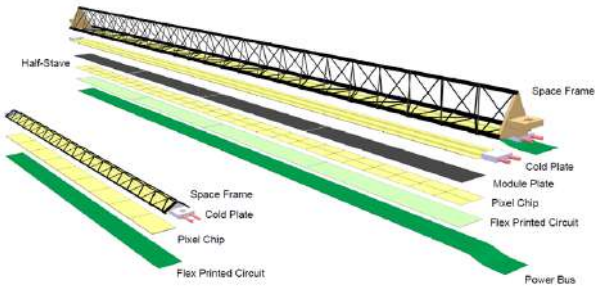

Figure 1: Schematic drawing of the IB (left) and OB (right) Staves [1]

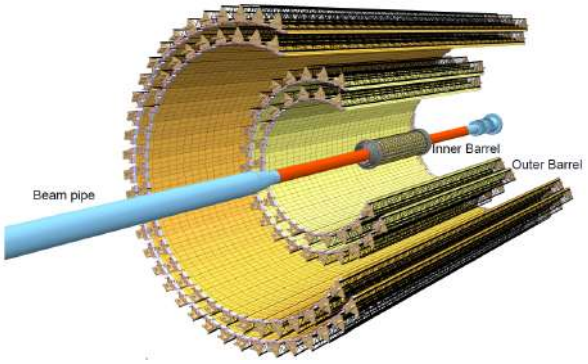

Figure 2: Layout of the ITS [1]

Major improvements following the upgrade are:

- The material budget decrease from 1.1% X_0 to 0.3 % X_0 for IB and 0.8% X_0 for OB.
- The pesudo-rapidity range increase from $|\eta| < 0.9$ to $|\eta| < 1.22$.
- The spatial resolution changes from 100 to 4 µm.
- The read-out rate increases from 1 kHz to 100 kHz for Pb-Pb collisions and 400 kHz for p-p collisions.

Characterization of the ITS2

During the pre-commissioning phase, started in May 2019 and ended in December 2020, the detector has been installed in an assembly clean room at CERN with all the detector services to perform the full commissioning of the detector on surface.
During this phase all the seven detector layers have been assembled and installed in half-barrels, where the staves have been mounted on the corresponding half-layer mechanical supports in order to build the 14 half-layers composing the ITS2 detector. The half-layers have been then progressively arranged together to form the two IB half-barrels and the two OB half-barrels [4]. The four half-barrels installed in the clean room are shown in Figure 3.

Figure 3: The four Half-Barrels installed in the clean room at CERN during the phase of pre-commissioning [5]

The standard data taking schedule followed during the pre-commissioning phase foresaw hourly execution of a threshold scan, a fake-hit rate run and a readout test.

Fake Hit Rate Study

The Fake Hit Rate (FHR) data were taken in absence of external source of radiation, for recurring periods of 100 seconds (runs) at a frequency of 11.2 kHz. So it is a measure of the noise (thermal and due to cosmic rays) of the detector. The product between the period of a single run and the frequency is the number of events. The Fake Hit Rate is defined as the number of signals generated (hits) per event per pixel. The work reported here was based on the analysis and the cataloguing of pixels with a FHR higher than 10^{-6}. This limit for the Fake Hit Rate was imposed by the request to perform a good track reconstruction performance. The FHR could be studied not only for the individual pixels, but also for the chips or the staves. A first conducted analysis regarded the study of the Fake Hit Rate of all the staves of the Outer Barrel. This analysis showed that the average FHR for each stave stayed below the imposed limit, at a value of about 10^{-8}. But the FHR could be further reduced applying a software mask that cut out from the conducted analysis those pixels with a FHR exceeding the limit. Several studies conducted during this work show how the Fake Hit Rate decreases with the application of these software masks. These studies are of great importance to identify and limit via software the detector noise, with the aim to guarantee the correct measurements during the periods of data taking. Software masking was carried out selecting all the noisy pixels (i.e. those with a FHR$>5\times10^{-6}$) for each run analyzed, and then excluding them from the count of the average Fake Hit Rate over the stave. For the number of events considered (11.2 kHz $\times$ 100 s = 1120000), imposing that the maximum FHR can be 5×10^{-6} means that each pixel can fire at most 5 times without being excluded from the analysis. Whit this mask only the 0.001% of pixels (in average) is masked. With only this small percentage of pixels masked, the FHR decreased of about 3 orders of magnitude, as can be seen in Figure 4.

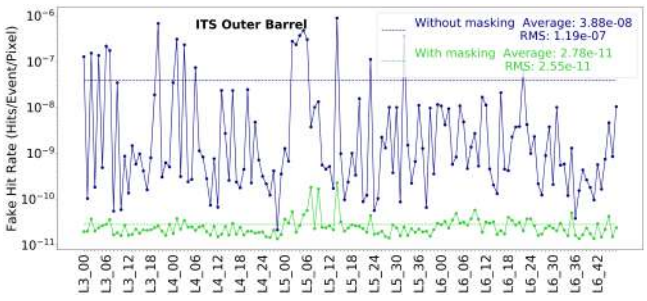

Figure 4: Comparison between the Fake Hit Rate of the Staves of the Outer Barrel before and after masking

Considering these plots shown above, the fact that with only the small percentages of pixel masked the FHR diminish of about three order of magnitude means that in general the staves aren't noisy, but there are inside them some individual pixels that, for certain reasons, show a FHR so high that make the average FHR of the stave increase even of more than one order of magnitude.

Correlation between wrong Threshold tuning and high Fake Hit Rate

The plot shown in figure Figure 5 demonstrates how there is a correlation between the bad tuning of the Thresholds and an high Fake Hit Rate.

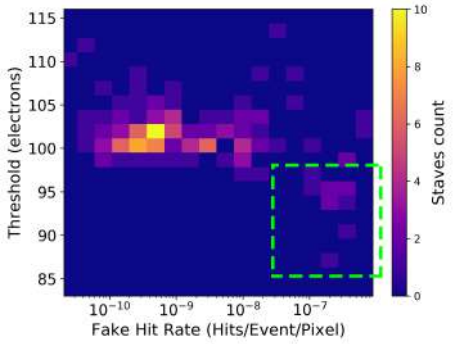

Figure 5: Bi-dimensional distribution of FHR and Threshold for all the staves of the Outer Barrel

In this plot it can be seen how the most part of the staves, those with a FHR$<10^{-8}$, have a Threshold value tuned around 100 electrons, that is the value at which thresholds are actually tuned, and it is a trade-off between pixel efficiency and amount of noise. But there is a small number of staves, those circled in green in Figure 6, that have a FHR between 10^{-8} and 10^{-6} and a Threshold value below the average. This means that those staves have a large number of pixels with a bad tuning, that influence the average Threshold of the stave, and consequently the average Fake Hit Rate of the stave. This happens because a lower Threshold means that more pixels are read, and then more fake hits are registered. There is also a very little fraction of staves that have an high FHR with a good Threshold: this could be due to a wrong preliminary hardware masking.

Mask stability

The developed code to mask the noisy pixels allows us to mask also pixels depending on their occurrence between the runs analyzed. The masks seen before were applied run by run for all the pixels which showed a FHR$>5\times10^{-6}$. These were the so called "full software masking".
A more interesting study that was conducted concerns the masking of only the noisy pixels common to the 100% of runs analyzed. This is a method to avoid efficiency losses in the track reconstruction, because applying this constraint it can be avoided to mask also particle tracks that maybe generate more than 5 hits in a single pixel. This is useful to develop a new hardware mask that can be used in the process of data taking during the LHC Runs.
An example of study conducted regarding the variation of the FHR as function of the mask of the noisy pixels

common to different percentage of runs out of their total number is presented in Figure 6.

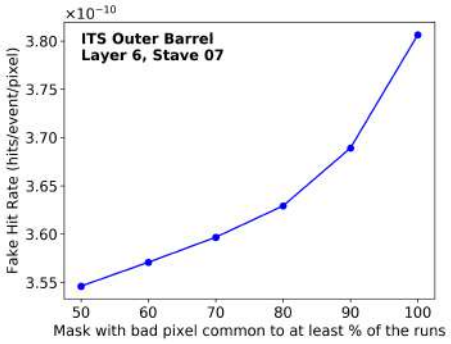

Figure 6: Fake Hit Rate of the stave L6_07 vs. amount of percentage of runs in which pixel are fired

This plot demonstrates how more strictly is the request of having pixel common to more runs, higher is the Fake Hit Rate after applying the mask, as already explained, but also just applying the most strict mask (that requires that only the pixels that fire in each run have to be masked) the Fake Hit Rate stays around 10^{-10}. This demonstrates that such degree of masking could be used to build the hardware mask to introduce during the LHC Runs, avoiding efficiency losses.

Observation of cosmic radiation

In this work also a qualitative study of the cosmic radiation seen by the half-barrels of the ITS2, during the period it was in the clean room at CERN, was performed. The performed study is a preliminary study, aimed to show the capability of the detector to find clusters of cosmic rays. Data used to perform this study were the same used for Fake Hit Rate studies. Inside this data the search for cosmic rays was performed using a clustering algorithm that finds neighbors fired pixels in the noise data matrix that represents a stave.
A plot showing the number of clusters of cosmic rays for stave of the OB is shown in Figure 7.

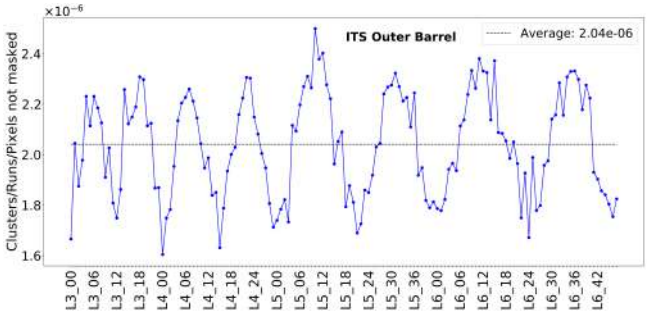

Figure 7: Number of clusters per run for each stave of the Outer Barrel

The results presented in this plot were obtained after applying the software mask discussed before, to eliminate from the data those pixels which fires repeatedly without any contribution from the cosmic rays. The particularity of this plot is that for each Layer there are two peaks. The reason for that is the configuration with which the half-barrels were installed in the clear room during the pre-commissioning phase, when noise data were taken, that was that already seen in Figure 3. Each layer was divided in two halves. In each half-layer the central staves were facing up, and the other were facing side-way. The peaks of the plot are placed in correspondence of those staves facing up: this is because cosmic rays have an higher probability to intercept staves that are placed horizontally rather than those placed obliquely/vertically. This study is only qualitative, that means that it was conducted only with the purpose to test the capability of the detector to pick up also smaller signals like those derived from cosmic radiation. This could be achieved also thanks to the low Fake Hit Rate of the detector and to the good software mask performed.
Another study conduced concerned the number of Pixels in each cluster. It was found that for all the staves of the OB the situation is similar: in average, each cluster fires in a stave around 4 pixels. Over a total of 112 or 196 chips, each of which contains more than 50 000 pixels, 4 pixels are a real small number, but the detector is still capable of detect them. For the small number of pixels that fires consequently the passage of cosmic rays, the Fake Hit Rate deriving from them is also very small. A comparison between the total FHR of the stave and the FHR due to cosmic radiation can be seen in Figure 8.

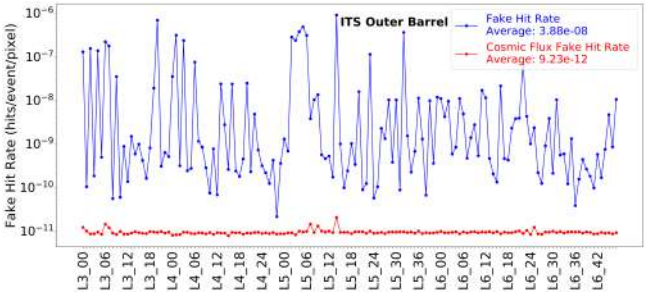

Figure 8: Comparison between the total Fake Hit Rate of the staves and the Fake Hit Rate due to the cosmic radiation

It can be seen that the noise deriving from the cosmic radiation is about three orders of magnitude smaller than the total noise. Again, this is a proof that the detector is so little noisy to discriminate the Fake Hit Rate due to thermal noise from the Fake Hit Rate due to cosmic radiation.

Conclusions

In this work, focused on the characterization of the new ITS2, an overview of the study of the Fake Hit Rate of the staves of the new ITS2 was presented.
Noise and threshold data were analyzed. The study of the

noise data was focused on the determination of the Fake Hit Rate of each stave of the Outer Barrel. It has been determined that with the technology of the ALPIDE chips the Fake Hit Rate for each stave stays beyond the limit value of 10^{-6}, with an average Fake Hit Rate among the OB staves of 3.88×10^{-8}. To make this value even smaller, a software mask was applied to noise data, with which the Fake Hit Rate for each stave decreased of about 3 orders of magnitude on average.
From the study of the Threshold data emerged that not all the Chips of the staves have been tuned correctly on the right value of Threshold. This resulted in high values of Fake Hit Rate for those Chips, that made the average Fake Hit Rate of the involved staves also increase. A correlation between low values of threshold and high values of FHR has been demonstrated.
Also a quantitative study of the cosmic radiation seen by the ITS has been carried out. This study demonstrated how the ITS is so little noisy that it has the capability to discriminate noise coming from the cosmic radiation from thermal noise.

References

[1] Abelev, B. et al. and the ALICE Collaboration: *Technical Design Report for the Upgrade of the ALICE Inner Tracking System.* J. Phys. G: Nucl. Part. Phys. **41** 087002 (2014) https://iopscience.iop.org/article/10.1088/0954-3899/41/8/087002

[2] ALICE Collaboration: *Conceptual Design Report for the Upgrade of the ALICE ITS.* CERN-LHCC-2012-005, LHCC-G-159, 2012 https://cds.cern.ch/record/1431539?ln=it

[3] CERN Document Server https://cds.cern.ch/record/2263642

[4] Alessandra Fantoni on behalf of the ALICE Collaboration: *Upgrade of the ALICE inner tracking system: Construction and commissioning.* Phys. Scr. **95** 084011 (2020) https://iopscience.iop.org/article/10.1088/1402-4896/aba0f7

[5] Domenico Colella for the ALICE Collaboration: *ALICE ITS Upgrade for LHC Run 3: Commissioning in the Laboratory.* arXiv:2012.01564v1 [physics.ins-det] https://arxiv.org/abs/2012.01564

Optical Crystallographic and Petrographic Characterization of Medieval Stuccoes Coming from Reggio Calabria and Rossano (Italy)

V. Vecchio[1,2]
[1] *Department of physics, Physics and Earth Science (MIFT), University of Messina, Viale F. Stagno d'Alcontres, 31, 98166 Messina, Italy*
[2] *National Archaeological Museum of Reggio Calabria, Piazza De Nava, 26, 89123 Reggio Calabria, Italy*

*Corresponding Author email: virgilio.vecchio@unime.it

Abstract

The National Archaeological Museum of Reggio Calabria houses a large and rare group of fragments of medieval architectural stuccoes, all dating to the 12^{th} century, from three Calabrian Arab-Norman churches: S. Maria of Terreti, S. Nicola of Calamizzi, both in Reggio Calabria, and La Panaghia in the town of Rossano. Observation under polarized light microscope of samples coming from one Terreti's plaque, from one plaque of not ascertained provenance church and from one Rossano's capital showed great similarity. All the samples contain traces of tiny anatase crystals.This unusual impurity has been assumed as provenance tracer in order to find the quarrying site. Analysis of samples coming from the historical gypsum quarry of Gipso, nearby Crotone, showed the residual presence of the same mineral.

Keywords: medieval stuccoes, gypsum, anatase, provenance study, polarised light microscopy.

Introduction

The medieval architectural stuccoes housed in the National Archaeological Museum of Reggio Calabria, all dating back to the 12^{th} century, come from three Calabrian Arab-Norman churches: S. Maria of Terreti, S. Nicola of Calamizzi, both in Reggio Calabria, and La Panaghia in the town of Rossano in the province of Cosenza. The Terreti stuccoes, including 2 small columns, numerous plaques fragments and a fragment of an arch, all with bas-relief decoration, were recovered by the illustrious archaeologist Paolo Orsi soon after the church's demolition in 1915, having deemed the damage it had suffered from the 1908 earthquake to be irreparable.The columns from Calamizzi are very similar to those of Terreti in shape and size and come from the ancient Basilian abbey rebuilt in the 12^{th} century by S. Cipriano and destroyed by the 1783 earthquake. From the small church of Rossano come four small capitals found in a cavity in the masonry. The 2019 exhibition dedicated to Paolo Orsi was an opportunity to restore and present part of the stuccoes to the public for the first time. In the first months of 2020 other fragments have been restored during a worksite school that the museum has started in collaboration with the diocese of Locri-Gerace.
Samples from a plaque from Terreti (inventory number 11800), from one plaque of not ascertained provenance but very similar to one plaque from the Terreti church with inventory n. 11802, and from one of the capitals of Rossano (provisional inventory number 33) were analyzed with the main purpose of establishing their mineralogical composition.
The presence of anatase (a titanium dioxide polymorph) in every sample has led to the hypothesis that the gypsum was extracted from the same quarry. This would be particularly significant given that the two sites are 300 km away from each other and that gypsum outcrops in Calabria are widespread. Therefore, attention is being focused on the gypsum quarries historically exploited in the Calabrian territory, in particular on those located in intermediate areas between the two sites. The best known, and then the first to be considered, is the one located in Gipso, near Crotone, whose exploitation started at least during Roman Empire.

Materials and Methods

An approximately $2cm^2$ plane face of each sample was sanded till 500 mesh and glued on frosted microscope's slide with epoxy resin (bisphenol A diglycidyl ether + triethylenetetramine). The samples were, then, sliced and lapped to obtain 30 µm thin sections.
Thin section were studied with polarized light microscopy. Gipso's samples were taken with in situ prospecting.

Results

Terreti's Plaque (inv. n. 11800)

The stucco is milky white coloured, porous, with sub-millimetric pores, fragile and prone to chalking. Under polarized light microscope (sample man-st-2) appear almost entirely made of gypsum ($CaSO_4 * 2H_2O$): texture is fairly homogeneous mainly composed of granular microcrystals, sometimes acicular, colourless and non-pleochroic, while interference colors range from white to gray.
Accessories minerals are carbonates of calcite group (general formula ACO_3 where A= Li, Mg, Ca, Fe, Zn), present as sparse microcrystals or microcrystalline aggregate (figure 2). Lumps of iron oxide and hydroxide ranging from 10µm to 500 µm are also present. Rare microcrystals of anatase (a TiO_2 polymorph) are observed (figure 3): colours range from green to blue, relief is strongly positive, the interference colours reach the fourth order but are often masked by the intense colours.

Figure 1: Terreti's plaque (inventory number 11800).

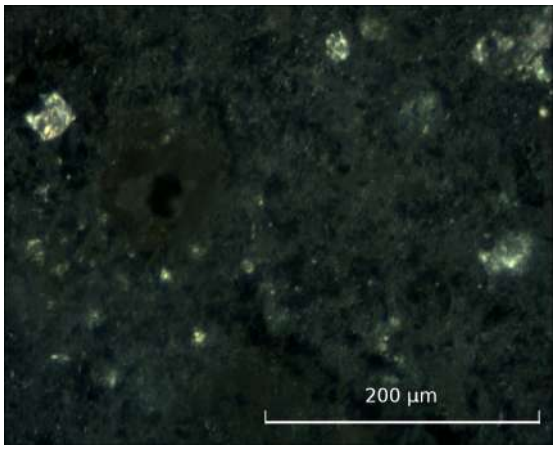

Figure 2: Sample MAN-ST-2, micrograph, crossed nicols.

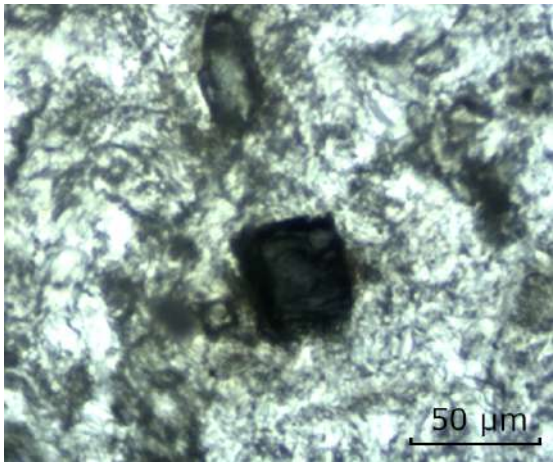

Figure 3: Sample MAN-ST-2, micrograph, parallel nicols.

Rossano's Capital (provisional inv. n. 33)

The capital's stucco appears milky white coloured, porous, with sub-millimetric pores, fragile and prone to chalking. Observation under polarized light microscope (sample man-st-3) reveals that gypsum is the prevailing component: texture is fairly homogeneous mainly composed of granular microcrystals, colourless and non-pleochroic (figure 4), while interference colors range from white to gray. Rare bassanite crystals ($CaSO_4 * 0.5H_2O$) are also present.
Accessories minerals are carbonates of calcite group, present as sparse microcrystals or microcrystalline aggregate (figure 6).
Anatase microcrystals are observed (figure 5): colors range from green to blue, relief is strongly positive, the interference colours reach the fourth order.

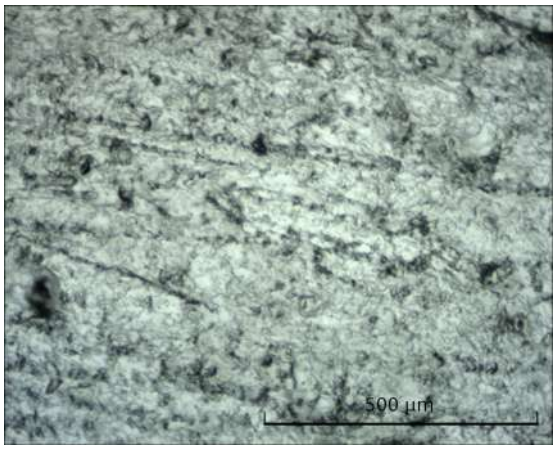

Figure 4: Sample MAN-ST-3, micrograph, parallel nicols.

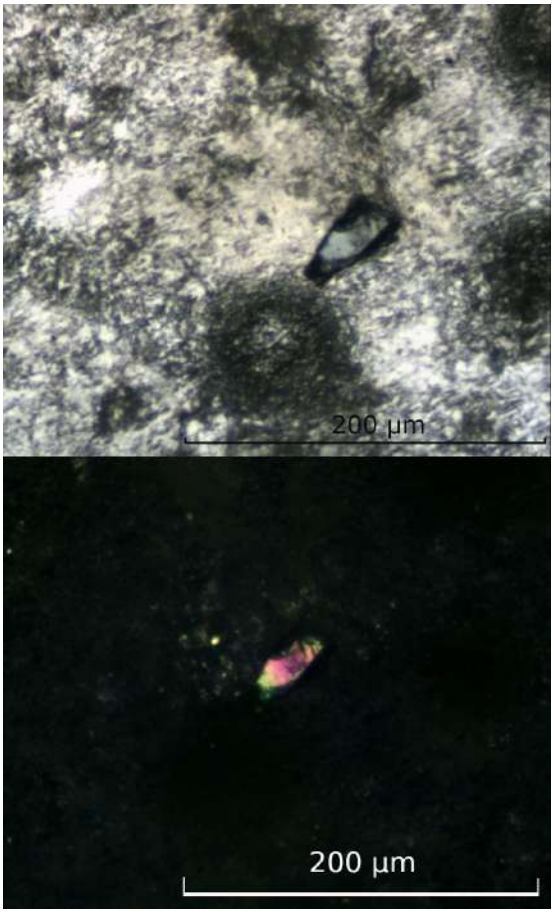

Figure 5: Sample MAN-ST-3, micrograph.Top: parallel nicols; bottom: crossed nicols.

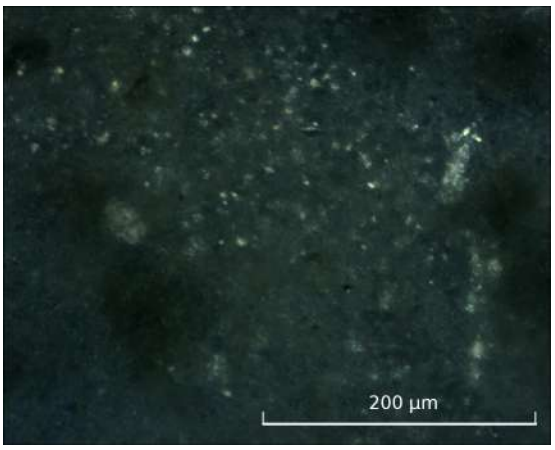

Figure 6: Sample MAN-ST-3, micrograph, crossed nicols.

Non Inventoried Plaque

Naked eye observation shows a medium sandy aggregate, milky white coloured. Under polarized light microscope gypsum is the main mineral component (sample man-st-4), constituting roughly thirty percent of the total volume while aggregates are prevailing.
Carbonates of calcite group, are both present as accessory components of the chalky binder (sparse microcrystals or microcrystalline cluster) and as part of the aggregates (figure 8). Aggregates are, also, constituted by quartz, plagioclase and chamotte.
Anatase microcrystals are observed (figure 8): colors range from green to blue, relief is strongly positive, the interference colours reach the fourth order.

Figure 7: Sample MAN-ST-3, micrograph, crossed nicols.

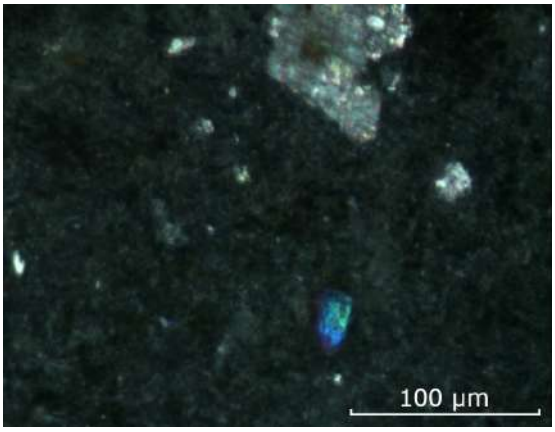

Figure 8: Sample MAN-ST-4, micrograph, crossed nicols.

Quarry of Gipso

Four sample coming from one quarry's stone have been studied. Under naked eye observation, the samples are compact, marmoreal, milky white with slight greyish and rare veins included. Observed under polarized light microscope, samples are mainly made up of gypsum which occurs in tabular microcrystals and includes rare anhydride crystals ($CaSO_4$).
Accessories minerals are carbonates of calcite group, present as microcrystalline clusters.
Anatase microcrystals are not rare: the color is intense blue or green-blue, the relief strongly positive, the high interference colour. The anatase appears to be of detrital

origin, being sometimes included in heterogeneous clusters (Figures 9, 10). Finally, the presence of traces of ferrous oxides and hydroxides is highlighted.

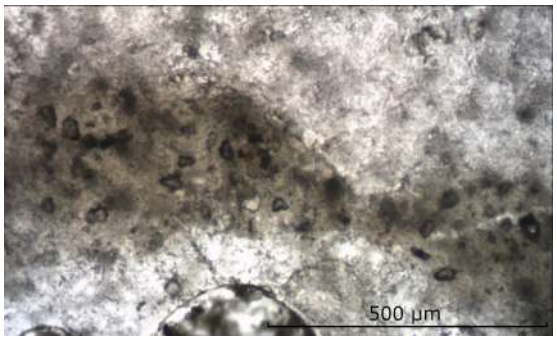

Figure 9: Sample Gipso-1, micrograph, parallel nicols.

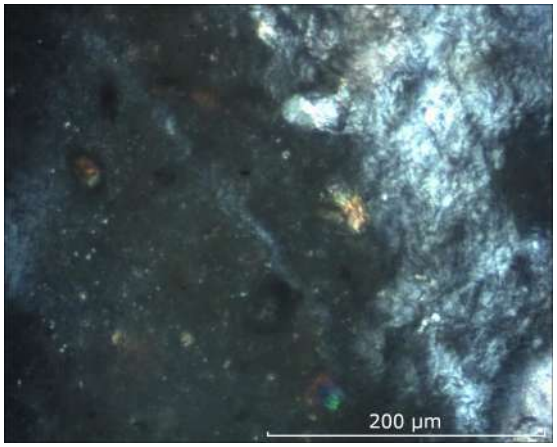

Figure 10: Sample Gipso-1, micrograph, crossed nicols.

Conclusions

The plaque from Terreti and the capital from Rossano showed great petrographic similarities. The stuccoes were made up using only the dehydrated quarry's gypsum without any addition, as was in use in medieval times. Accessories or traces component are to be considered as impurities coming from the raw material.
Stucco of the not inventoried plaque was, instead, made up using dehydrated gypsum (and, probably, little amount of lime putty) as binder of medium sandy agglomerates mainly constituted of quartz, plagioclase and chamotte. Every sample coming from these stuccoes contains little quantities of anatase's microcrystals that constitute the unique unusual mineralogical species detected.
Analysis of samples coming from the quarry of Gipso showed great compositional compatibility with the raw material used in these medieval stuccoes. In particular, anatase is always present, sometimes included in heterogeneous clusters suggesting a detrital origin.
The quarry of Gipso can be considered, therefore, the source of the gypsum used in both Terreti's and Rossano's churches.
Further analyses are being carried out in order to better characterize structure and composition of these materials.

References

[1] Dedić, Ž., Ilijanić, N. and Miko, S.: *A mineralogical and petrographic study of evaporites from the Mali Kukor, Vranjkovići, and Slane Stine deposits (Upper Permian, Dalmatia, Croatia)* Journal of the Croatian Geological Survey and the Croatian Geological Society, **71/1**, 19–28 (2018).

[2] Lipinsky, A.: *Stucchi medievali in Calabria* Almanacco calabrese (1963).

[3] Orsi, P.: *Placche in gesso decorate di arte arabonormanna da S. Maria di Terreti presso Reggio Calabria* Bollettino d'arte, Roma**15**, 546–562 (1921/22).

[4] Rende, P.: *Risorse minerarie ed attività estrattiva in alcune aree del Crotonese e della Sila in età antica* www.archiviostoricocrotone.it

Synthesis, Characterization and Photocatalytic Activity of Electrospun Zinc and/or Titanium Oxide Nanofibers for Methylene Blue Degradation

Z. Dahrouch[1,*], C. Triolo[2], S. Santangelo[2], S. Patanè[1]
[1] *Dipartimento di Scienze Matematiche e Informatiche, Scienze Fisiche e Scienze della Terra (MIFT), Università di Messina, 98166 Messina, Italy.*
[2] *Dipartimento di Ingegneria Civile, dell'Energia, dell'Ambiente e dei Materiali (DICEAM), Università "Mediterranea", 89122 Reggio Calabria, Italy*

*Corresponding Author email: zainabdahrouch@gmail.com

Abstract

Dispersion of Synthetic dyes in water is detrimental to the environment (inhibit transmission of light) and have negative effects on human health due to their toxic and non-biodegradable nature. Methylene blue (MB) is one of the most common dyes widely used in multiple fields. This study focuses on electrospun Ti and/or Zn oxide nanofibers (NFs) with specific architecture and surface used as photocatalysts for the MB degradation under UV irradiation. The thorough characterization of the elaborated photocatalysts shows the higher catalytic activity of the binary oxides compared to the ternary ones, and the better activity at lower load of the Anatase, as well as the possibility to be reused twice without any regeneration treatment with only 5.2% and 18.7% activity decrease after second and third use, respectively.

Keywords: Anatase, capture centers, Methylene blue dye, nanofibers, photodegradation, Zinc oxide.

Introduction

The growing of the world population along with the consequences of climate change and the increase in the level of water pollution due to anthropogenic factors are making the availability of drinking water insufficient to satisfy the rising demand.
Dispersion of the dyes in water and discharge into the nature represents a serious damage to the environment [1] and cause negative effects on human health [2–4]. Methylene blue (MB) is largely used in textile [5], pharmaceutical, cosmetics, printing, leather, and food industry [6]. In this study, we aim to use advanced oxidation processes "heterogeneous catalysis" to remove inorganic contaminants (dyes) from the water. We focus on semiconducting metal oxides: zinc oxide (ZnO) and titanium dioxide (TiO_2), with engineered architecture and surface characterized by chemical stability, non-toxicity, biocompatibility, and low-cost, for the photo assisted degradation of MB from aqueous solution under ultraviolet (UV) and visible (VIS) light irradiation [7, 8].
The photocatalysts (Ti and/or Zn oxide NFs) were prepared using electrospinning technique, followed by calcination and rapid cooling to produce porous NFs with capture centers at the boundaries between the oxide grains in order to reduce the probability of the e^-- h^+ recombination and increase the photocatalytic efficiency.

Experimental section

Synthesis of the photocatalysts

Sol–gel method was used to prepare the precursor solution. the appropriate amount of polyacrylonitrile polymer (PAN) was dissolved in dimethylformamide solvent (DMF) and agitated until the mixture became clear. Stoichiometric amounts of zinc acetate ($ZnAc_2$) and/or Titanium butoxide (TiBO) were added and magnetically stirred for 2 h at room temperature (RT). The homogeneous solution was then electrospun via a CH-01 Electrospinner 2.0 at 20 ± 1 °C and 40% relative air humidity. The calcination and cooling were operated at fast rates to create largely hollow NFs composed of linked nanograins [9]. Heating was carried out at 10 °C min^{-1}, the crucible was removed from the oven after 2 hours at 600°C and placed in an ice bath to cool quickly the sample and generate capture centers [10].

Characterization techniques

The resulting photocatalysts (NF) were thoroughly characterized using Scanning Electron Microscopy (SEM) and Atomic Force Microscopy (AFM) to investigate the texture and morphology, X-ray powder diffraction (XRPD) to identify the crystalline phase of the oxide, and the micro-Raman spectroscopy (MRS) to evaluate the crys-

tallinity degree, with spectra recorded from several random locations on each specimen and averaged to have a reliable picture of the entire sample in order to evaluate the spatial homogeneity of the samples [10, 11].

Evaluation of the Photocatalytic Activity and Assessment of the Optimal Load

The photocatalysts' activity towards the MB degradation was evaluated under UV irradiation, 350 nm lamp (3.54 eV) with 10 mW cm^{-2} power density. The appropriate amount of photocatalyst was dispersed in 3 mL of 15 µM MB solution and magnetically stirred for 1 hour in the dark to reach adsorption/desorption equilibrium between the photocatalyst and dye solution, then centrifuged (1000 rpm, 2 min) to separate the photocatalyst particles from the solution before performing zero-time measurement. The suspension was irradiated for several time intervals, between which the solution was centrifuged, and the optical absorbance was measured to calculate the remaining MB concentration. The measurements were also conducted on 3 mL of 15 µM MB without adding the catalyst (reference). Different amounts of the oxide NFs (0.3, 1.0, 2.0 and 3.0 mg, corresponding to loading of 0.10, 0.33, 0.66, and 1.00 mg mL^{-1}) were tested in order to evaluate the influence of the photocatalyst concentration on the photodegradation efficiency, we have also evaluated the reusability of the best performing photocatalyst under optimal load conditions without separation or washing process.

Results and discussion

Morphological and Textural Properties of the Photocatalysts

The results of SEM analysis are represented in fig.1. The variation of the Ti:Zn molar ratio reflects important modifications in the NF morphology (fig.1a-e), and diameters (insets of fig.1a-e) with the associated ranges and center values reported in fig.1f rising in the following order TZ01 < TZ10 < TZ11 < TZ21 < TZ12.

Crystalline Phase, Spatial Homogeneity, and Crystallinity Degree of the Oxide

The oxide's crystalline phase (fig.2a) strongly depends on the Ti:Zn molar ratio in the precursor solution. The average size of the crystallites was calculated using the most intense peak of the XRPD pattern, which ranged between 6.5 and 27.6 nm and increased in the order TZ11 < TZ12 < TZ21 < TZ01 < TZ10. MRS evaluated the spatial homogeneity of the samples as well as their crystallinity degree (fig.2b). The lack of variation in the peak's positions and relative intensities in the spectra obtained at different random locations in each sample (fig.3a,b,c,d) demonstrates the strong spatial uniformity of the generated photocatalysts. TZ11 sample has the lowest crystallinity degree, with no evident Raman peak and a strong photoluminescence (PL) background in its spectra (Figure 3c).

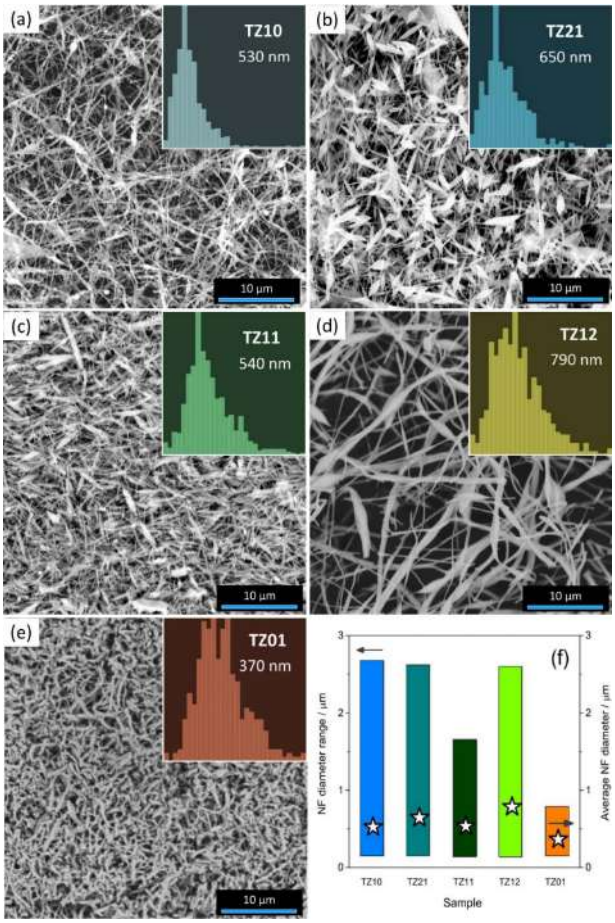

Figure 1: Results of the SEM analysis; (a–e) SEM micrographs of photocatalysts a) TZ10, b) TZ21, c) TZ11, d) TZ12, and e) TZ01 (insets: NF diameter distributions), f) NF diameter range and average value

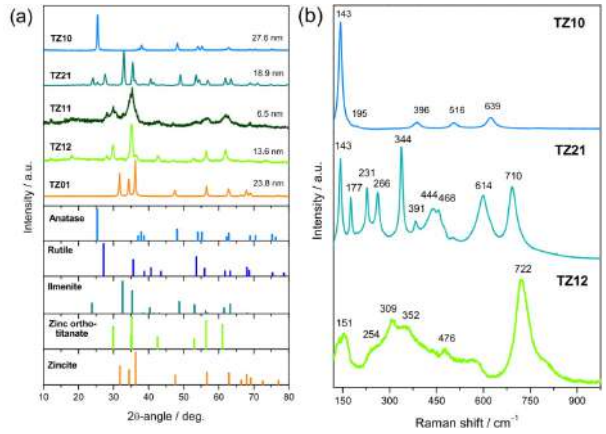

Figure 2: Results of a) XRPD and b) MRS analyses

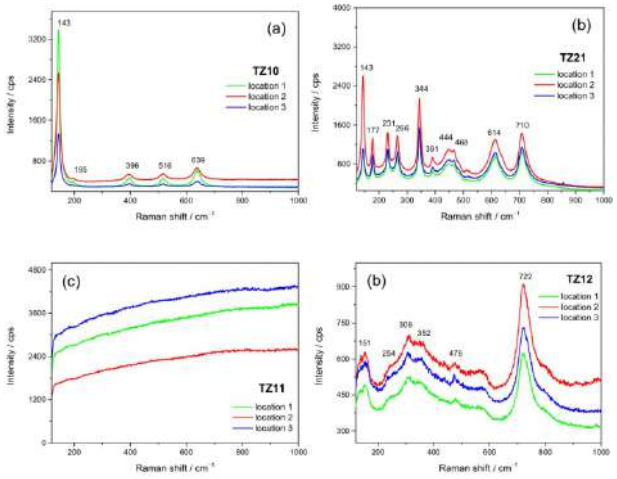

Figure 3: Micro-Raman spectra, as measured at different random locations, within each sample

Effect of the Variation of the Ti:Zn Molar Ratio in the Precursor Solution on the Photocatalytic activity of the Resulting Electrospun Oxide NFs

Photocatalytic activity was determined by dispersing the oxide NFs (0.33 mg mL^{-1}) in MB aqueous solution (15 µM) and measuring the absorbance after exposure to UV light (350 nm - 3.54 eV) for various time intervals. The decrease of the intensity of MB absorption bands with increasing irradiation time (fig.4a) indicates the gradual degradation of the cationic dye. fig.4b shows the evolution with time of dye degradation percentage D (%). Ti/Zn-oxide NFs exhibit lower activity compared to the TiO_2 and ZnO NFs. Sample TZ11 has the lowest degradation rate, with just 12% of MB degradation after 2 hours.

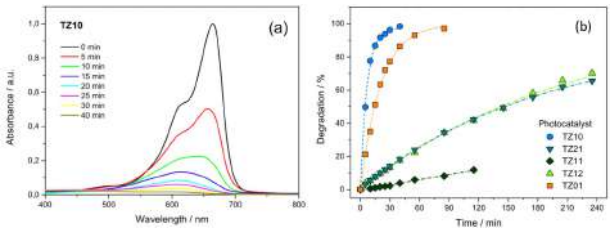

Figure 4: Time–evolution of the absorbance spectra of an aqueous MB solution with initial concentration of 15 µM and catalyst load of 0.33 mg mL^{-1}, under exposure to 350 nm UV radiation; the shown spectra a) refer to photocatalyst TZ10. b) Corresponding degradation rates as a function of time for photocatalysts TZ10, TZ21, TZ11, TZ12, and TZ01

Specific surface area

The photocatalytic activity greatly depends on the specific surface area: the larger the specific surface area, the greater the number of accessible sites for dye molecules adsorption, hence the higher the catalytic activity. To improve the nanomaterials surface area, we adopt chemical etching with strong base [12, 13]. For this purpose, a portion of sample TZ21 was immersed into 2.5 M solution of NaOH, after 2 h stirring at RT, the sample was washed with de-ionized water several times and dried overnight at 80 °C. The so-obtained material was coded as TZ21NaOH. Chemical etching treatment has no effect on the oxide's morphology or crystalline phase, it leads to the NF thinning and increase in average crystallite size and results in a significant increase in the surface area [13]. The results demonstrate that the activity of TZ21NaOH improves only to a limited extent compared to the un-etched one: 51% of the MB has been degraded using TZ21NaOH (against 42% for the untreated one), and indicate that the activity of the photocatalysts toward dye degradation is not limited by their specific surface area.

Visible light

We have evaluated the photocatalytic activity of the Ti/Zn-oxide NFs toward the MB degradation under VIS light, 550 nm (2.25 eV). The results of dispersing 0.33 mg mL^{-1} of TZ12 and TZ21NaOH in aqueous MB solution (15 µM) are shown in fig.5. TZ12 is almost photocatalytically inactive, D is <9% after 2 hours (VIS light does not have sufficient energy to activate the catalyst by creating the electron–hole pairs required for redox reactions with the species adsorbed on its surface [14, 15]). After exposure to higher energy radiation (3.54 eV), the activity of the electrospun NFs toward the MB degradation improves in the order TZ11< TZ12 ≈ TZ21< TZ01< TZ10, (fig.4b).

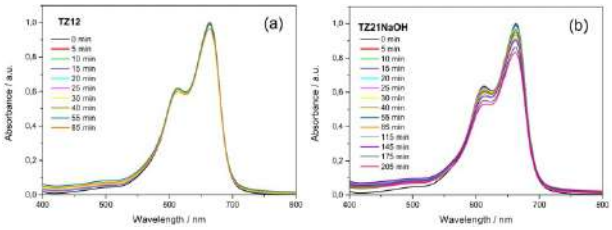

Figure 5: Absorbance spectra recorded at different time intervals on aqueous MB solution with initial 15 µM concentration, under exposure to 550 nm VIS radiation (power density: 7 mW cm^{-2}) with 0.33 mg mL^{-1} catalyst concentration. The spectra refer to photocatalysts a) TZ12 and b) TZ21NaOH

Energy Gap

The photocatalytic activity correlates with energy gap of the samples, the smaller the gap, the more active the catalyst. The photocatalysts energy gap increases in the order: TiO_2 (Anatase 3.20 eV. Rutile 3.00 eV [16, 17]) < ZnO (3.37 eV [18]) < $ZnTiO_3$ (3.67 eV [19]) < Zn_2TiO_4 (4.01 eV [20]).

Crystallinity degree

The photocatalytic activity strongly depends on the oxide's crystallinity degree, The larger the average crystallite size, the higher the MB degradation activity [21]. The oxides' crystalline degree increases in the order TZ11 < TZ12 < TZ21 < TZ01 < TZ10, it corresponds to the improvement in the activity of the oxide NFs (TZ11 < TZ12 ≈ TZ21 < TZ01 < TZ10).

Effect of the photocatalyst load

We focus on a-TiO_2 and ZnO NFs that outperform the Ti/Zn-oxide NFs and most state-of-art anatase and zinc oxide photocatalysts. The photocatalyst optimal load is critical for scaling up the process to an industrial scale, it has a significant influence on the economic aspects of the overall discoloration process. We have studied the effect of the photocatalyst load (0.10, 0.33, 0.66, or 1.00 mg mL^{-1}) on the dye degradation efficiency. fig.6a and 6b demonstrate the time–evolution of photocatalyst's degradation rates. TZ10 exhibits exceptional degradation performance.fig.6c shows the load dependency of the reaction rate constants for TZ10 and TZ01. For both cases small relative amount of photocatalyst allows the dye to be successfully degraded.

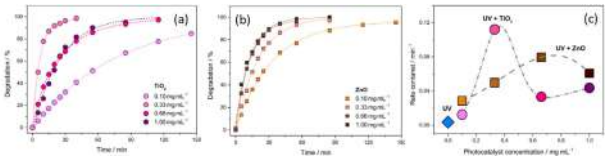

Figure 6: Degradation rates of photocatalysts a) TZ10 and b) TZ01 as a function of time. c) Concentration-dependence of the corresponding rate constants

a-TiO_2 NFs represents a sharp maximum at 0.33 mg mL^{-1}, while the optimal load value for ZnO NFs is 0.66 mg mL^{-1}. The improvement in the discoloration efficiency reflects the increase in the number of photocatalyst active sites [22, 23]. The worsening at higher loads may be due to higher concentration of the active material that favors the agglomeration of the catalyst NFs, and reduces the active surface area, it also reflects on greater turbidity of the catalyst suspension that hampers the light penetration. A greater activity with lower load approach is effective for scaling up the process to an industrial scale. a-TiO_2 NFs exhibit stronger activity toward MB degradation (k = 1.12 * $10^{-1} min^{-1}$) at a lower load (0.33 mg mL^{-1}) compared to ZnO NFs.

On the Best Performing Oxide NFs

Due to its architecture, a-TiO_2 NF at the optimal load (0.33 mg mL^{-1}) exhibits strong activity toward MB degradation (k = 1.12 10^{-1} min^{-1}, i.e., 6.72 h^{-1}) compared to the photocatalysis benchmark P25-TiO_2. To better understand its morphology, AFM measurements were carried out on the photocatalyst. The architecture of a-TiO_2 NFs consists of interconnected oxide nanoplatelets, polycrystalline and larger in diameter, made up of both thinner and thicker NPs compared to ZnO NFs [2]. High magnification SEM/EDX analysis provides further information regarding the photocatalyst TZ10. The defects at grain boundaries (oxide's oxygen-deficiency (5%)) act as traps for the photogenerated $e^- - h^+$ couples, reducing their recombination rate making them available for reduction and oxidation processes. We have investigated the stability and reusability of the best performing photocatalyst (TZ10) (0.33 mg mL^{-1} load), It can be reused without being separated from the reaction medium or being washed, and the dye's initial concentration (15 M) was restored by adding the appropriate amount of MB to the discolored solution. The activity of TiO_2 NFs decreased moderately.

Conclusion

The binary and ternary oxide NFs were prepared via electrospinning and subsequent calcination and evaluated as photocatalysts. The electrospinning technique provides a new perspective towards the sustainable large-scale manufacture of photocatalysts for the treatment of industry effluents. Due to their generated capture centers, the binary oxide NFs (ZnO-TiO_2) exhibit higher catalytic ac-

tivity towards dye degradation compared to the ternary oxides ($ZnTiO_3$-Zn_2TiO_4) (higher band gap and lower crystallinity). This result indicates that the activity of the photocatalysts toward dye degradation is not limited by the specific surface area. The optimal loads were determined to maximize the efficiency of the photocatalytic process, they are important for scaling up the process to an industrial scale. Using Anatase TiO_2 NFs, with lower catalyst load (0,33 mg ml^{-1}), the reaction rate constant (1,12 * 10^{-1}) exceeds the values reported for the state of art electrospun photocatalysts.

References

[1] Lellis, B. et al.: *Effects of textile dyes on health and the environment and bioremediation potential of living organisms.* Biotechnol. Res. Innov. 2019, **3**, 275–290.

[2] Fito, J., Abrham, S., Angassa, K: *"Adsorption of methylene blue from textile industrial wastewater onto activated carbon of Parthenium hysterophorus."* Int. J. Environ. Res. 2020, **14**, 501–511.

[3] Mahvi, A.H. et al.: *Mineralization and discoloration of textile wastewater by TiO2 nanoparticles* . Desalination 2009, **239**,309–316

[4] Balcha, A.; Yadav, O.P.; Dey, T.: *Photocatalytic degradation of methylene blue dye by zinc oxide nanoparticles obtained from precipitation and sol-gel methods* .Environ. Sci. Pollut. Res.2016, **23**,25485–25493.

[5] Zamel, D.; Khan, A.U.: *Bacterial immobilization on cellulose acetate-based nanofibers for methylene blue removal from wastewater: Mini-review.* Inorg. Chem. Commun.2021, **131**, 108766.

[6] *Methylene Blue Market Size, Industry Analysis Report, Regional Outlook, Application Development Potential, Price Trends, Competitive Market Share & Forecast*, 2021–2027. Available online: https://www.gminsights.com/industry-analysis/methyleneblue-market (accessed on 30 July 2021).

[7] Zheng, F.; Zhu, Z.: *Flexible, freestanding, and functional SiO2 nanofibrous mat for dye-sensitized solar cell and photocatalytic dye degradation.* ACS Appl.Nano Mater. 2018, **1**,1141–1149.

[8] Ramar, V.; Balasubramanian, K.: *Reduced Graphene Oxide/WO3 Nanorod Composites for Photocatalytic Degradation of Methylene Blue under Sunlight Irradiation*.ACS Appl. Nano Mater.2021.

[9] Ponti, A. et al.: *Structure, Defects, and Magnetism of Electrospun Hematite Nanofibers Silica-Coated by Atomic Layer Deposition* . Langmuir 2020, **36**,1305–1319.

[10] Pantò, F. et al.: *Photocatalytic degradation of methylene blue dye by porous zinc oxide nanofibers prepared via electrospinning: When defects become merits* .Appl. Surf. Sci. 2021, **557**,149830.

[11] Santangelo, S. et al.: *Effect of calcium-and/or aluminumincorporation on morphological, structural and photoluminescence properties of electro-spun zinc oxide fibers* . Mater. Res. Bull.2017, **92**,9–18

[12] Rafidah, J.et al.: *Effect of sodium hydroxide pretreatment on chemical composition of treated acacia mangium using response surface methodology* . J. Trop. For. Sci. 2020, **32**,391–401

[13] He, G. et al.: *Electrospun anatase-phase TiO2 nanofibers with different morphological structures and specific surface areas* . J. Colloid Interface Sci. 2013, **398**,103–111.

[14] Kumar, K. et al.: *Photocatalytic, optical and magnetic properties of Fe-doped ZnO nanoparticles prepared by chemical route* . J. Alloys Compd. 2014, **588**, 681–689.

[15] Zhang, Y. et al.: *Enhanced photocatalytic activity of iron doped zinc oxide nanowires for water decontamination* . Surf. Coat. Technol. 2013, **217**, 119–123.

[16] Someswararao, M.V. et al.: *Electrospun composite nanofibers prepared by varying concentrations of TiO2/ZnO solutions for photocatalytic applications* . J. Photochem. Photobiol. A 2021, **6**,100016

[17] Choudhury, B. et al.: *Narrowing of band gap and effective charge carrier separation in oxygen deficient TiO2 nanotubes with improved visible light photocatalytic activity* .J. Colloid Interface Sci. 2016, **465**,1–10.

[18] Montenegro, D.N. et al.: *Non-radiative recombination centres in catalyst-free ZnO nanorods grown by atmospheric-metal organic chemical vapour deposition* . J. Phys. D Appl. Phys. 2013, **46**,235302.

[19] Ranjith, K.S.; Uyar, T.: *Conscientious design of Zn-S/Ti-N layer by transformation of ZnTiO3 on electrospun ZnTiO3@ TiO2 nanofibers: Stability and reusable photocatalytic performance under visible irradiation* . ACS Sustain. Chem. Eng. 2018, **6**, 12980–12992.

[20] Sarkar, K. et al.: *Spray-deposited zinc titanate films obtained via sol–gel synthesis for application in dye-sensitized solar cells.* . J. Mater. Chem. A 2014, **2**, 15008–15014.

[21] Mekasuwandumrong, O. et al.: *Effects of Synthesis Conditions and Annealing Post Treatment on the Photocatalytic Activities of ZnO Nanoparticles in the Degradation of Methylene Blue Dye.* . Chem. Eng. J. 2010, **164**,77–84.

[22] Al-Shamali, S.S.: *Photocatalytic degradation of methylene blue in the presence of TiO2 catalyst assisted solar radiation* . Aust. J. Basic Appl. Sci. 2013, **7**,172–176

[23] Ali, A.S. et al.: *Photo-Fenton degradation of methylene blue using hematite-enriched slag under visible light* .J. Radioanal. Nucl. Chem. 2020, **325**, 537–549.

Seminari del Dottorato di Ricerca in Fisica

(Svolti nel 2021)

SEMINARI DEL DOTTORATO DI RICERCA IN FISICA

DOTTORATO DI RICERCA IN FISICA DELL'UNIVERSITÀ DEGLI STUDI DI MESSINA

28 Gennaio 2021, ore 15.30, Webinar su Piattaforma informatica *Microsoft Teams*

Structuring light with extreme metamaterials

Dr. Nader Engheta
University of Pennsylvania, Philadelphia, USA

Abstract

Materials are often used to manipulate waves. Metamaterials have provided far- reaching possibilities in achieving "extremes" in such wave-matter interaction. Various exciting functionalities have been achieved in exploiting metamaterials and metasurfaces in nanophotonics and nano-optics. We have been exploring how extreme metamaterials can give us new platforms in metaphotonics for exploiting waves to do certain useful functions for us. Several research topics are being investigated in my group. In one of these programs, we have been developing metastructure platforms that can perform analog computation such as solving integral and differential equations and inverting matrices with waves as waves interact with them. Such "metamaterial machines" can function as wave-based, near-speed-of-light analog computing machines, suitable for micro- and nanoscale integration. Another research program is the near-zero-index (NZI) media in which the effective relative permittivity and/or relative permeability can attain near-zero values around the operating frequencies of interest. In such NZI structures, effective wavelength "stretches", and consequently numerous unprecedented wave phenomena emerge. In this talk, I will present some of our ongoing work on extreme material platforms for metaphotonics, and will forecast possible future research directions in these paradigms.

⋆⋆⋆⋆⋆

DOTTORATO DI RICERCA IN FISICA DELL'UNIVERSITÀ DEGLI STUDI DI MESSINA

17 Febbraio 2021 & 19 Febbraio 2021, ore 14.15 - 16.45, Webinar su Piattaforma informatica *Microsoft Teams*

VISPEC online

12 febbraio 2021

14.15: Introduzione dei lavori

14.30: Wavelength dependence of the enhancement in SERS substrates
Roberto Pilot (Università di Padova e Consorzio INSTM)

15:15: Label-free SERS and metabolomics
Alois Bonifacio (Università di Trieste)

16:00: SERS methodologies and practical considerations for analyses in cultural heritage
Brenda Doherty (CNR Perugia)

19 febbraio 2021

14:15: Introduzione dei lavori

14:30: Recent advances in Synchrotron UV Resonance Raman spectroscopy for exploring small and large molecules
Barbara Rossi (Elettra-Sincrotrone Trieste)

15:15: Dry-state SERS for the "in-situ" identification of natural textile dyes
Margherita Longoni (Università di Milano)

16:00: Manipulation of optical nanoantennas for nanospectroscopy (SERS) and nanoscale imaging (TERS)
Pietro Gucciardi (IPCF CNR Messina)

16:45: Conclusioni

Abstract

VISPEC online vuole essere un'occasione per unire quanti sono interessati alla spettroscopia vibrazionale, nelle sue varie forme e applicazioni. VISPEC online rappresenta un ponte di collegamento ideale tra l'ultimo convegno VISPEC2019 tenutosi a Brescia e il prossimo convegno VISPEC che si terrà a Perugia. Attraverso questa iniziativa desideriamo stimolare la discussione scientifica sulla spettroscopia vibrazionale, favorire le collaborazioni, e accogliere chi sia interessato ad avvicinarsi all'uso di queste tecniche.

⋆ ⋆ ⋆ ⋆ ⋆

Dottorato di Ricerca in Fisica dell'Università degli Studi di Messina

10 Febbraio 2021, ore 15.30, Webinar su Piattaforma informatica *Microsoft Teams*

Self-assembled nanostructures for applications in plasmonic metamaterials

Dott.ssa Rossella Grillo
Dipartimento DIIES, Università Mediterranea di Reggio Calabria

Abstract

Spherical organization of metallic nanoparticles, also known as core-shell clusters, have stimulated the interest of the metamaterials community, both from a theoretical 1 , and experimental2 point of view. The main advantage of such arrangements involves their highly tunable optical properties and it has been proposed that they will facilitate improvements towards materials with double negative properties at optical frequencies. This talk involves the design, fabrication and characterization of metamaterials based on meta-atoms and its assemblies. The approach starts with the bottom-up preparation of nanoresonators, which consist in core-shell structures made of plasmonic nanoparticles covering a dielectric core. The coupling between the plasmonic units leads to new plasmon resonances that have a magnetic dipole character. The next step involves the meta-atoms organization on surfaces. Highly ordered monolayers of core-shell clusters over large area were obtained via a combination of blade coating deposition and electrostatic self- assembly. The structural and optical properties of such complex plasmonic core-shell clusters array are investigated and compared to rigorous simulations.

⋆ ⋆ ⋆ ⋆ ⋆

Dottorato di Ricerca in Fisica dell'Università degli Studi di Messina

4 Marzo 2021, ore 15.30, Webinar su Piattaforma informatica *Microsoft Teams*

Correlating topography and elastic properties of Elastin-Like Polypeptide scaffolds probed at the nanoscale using Intermodulation-AFM

Dr. Nisha Rani Agarwal
Nano-imaging and Spectroscopy Laboratory, University of Ontario Institute of Technology, Oshawa, Canada

Abstract

Most phenomena or interactions whether they be physical, chemical or biological in nature take place at the nanoscale. Hence, materials under study should be characterized for various properties such as structural, mechanical, optical and chemical at high resolution. Not many techniques are capable of nanoscale measurements. Development of novel techniques for this purpose is possible by employing recent advances in technology. One such advancement is the development of Multifrequency Lock-in Amplifier (MLA) that outperforms conventional lock-in amplifiers in many ways. This MLA is able to simultaneously detect more than 20 close by frequencies with no interference from each other. Thus, making it possible for incorporating MLA to develop new techniques. In my talk, a novel method has been developed in order to measure the elastic property in combination with structural property at the nanoscale which is achieved by intermodulation Atomic Force Microscopy (AFM) while driving the tip at two frequencies. This results in generation of other frequencies from which the force curve can be reconstructed to be fitted with various force models in order to

extract the elastic values. A very important consideration to be made is that the handling of force curves and data processing not only depends on the surface properties of the sample but also depends on the morphology of the samples and on the tip properties. ImAFM is particularly of interest for measuring visco-elastic properties i.e probing nanoscale properties of biomaterials.

⋆⋆⋆⋆⋆

Dottorato di Ricerca in Fisica dell'Università degli Studi di Messina

31 Marzo 2021, ore 16.00, Webinar su Piattaforma informatica *Microsoft Teams*

Nanostructured films of two-dimensional materials: Electronic transport, printed heterojunctions and wearable electronics

Dr. Felice Torrisi
Molecular Science Research Hub, Imperial College London, UK & Dipartimento di Fisica e Astronomia, Università di Catania, Italy

Abstract

Wearable electronics is a primary technology to enable remote healthcare provision, which is highly important in a post-pandemic society. Graphene and related 2D materials (GRMs) hold a great potential for wearable electronics for their novel electrical and optical properties. In particular low temperature production and deposition of nanostructured GRM films (fig.1a) from GRM-based solutions is extremely attractive for printed flexible and wearable electronics [1,2]. GRM-based inks enable a large range of printed device and integration options, such as digital, lithographic printing and roll-to-roll coating, which are ideal to deposit nanostructured GRM films. Liquid Phase Exfoliation (LPE) of bulk precursor layered materials (such as graphite, MoS_2 crystals, etc.) is a scalable approach ideally suited to produce inks. However, the low-yield of the LPE process, the absence of deposition parameters and the undetermined transport properties of the GRMs have limited the full scale applications of these materials in printed and wearable electronics. I will give a brief overview on the development of high-yield, cost-effective and large-scale production techniques for GRM-based inks, and the portfolio of reproducible deposition processes enabling GRM-based printable devices on flexible and textile substrates (fig.1b) [3]. Then I will show how careful tuning of the flakes- substrate surface interaction and GRM deposition process enables hybrid heterojunctions from 2D materials (fig.1c), achieving mobility > 100 cm^2 V^{-1} s^{-1} at room temperature [4]. Finally, I will demonstrate how unveiling of the electronic transport in printed networks of 2D materials paves the way to high-performance inkjet printed integrated circuits of 2D semiconductors, such as MoS_2 [5] (fig.1d).

[1] F. Torrisi et al. ACS Nano, 6, 4, 2992 (2012)

[2] F. Torrisi & J. N. Coleman Nature Nanotechnol. 9, 10, 738, (2014)

[3] S. Qiang et al. Nanoscale 11 (20), 9912-9919, (2019)

[4] T. Carey et al. Nature Commun., DOI : 10.1038/s41467-017-01210-2, (2017)

[5] T. Carey et al. arXiv:2011.12359 (2020)

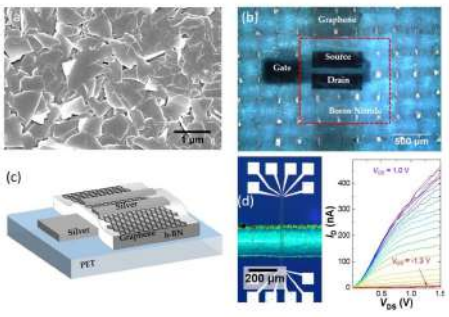

Figure 1: a) Nanostructured GRM films, b) GRM-based hybrid heterojunction on textile, c) Inkjet printed GRM heterojunction layout, d) Printer MoS_2 field effect transistor and output characteristics.

⋆⋆⋆⋆⋆

Dottorato di Ricerca in Fisica dell'Università degli Studi di Messina

21 Aprile 2021, ore 16.00, Webinar su Piattaforma informatica *Microsoft Teams*

From a catalogue of metastable nanoalloys to the study of the structure-property relationship for nanomedicine, plasmonics or catalysis

Prof. Vincenzo Amendola
Dipartimento di Scienze Chimiche, Università di Padova.

Abstract

Alloy nanoparticles containing noble and transition metals are appealing for a series of applications and fundamental studies in catalysis, optics and nanomedicine. However, the thermodynamics is unfavorable to the largest part of these alloys, which can be obtained only by non-equilibrium routes. To this end, laser ablation in liquid (LAL) is a powerful technique for the synthesis of metal alloys, also with thermodynamically forbidden composition. By mastering the LAL synthesis, a whole catalogue of alloys is accessible for fundamental studies about the structural motifs adopted by elements frozen at the nanoscale and the consequent set of physical-chemical properties. The insights on the structure-properties relation provided the basis for further optimization of the nanoalloys for specific applications. The cases of Y alloys designed to climb the volcano plot for oxygen reduction catalysis, Ag alloys where the coexistence of magnetic and plasmonic properties is maximized, and noble metal alloys acting as 4-D multimodal contrast agents with enhanced clearance from the body will be discussed. Though not yet optimal for real- world applications, these nanosystems provided clear directions for further development of the intended functionalities, which are the subject of ongoing efforts. Hence, this is a general demonstration of the range of innovative results and functional optimization expected by the synergy between LAL synthesis, structural modelling, and experimental verification of functional properties in nonequilibrium nanoalloys.

⋆⋆⋆⋆⋆

Dottorato di Ricerca in Fisica dell'Università degli Studi di Messina

6 Maggio 2021, ore 16.00, Webinar su Piattaforma informatica *Microsoft Teams*

Machine learning against epidemics.

Prof. Giovanni Volpe
Department of Physics, University of Gothenburg, Sweden

Abstract

Containment of epidemic outbreaks entails great societal and economic costs. Cost- effective containment strategies rely on efficiently identifying infected individuals, making the best possible use of the available testing resources. Therefore, quickly identifying the optimal testing strategy is of critical importance. Here, we demonstrate that machine learning can be used to identify which individuals are most beneficial to test, automatically and dynamically adapting the testing strategy to the characteristics of the disease outbreak. Specifically, we simulate an outbreak using the archetypal susceptible- infectious-recovered (SIR) model and we use data about the first confirmed cases to train a neural network that learns to make predictions about the rest of the population. Using these predictions, we manage to contain the outbreak more effectively and more quickly than with standard approaches. Furthermore, we demonstrate how this method can be used also when there is a possibility of reinfection (SIRS model) to efficiently eradicate an endemic disease.

⋆⋆⋆⋆⋆

Dottorato di Ricerca in Fisica dell'Università degli Studi di Messina

20 Maggio 2021, ore 16.30, Webinar su Piattaforma informatica *Microsoft Teams*

Spontaneous emission, superradiance and subradiance of atoms in dynamical environments

Prof.ssa Lucia Rizzuto
Dip. di Fisica e Chimica – Emilio Segrè, Università degli Studi di Palermo & INFN, Laboratori Nazionali del Sud, Catania

Abstract

It is well known that a structured environment such as a cavity, a mirror or a photonic crystal, can strongly affect radiative properties of atomic systems, for example the spontaneous emission process by single atoms or the cooperative spontaneous emission (superradiance or subradiance) by multi-atom systems. Recently, much interest has been devoted in investigating the effects of a dynamical (i.e. time-dependent) environment (for example oscillating cavities, dynamical mirrors or dynamical photonic crystals, that is photonic crystals whose dielectric properties change on time) on radiative properties of atoms or molecules placed nearby. These investigations are also related to the so-called Dynamical Casimir effect. In this talk, we discuss how the adiabatic motion of a perfectly conducting plate can affect the spontaneous emission of an atom nearby, or the cooperative spontaneous emission of two identical atoms, prepared in a correlated (symmetric or antisymmetric) state, placed near the oscillating mirror. We first consider one atom, prepared in an excited state, and interacting with the quantum electromagnetic field in the vacuum state, in the presence of an oscillating perfectly reflecting mirror. We suppose that the perfectly reflecting plate oscillates adiabatically. Using perturbation theory, we evaluate the transition rate to the ground-state and the emitted spectrum. We show that the presence of the oscillating mirror changes the physical features of the spontaneous emission by the atom, in particular the emitted spectrum. In particular, we find the appearance of two lateral peaks in the spectrum separated from the central peak by the modulation frequency, not present in the case of a static mirror, due to the presence of the modulated environment [1]. Also, we briefly discuss the spontaneous emission of an excited atom placed inside a photonic crystal with time-dependent properties (dynamical photonic crystal) [2]. We finally consider two identical atoms, one in the ground state and the other in the excited state, prepared in a correlated (symmetric or antisymmetric) *Bell-type* state, and placed near an oscillating mirror. We evaluate the transition rate to the collective ground state of the two-atom system in both cases of the superradiant (symmetric) and subradiant (antisymmetric) state. We show that the presence of the oscillating mirror significantly affects the physical features of the superradiant and subradiant emission by the two correlated atoms, that can be enhanced or inhibited compared to the case of atoms in vacuum space or near a static boundary [3]. These results indicate that dynamical environments can be exploited to manipulate and control the radiative properties of atoms or molecules embedded in.

[1] A. Ferreri, M. Domina, L. Rizzuto, R. Passante, Symmetry, 11 1384 (2019)

[2] G. Calajò, L. Rizzuto, R. Passante, Phys. Rev. A, 96 023802 (2017)

[3] M. Reina, A. Ferreri, M. Domina, A. Noto, G. Fiscelli, L. Rizzuto, R. Passante, Phys. Rev. A 103, 033710 (2021)

⋆⋆⋆⋆⋆

Dottorato di Ricerca in Fisica dell'Università degli Studi di Messina

20 Maggio - 21 Maggio - 22 Giugno - 24 Giugno 2021, Webinars su Piattaforma informatica *Microsoft Teams*

Webinars nell'ambito della collaborazione tra SIFI e UNIME

Ciclo di Webinars

20 Maggio 2021
Dott. L. Inferrera
15.00 – 16:00: Anatomy and Physiology of the eye

21 Maggio 2021
Dott. G. Oliviero
15.00 – 16:00: Cataract Surgery and Refractive Disorders

22 Giugno 2021

Ph.D. Maria Cristina Curatolo
15.00 – 16:00: Intraocular Lenses: latest technologies

24 Giugno 2021
Ph.D. Junzhong Liang
17.00 – 18:00 : Wavefront optic applied to Intraocula Lenses

Abstract

Many applications in quantum technologies, such as quantum cryptography or optical quantum information processing, require light sources with a precise number of photons. Photon (phonon) blockade is the quantum phenomenon that occurs in a driven nonlinear system, in which a system cannot emit more than one photon each time. These effects are described by the sub-Poissonian excitation-number statistics. In this talk, we describe unconventional photon blockade in a hybrid system which is comprised of photonic and phononic mode such that a combined photon-phonon mode exhibits sub-Poissonian statistics while each mode,if analyzed separately, exhibits super-Poissonian statistics. Moreover, I will show that it is possible to achieve photon blockade in the driven cavity without an atom or any other kind of nonlinearity, but instead coupled to a nonlinear (i.e., squeezed) reservoir [1].

[1] A. Kowalewska-Kudlaszyk, S. I. Abo, G. Chimczak, J. Perina, F. Nori, and A. Miranowicz, Twophoton blockade and photon-induced tunneling generated by squeezing, Physical Review A 100 (2019), 10.1103/physreva.100.053857.

⋆⋆⋆⋆⋆

Dottorato di Ricerca in Fisica dell'Università degli Studi di Messina

6 Dicembre 2021, ore 15.30, Webinar su Piattaforma informatica *Microsoft Teams*

Sound vs Light: the story of a catch up

Prof. Gianluca Memoli
School of Engineering and Informatics, University of Sussex, UK

Abstract

Centuries of development have given us multiple tools for the precise delivery of light. We call them lenses, mirrors or holographic filters...and they are so common that each of us has an advanced light control system in his/her pocket. But there is no such a thing for sound. Localised sound delivery still requires headphones. Acoustic lenses are bulky and therefore not usable in practice. Or, are they? In this talk I will describe how metamaterials are helping acoustics to bridge this technology gap, building on interference and diffraction. We will look together at different applications, including manipulation, and discuss how metamaterials are playing a key role in them.

Premi e Riconoscimenti

Premio della Società Italiana di Fisica (SIF) per la seconda migliore comunicazione della Sezione 1: Fisica nucleare e subnucleare al Congresso Nazionale SIF 2021 al Dott. Fabio Risitano, dottore di Ricerca in Fisica del XXXVI ciclo

Il Dott. Fabio Risitano, dottore di Ricerca in Fisica del XXXVI ciclo, Tutor. Prof.ssa Marina Trimarchi, ha vinto il Premio della Società Italiana di Fisica (SIF) per la seconda migliore comunicazione della Sezione 1: Fisica nucleare e subnucleare al Congresso Nazionale SIF 2021, dal titolo "Studio simulativo di produzione di fasci radioattivi presso FRAISE (LNS)".

https://www.sif.it/attivita/congresso/107/comunicazioni

⋆⋆⋆⋆⋆

Organizzazione del Dottorato di Ricerca in Fisica

Coordinatore:
Prof.ssa Vincenza Crupi

Direttore del Dipartimento di Scienze Matematiche e Informatiche, Scienze Fisiche e Scienze della Terra - Università degli Studi di Messina:
Prof. Domenico Majolino

Segretaria del Corso di Dottorato di Ricerca in Fisica:
Dott.ssa Paola Donato

Unità di staff della segreteria del Corso di Dottorato di Ricerca in Fisica:
Sig.ra Alessandra Spano'

Delegato per il sito Web del Dottorato di Ricerca in Fisica:
Prof. Alessandro Sergi

OFFERTA FORMATIVA CICLO XXXVII

Anno Accademico 2021-2022

5 posti con borsa su fondi di Ateneo UNIME + 1 posto senza borsa. Sono state inoltre assegnate n. 2 borse aggiuntive a valere sul PON "Ricerca e Innovazione" 2014-2020 Azioni IV.4 "Dottorati e contratti di ricerca su tematiche dell'innovazione" e Azione IV.5 "Dottorati su tematiche Green".

Attività di formazione

Linguistica: Si prevedono attività formative in lingua Inglese finalizzate innanzitutto a facilitare la redazione della tesi finale in inglese e ad incentivare le molteplici collaborazioni scientifiche internazionali peculiari del percorso di dottorato. Tali abilità linguistiche inoltre favoriranno l'esposizione dei risultati della ricerca sia in forma orale (congressi/scuole internazionali) che scritta (stesura di eventuali progetti di ricerca internazionali e prodotti della ricerca).

Informatica: Si prevedono attività formative di inizializzazione informatica presso il nostro Ateneo, finalizzate all'acquisizione di abilità nell'utilizzo di linguaggi di scrittura come il sistema LATEX per la preparazione di testi scientifici, nell'utilizzo dell'architettura GRID e di calcolo parallelo per l'elaborazione di grandi set di dati.

Gestione della ricerca, della conoscenza dei sistemi di ricerca e dei sistemi di finanziamento: Si prevede una serie di seminari specialistici da parte di esperti del settore inerenti la gestione della ricerca a livello nazionale ed internazionale, il coordinamento di gruppi di ricercatori e le modalità di ricerca dei canali di finanziamento nazionali ed internazionali al fine di fornire ai dottorandi le giuste abilità per la compilazione di progetti di finanziamento anche internazionali.

Valorizzazione dei risultati della ricerca e della proprietà intellettuale: Si prevedono seminari specialistici inerenti la valorizzazione dei risultati della ricerca e della proprietà intellettuale. Saranno svolti da docenti coinvolti in esperienze di ricerca nazionale ed internazionale, nonché da personale docente e/o funzionari delle strutture di Ateneo operante nel campo dell'attrazione di risorse e della valorizzazione della proprietà intellettuale. Tale attività favorirà la partecipazione dei dottorandi a seminari ed eventi culturali sia in Italia che all'estero.

Offerta formativa e articolazione in CFU

L'impegno complessivo è di 180 crediti formativi, distribuiti uniformemente sui tre anni di corso (60 CFU per ogni singolo anno). L'attività formativa prevede durante il I anno l'acquisizione di 22 CFU grazie alla frequenza di insegnamenti (lezioni frontali) tenuti da docenti del collegio di Dottorato di Ricerca in Fisica dell'Università degli Studi di Messina. Ogni CFU equivale a 6 ore di lezioni frontali. Il restante numero di crediti formativi necessari per il raggiungimento dei 60 CFU (38 CFU) viene attribuito dal Collegio dei Docenti alle attività connesse alla ricerca scientifica specifica dei singoli dottorandi, incluse le attività di partecipazione a seminari, congressi, scuole, soggiorni all'estero, alla redazione in lingua inglese, nel volume del report annuale di dottorato (Activity Report), dell'attività di ricerca svolta e ad attività a scelta libera. I 60 CFU del II e III anno, saranno acquisiti con attività formative connesse alla ricerca scientifica specifica dei singoli dottorandi incluse le partecipazioni a congressi, scuole, soggiorni all'estero su territorio nazionale e internazionale, alla redazione in lingua inglese, nel volume del report annuale di dottorato (Activity Report), dell'attività di ricerca svolta e, alla redazione della tesi finale di dottorato durante il III anno. Anche per il II e III anno, l'acquisizione dei CFU annuali potrà essere completata con attività a scelta libera.

Nello specifico, i crediti formativi sono così distribuiti:

I ANNO

- Cicli di lezioni (n. 22 CFU).
- Attività individuale di ricerca da discutere per il passaggio all'anno successivo al primo (n. 23 CFU).
- Redazione in lingua inglese dell'attività di ricerca svolta nel volume del report annuale del DdR in Fisica (Activity Report, ISSN 2038-5889) (n. CFU 10)
- Partecipazione a seminari, congressi, scuole, soggiorni all'estero e in Italia (n. max CFU 8).
- Attività a scelta libera (n. max CFU 8).

II ANNO

- Attività individuale di ricerca da discutere per il passaggio all'anno successivo al secondo (n. 25 CFU).
- Redazione in lingua inglese dell'attività di ricerca svolta nel volume del report annuale del DdR in Fisica (Activity Report, ISSN 2038-5889) (n. CFU 10).
- Partecipazione a seminari, congressi, scuole, soggiorni all'estero e in Italia, presentazione di contributi sotto forma di abstract, poster o come relatore (n. max CFU 23).
- Attività a scelta libera (n. max CFU 8).

III ANNO

- Stesura tesi e relativa discussione (n. CFU 35).
- Attività individuale di ricerca da discutere per l'ammissione all'esame finale (n. 23 CFU).
- Attività a scelta libera (n. max CFU 8).

Legenda per l'attribuzione dei crediti alle attività formative a scelta

- Soggiorno di ricerca all'estero di tipo Erasmus o di altro tipo del dottorando, sarà valutata dal consiglio dei docenti ai fini dell'attribuzione dei crediti formativi e della sua quantificazione
- La frequenza di corsi di specializzazione o di attività formative certificabili connesse con l'attività formativa e di ricerca del dottorando sarà valutata dal consiglio dei docenti ai fini dell'attribuzione dei crediti formativi e della sua quantificazione
- La pubblicazione di articoli scientifici su rivista, di saggi in volume, di capitoli di libro o di monografia, per la quale farà fede la data di accettazione del contributo o la pubblicazione del volume, sarà valutata dal consiglio dei docenti ai fini dell'attribuzione dei crediti formativi e della sua quantificazione
- L'attività di tutorato degli studenti nei corsi di Laurea e Laurea magistrale dell'Università Messina sarà valutata dal consiglio dei docenti ai fini dell'attribuzione dei crediti formativi e della sua quantificazione
- L'attività di didattica integrativa sarà valutata dal consiglio dei docenti ai fini dell'attribuzione dei crediti formativi e della sua quantificazione

  Si precisa che le attività formative a scelta non possono superare la totalità di 8 CFU per ogni singolo anno di corso. I crediti formativi in esubero, dunque, non saranno computati ai fini del raggiungimento della soglia annua.

Carattere Internazionale del Dottorato

Principali Atenei e centri di ricerca internazionali con i quali il collegio mantiene collaborazioni di ricerca:

- CERN, Ginevra (CH)
- Academy of Science of Czech Republic (ASCR) and PALS Laboratory of Prague (Repubblica Ceca)
- Rutherford Appleton Laboratory, Didcot-Oxfordshire (UK)
- Budapest Neutron Centre, Budapest (Ungheria)
- Riken Cluster for Pioneering Research, Wako, Saitama (Giappone)
- University of Bonn, Bonn (Germania)
- University of Novosibirsk, Novosibirsk (Russia)
- Budker Institute for Nuclear Physiscs, Novosibirsk (Russia)
- Institut Laue-Langevin (ILL) Grenoble (Fr)
- IPPLM, Warsaw (PL)
- Military University of Technology (MUT), Warsaw (PL)

OFFERTA FORMATIVA CICLO XXXVI

Anno Accademico 2020-2021

6 Posti ciascuno con borsa di studio

Una delle 6 borse di studio è stata assegnata su progetto finanziato nell'ambito del Programma Operativo Complementare Ricerca e Innovazione 2014 – 2020 (POC R&I), Asse Tematico 1 "Capitale Umano" – Azione I.1 "Dottorati Innovativi con caratterizzazione industriale"

Attività di formazione

Linguistica: Si prevedono attività formative in lingua Inglese finalizzate innanzitutto a facilitare la redazione della tesi finale in inglese e ad incentivare le molteplici collaborazioni scientifiche internazionali peculiari del percorso di dottorato. Tali abilità linguistiche inoltre favoriranno l'esposizione dei risultati della ricerca sia in forma orale (congressi/scuole internazionali) che scritta (stesura di eventuali progetti di ricerca internazionali e prodotti della ricerca).

Informatica: Si prevedono attività formative di inizializzazione informatica presso il nostro Ateneo, finalizzate all'acquisizione di abilità nell'utilizzo di linguaggi di scrittura come il sistema LATEX per la preparazione di testi scientifici, nell'utilizzo dell'architettura GRID e di calcolo parallelo per l'elaborazione di grandi set di dati.

Gestione della ricerca, della conoscenza dei sistemi di ricerca e dei sistemi di finanziamento: Si prevede una serie di seminari specialistici da parte di esperti del settore inerenti la gestione della ricerca a livello nazionale ed internazionale, il coordinamento di gruppi di ricercatori e le modalità di ricerca dei canali di finanziamento nazionali ed internazionali al fine di fornire ai dottorandi le giuste abilità per la compilazione di progetti di finanziamento anche internazionali.

Valorizzazione dei risultati della ricerca e della proprietà intellettuale: Si prevedono seminari specialistici inerenti la valorizzazione dei risultati della ricerca e della proprietà intellettuale. Saranno svolti da docenti coinvolti in esperienze di ricerca nazionale ed internazionale, nonché da personale docente e/o funzionari delle strutture di Ateneo operante nel campo dell'attrazione di risorse e della valorizzazione della proprietà intellettuale. Tale attività favorirà la partecipazione dei dottorandi a seminari ed eventi culturali sia in Italia che all'estero.

Offerta formativa e articolazione in CFU

L'impegno complessivo è di 180 crediti formativi, distribuiti uniformemente sui tre anni di corso (60 CFU per ogni singolo anno). L'attività formativa prevede durante il I anno l'acquisizione di 22 CFU ottenuti grazie alla frequenza di insegnamenti (lezioni frontali) tenuti da docenti del collegio di Dottorato di Ricerca in Fisica dell'Università degli Studi di Messina. Ogni CFU equivale a 6 ore di lezioni frontali. Il restante numero di crediti formativi (38 CFU) viene attribuito dal collegio docenti alle attività connesse con la ricerca specifica dei singoli dottorandi, incluse le attività di partecipazione a seminari, congressi, scuole, soggiorni all'estero e alla redazione in lingua inglese nel volume del report annuale di dottorato (Activity Report) dell'attività di ricerca svolta. Infine, l'acquisizione dei 38 CFU potrà essere completata con attività a scelta libera. I 60 CFU del II e III anno, saranno acquisiti con attività formative connesse alla ricerca specifica dei singoli dottorandi incluse le partecipazioni a congressi, scuole, soggiorni all'estero e su territorio nazionale e la redazione della tesi finale di dottorato durante il III anno. Anche per il II e III anno, l'acquisizione dei CFU annuali potrà essere completata con attività a scelta libera.

Nello specifico, i crediti formativi sono così distribuiti:

I ANNO

- Cicli di lezioni (n. 22 CFU).
- Attività individuale di ricerca da discutere per il passaggio all'anno successivo al primo (n. 23 CFU).
- Redazione in lingua inglese dell'attività di ricerca svolta nel volume del report annuale del DdR in Fisica (Activity Report, ISSN 2038-5889) (n. CFU 10)
- Partecipazione a seminari, congressi, scuole, soggiorni all'estero e in Italia (n. max CFU 8).
- Attività a scelta libera (n. max CFU 8).

II ANNO

- Attività individuale di ricerca da discutere per il passaggio all'anno successivo al secondo (n. 23 CFU).
- Redazione in lingua inglese dell'attività di ricerca svolta nel volume del report annuale del DdR in Fisica (Activity Report, ISSN 2038-5889) (n. CFU 10).
- Partecipazione a seminari, congressi, scuole, soggiorni all'estero e in Italia, presentazione di contributi sotto forma di abstract, poster o come relatore (n. max CFU 25).
- Attività a scelta libera (n. max CFU 8).

III ANNO

- Stesura tesi e relativa discussione (n. CFU 35).
- Attività individuale di ricerca da discutere per l'ammissione all'esame finale (n. 23 CFU).
- Attività a scelta libera (n. max CFU 8).

Legenda per l'attribuzione dei crediti alle attività formative a scelta

- Soggiorno di ricerca all'estero di tipo Erasmus o di altro tipo del dottorando, sarà valutata dal consiglio dei docenti ai fini dell'attribuzione dei crediti formativi e della sua quantificazione
- La frequenza di corsi di specializzazione o di attività formative certificabili connesse con l'attività formativa e di ricerca del dottorando sarà valutata dal consiglio dei docenti ai fini dell'attribuzione dei crediti formativi e della sua quantificazione
- La pubblicazione di articoli scientifici su rivista, di saggi in volume, di capitoli di libro o di monografia, per la quale farà fede la data di accettazione del contributo o la pubblicazione del volume, sarà valutata dal consiglio dei docenti ai fini dell'attribuzione dei crediti formativi e della sua quantificazione
- L'attività di tutorato degli studenti nei corsi di Laurea e Laurea magistrale dell'Università Messina sarà valutata dal consiglio dei docenti ai fini dell'attribuzione dei crediti formativi e della sua quantificazione
- L'attività di didattica integrativa sarà valutata dal consiglio dei docenti ai fini dell'attribuzione dei crediti formativi e della sua quantificazione

Carattere Internazionale del Dottorato

Alcuni fra i principali Atenei e centri di ricerca internazionali con i quali i componenti del collegio dei docenti intrattengono collaborazioni di ricerca:

- Academy of Science of Czech Republic (ASCR) and PALS Laboratory of Prague (Repubblica Ceca)
- Rutherford Appleton Laboratory, Didcot-Oxfordshire (UK)
- Budapest Neutron Centre, Budapest (Ungheria)
- Riken Cluster for Pioneering Research, Wako, Saitama (Giappone)
- University of Bonn, Bonn (Germania)
- University of Novosibirsk, Novosibirsk (Russia)
- Budker Institute for Nuclear Physiscs, Novosibirsk (Russia)
- Institut Laue-Langevin (ILL) Grenoble (Fr)
- CERN, Ginevra (CH)
- IPPLM, Warsaw (PL)
- Military University of Technology (MUT), Warsaw (PL)

OFFERTA FORMATIVA CICLO XXXV

Anno Accademico 2019-2020

6 Posti ciascuno con borsa di studio

Una delle 6 borse di studio è stata assegnata su progetto finanziato nell'ambito del Programma Operativo Complementare Ricerca e Innovazione 2014 – 2020 (POC R&I), Asse Tematico 1 "Capitale Umano" – Azione I.1 "Dottorati Innovativi con caratterizzazione industriale"

Attività di formazione

Linguistica: Si prevedono attività formative in lingua Inglese finalizzate a facilitare la stesura della tesi finale in inglese e ad incentivare le molteplici collaborazioni scientifiche internazionali peculiari del percorso di dottorato. Infine, è ormai consolidata l'organizzazione di una "giornata di studio" in occasione della quale i dottorandi sono invitati a redigere in inglese un lavoro sul Report Annuale (ISSN 2038-5889) del DdR in Fisica riguardante l'attività di ricerca svolta annualmente.

Informatica: Si prevedono attività formative di inizializzazione informatica presso il nostro Ateneo, finalizzate a fornire ai dottorandi abilità nell'utilizzo di linguaggi di scrittura come il sistema LATEX per la preparazione di testi scientifici, nell'utilizzo dell'architettura GRID e di calcolo parallelo per l'elaborazione di grandi set di dati.

Gestione della ricerca, della conoscenza dei sistemi di ricerca e dei sistemi di finanziamento: Si prevede una serie di seminari specialistici da parte di esperti del settore inerenti la gestione della ricerca a livello nazionale ed internazionale, il coordinamento di gruppi di ricercatori e le modalità di ricerca dei canali di finanziamento nazionali ed internazionali al fine di fornire ai dottorandi le giuste abilità per la stesura di progetti di finanziamento anche internazionali.

Valorizzazione dei risultati della ricerca e della proprietà intellettuale: Si prevedono seminari specialistici inerenti la valorizzazione dei risultati della ricerca e della proprietà intellettuale. Saranno svolti da docenti coinvolti in esperienze di ricerca nazionale ed internazionale, nonché da personale docente e/o funzionari delle strutture di Ateneo operante nel campo dell'attrazione di risorse e della valorizzazione della proprietà intellettuale.

Offerta formativa e articolazione in CFU

L'impegno complessivo è di 180 crediti formativi, distribuiti uniformemente sui tre anni di corso (60 CFU per ogni singolo anno). Nello specifico, i crediti formativi saranno così distribuiti:

I ANNO

- Cicli di lezioni e attività formativa specialistica (n. 18 CFU).
- Attività individuale di ricerca da discutere per il passaggio all'anno successivo al primo (n. 23 CFU).
- Redazione in lingua inglese dell'attività di ricerca svolta nel volume del report annuale del DdR in Fisica (Activity Report, ISSN 2038-5889) (n. CFU 10).
- Partecipazione a seminari, congressi, scuole, soggiorni all'estero e in Italia (n. max CFU 10).
- Attività a scelta libera (n. max CFU 8).

II ANNO

- Attività individuale di ricerca da discutere per il passaggio all'anno successivo al secondo (n. 23 CFU).
- Redazione in lingua inglese dell'attività di ricerca svolta nel volume del report annuale del DdR in Fisica (Activity Report, ISSN 2038-5889) (n. CFU 10).
- Partecipazione a seminari, congressi, scuole, soggiorni all'estero e in Italia, presentazione di contributi sotto forma di abstract, poster o come relatore (n. max CFU 25).
- Attività a scelta libera (n. max CFU 8).

III ANNO

- Stesura tesi e relativa discussione (n. CFU 35).
- Attività individuale di ricerca da discutere per l'ammissione all'esame finale (n. 23 CFU).
- Attività a scelta libera (n. max CFU 8).

Legenda per l'attribuzione dei crediti alle attività formative a scelta

- Soggiorno di ricerca all'estero di tipo Erasmus o di altro tipo del dottorando, sarà valutata dal consiglio dei docenti ai fini dell'attribuzione dei crediti formativi e della sua quantificazione
- La frequenza di corsi di specializzazione o di attività formative certificabili connesse con l'attività formativa e di ricerca del dottorando sarà valutata dal consiglio dei docenti ai fini dell'attribuzione dei crediti formativi e della sua quantificazione
- La pubblicazione di articoli scientifici su rivista, di saggi in volume, di capitoli di libro o di monografia, per la quale farà fede la data di accettazione del contributo o la pubblicazione del volume, sarà valutata dal consiglio dei docenti ai fini dell'attribuzione dei crediti formativi e della sua quantificazione
- L'attività di tutorato degli studenti nei corsi di Laurea e Laurea magistrale dell'Università Messina sarà valutata dal consiglio dei docenti ai fini dell'attribuzione dei crediti formativi e della sua quantificazione
- L'attività di didattica integrativa sarà valutata dal consiglio dei docenti ai fini dell'attribuzione dei crediti formativi e della sua quantificazione. Si precisa che le attività formative a scelta non possono superare la totalità di 8 CFU per ogni singolo anno di corso. I crediti formativi in esubero, dunque, non saranno computati ai fini del raggiungimento della soglia annua.

Carattere Internazionale del Dottorato

Alcuni fra i principali Atenei e centri di ricerca internazionali con i quali i componenti del collegio dei docenti intrattengono collaborazioni di ricerca:

- Academy of Science of Czech Republic (ASCR) and PALS Laboratory of Prague (Repubblica Ceca)
- Rutherford Appleton Laboratory, Didcot-Oxfordshire (UK)
- Budapest Neutron Centre, Budapest (Ungheria)
- Joint Institute for Nuclear Research, Dubna (Russia)
- University of Bonn, Bonn (Germania)
- University of Novosibirsk, Novosibirsk (Russia)

- Budker Institute for Nuclear Physiscs, Novosibirsk (Russia)
- Institut Laue-Langevin (ILL) Grenoble (Fr)
- Laboratoire Lèon Brillouin (LLB), Saclay (Fr)
- ESRF – European Synchrotron Radiation Facility, Grenoble (Fr)
- CERN, Ginevra (CH)
- IPPLM, Warsaw (PL)
- Military University of Technology (MUT), Warsaw (PL)
- Centro di Ricerca RIKEN (Giappone).

Collegio dei Docenti del Dottorato di Ricerca in Fisica

Collegio dei Docenti del Dottorato di Ricerca in Fisica

Docente	e-mail
1. Branca Caterina	cbranca@unime.it
2. Calabretta Michele	michele.calabretta@st.com
3. Caridi Francesco	fcaridi@unime.it
4. Corsaro Carmelo	ccorsaro@unime.it
5. Costa Dino	dcosta@unime.it
6. Crupi Vincenza	vincenza.crupi@unime.it
7. Curatolo Maria Cristina	cristina.curatolo@sifigroup.com
8. Cutroneo Mariapompea	cutroneo@ujf.cas.cz
9. Di Stefano Omar	odistefano@unime.it
10. Fazio Enza	enfazio@unime.it
11. Gucciardi Pietro	Gucciardi@me.cnr.it
12. Iati' Maria Antonia	mariaantonia.iati@cnr.it
13. Magazù Salvatore	smagazu@unime.it
14. Majolino Domenico	domenico.majolino@unime.it
15. Mandaglio Giuseppe	giuseppe.mandaglio@unime.it
16. Maragò Onofrio	marago@me.cnr.it
17. Munaò Gianmarco	gmunao@unime.it
18. Neri Fortunato	fortunato.neri@unime.it
19. Orecchio Barbara	barbara.orecchio@unime.it
20. Patanè Salvatore	salvatore.patane@unime.it
21. Presti Debora	dpresti@unime.it
22. Prestipino Giarritta Santi	sprestipino@unime.it
23. Puglisi Rosaria Anna	rosaria.puglisi@imm.cnr.it
24. Saija Franz	saija@me.cnr.it
25. Saija Rosalba	rosalba.saija@unime.it
26. Savasta Salvatore	salvatore.savasta@unime.it
27. Sergi Alessandro	alessandro.sergi@unime.it
28. Silipigni Letteria	letteria.silipigni@unime.ut
29. Stassi Roberto	roberto.stassi@unime.it
30. Torrisi Lorenzo	lorenzo.torrisi@unime.it
31. Trifirò Antonio	atrifiro@unime.it
32. Trimarchi Marina	marina.trimarchi@unime.it
33. Trusso Sebastiano	trusso@me.cnr.it
34. Venuti Valentina	valentina.venuti@unime.it
35. Wanderlingh Ulderico	ulderico.wanderlingh@unime.it

Tesi ed Argomenti di Ricerca Studenti del Dottorato di Ricerca in Fisica

Tesi degli Studenti del Dottorato di Ricerca in Fisica Ciclo XXXIV

DOTTORANDO	TITOLO DELLA TESI	TUTOR CO-TUTOR
Dott. Giovanni Borgh gborgh@unime.it	Silicon nanowires: a new perspective for an old material	Prof. S. Patanè Dott.ssa R.A. Puglisi
Dott. Sergio Gurgone sgurgone@unime.it	Myoelectric control and functional Near-Infrared spectroscopy in cognitive neurosciences: applications to neuro-motor control and neurological disorders	Prof.ssa V. Venuti Dott. G. Acri
Dott.ssa Bruna Mazza bruna.mazza93@gmail.com	Defects and traps electrical characterization in 4H-SiC PowerMOSFET	Prof. S. Patanè Ing. C. Belfiore
Dott. Daniele Pistone daniele.pistone@hotmail.it	Applications of Monte Carlo simulation in internal dosimetry of radiopharmaceuticals employed in nuclear medicine	Prof. G. Mandaglio Prof. E. Amato
Dott. Paolo Polimeno polimenop@unime.it	Electromagnetic scattering calculations for optical trapping and space applications	Prof.ssa R. Saija Dott. O. Maragò Dott.ssa M.A. Iatì
Dott. Davide Romano dromano@unime.it	Natural radioactivity due to radon in northeastern Sicily (Italy): application, measurement and radiological hazard	Prof. S. Magazù Dott. F. Italiano Dott. G. Sabatino

VALUTATORI dei lavori di TESI

DOTTORANDO	REFEREE
Dott. Giovanni BORGH	1) Prof. Jost Adam, *University of Southern Denmark (DK)* 2) Prof. Francesco Fuso, *Università di Pisa (PI)*
Dott. Sergio GURGONE	1) Prof. Domenico Prattichizzo, *Università degli Studi di Siena (SI)* 2) Prof. Marco Bove, *Università degli Studi di Genova*
Dott.ssa Bruna MAZZA	1) Dott. Mattia Rossetti, *STMicroelectronics, Agrate Brianza (MB)* 2) Dott. Patrick Fiorenza, *Consiglio Nazionale delle Ricerche – Istituto per la Microelettronica e Microsistemi (CNR-IMM), Catania*
Dott. Daniele PISTONE	1) Dr. Manuel Bardies, *Cancer Research Institute of Montpellier - Montpellier University (F)* 2) Prof.ssa Susanna Guatelli, *University of Wollongong - Australia*
Dott. Paolo POLIMENO	1) Prof. Alessandro Veltri, *Universidad de San Francisco de Quito in Quito, Ecuador* 2) Dott. Cesare Cecchi Pestellini, *Istituto Nazionale di astrofisica (INAF)*
Dott. Davide ROMANO	1) Prof. Galip Yuce, *Hacettepe University (Ankara, TUR)* 2) Dott.ssa Alessandra Sciarra, *INGV Sez. Roma1, Roma*

Argomenti di Ricerca del Dottorato in Fisica
Cicli XXXV, XXXVI

CICLO XXXV		
DOTTORANDO	**ARGOMENTO DI RICERCA**	**TUTOR & CO-TUTOR**
Dott.ssa Laura Anoldo laura.anoldo@unime.it	Metodologie spettroscopiche applicate al Carburo di Silicio (Sic) per la diagnostica dei meccanismi di Fallimento	Prof. S. Patane' Dott.ssa S. Bevilacqua
Dott. Letterio Biondo lbiondo@unime.it	Exotic hadrons search using the CLAS 12 detector at Jefferson Lab	Prof. G. Mandaglio Dott. M. Battaglieri
Dott.ssa Rosa Musotto rosa.musotto@unime.it	Modellizzazione fisica delle interazioni neuro-gliali tramite tecniche e metodologie fisico-numeriche per l'acquisizione e l'elaborazione multiscala di dati sperimentali funzionali alla realizzazione di unità di elaborazione basate su sinapsi tripartita in un network fortemente interconnesso	Prof. U. Wanderlingh Ing. G. Pioggia
Dott.ssa Antonina Rosano antonina.rosano@unime.it	Studio delle risonanze adroniche in collisioni ultra-relativistiche tra ioni pesanti con il rivelatore ALICE presso il Large Hadron Collider del CERN	Prof. G. Mandaglio Prof.ssa M. Trimarchi
Dott.ssa Abir Saidi abir.saidi@unime.it	Modeling of optical forces on particulate matter in specific atmospheric and planetary environments	Prof. R. Saija Dott.ssa M. A. Iatì

CICLO XXXVI		
DOTTORANDO	**ARGOMENTO DI RICERCA**	**TUTOR & CO-TUTOR**
Dott. Grazzi Stefano stefano.grazzi@unime.it	Studio su particolari forme della materia (mesoni ibridi, multiquarks o stati composti esclusivamente di gluoni). Esperimenti CLAS12 e GLUEX presso JEFFERSON LAB, Esperimento EEE	Prof. G. Mandaglio Dott. M. Battaglieri
Dott. Grimaldi Andrea andrea.grimaldi@unime.it	Probabilistic computing, spintronics, Ising machines	Prof.ssa V. Crupi Prof. G. Finocchio
Dott.ssa Malta Giuliana giumalta@unime.it	Indagini su scala sub-micrometrica del componente MOM in dispositivi elettronici BCD	Prof. S. Patanè Dott. G. Romano
Dott. Mauceri Fabio fabio.mauceri@unime.it	Cavity QED in extreme coupling regime	Dott. O. Di Stefano Prof. S. Savasta
Dott. Mercurio Alberto alberto.mercurio@unime.it	Cavity QED in electron systems	Prof. S. Savasta Dott. V. Macrì
Dott. Piccione Giuseppe Gabriele giupiccione@unime.it	Wide BANDGAB semiconductors for power electronics: Innovative Technologies and Open Issues	Prof. S. Patanè Dott. M. Calabretta
Dott. Risitano Fabio fabio.risitano@unime.it	Fisica degli ioni pesanti	Prof.ssa M. Trimarchi Dott.ssa Brunilde Gnoffo
Dott. Semprebello Agostino semprebelloa@unime.it	Tecniche spettroscopiche e modelli previsionali	Prof. S. Magazù Dott.ssa M. T. Caccamo
Dott.ssa Vacalebre Martina martina.vacalebre@unime.it	Architetture ottiche innovative per applicazioni oftalmologiche	Prof.ssa E. Fazio Ing.re M. C. Curatolo
Dott. Bronte Ciriza David brontecir@ipcf.cnr.it	Active matter in optical landscapes	Prof.ssa R. Saija/Dott. O. Maragò Dott.ssa M. A. Iatì

Pubblicazioni degli Studenti del Dottorato di Ricerca in Fisica

2021

PUBBLICAZIONI 2021 XXXV Ciclo

Laura Anoldo

1. Anoldo, L., Triolo, C., Panarello, S., Garesci, F., Russo, S., Messina, A.A., Calabretta, M., Patane, S. Study of the Thermomechanical Strain Induced by Current Pulses in SiC-Based Power MOSFET (2021). IEEE Electron Device Letters, 42 (7), art. no. 9420737, pp. 1089-1092. https://www.scopus.com/inward/record.uri?eid=2-s2.0-85105865395&doi=10.1109%2fLED.2021.3077064&partnerID=40&md5=f50a559a251acb7b7f7863d9d2cb9344

   DOI: 10.1109/LED.2021.3077064

2. Anoldo, L., Piccione, G.G., Mauromicale, G., Sitta, A., Fazio, E., Calabretta, M., Lionetto, A., Messina, A., Di Guardo, M., Patanè, S. Thermal simulation of a 7kW interleaved module for fast automotive charger (2021). 21st IEEE International Conference on Environment and Electrical Engineering and 2021 5th IEEE Industrial and Commercial Power System Europe, EEEIC / I and CPS Europe 2021 - Proceedings. https://www.scopus.com/inward/record.uri?eid=2-s2.0-85126454729&doi=10.1109%2fEEEIC%2fICPSEurope51590.2021.9584683&partnerID=40&md5=7cfbb1e06137606b33a790e535096609

   DOI: 10.1109/EEEIC/ICPSEurope51590.2021.9584683

⋆⋆⋆⋆⋆

Letterio Biondo

1. Biondo, L. et al. (CLAS Collaboration). Improved Λp Elastic Scattering Cross Sections between 0.9 and 2.0 GeV/c as a Main Ingredient of the Neutron Star Equation of State (2021). Physical Review Letters, 127 (27), art. no. 272303. https://www.scopus.com/inward/record.uri?eid=2-s2.0-85122493659&doi=10.1103%2fPhysRevLett.127.272303&partnerID=40&md5=40c89736c0c269c6b17a795183c77c45

   DOI: 10.1103/PhysRevLett.127.272303

2. Biondo, L. et al. First Measurement of Timelike Compton Scattering (2021). Physical Review Letters, 127 (26), art. no. 262501. https://www.scopus.com/inward/record.uri?eid=2-s2.0-85122535205&doi=10.1103%2fPhysRevLett.127.262501&partnerID=40&md5=d9df4004673df8b01f48b9e41739e6db

   DOI: 10.1103/PhysRevLett.127.262501

⋆⋆⋆⋆⋆

Antonia Rosano

1. Rosano A. et al. (A Large Ion Collider Experiment Collaboration). Measurement of the Cross Sections of Ξ_c^0 and Ξ_c^+ Baryons and of the Branching-Fraction Ratio BR($\Xi_c^0 \to \Xi^- e^+ \nu_e$)/BR ($\Xi_c^0 \to \Xi^- \pi^+$) in pp Collisions at $\sqrt{s}$ =13 TeV (2021) Physical Review Letters, 127 (27), art. no. 272001, .

   DOI: 10.1103/PhysRevLett.127.272001

2. Rosano A. et al. (ALICE Collaboration). Inclusive J / Ψ production at midrapidity in pp collisions at $\sqrt{s}$=13 TeV (2021). European Physical Journal C, 81 (12), art. no. 1121, . DOI: 10.1140/epjc/s10052-021-09873-4

3. Rosano A. et al. (ALICE Collaboration). Λ_c^+ Production and Baryon-to-Meson Ratios in pp and p-Pb Collisions at $\sqrt{s_{NN}}$ =5.02 TeV at the LHC (2021). Physical Review Letters, 127 (20), art. no. 202301.

   DOI: 10.1103/PhysRevLett.127.202301

⋆⋆⋆⋆⋆

Abir Saidi

1. Polimeno P., Magazzù A., Iatì M.A., Saija R., Folco L., Bronte Ciriza D., Donato M.G., Foti A., Gucciardi P.G., Saidi A., Cecchi-Pestellini C., Jimenez Escobar A., Ammannito E., Sindoni G., Bertini I., Della Corte V., Inno L., Ciaravella A., Rotundi A., Maragò O.M. Optical tweezers in a dusty universe: Modeling optical forces for space tweezers applications (2021). European Physical Journal Plus, 136 (3), art. no. 339.
   DOI: 10.1140/epjp/s13360-021-01316-z

PUBBLICAZIONI 2021 XXXVI Ciclo

Stefano Grazzi

1. Grazzi, S. et al. (EEE Collaboration). The Extreme-Energy Events Project: a bridge between school and professional research (2021). Proceedings of Science, 397, art. no. 112. https://www.scopus.com/inward/record.uri?eid=2-s2.0-85123692930&partnerID=40&md5=4028eb9a062b780758e5cf783fb2741a

2. Grazzi, S. et al. First results from PolarquEEEst (2021). Proceedings of Science, 358, art. no. 371. https://www.scopus.com/inward/record.uri?eid=2-s2.0-85127507410&partnerID=40&md5=afac0a297a8bda2da5
a4fd970d4bb4e6

3. Grazzi, S. et al. The Extreme Energy Events experiment (2021). Proceedings of Science, 358, art. no. 389. https://www.scopus.com/inward/record.uri?eid=2-s2.0-85127501935&partnerID=40&md5=7611054ffc8f4f0abb4a1d947c7320cf

4. Grazzi, S. et al. The cosmic muon and detector simulation framework of the extreme energy events (EEE) experiment (2021). European Physical Journal C, 81 (5), art. no. 464. https://www.scopus.com/inward/record.uri?eid=2-s2.0-85107000667&doi=10.1140%2fepjc%2fs10052-021-09237-y&partnerID=40&md5=66f9482b24570
a8689fd5c950a8c3ce9

   DOI: 10.1140/epjc/s10052-021-09237-y

5. Grazzi, S. et al. The eee multigap resistive plate chambers as tracking devices to monitor the stability of a civil building (2021). Journal of Instrumentation, 16 (4), art. no. C04003. https://www.scopus.com/inward/record.uri?eid=2-s2.0-85105446240&doi=10.1088%2f1748-0221%2f16%2f04%2fC04003&partnerID=40&md5=d67595a5fe6476
77058e532ca497bddb

   DOI: 10.1088/1748-0221/16/04/C04003

6. Grazzi, S. et al. Transition to ecological gas mixtures in EEE MRPC-based muon telescopes (2021). Proceedings of Science, 398, art. no. 739. https://www.scopus.com/inward/record.uri?eid=2-s2.0-85129378740&partnerID=40&md5=ecc43f97427474fade3acc4b60e1310c

⋆⋆⋆⋆⋆

Andrea Grimaldi

1. Aadit, N.A., Grimaldi, A., Carpentieri, M., Theogarajan, L., Finocchio, G., Camsari, K.Y. Computing with Invertible Logic: Combinatorial Optimization with Probabilistic Bits (2021). Technical Digest - International Electron Devices Meeting, IEDM, 2021-December, pp. 40.3.1-40.3.4. https://www.scopus.com/inward/record.uri?eid=2-s2.0-85117079665&doi=10.1109%2fIEDM19574.2021.9720514&partnerID=40&md5=3c779efd8dd7036140
584f16194c9493

   DOI: 10.1109/IEDM19574.2021.9720514

2. Raimondo, E., Giordano, A., Grimaldi, A., Puliafito, V., Carpentieri, M., Zeng, Z., Tomasello, R., Finocchio, G. Reliability of Neural Networks Based on Spintronic Neurons (2021). IEEE Magnetics Letters, 12. https://www.scopus.com/inward/record.uri?eid=2-s2.0-85111595875&doi=10.1109%2fLMAG.2021.3100317&partnerID=40&md5=f570349bebebcf510a5547c75cdff9db

   DOI: 10.1109/LMAG.2021.3100317

3. Grimaldi A., Sergi A., Messina A. Evolution of a non-hermitian quantum single-molecule junction at constant temperature (2021). Entropy, 23 (2), art. no. 147, pp. 1 - 22. DOI: 10.3390/e23020147 https://www.scopus.com/inward/record.uri?eid=2-s2.0-85100335105&doi=10.3390%2fe23020147&partnerID=40&md5=7f633572f92d1106afa824246b3a781a

⋆⋆⋆⋆⋆

Giuseppe Gabriele Piccione

1. Anoldo L., Piccione G.G., Mauromicale G., Sitta A., Fazio E., Calabretta M., Lionetto A., Messina A., Di Guardo M., Patanè S. Thermal simulation of a 7kW interleaved module for fast automotive charger (2021). 21st IEEE International Conference on Environment and Electrical Engineering and 2021 5th IEEE Industrial and Commercial Power System Europe, EEEIC / I and CPS Europe 2021 - Proceedings

   DOI: 10.1109/EEEIC/ICPSEurope51590.2021.9584683

⋆⋆⋆⋆⋆

Fabio Risitano

1. Cardella G., Favela F., Martorana N.S., Acosta L., Camaiani A., De Filippo E., Gelli N., Geraci E., Gnoffo B., Guazzoni C., Immè G., Marín-Lámbarri D.J., Lanzalone G., Lombardo I., Lo Monaco L., Maiolino C., Nannini A., Pagano A., Pagano E.V., Papa M., Pirrone S., Politi G., Pollacco E., Quattrocchi L., Risitano F., Rizzo F., Russotto P., Sicari V.L., Santonocito D., Trifirò A., Trimarchi M. Investigating γ-ray decay of excited ^{12}C levels with a multifold coincidence analysis (2021). Physical Review C, 104 (6), art. no. 064315

   DOI: 10.1103/PhysRevC.104.064315

⋆⋆⋆⋆⋆

Agostino Semprebello

1. Rizza, U., Donnadieu, F., Magazu, S., Passerini, G., Castorina, G., Semprebello, A., Morichetti, M., Virgili, S., Mancinelli, E. Effects of variable eruption source parameters on volcanic plume transport: Example of the 23 november 2013 paroxysm of etna (2021). Remote Sensing, 13 (20), art. no. 4037. https://www.scopus.com/inward/record.uri?eid=2-s2.0-85117170914&doi=10.3390%2frs13204037&partnerID=40&md5=1b82997d971a369ec4d6a93adf44377e

   DOI: 10.3390/rs13204037

2. Gugliandolo, G., Caccamo, M.T., Castorina, G., Chillemi, D.L., Famoso, F., Munao, G., Raffaele, M., Schifilliti, V., Semprebello, A., Magazu, S. A machine learning-based predictive model for risk assessment in airport areas (2021). 2021 IEEE International Workshop on Metrology for AeroSpace, MetroAeroSpace 2021 - Proceedings, art. no. 9511695, pp. 53-57. https://www.scopus.com/inward/record.uri?eid=2-s2.0-85114014698&doi=10.1109%2fMetroAeroSpace51421.2021.9511695&partnerID=40&md5=8e70815c2b1bc7c0ec28949b499fbc1f

   DOI: 10.1109/MetroAeroSpace51421.2021.9511695

3. Semprebello, A., Magazù, S., Caccamo, M.T. Joseph fourier: A didactic path crossing life and works (2021). AAPP Atti della Accademia Peloritana dei Pericolanti, Classe di Scienze Fisiche, Matematiche e Naturali, 99, art. no. 99S1A8. https://www.scopus.com/inward/record.uri?eid=2-s2.0-85116849029&doi=10.1478%2fAAPP.99S1A8&partnerID=40&md5=1e1f9068849789fae37fd4e0523181e7

   DOI: 10.1478/AAPP.99S1A8

4. Marrara, S., Semprebello, A., Vasi, S. Physical and historical principles of ionizing radiations with the flipped classroom method (2021). AAPP Atti della Accademia Peloritana dei Pericolanti, Classe di Scienze Fisiche, Matematiche e Naturali, 99, art. no. 99S1A38, . https://www.scopus.com/inward/record.uri?eid=2-s2.0-85116738080&doi=10.1478%2fAAPP.99S1A38&partnerID=40&md5=26f514623d63fdcc24190a229336e60a

   DOI: 10.1478/AAPP.99S1A38

⋆⋆⋆⋆⋆

David Bronte Ciriza

1. Bronte-Ciriza, D., Birkenfeld, J.S., de la Hoz, A., Curatolo, A., Germann, J.A., Villegas, L., Varea, A., Martínez-Enríquez, E., Marcos, S. Estimation of scleral mechanical properties from air-puff optical coherence tomography (2021). Biomedical Optics Express, 12 (10), pp. 6341-6359. https://www.scopus.com/inward/record.uri?eid=2-s2.0-85115887835&doi=10.1364%2fBOE.437981&partnerID=40&md5=b573ae7795bf4d7a36a62ba02bf479d2

   DOI: 10.1364/BOE.437981

2. Polimeno, P., Magazzù, A., Iatì, M.A., Saija, R., Folco, L., Bronte Ciriza, D., Donato, M.G., Foti, A., Gucciardi, P.G., Saidi, A., Cecchi-Pestellini, C., Jimenez Escobar, A., Ammannito, E., Sindoni, G., Bertini, I., Della Corte, V., Inno, L., Ciaravella, A., Rotundi, A., Maragò, O.M. Optical tweezers in a dusty universe: Modeling optical forces for space tweezers applications (2021) European Physical Journal Plus, 136 (3), art. no. 339. https://www.scopus.com/inward/record.uri?eid=2-s2.0-85103354814&doi=10.1140%2fepjp%2fs13360-021-01316-z&partnerID=40&md5=2654bf5deafea074083ade28cebad471

   DOI: 10.1140/epjp/s13360-021-01316-z

3. Birkenfeld, J.S., Bronte-Ciriza, D., De La Hoz, A., Curatolo, A., Villegas, L., Germann, J.A., Varea, A., Martinez-Enriquez, E., Marcos, S. Method to estimate scleral mechanical properties from air-puff optical coherence tomography: A proof-of-concept (2021). Progress in Biomedical Optics and Imaging - Proceedings of SPIE, 11921, art. no. 1192107. https://www.scopus.com/inward/record.uri?eid=2-s2.0-85122918965&doi=10.1117%2f12.2615454&partnerID=40&md5=6e4f0bb0f3552e4b2c088f9e50bac585

   DOI: 10.1117/12.2615454

4. Magazzú, A., Bronte Ciriza, D., Polimeno, P., Musolino, A., Donato, M.G., Foti, A., Gucciardi, P.G., Iatí, M.A., Saija, R., Folco, L., Rotundi, A., Maragó, O.M. Cosmic dust investigation by optical tweezers for space exploration (2021). Optics InfoBase Conference Papers, art. no. AF2D.5. https://www.scopus.com/inward/record.uri?eid=2-s2.0-85120475430&partnerID=40&md5=e4f572ec9c07b440f0ce932a55aa435d

5. Birkenfeld, J.S., Bronte-Ciriza, D., de la Hoz, A., Curatolo, A., Villegas, L., Germann, J.A., Varea, A., Martínez-Enríquez, E., Marcos, S. Method to estimate scleral mechanical properties from air-puff optical coherence tomography: a proof-of-concept (2021). Optics InfoBase Conference Papers, art. no. ETh2B.2.

Alta Formazione
e
Ricerca Scientifica

Alta Formazione e Ricerca Scientifica
Via Consolato del Mare 41 (Palazzo Mariani)

Dottorati di Ricerca

I Corsi di Dottorato di Ricerca hanno la finalità di fornire agli iscritti competenze di alto livello e qualificazione scientifica, acquisite mediante attività di formazione alla ricerca e di didattica strutturata, necessarie all'esercizio di mansioni di ricerca e di elevata professionalità presso Enti pubblici e privati, rappresentano, pertanto, il terzo livello degli studi universitari.
I Corsi di Dottorato hanno durata triennale/quadriennale e prevedono la frequenza obbligatoria. Requisito di ammissione è il possesso della Laurea Specialistica e/o Magistrale o il Diploma di Laurea conseguito prima dell'entrata in vigore del D.M.5009/99 ovvero di altro titolo di studio conseguito all'estero e riconosciuto idoneo, oltre il superamento delle prove di esame previste dai Bandi di concorso emanati dall'Università e pubblicati nella Gazzetta Ufficiale della Repubblica Italiana.
Almeno la metà dei posti messi a concorso è coperta da borse di studio in parte finanziate dal MIUR e dall'Ateneo, in parte da altre Università o Enti esterni pubblici o privati.
Il titolo di Dottore di Ricerca si consegue all'atto del superamento dell'esame finale che consiste nella discussione della Tesi di Dottorato e che può essere ripetuto una sola volta.
È possibile, inoltre, ottenere una certificazione di "Doctor Europaeus" - aggiuntiva al titolo nazionale del dottorato - nel rispetto delle condizioni richieste dall'European University Association, in seguito ad un soggiorno di ricerca di almeno un trimestre, anche non continuativo, in una struttura di un altro Paese dell'Unione Europea.

https://www.unime.it/it/ricerca/dottorati-ricerca/contatti-dottorati-di-ricerca

Attività di Ricerca Post-Dottorato

L'attività Post-Dottorato può proseguire con gli Assegni di Ricerca. Queste borse di studio vengono conferite, tramite un concorso per titoli ed esami, ai possessori del titolo di Dottore di Ricerca.

L'Università degli Studi di Messina può conferire assegni di ricerca delle seguenti tipologie: Tipo A): assegni banditi dall'Ateneo e finanziati dal bilancio universitario; Tipo B): assegni interamente finanziati da strutture universitarie, a carico di progetti di ricerca, ovvero finanziati da convenzioni o contratti con enti esterni, che prevedano tali finalità. Questi assegni sono banditi autonomamente dai Dipartimenti o da altre strutture autonome dell'Ateneo, a seguito di approvazione del Consiglio della Struttura interessata che verifica la copertura economica della spesa.

Perfezionamento Estero

Le borse di perfezionamento estero hanno una durata annuale e vengono assegnate, con un concorso per titoli ed esami, ai possessori della Laurea Specialistica e/o Magistrale o il Diploma di Laurea conseguito prima dell'entrata in vigore del D.M.5009/99 ovvero di altro titolo di studio conseguito all'estero e riconosciuto idoneo; di età inferiore ai 29 anni che documentino un impegno formare di attività di perfezionamento presso istituzioni estere o internazionali di livello universitario.

Borse Private

Le borse private, o alla memoria, vengono finanziate da soggetti privati esterni all'Università e prevedono anch'esse lo svolgimento di un particolare progetto di ricerca specificato nel bando di concorso.

UNITÁ DI COORDINAMENTO TECNICO
Via Consolato del Mare 41 (Palazzo Mariani)

Responsabile

Ing. Carlo Costanzo
ccostanzo@unime.it – 090 676 8909

Staff

Sig.ra Rosita Di Perna
rdiperna@unime.it – 090 676 8502

UNITA' ORGANIZZATIVA SERVIZI ALLA RICERCA

Responsabile

Dott.ssa Maria Pia Mangano
mpmangano@unime.it – 090 676 8503

UNITA' OPERATIVA "DOTTORATI DI RICERCA"

Responsabile

Dott.ssa Angelina Venezia
avenezia@unime.it – 090 676 8716

Staff

Dott.ssa Valeria Zuccarello Marcolini
valeria.zuccarellomarcolini@unime.it – 090 6768286
Sig.ra Caterina Agnello
cagnello@unime.it

UNITA' OPERATIVA PROGRAMMI DI RICERCA INTERNAZIONALE

Responsabile

Dott.ssa Danila Nostro
danila.nostro@unime.it – 090 676 8050

D. A. Ricerca Scientifica e Internazionalizzazione

Dott.ssa Barbara Cafiso
barbara.cafiso@unime.it – 090 6768283
Dott.ssa Angela Garozzo
angela.garozzo@unime.it – 090 6768505
Dott. Fabio Paci
fabio.paci@unime.it – 090 6768281

Dipartimento di Scienze Matematiche e Informatiche, Scienze Fisiche e Scienze della Terra (MIFT)
UNIVERSITÀ DEGLI STUDI DI MESSINA

V.le F. Stagno D'Alcontres
S. Agata, Messina, Italy
e-mail: vcrupi@unime.it

ISSN: 2038-5889